

**DOKUZ EYLÜL UNIVERSITY
GRADUATE SCHOOL OF NATURAL AND APPLIED
SCIENCES**

**THE FABRICATION AND TECHNICAL
APPLICATIONS OF MULTIFUNCTIONAL
MATERIALS**

**by
Hüsnügül YILMAZ ATAY**

**March, 2013
İZMİR**

**THE FABRICATION AND TECHNICAL
APPLICATIONS OF MULTIFUNCTIONAL
MATERIALS**

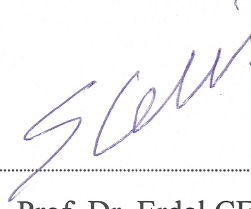
**A Thesis Submitted to the
Graduate School of Natural and Applied Sciences of Dokuz Eylül University
In Partial Fulfillment of the Requirements for the Degree of Doctor of
Philosophy in
Metallurgical and Material Science Engineering**

**by
Hüsnügül YILMAZ ATAY**

**March, 2013
İZMİR**

Ph.D. THESIS EXAMINATION RESULT FORM

We have read the thesis entitled “**THE FABRICATION AND TECHNICAL APPLICATIONS OF MULTIFUNCTIONAL MATERIALS**” completed by **HÜSNÜGÜL YILMAZ ATAY** under supervision of **PROF.DR. ERDAL ÇELİK** and we certify that in our opinion it is fully adequate, in scope and in quality, as a thesis for the degree of Doctor of Philosophy.



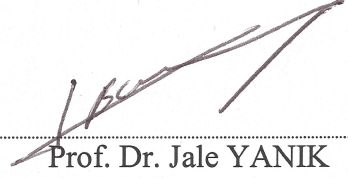
Prof. Dr. Erdal ÇELİK

Supervisor



Doç. Dr. Uğur MALAYOĞLU

Thesis Committee Member



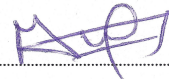
Prof. Dr. Jale YANIK

Thesis Committee Member



Prof. Dr. Ahmet TÜRK

Examining Committee Member



Doç. Dr. Mustafa TOPARLI

Examining Committee Member



Prof. Dr. Ayşe OKUR

Director

Graduate School of Natural and Applied Sciences

ACKNOWLEDGEMENTS

First of all, I would like to express my deep sense of gratitude to my advisor Prof. Dr. Erdal ÇELİK for his constructive ideas, help, constant support, guidance and contributions during my PhD research. I would also like to thank my committee members, Prof. Dr. Jale YANIK and Assoc. Prof. Dr. Uğur MALAYOĞLU for reviewing my work and offering valuable suggestions and sharing their visions about the content of my thesis.

I wish to extend my sincere thanks to Assist. Prof. Dr. Mehmet Faruk EBEOĞLUGİL at Dumlupınar University for all of his assistance. I am especially indebted to Assist. Prof. Dr. Işıl BİRLİK, Dr. Esra DOKUMACI, Mustafa EROL, Orkut SANCAKOĞLU, Kadir Cihan TEKİN and Tuncay DİKİCİ for sharing their valuable knowledge. In addition, I would like to thank to Assist. Prof. Dr. Sevinç AYDINLIK BECHTELER and Dr. Leyla ERAL DOĞAN at Izmir Institute of Technology, Meriyod ALPASLAN at Ege University and Metin NİL at VESTEL for their assistance and friendship. I would also like to express my genuine gratitude to each of people, although it would be impossible for me to name all.

The successful completion of this work has been aided by a number of people at Dokuz Eylül University. I would like to thank Assoc. Prof. Dr. İhsan YAŞA at Ege University. I would like also thank to The State Planning Organization (DPT) for infrastructure project entitled “Foundation of center for production and application of electronic materials” at Dokuz Eylül University, and to KOSGEB, TEKNOBİM Inc. and Likya Minelco Inc. for research-development and innovation project entitled “Fabrication and industrial applications of multifunctional coatings using Nano technological methods” for supporting during this study.

A special thank goes to my family for their concern, confidence and support. Finally, I extend my greatest thanks to my husband *Özgür ATAY* who unconditionally supported me. The successful completion of this study would not have been possible without his constant love and encouragement.

Hüsniğül YILMAZ ATAY

THE FABRICATION AND TECHNICAL APPLICATION OF MULTIFUNCTIONAL MATERIALS

ABSTRACT

The ability for materials to respond to the needs in a useful manner has broad technological impact. Such "smart" systems are being developed in which material properties (such as mechanical, electrical, optical or magnetic characteristics) respond to external stimuli. Composite materials are ideally suited to achieve multifunctionality since the best features of different materials can be combined to form a new material that has a broad spectrum of desired properties. In this study, the aim is to further the investigations of these types of materials and to advance the molecular understanding of novel multifunctional materials for applications across different scientific disciplines. Regarding the production of multifunctional materials; 4 types of materials will be added to polymer matrix to obtain those properties to the final product; antibacterial painting/coating, radar absorbing materials, self-healing materials and flame retardant material. In this research, an epoxy dye was converted to a multifunctional material which is capable of performing multiple functions. In order to reinforce the polyurethane/epoxy dyes, Ag nanoparticles, huntite/hydromagnesite minerals, barium hex ferrite particles and chitosan were utilized for multifunction property. Adding by those materials to the polymer matrix with different loading level and coating the substrates, different types of coated samples are obtained. Subsequently the samples were characterized by antibacterial tests, flame retardant tests, radar absorbing tests and self-healing tests. It was concluded that these materials exhibited a synergetic beneficial effects.

Keywords: Multifunctional materials, antibacterial coatings, radar absorbing materials, self-healing materials, flame retardant materials

ÇOK FONKSİYONLU MALZEMELERİN ÜRETİMİ VE TEKNİK UYGULAMALARI

ÖZ

Malzemelerin ihtiyaçlara yararlı bir şekilde cevap verme yeteneğinin büyük bir teknolojik etkisi vardır. Bu tür "akıllı" sistemlerde malzeme özellikleri (örneğin, mekanik, elektrik, optik veya manyetik özellikler gibi) dış uyaranlara yanıt verecek şekilde geliştirilmektedir. Kompozit malzemeler ideal olarak çok amaçlı yeni bir madde oluşturmak üzere farklı malzemelerin en iyi özelliklerini birleştirilebildiği için istenen geniş spektrumlu nitelikleri elde etmek açısından çok uygundur. Bu çalışmada amaç malzemelerle ilgili olarak bu tür çalışmaları ilerletmek ve farklı bilimsel disiplinlere uygulanması için gerekli olan çok fonksiyonlu malzemelerin moleküler anlayışını ilerletmektir. Çok fonksiyonlu malzemelerin üretimi nihai ürünün bu özelliklere sahip olabilmesi için polimer matrise 4 tip farklı malzeme eklenmesi şeklinde yapılır. Bu malzemeler antibakteriyel boya/kaplama, radar absorblayan malzeme, kendi kendini iyileştiren malzeme ve alev geciktirici malzemedir. Bu çalışmada, bir epoksi boya çok fonksiyonlu performansa sahip bir çokfonksiyonlu malzemeye dönüştürülmüştür. Poliüretan/epoksi boyaların güçlendirilmesi için Ag nano parçacıkları, huntit/hidromanyezit minerali, baryum hegzaferit minerali ve kitosan kullanılmıştır. Bu malzemelerin farklı oranlarda polimer matrikse eklenmesi ve altlıkların boyanması ile kaplanmış farklı numuneler elde edilmiştir. Daha sonra bu numuneler antibakteriyel, alev geciktirici, radar absorblayan ve kendi kendini iyileştirebilme testlerine tabi tutulmuşlardır. Sonuçta bu malzemelerin birbirleri adına yararlı etkiler gösterdikleri tespit edilmiştir.

Anahtar sözcükler: Çok fonksiyonlu malzemeler, antibakteriyel kaplamalar, radar absorblayabilen malzemeler, kendi kendini tamir edebilen malzemeler, alev geciktiriciler.

2.1.3.1 Minimising the Reflection	37
2.1.3.2 Calculations For Minimising Reflection.....	39
2.1.3.3 Radar Absorbing Materials	41
2.1.4 Self-Healing Property	47
2.1.4.1 Chitosan	51
2.1.4.2 Working Mechanism.....	53
2.1.4.3 Applications	54
CHAPTER THREE-EXPERIMENTAL PROCEDURE.....	59
3.1 Purpose	59
3.2 Materials	59
3.2.1 Substrate Materials	59
3.2.2 Starting Materials.....	60
3.3 Production Technique	61
3.3.1 Multifunctional Component Production	61
3.3.1.1 Antibacterial Ag Nanoparticles.....	61
3.3.1.2 Flame Retardant Nano powders	62
3.3.1.3 Radar Absorbing Powder	65
3.3.1.4 Self-healing Solution.....	67
3.3.2 Composite Coating Production.....	67
3.3.2.1 Antibacterial Coatings.....	67
3.3.2.2 Flame Retardant Coatings	69
3.3.2.3 Radar Absorbing Coatings	71
3.3.2.4 Self-healing Coatings	73
3.3.2.5 Multifunctional Coatings	74
3.4 Characterization	75
3.4.1 Ag ⁺ ion Determination.....	75
3.4.2 Glucose Determination	76
3.4.2.1 Fehling Method	76
3.4.2.2 DNS Method	77

3.4.3 The pH Determination	77
3.4.4 Turbidity Measurement.....	78
3.4.5 Particle Size Measurement.....	79
3.4.6 Differential Thermal Analysis-Thermogravimetry (DTA-TG)	81
3.4.7 Fourier Transform Infrared Spectroscopy (FTIR)	82
3.4.8 X-Ray Diffractometer (XRD)	84
3.4.9 Scanning Electron Microscopy-Energy Dispersive Spectroscopy (SEM-EDS).....	84
3.4.10 Atomic Force Microscopy (AFM).....	85
3.4.11 Vibrating Sample Magnetometer (VSM)	86
3.4.12 Scratch Testing Machine	88
3.4.13 Surface Profilometer	89
3.4.14 Antibacterial Test.....	90
3.4.14.1 Inhibition Zone Test.....	90
3.4.14.2 Percent Decreasing Test.....	91
3.4.15 Flame Retardant Test	92
3.4.15.1 Limiting Oxygen Index (LOI).....	92
3.4.15.2 UL94 Classification	93
3.4.16 Radar Absorbing Test	96
3.4.17 Self-healing Test	97

CHAPTER FOUR-RESULTS AND DISCUSSION 99

4.1 Ag Nanoparticle Added Polymeric Coatings.....	99
4.1.1 Solution Characteristics	99
4.1.1.1 Production of Ag Nanoparticles.....	99
4.1.1.2 Ag+ Ion Determination	100
4.1.1.3 Glucose Determination.....	101
4.1.1.4 Asidic/Basic Characteristics.....	101
4.1.1.5 Turbidity.....	101
4.1.1.6 Particle Size Analyzer	102

4.1.2 Coating Characteristics	103
4.1.2.1 FTIR Analysis	103
4.1.2.2 Phase Analysis	104
4.1.2.3 SEM-EDS Analysis.....	106
4.1.2.4 AFM Analysis	110
4.1.2.5 Adhesion Properties	112
4.1.2.6 Antibacterial Behaviour	115
4.2 Flame Retardant Reinforced Composite Coatings.....	122
4.2.1 Powder Characteristics	122
4.2.1.1 DTA-TG Analysis.....	122
4.2.1.2 Phase Analysis	125
4.2.1.3 SEM-EDS Analysis.....	126
4.2.2 Coating Characteristics	128
4.2.2.1 Huntite/hydromagnesite Reinforced Polymeric Coatings.....	128
4.2.2.2 Boric acid, Antimony Oxide and Huntite/hydromagnesite Reinforced Coatings	132
4.3 Barium Hexaferrite Reinforced Composite Coatings.....	150
4.3.1 Powder Characteristics	151
4.3.1.1 Phase Analysis	151
4.3.1.2 SEM Analysis	152
4.3.2 Coating Characteristics	152
4.3.2.1 FTIR Analysis	153
4.3.2.2 SEM-EDS Analysis.....	154
4.3.2.3 Magnetic Properties	156
4.3.2.4 Radar Absorbing Behaviour.....	157
4.4 Chitosan Added Composite Coatings	158
4.4.1 Colloid Characteristics.....	158
4.4.2 Coating Characteristics	158
4.4.2.1 FTIR Analysis	159
4.4.2.2 SEM-EDS Analysis.....	160
4.4.2.3 Self Healing Property.....	166

4.4.2.4 Antibacterial Property	174
4.4 Multifunctional Coatings	174
4.4.1 FTIR Analysis.....	175
4.4.2 Surface Profilometer	176
4.4.3 Adhesion Properties	176
4.4.4 Antibacterial Behaviour	177
4.4.5 Flame Retardant Properties.....	181
4.4.6 Radar Absorbing Behaviour	184
4.4.7 Self Healing Properties	186
CHAPTER FIVE-CONCLUSIONS AND FUTURE PLANS.....	191
REFERENCES.....	197

CHAPTER ONE

INTRODUCTION

Multifunctional materials systems are capable of performing multiple "primary" functions simultaneously or sequentially in time. They have been specifically developed to improve system performance by reducing the redundancy between sub-system materials and functions. Depending upon the process, any property can be given to material that was not its own characteristics (mechanical, electrical, appearance, structure, composition, antibacterial, flame retardant, radar absorbing, self-healing and/or response). These materials are usually embedded into systems whose inherent properties change favorably in order to meet performance needs (Alan et al, 2008).

This evolution establishes the need to integrate technologies from different disciplines in order to provide structural health monitoring for materials, systems, devices and structures at the micro-scale level in order to ensure their integrity. The focus is on novel concepts that effectively combine materials, mechanics and physics to produce multifunctional systems. Materials and structures research strives to attain superior combinations of higher performance, lower weight and affordability and lower cost (Alan et al, 2008).

An example of a multifunctional material is layered double hydroxides. Leroux et al. (Leroux & Nanosci, 2006) produced layered double hydroxides based on the brucite ($Mg(OH)_2$) structure, with part of the divalent metals isomorphically replaced by trivalent metals, inducing positive charges in the layers that are compensated for by interlayer hydrated anions. When intercalated with dyes layered double hydroxides act not only as filler materials for synthetic polymers but also as multifunctional materials that are capable of conferring additional properties on the polymeric matrix, such as color, transparency, photo/ultra violet (UV) and thermal stability, and flame-retardant capability (Leroux & Nanosci, 2006).

Researchers in China (Li, 2009) have further advanced the nanotechnology application of silver by developing a novel multi-action Nano fiber membrane containing four active components, each playing a different role in the membrane's excellent antibacterial function. Using an electro spinning technique, they have prepared a new kind of free-standing antibacterial membranes, which contain silver, silver bromide, titanium dioxide, and hydroxyapatite as four active components. In this antibacterial membrane, each component serves a different function: apatite as the adsorption material for capturing bacteria, silver nanoparticles as the release-active antibacterial agent, silver bromide nanoparticles as the visible sensitive and release-active antibacterial agent, and titanium dioxide as the UV sensitive antibacterial material and substrate for other functional components (Li, 2009).

Lynch and Dawson (2008) aim to further the fundamental physical knowledge of these types of materials. Coupled to the potential of smart materials are those with multiple functionalities. Some investigations seek to advance the molecular understanding of novel multifunctional materials for applications across different scientific disciplines, including Nano electronics, energy and medicine. It is developed a structural model of a protein nanoparticle which the key role of protein-nanoparticle interactions in Nano medicine and Nano toxicity has. Highly selective protein adsorption, added to the fact that particles can reach subcellular locations, results in significant new potential impacts for nanoparticles on protein interactions and cellular behavior (Lynch & Dawson, 2008).

Owing to its antimicrobial property, it can be seen the large number of investigations about silver in literature. Sondi and Salopek (2007) reported antimicrobial activity of silver nanoparticles against *E. coli* as a model for gram-negative bacteria. Butkus, Labare, Starke, Moon & Talbot (2004) studied the synergistic effect of silver ions and UV radiation on a RNA virus, which can efficiently enhance the effectiveness of UV radiation. Yamanaka, Hara & Kudo. (2005) investigated the antibacterial efficacy of silver ions using *E. coli* as a model organism with the help of energy-filtering transmission electron microscope (TEM), two dimensional electrophoreses and matrix-assisted laser desorption ionization-

time-of-flight mass spectrometry. They conclude that bactericidal action of silver ions is basically caused due to the interaction of silver ions with ribosome and the suppression and expression of enzymes and proteins necessary for ATP production. Pal, Tak & Song (2007) investigated the antibacterial properties of silver nanoparticles of different shapes and found that the antibacterial efficacy of silver nanoparticles is shape dependent. Shrivastava, Bera, Roy, Singh, Ramachandrarao & Dash (2007) reported synthesis of silver nanoparticles in the size range of 10–15 nm and its dose dependent effect on the gram-negative and gram-positive microorganisms.

Although huntite hydromagnesite mineral has been found in the last century and its flame retardant property has recently been studied, there are a few investigations in the literature. Fernandez, Haurie, Formosa, Chimenos, Antunes & Velasco (2009) studied as a non-halogenated flame retardant filler in a 28 % vinyl acetate (VA) content poly(ethylene-co-vinyl acetate) matrix. The solid was characterized by X-ray fluorescence (XRF) and the crystalline phases determined by X-ray diffraction (XRD), composed predominantly of $Mg(OH)_2$ and calcium and magnesium carbonates. Basfar & Bae (2009) used flame retardants including magnesium hydroxide (MH) and huntite hydromagnesite (HH) to develop halogen free flame retardant (HFFR) compounds based on ethylene vinyl acetate (EVA) for wire and cable applications. Cone calorimeter and limiting oxygen index (LOI) results showed that cross-linking affects not only mechanical properties, but also flame retardancy. Haurie, Fernandez, Velasco, Chimenos, Cuesta & Espiell (2006) used synthetic hydromagnesite in combination with aluminum hydroxide (ATH) and compared with commercial flame retardants like magnesium hydroxide (MH) and natural hydromagnesite huntite in a polyolefin system of low-density polyethylene/poly(ethylene-co-vinyl acetate) (LDPE/EVA). They showed that synthetic hydromagnesite could be an alternative solution to the use of MH in non-halogenated flame retardant systems in EVA. Morgan, Cogen, Opperman & Harris (2007) used natural magnesium carbonate (magnesite), synthetic magnesium carbonate (hydromagnesite), and hydromagnesite/huntite blends were combined with EVA and tested for flame retardancy effectiveness with the cone calorimeter. They reported

some polymer–clay (organically treated montmorillonite and magadiite) + magnesium carbonate flame retardant results which showed that the nanocomposite yielded mixed results.

There are some investigations about radar absorbing materials and barium hexaferrite in the literature. To illustrate this, Aksit, Onar, Ebeoglugil, Birlik, Celik & Ozdemir (2009), produced fabrics with microwave absorbing properties in broad band. For this purpose, the cotton fabrics were coated with polyaniline by using chemical oxidative polymerization method. They concluded that microwave absorber for a textile material can be successfully produced by this process. Jotania, Khomane, Chauhan, Menon & Kulkarni (2008) investigated the preparation of W-type hexaferrite particles with the composition $\text{BaCa}_2\text{Fe}_{16}\text{O}_{27}$ by microemulsion and a stearic acid sol–gel method with/without surfactant at various sintering temperatures. A simple sol–gel method in the presence of different types of surfactants as well as in a microemulsion system is used for the preparation of barium–calcium hexaferrite particles. It has been observed that the type of surfactant plays a crucial role in deciding the morphology of the particles. The magnetic studies carried out using a vibrating sample magnetometer (VSM) showed that low coercivity was found in the presence of surfactants. Moaffari, Taheri & Amighian (2009) prepared a series of barium hexaferrite nanoparticles ($\text{BaO}\cdot n\text{Fe}_2\text{O}_3$) with different n values by the sol–gel method, using goethite and barcarbonate as raw materials. The results show that the samples have nonzero coercivities, which shows the particle size are not less than the critical size of Ba ferrite and then are not superparamagnet.

Inasmuch as self-healing is a new trend in material science; there are a few literature knowledges about this subject. White et al. (2001) reported of a completely autonomous man-made self-healing material. They reported an epoxy system containing microcapsules. These microcapsules were filled with a liquid-thermosetting monomer. If a microcrack occurs in this system, the microcapsule will rupture and the monomer will fill the crack. Ghosh & Urban (2009) reported the development of polyurethane networks that exhibit self-repairing characteristics upon exposure to ultraviolet light. The network consists of an oxetane-substituted

chitosan precursor incorporated into two-component polyurethane. Upon mechanical damage of the network, four-member oxetane rings open to create two reactive ends. When exposed to ultraviolet light, chitosan chain scission occurs, which forms crosslinks with the reactive oxetane ends, thus repairing the network. Yoon et al. (2012) synthesized self-healing polymeric materials with branched architectures and reversible cross-linking functionalities at the periphery of branches by atom transfer radical polymerization (ATRP). Poly(n-butyl acrylate) grafted star polymers were prepared by chain extension ATRP from cross-linked cores comprised of poly(ethylene glycol diacrylate). They demonstrated the suitability of grafted multiarm polymer architectures as building blocks of self-healing polymeric materials and pointed to the importance of low intrinsic viscosity of material and high accessibility of functional groups responsible for healing.

1.1 Organization of the Thesis

The aim of this thesis is designing a material to accomplish multiple performance objectives in a single system to respond the required needs as mentioned above; antibacterial, flame retardant, radar absorbing and self-healing. There is no any literature knowledge regarding as kind of multifunctional material having those four properties. In this study, polyurethan and epoxy dyes were converted to multifunctional materials which are capable of performing multiple functions. In order to reinforce the polyurethan and epoxy dyes, Ag nanoparticles, huntite and hydromagnesite minerals, barium hexaferrite particles and chitosan were used for multifunction property. Adding by those materials to the polymer matrix with different loading level and coating the substrates, different types of coated samples are obtained and subsequently the samples were characterized by antibacterial tests, flame retardant tests, radar absorbing tests and self-healing tests. These materials exhibited synergitic beneficial effects.

With this context, chapters can be explained in details. Chapter one provides a brief introduction to the area of research and the research objectives of this thesis. In Chapter two, a comprehensive literature reviews concerning multifunctional

properties/behaviors and mechanisms such as antibacterial, flame retardant, radar absorbing and self-healing in details. Chapters three, the experimental procedures of polymeric paints/coatings with Ag nanoparticles, huntite and hydromagnesite minerals, barium hexaferrite particles and chitosan are explained. In Chapter four, the results concerning pure polymeric dye and effect of Ag nanoparticles, huntite and hydromagnesite minerals, barium hexaferrite particles and chitosan additives on the stability of coating structure are demonstrated and discussed in details. Characterization of pure and reinforced dye coatings is also analyzed in the same chapter. The conclusion and future plans are summarized in Chapter five.

CHAPTER TWO

THEORITICAL BACKGROUND

2.1 Multifunctional Properties

Multifunctional materials can respond to environmental stimuli by exhibiting particular changes in some of their properties. By integrating sensors and actuators into structures, real-time monitoring of potentially damaging structural responses within large-scale infrastructures becomes possible. Such responses might include, for example, fatigue cracks, degradation of structural connections or bearing wear in rotating machinery (Lau, Lu, Varadan, Chang, Tu & Lam, 2008).

Designing materials to accomplish multiple performance objectives in a single system gets the materials to respond the required needs (Figure 2.1). Encompassing traditional systems, such as firehardened structural composite armor, to newer systems include blast, sensors and actuators, power harvesting, communications, and electro-optical capabilities (Mult. Mat., 2012).



Figure 2.1 An example of multifunctional material - pocket knife (Mult. Mat., 2012).

Multifunctional structural materials possess attributes beyond the basic strength and stiffness that typically drive the science and engineering of the material for structural systems. Structural materials can be designed to have integrated electrical,

magnetic, optical, locomotive, power generative, and possibly other functionalities that work in synergy to provide drawbacks that reach beyond that of the sum of the individual capabilities. Materials of this kind have tremendous potential to impact future structural performance by reducing size, weight, cost, power consumption, and complexity while improving efficiency, safety, and versatility (Nemat-Nasser, Plaisted, Starr & Amirkhizi, 2005).

Nature offers numerous examples of materials that serve multiple functions. Biological materials routinely contain sensing, healing, actuation, and other functions built into the primary structures of an organism. The human skin, for instance as seen from Figure 2.2, consists of many layers of cells, each of which contains oil and perspiration glands, sensory receptors, hair follicles, blood vessels, and other components with functions other than providing the basic structure and protection for the internal organs. These structures have evolved in nature over eons to the level of seamless integration and perfection with which they serve their functions. Scientists now seek to mimic these material systems in designing synthetic multifunctional materials using physics, chemistry, and mathematics to their advantage in competing with the unlimited time frame of nature's evolutionary design process. The multifunctionality of these materials often occurs at scales that are nano through macro and on various temporal and compositional levels (Nemat-Nasser, Plaisted, Starr & Amirkhizi, 2005).

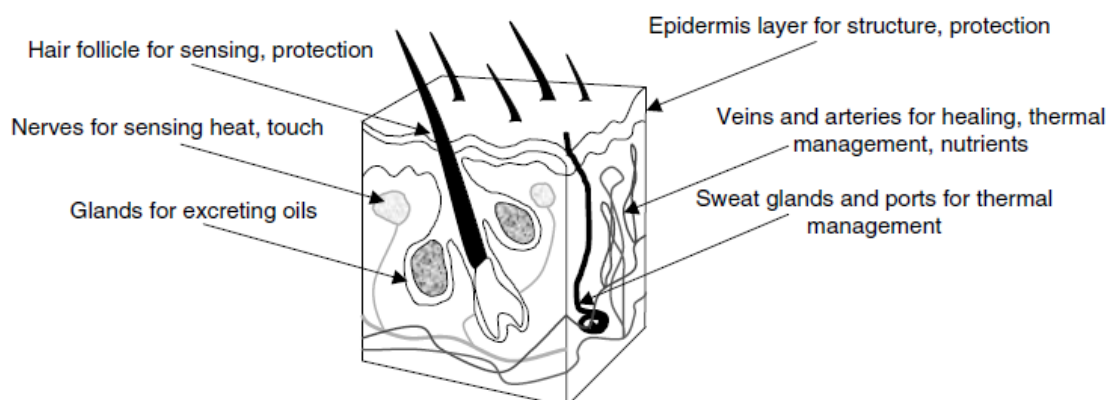


Figure 2.2 Illustration of the many integrated functions within the human skin (Nemat-Nasser, Plaisted, Starr & Amirkhizi, 2005).

Composite materials are ideally suited to achieve multifunctionality since the best features of different materials can be combined to form a new material that has a broad spectrum of desired properties. Due to that, it has been integrated multiple functions into reinforced materials, and those composites can also perform other functions with the basic structural attributes (Torquato, Hyun & Donev 2003).

These advanced materials outperform conventional materials with superior properties such as high electrical, magnetic, optical and mechanical strength. They can possess novel properties including the ability to recognise shape or sense changes in the environment and respond. The development of multifunctional materials can even lead to the design completely new products including medical implants, miniature energy storage devices, display devices, etc. New or improved advanced materials with superior performance for specific applications are nano materials, polymers, super/metallic alloys, ceramic materials, biological materials composites, electronic materials, semiconductors and so on (Selvasekarapandian, 2012).

2.1.1 Antibacterial Behaviours

Antibacterial and antimicrobial materials/systems are becoming increasingly important not only in the hospital and healthcare environments, but also for laboratory, home, marine and some industrial applications. Materials and systems are being developed to prevent the build up, spread and transfer of harmful bacteria and viruses, as well as actively disabling them (Crocker, 2007).

For centuries silver has been in use for the treatment of burns and chronic wounds (Rai, Yadav & Gade, 2008). As early as 1000 B.C, it was used to make water potable (Castellano, Shafii, Ko, Donate, Wright & Mannari 2007). Silver nitrate was used in its solid form and was known by different terms like, “lunar caustic” in English, “lapis infernale” in Latin and “Pierre infernale” in French (Klasen, 2000). In 1700, silver nitrate was used for the treatment of venereal diseases, fistulae from salivary glands, and bone and perianal abscesses (Landsdown, 2002). In the 19th century,

granulation tissues were removed using silver nitrate to allow epithelization and promote crust formation on the surface of wounds. Varying concentrations of silver nitrate was used to treat fresh burns. In 1881, Carl S.F. Crede cured ophthalmia neonatorum using silver nitrate eye drops. Crede's son, B. Crede designed silver impregnated dressings for skin grafting (Klasen, 2000). In the 1940s, after penicillin was introduced the use of silver for the treatment of bacterial infections minimized (Rai, Yadav & Gade 2009). Silver again came in picture in the 1960s when Moyer introduced the use of 0.5 % silver nitrate for the treatment of burns. He proposed that this solution does not interfere with epidermal proliferation and possess antibacterial property against *Staphylococcus aureus*, *Pseudomonas aeruginosa* and *Escherichia coli*. In 1968, silver nitrate was combined with sulfonamide to form silver sulfadiazine cream, which served as a broad-spectrum antibacterial agent and was used for the treatment of burns. Silver sulfadiazine is effective against bacteria like *E. coli*, *S. aureus*, *Klebsiella sp.* and *Pseudomonas sp.* It also possesses some antifungal and antiviral activities (Rai, Yadav & Gade 2009). Recently, due to the emergence of antibiotic-resistant bacteria and limitations of the use of antibiotics the clinicians have returned to silver wound dressings containing varying level of silver (Chopra, 2007).

The antimicrobial property of silver is related to the amount of silver and the rate of silver released. Silver in its metallic state is inert but it reacts with the moisture in the skin and the fluid of the wound and gets ionized (Rai, Yadav & Gade 2009). The ionized silver is highly reactive, as it binds to tissue proteins and brings structural changes in the bacterial cell wall and nuclear membrane leading to cell distortion and death (Landsdown, 2002).

Silver sulfadiazine is a combination of silver and sulfadiazine. Silver sulfadiazine is used as a 1 % water-soluble cream. Silver sulfadiazine works as a broad-spectrum antibiotic. Silver sulfadiazine binds to cell components including DNA and cause membrane damage (Atiyeh, Costagliola, Hayek & Dibo, 2007). It achieves bacterial inhibition by binding to the base pairs in DNA helix and thus inhibits transcription. In similar way it also binds to phage DNA (McDonnell & Russell 1999).

Silver zeolite is made by complexing alkaline earth metal with crystal aluminosilicate, which is partially replaced by silver ions using ion exchange method. In Japan, ceramics are manufactured by coating with silver zeolite to apply antimicrobial property (Matsumura, Yoshikata, Kunisaki & Tsuchido, 2003)

Unlike antibiotics, which are usefull only to bacteria, silver is effective to other microorganisms such as anaerobic bacteria, viruses, yeasts, and fungus. Silver works for destroying the enzymes of those microorganisms for disabling them. Regarding those microorganisms are not able to improve any resistance to silver, because it attacks their food source, but not them directly (Thurman, & Gerba, 1989, Brown, 1998). Moreover, on account of the fact that silver ion has higher redox potential, it will be dissociated after the bacteria are destroyed. Then it will continue to destroy other bacteria. The process will be recycled as shown in Figure 2.3 (Texcare, 2012).

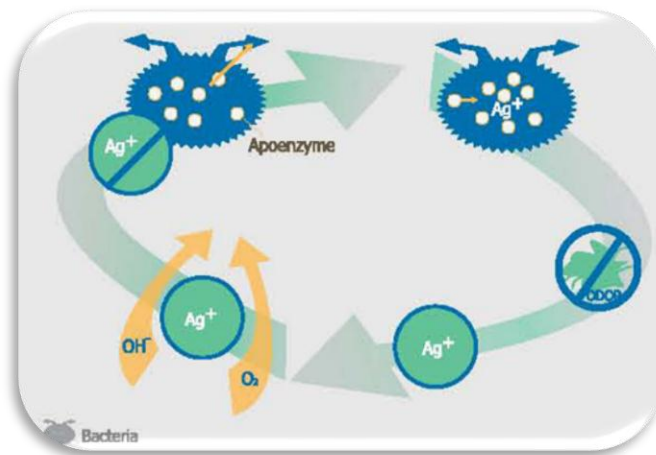


Figure 2.3 The sterilizing process of silver (Texcare, 2012)

As mentioned above that silver has many superiorities compared with antibiotics, Figure 2.4 shows the comparison of working mechanism of antibiotics and silver ions. It can be seen from the figure that unlike antibiotics, silver ions attack the bacteria all around the cell and bacteria can not develop any resistance (Donnan, 2012).

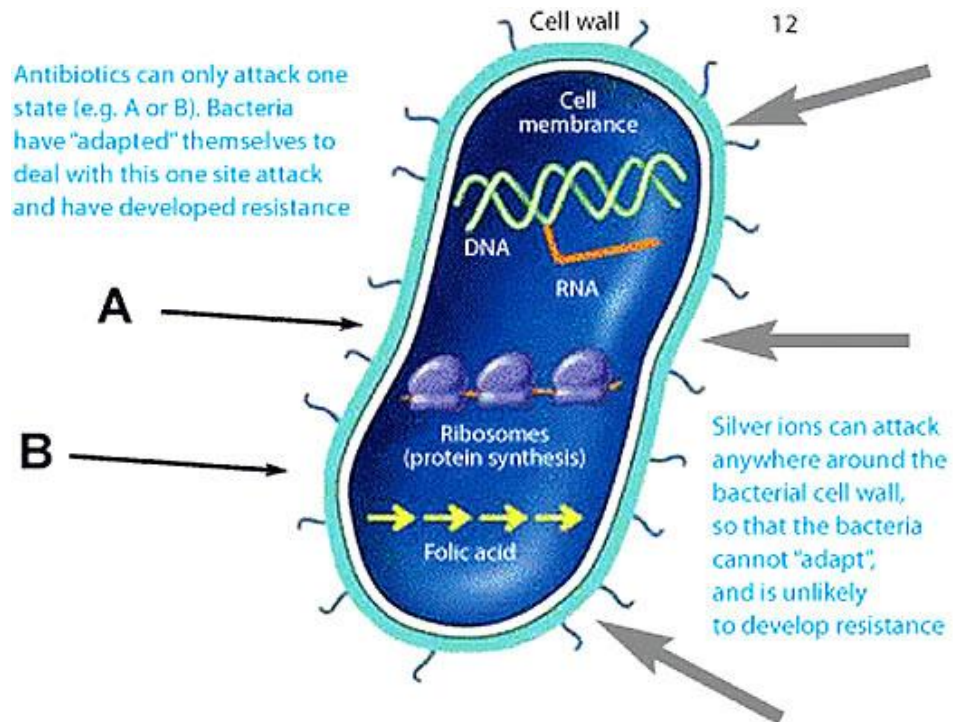


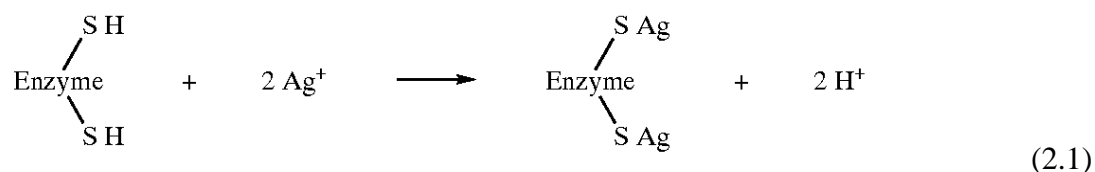
Figure 2.4 Comparison of antibiotics and silver ions (Donnan, 2012)

The Ag-antimicrobial coating inhibits the growth of bacteria, molds, fungi and other microbes through the release of silver (Ag) ions. The controlled release of silver ions provides continuous antimicrobial protection for the product for the life of the coating. Silver ions are released from the coating; come in contact with microbes and the microbes are inhibited (Thurman, & Gerba, 1989, Brown, 1998).

Researchers at numerous universities and facilities have presented findings for ionic silver's antimicrobial mechanism, a simplified version of which follows (Thurman, & Gerba, 1989, Brown, 1998). Monovalent or ionic silver (silver with a +1 charge) has an affinity for hydrogen ions, joining with them on the sulfhydryl groups present in microbes, disrupting electron transfer and respiration in bacteria and other microbes.

Other non-ionic forms of silver employ other, equally effective mechanisms, such as catalyzing the interaction of atomic oxygen (O) with the sulfhydryl group resulting in an OH molecule and a sulfur bond that prevents further respiration within the microbe (Brown, 1998).

The exact mechanism of action of silver on the microbes is still not known but the possible mechanism of action of metallic silver, silver ions and silver nanoparticles have been suggested according to the morphological and structural changes found in the bacterial cells. But in general, the antimicrobial activity of the silver can be explained by the following reaction (Equation 2.1) (Yan & Cheng, 2005).



The mechanism of action of silver is linked with its interaction with thiol group compounds found in the respiratory enzymes of bacterial cells. Silver binds to the bacterial cell wall and cell membrane and inhibits the respiration process (Klasen, 2000). In case of *E. coli*, silver acts by inhibiting the uptake of phosphate and releasing phosphate, mannitol, succinate, proline and glutamine from *E. coli* cells (Yan & Cheng 2005).

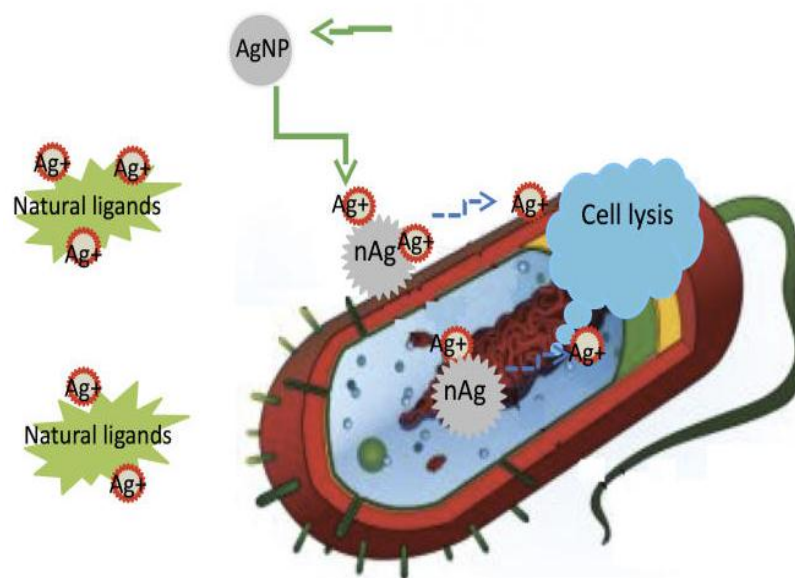


Figure 2.5 A bacteria lysis with silver nanoparticles (Xiu, Zhang, Puppala, Colvin & Alvarez, 2012)

Figure 2.5 depicts bacterial lysis. Silver ions delivered by nanoparticles to bacteria promote lysis, the process by which cells break down and ultimately die, which makes silver nanoparticles a superior and widely used antibacterial agent. Silver ions, not the particles themselves, are toxic to bacteria. Ligands in the vicinity of a bacterium can bind silver ions and prevent them from reaching their target (Xiu, Zhang, Puppala, Colvin & Alvarez, 2012).

The mechanism for the antimicrobial action of silver ions is not properly understood however, the effect of silver ions on bacteria can be observed by the structural and morphological changes. It is suggested that when DNA molecules are in relaxed state the replication of DNA can be effectively conducted. But when the DNA is in condensed form it loses its replication ability hence, when the silver ions penetrate inside the bacterial cell the DNA molecule turns into condensed form and loses its replication ability leading to cell death. Also, it has been reported that heavy metals react with proteins by getting attached with the thiol group and the proteins get inactivated (Feng, Wu, Chen, Cui, Kim & Kim 2000, Liao, Read, Pugh, Furr & Russell, 1997). When silver nanoparticles enter the bacterial cell it forms a low molecular weight region in the center of the bacteria to which the bacteria conglomerates thus, protecting the DNA from the silver ions. The nanoparticles preferably attack the respiratory chain, cell division finally leading to cell death. The nanoparticles release silver ions in the bacterial cells, which enhance their bactericidal activity (Feng et al., 2000, Morones, Elechiguerra, Camacho, Ramirez, 2005, Song, Ko, Oh, Lee, 2006).

2.1.1.1 Effect of Size and Shape on The Antimicrobial Activity of Nanoparticles

The nanoparticles smaller than 10 nm interact with bacteria and produce electronic effects, which enhance the reactivity of nanoparticles. Thus, it is corroborated that the bactericidal effect of silver nanoparticles is size dependent (Raimondi, Scherer, Kotz & Wokaun, 2005).

2.1.1.2 Use of Silver Nanoparticles for Impregnation

Silver nanoparticles are also considered as candidate for coating medical devices. Medical devices coated with silver ions or metallic silver proved to be disappointing in clinical tests. The reason for this might be the inactivation of metallic silver when it comes in contact with blood plasma and the lack of durability of the coatings. The metallic silver also failed to improve the antimicrobial activity. The use of silver nanoparticles for impregnation of polymeric medical devices increases their antimicrobial efficacy (Riley, Classen, Stevens & Burke, 1995, Furno, Morley, Wong, Sharp, Arnold & Howdle, 2004). Silver nanoparticles can be used for the impregnation of medical devices and lead to promising antimicrobial activity. They are also used for coating surgical masks. The advantage of impregnation of medical devices with silver nanoparticles is that it protects both outer and inner surfaces of devices and there is continuous release of silver ions providing antimicrobial activity (Li, Leung, Song & Newton, 2006). Nonetheless, the antibacterial efficiency of silver nanoparticles reduces after washing process (Furno, Morley, Wong, Sharp, Arnold & Howdle, 2004).

2.1.1.3 Silver Coated Textile Fabrics

Due to the fact that silver is non-toxic and possesses antimicrobial properties, it has encouraged workers to use silver nanoparticles in different textile fabrics. In this direction, silver nanocomposite fibres were prepared containing silver nanoparticles incorporated inside the fabric but from the scanning electron microscopic study it was concluded that the silver nanoparticles incorporated in the sheath part of fabrics possessed significant antibacterial property compared to the fabrics incorporated with silver nanoparticles in the core part (Yeo & Jeong, 2003).

2.1.1.4 Silver Toxicity

Silver nanoparticles in most studies are suggested to be non-toxic. But due to their small size and variable properties they are suggested to be hazardous to the

environment. The cytotoxicity of silver nanoparticles to the mitochondrial activity increased with the increase in the concentration of silver nanoparticles (Rai, Yadav & Gade, 2009). It can be concluded that the use of nanoparticles in biomedical and therapeutic applications has opened up a wide area to nanotechnology in the fields like electronics, engineering, medicine, etc. but the possible side effects of nanoparticles have not been much studied hence, detailed study needs to be carried out before the introduction of products related to nanomedicine in the market (Yeo & Jeong, 2003).

2.1.1.5 Applications

Silver has been known to possess strong antimicrobial properties both in its metallic and nanoparticle forms hence, it has found a variety of applications in different fields: Treatment of burns and various infections (Feng, Wu, Chen, Cui & Kim, 2000). The Fe_3O_4 attached Ag nanoparticles can be used for the treatment of water and easily removed using magnetic field to avoid contamination of the environment (Gong, Li, He, Wang, Hu & Tan, 2007). Silver sulfadiazine depicts better healing of burn wounds due to its slow and steady reaction with serum and other body fluids (Fox & Modak, 1974). The nanocrystalline silver dressings, creams, gel effectively reduce bacterial infections in chronic wounds (Leaper, 2006). The silver nanoparticle containing poly vinyl nano-fibres also show efficient antibacterial property as wound dressing (Jun, Yuan-Yuan, Shao-hai, Shao-feng & Zhong-yi, 2007). The silver nanoparticles are reported to show better wound healing capacity, better cosmetic appearance and scarless healing when tested using an animal model (Tian, Wong, Ho, Lok, Yu & Che, 2006). Silver impregnated medical devices like surgical masks and implantable devices show significant antimicrobial efficiency (Furno, Morley, Wong, Sharp, Arnold & Howdle, 2004). Environmental-friendly antimicrobial nanopaint can be developed (Kumar, Vemula, Ajayan & John, 2008). Silica gel micro-spheres mixed with silica thio-sulfate are used for long lasting antibacterial activity (Gupta & Silver, 1998). Silver zeolite is used in food preservation, disinfection and decontamination of products (Nikawa, Hamada, Rahardjo, Nakaando, 1997). Silver nanoparticles can be used for water filtration (Jain &

Pradeep, 2005). Figure 2.6 shows an example of application areas of silver; antibacterial carpets (Puretex, 2012).

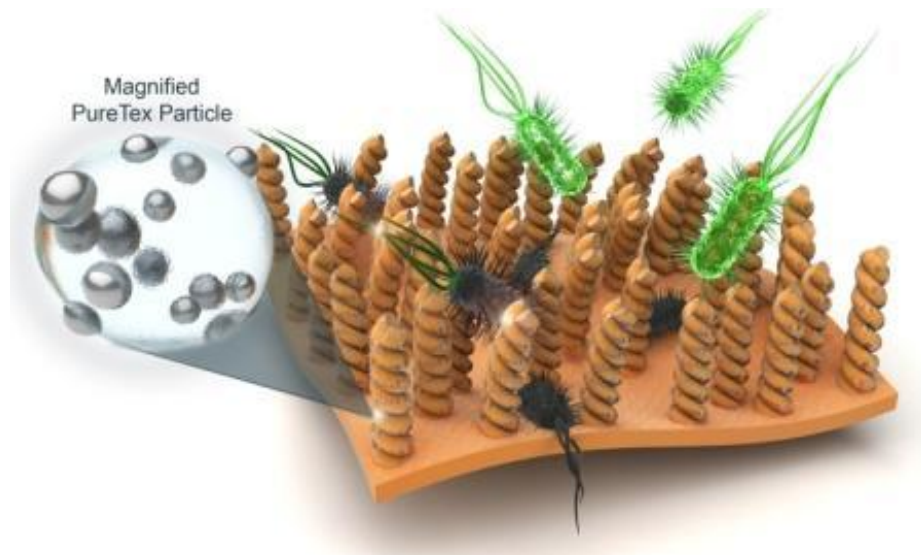


Figure 2.6 Antibacterial carpet with silver nanoparticles (Puretex,2012).

2.1.1.6 Different Synthesing Methods of Silver Nanoparticles

In general, silver nanoparticles are synthesized using various techniques resulting in different shapes and sizes for use in numerous applications. The synthesis techniques are categorized into top-down and bottom-up approaches (Balaguera-Gelves, 2006). The top-down techniques use silver metal in its bulk form, then, mechanically reduce its size to the nanoscale via specialized methodologies such as lithography and laser ablation (Amendola, Polizzi & Meneghetti, 2007). The bottom-up (also known as self-assembly) technique involves the dissolution of silver salt into a solvent and the subsequent addition of a reducing agent, with the supplemental use of stabilizing agents, if warranted, to prevent agglomeration of nanoparticles. Indeed, the solvents and reducing agents used in these processes affect the physical and morphological characteristics of manufactured silver nanoparticles. Furthermore, the incorporation of silver nanoparticles in nanocomposites and bimetallic nanoparticles may augment environmental concerns due to the uncertainty surrounding the inclusion of another metal or polymer, possibly increasing nanoparticle toxicity (Tan, Erol, Attygalle, Du & Sukhishvili, 2007 & Tolaymat, Genaidy, Schekel, Luxton &

Suidan 2009). An analysis of the evidence is presented separately by metal salt precursor, solvents, and reducing and stabilizing agents (Kildeby, Roge, Larsen, Petersen, Riis & Bozhevolnyi 2005).

Silver salt precursors are used in bottom-up techniques to produce ionic silver, which can be reduced and precipitated to form nanoparticles. Silver nitrate (AgNO_3) is the most widely used salt precursor accounting for almost 83 % of those reported in studies of general and specific synthesis methods (Lee, K.J., Lee, Y., Shim, Jun, Cho & Joung, 2007).

Solvents are used to solubilize silver salts and other chemicals included in the synthesis processes. Even though organic and inorganic solvents are used in synthesizing silver nanomaterials, approximately 80 % of synthesis processes use water as a solvent in the reported studies. A good share of organic solvents is particularly used in the production of relatively high particle concentrations coupled with predefined shapes and sizes (Dorjnamjin, Ariunaa & Shim, 2008, Yang, Lee & Too, 2005).

In the context of the bottom-up methodology, a reducing agent is a chemical agent, plant extract, biological agent, or irradiation method that provides the free electrons needed to reduce silver ions and to form silver nanoparticles. In spite the fact that a strong reducing agent such as sodium borohydride (NaBH_4) tends to produce a narrow range of small monodispersed particles, a weaker reducing agent such as ascorbic acid produces larger particle sizes (Chen, Feng, Wang, Li, Zhang & Qian, 2007). In essence, the four hydrogen atoms participate in the reduction process leaving a surface particle that is contaminated with borides (Sardar, Park & Shumaker-Parry, 2007).

A stabilizing agent (also known as capping agent) is used in the synthesis process to prevent nanoparticles from aggregation and to control the size of final product, with agglomeration mainly caused by excess surface energy and high thermodynamic instability of the nanoparticle surface (Olenin, Krutyakov, Kudrinskii & Lisichkin, 2008). The growing importance of materials prevents

microbial adhesion: antimicrobial effect of medical devices containing silver. The properties required for polymers resist bacterial colonisation for use in medical devices. The increase in antibiotic-resistant microorganisms has prompted interest in the use of silver as an antimicrobial agent as indicated in Figure 2.7 (Monteiro, Gorup, Takamiya, Ruvollo-Filho, Camargo & Barbosa, 2009).

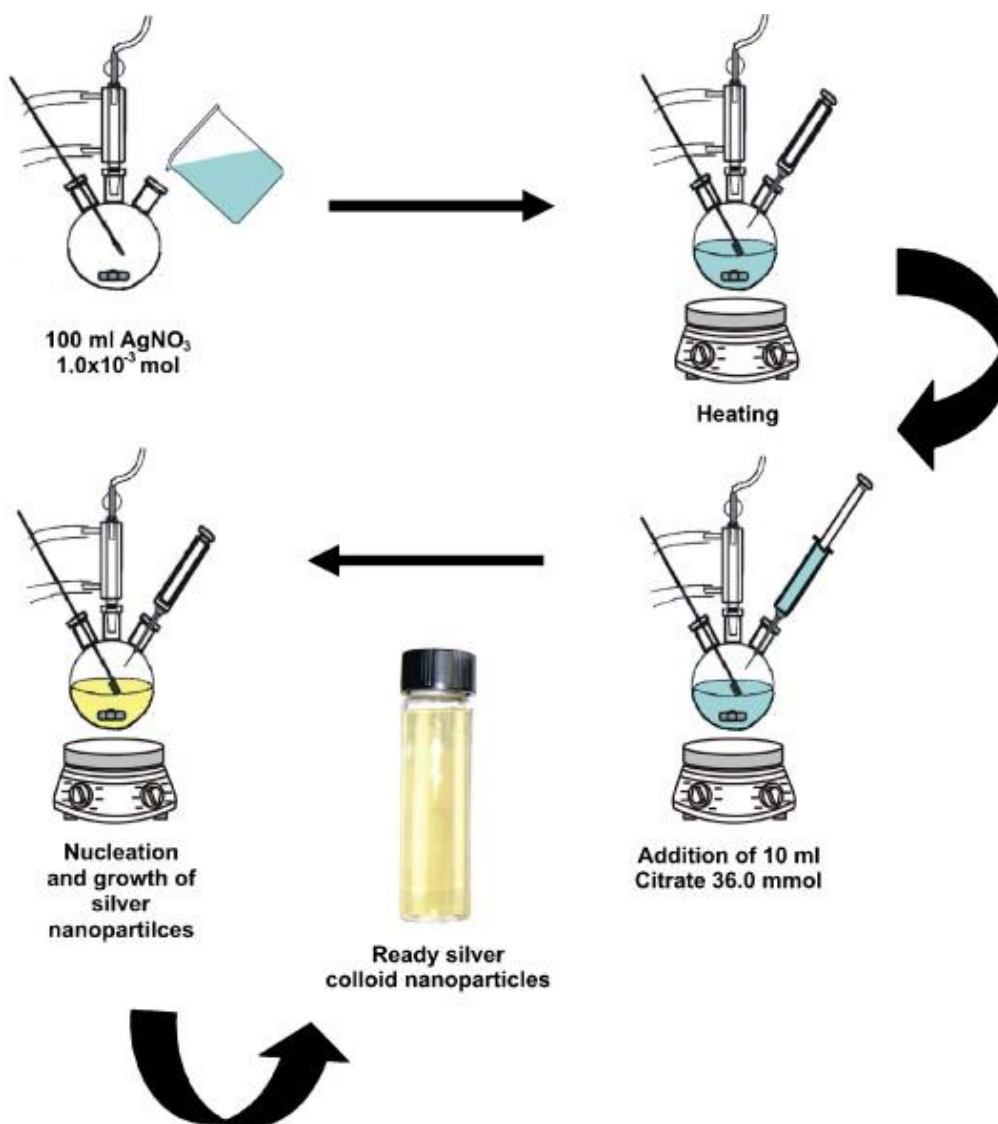


Figure 2.7 Schematic illustration of the synthesis of silver (Monteiro, Gorup, Takamiya, Ruvollo-Filho, Camargo & Barbosa, 2009).

As mentioned earlier, silver has been used as an antibacterial agent by civilizations throughout the world for thousands of years. It was also used for storing

wine to prevent spoilage, storing milk to keep it fresh, storing drinking water to safe it from bacteria, algae, etc. Nevertheless, notwithstanding its fantastic powers were known even the ancient Greek and Roman Empires people, until 1800's there was no any significiant study related with silver. Just by the late part of 1800s, investigations had been started and by following this, use of silver was becoming widespread as a medicine and antibacterial substance. It will be not a wrong fixing that it has been just started to discovering the power of silver (Purest colloids, 2012).

2.1.2 Flame Retardant Characteristics

The utilization of polymeric materials continues to increase each year. Scientists and engineers are now able to develop new materials that meet specific needs. In ancient times, warriors wore metal to protect themselves in battle; now soldiers wear synthetics, and they are quite possibly safer than the early warriors were. In the home, plastic has replaced many items that were once metal. In the transportation field, the weight savings achieved by replacing a metal with a plastic is a potent driving force. All of these changes provide opportunities for scientists, because plastic materials are inherently flammable, unlike the metal items that they have replaced (Bras, Wilkie & Bourbigot, 2005).

Since risk of fire cannot be eliminated in many application areas, products should be well-protected against fire. In a lot of cases the open question is how to ensure such levels of protection against fire attacks (Mureinik, 1997). Actually the early history of fire retardant systems begins with the painting of wood fortifications with vinegar in 360 BC. In the 1600s, a combination of clay and gypsum was used to fire retard canvas. The first patent was granted in 1735 in England for fire retardancy of textiles using alum, borax and vitriol (zinc, copper or iron sulfate) (Bras, Wilkie & Bourbigot, 2005).

Safety requirements are currently becoming more and more drastic in terms of polymers' reaction to fire and their fire resistance performances, whilst various flame retardant additives. The combined challenge thus consists in developing effective and

environmentally friendly flame retardant systems for polymer materials. The scientific and technical literature contains very diverse and efficient strategies for improving polymer fire resistance, which depend primarily on the nature and chemical structure of the polymer concerned, its decomposition mode and the required level of fire safety, and also the global performances of the resulting materials. The development of flame retardant materials and understanding the phenomena that take place during combustion often require close collaboration between several fields of scientific expertise (macromolecular and physical chemistry, physics of mass and heat transfer, rheology, etc.) (Laoutid, Bonnaud, Alexandre, Lopez-Cuesta & Dubois, 2009).

2.1.2.1 Flame Retardant Materials

Flame retardant materials play an important role in this point for saving life. Even if ignition does occur, flame retardants will act to delay the spread of flame, providing extra time in the tearly stages when the fire can be extinguished or an escape can be made. Used in combination with smoke detectors, fire alarms and sprinkler systems, flame retardants provide the most effective method available of protecting life and property (see Figure 2.8 for details) (Efra, 2012).

Those materials or substances inhibit or slow down the growth of a fire. As such, the term “flame retardant” does not refer to a specific class of chemical rather it describes the function of retarding a flame. This concept is not always understood. They are incorporated in different materials to reduce the risk of fire either by providing increased resistance to ignition, acting to slow down combustion and thereby delay the spread of flames; they save lives, prevent injuries and property losses, and contribute to protecting the environment (Efra, 2012).

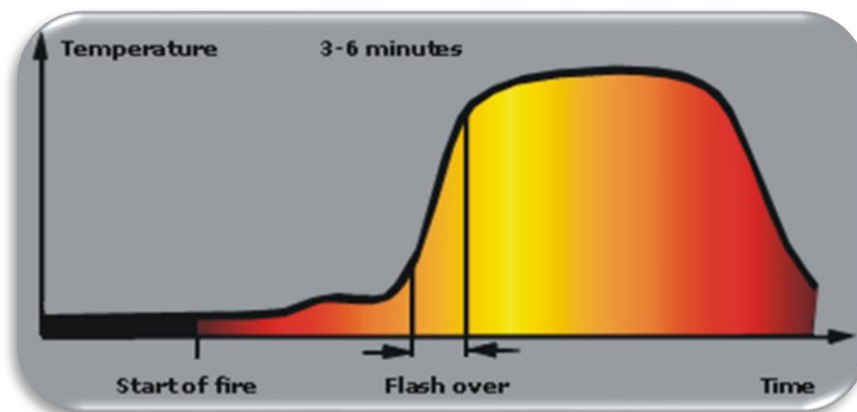


Figure 2.8 Spreading of fire depending on the time (Efra, 2012).

To the turning of the raw material into the finished product, ancillary materials are added in the formulation of polymers. Those materials impart to the compound the required properties of; flowability of the melt, tensile strength, bending strength, resistance to breakage by impact, resistance to the effects of oxygen or UV light, resistance to fire, suppression of smoke in the event of ultimate burning (Mureinik, 1997).

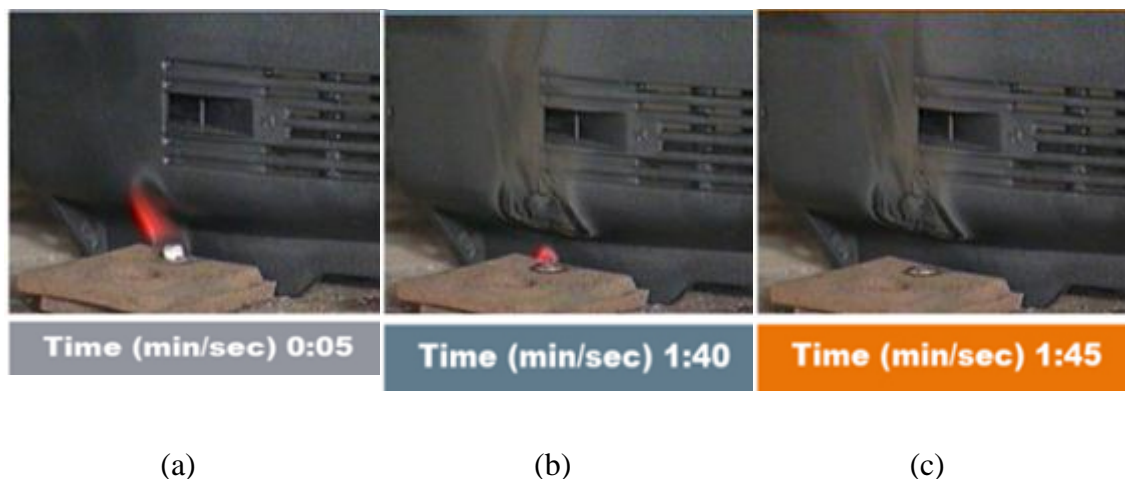


Figure 2.9 Performance of flame retardant material (Efra, 2012).

Flame retardants can thus make a decisive contribution to the safety of people, animals, buildings, furniture, electric and electronic apparatus (Figure 2.9), textiles, public transport and cars. As it can be seen in Figure 2.9.a, five seconds after a lit methamine tablet (a small fuel tablet) is placed underneath the TV backplate, which

is part of the plastic housing, the TV resists ignition quite well in Figure 2.9.b. After the fuel pellet has been burning for about 100 seconds, the TV backplate is only slightly affected in Figure 2.9.c. Once the fuel pellet consumes itself, there is no sustained burning on the TV. The fire goes out by itself and the TV has hardly been damaged (Efra, 2012).

Several products are used in many applications. They are used either alone or in combination with other mineral flame retardants. A review of those applications can be classified as three groups, including;

- wire and cable applications such as wiring in telecommunication, under the hood automotive wiring, wiring in naval vessels, power stations and low smoke PVC cabling,

- construction industry applications, such as flooring, roofing tiles, conduits, profiles, coils, sheets, films to replace brominated flame retardants and PVC, partitions and panelling and insulating foams, and

- electronic/electrical applications, such as relays, switches, plugs and sockets based on nylon, housing for electrical equipment, insulating and connecting parts and printed circuit boards (Weber, M. 1999).

Particularly by adding fire resisting additives to the polymers, the thermal stability, resistance to ignition/combustion, and the amount/nature of the combustion gases in terms of smoke, corrosion and toxicity can be improved (Rothon, 2003).

2.1.2.2 Polymer Combustion

Due to their chemical structure, made up mainly of carbon and hydrogen, polymers are highly combustible. The combustion reaction involves two factors: one or more combustibles (reducing agents) and a combustive (oxidizing agent). The combustive is generally the oxygen in the air. The whole process usually starts with an increase in the temperature of the polymeric material in terms of a heat source, to such an extent that it induces polymer bond scissions. The volatile fraction of the resulting polymer fragments diffuses into the air and creates a combustible gaseous

mixture (also called fuel). This gaseous mixture ignites when the auto-ignition temperature (defined as the temperature at which the activation energy of the combustion reaction is attained) is reached, liberating heat. Alternatively, the fuel can also ignite at a lower temperature (called the flash point) upon reaction with an external source of intense energy (spark, flame, etc.) (Laoutid, Bonnaud, Alexandre, Lopez-Cuesta & Dubois, 2009).

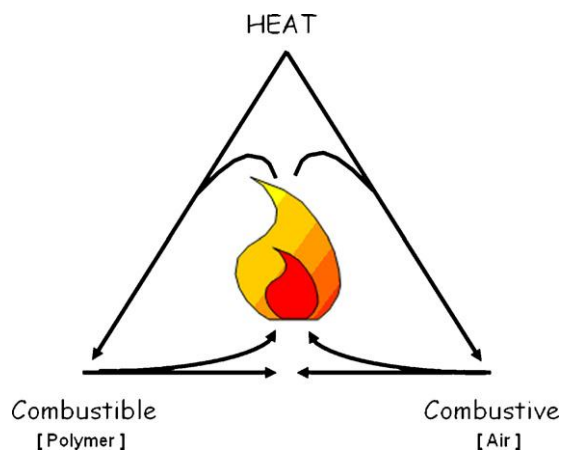


Figure 2.10 Principle of the combustion cycle (Laoutid, Bonnaud, Alexandre, Lopez-Cuesta & Dubois 2009).

The life span of the combustion cycle depends on the quantity of heat liberated during the combustion of the fuel. When the amount of heat liberated reaches a certain level, new decomposition reactions are induced in the solid phase, and therefore more combustibles are produced. The combustion cycle is thus maintained, and called a fire triangle as presented in Figure 2.10 (Laoutid, Bonnaud, Alexandre, Lopez-Cuesta & Dubois 2009).

The thermal decomposition of a polymer (i.e. covalent bond dissociation) is an endothermic phenomenon, which requires an input of energy. The energy provided to the system must be higher than the binding energy between the covalently linked atoms (200–400 kJ/mol for most C–C polymers). The decomposition mechanism is highly dependent on the weakest bonds, and also on the presence or absence of oxygen in the solid and gas phases. Generally speaking, thermal decomposition is the result of a combination of the effects of heat and oxygen (Laoutid, Bonnaud, Alexandre, Lopez-Cuesta & Dubois, 2009).

2.1.2.3 Flame Retardants Working Mechanism

Coupled with the release of inert gases, fire retardant fillers have endothermic decomposition. These two processes are generally found together, principally in some carbonates, hydrates and hydroxides. Beside importance of this, they must occur above the polymer processing temperature, and close to the polymer pyrolysis temperature such as calcium carbonate. Notwithstanding this mineral decomposes with a large endotherm and release of carbon dioxide, it is not effective as a flame retardant because its decomposition occurs well above pyrolysis temperatures of common polymers (Rothon, 2003).

There are many different flame retardants, and these work in a number of different ways. Some flame retardants are effective on their own; other products are used mainly or only as “synergists”, acting to increase the effect of other types of flame retardant. To understand how flame retardants work, it is first necessary to see how materials burn. Solid materials do not burn directly; they must be first decomposed by heat (pyrolysis) to release flammable gases. Visible flames appear when these flammable gases burn with the oxygen (O_2) in the air. If solid materials do not break down into gases, then they will only smoulder slowly and often self extinguish, particularly if they “char” and form a stable carbonaceous barrier which prevents access of the flame to the underlying material. However, as we all know, even materials such as wood do in fact burn vigorously, because once ignited the heat generated breaks down long-chain solid molecules into smaller molecules which transpire as gases (Figure 2.11) (Efra, 2012).

The gas flame itself is maintained by the action of high energy “radicals” which decompose molecules to give free carbon which can react with oxygen in air to “burn” to CO_2 , generating heat energy (Efra, 2012).

Flame retardant materials can act chemically and/or physically in the condensed phase or in the gas phase. In reality, combustion is a complex process occurring

through simultaneous multiple paths that involve competing chemical reactions. Heat produces flammable gases from pyrolysis of the polymer and when the required ratio between these gases and oxygen is achieved, ignition and combustion of the polymer will take place (Xanthos, 2004).

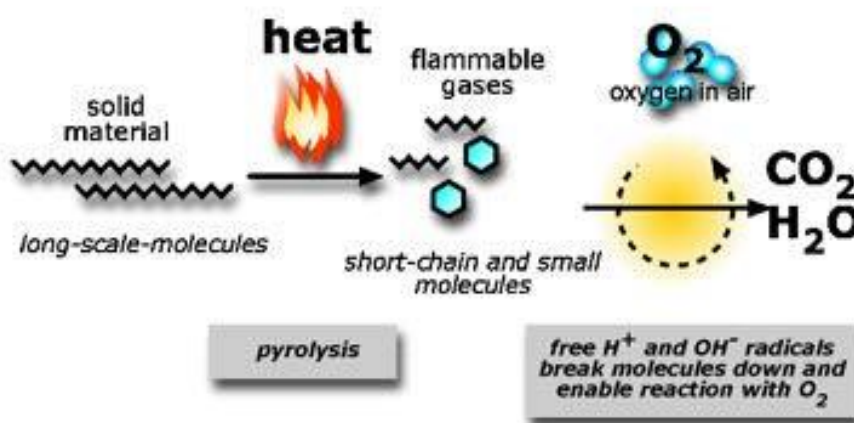


Figure 2.11 Working mechanism of flame retardant materials (Efra, 2012).

Three types of processes can be seen in the condensed phase, (Xanthos, 2004)

- The polymer can be broken down, this can be accelerated by flame retardants and leads to its pronounced flow by decreasing the impact of the flame.
- Flame retardant material can leave a layer of carbon (charring) on the polymer's surface. This occurs through the dehydrating action of the flame retardant generating double bonds in the polymer. As a result of cyclization and cross linking, these processes form a carbonaceous layer (Figure 2.12).
- Heat absorption through materials.

Flame-retarding polymers by intumescence are essentially a special case of a condensed phase activity without apparent involvement of radical trap mechanisms in the gaseous phase. Intumescence involves an increase in volume of the burning substrate as a result of network or char formation. For ingress of oxygen to the fuel, this char serves as a barrier and also as a medium in which heat can be dissipated (Figure 2.12).

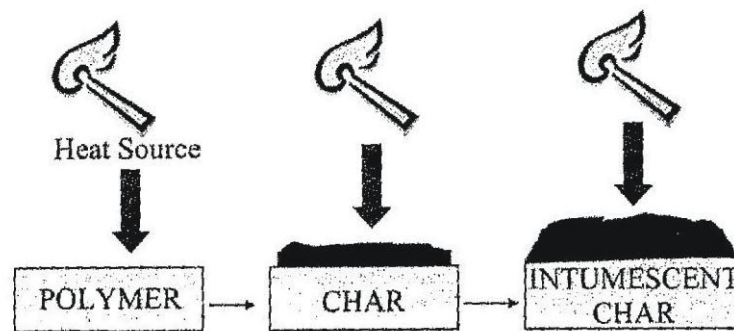


Figure 2.12 Char and intumescence formation (Xanthos, 2004).

The produced fuel amount is greatly diminished in intumescence and char rather than combustible gases is formed. The char constitutes a two-way barrier, both for hindering the passage of combustible gases and molten polymer to the flame as well as for shielding the polymer from the heat of the flame (Xanthos, 2004).

As mentioned above, typical flame retardant materials include hydroxides. Those structures endothermically decompose at temperatures between 200 °C and 400 °C and liberate water steam and/or carbon dioxide. Besides the cooling effect and extinguishing of the flames by inert gases, the flame retardancy effect is improved by formation of a kind of ceramic layer formed on the compound surface and this surface protects the ignitable materials from further attacks by flames and heat (Schmidt, 1999, Yılmaz Atay & Çelik, 2010).

2.1.2.4 Classification of Flame Retardant Materials

Amongst the flame retardant materials used in the various markets, generally two main categories can be seen; halogenated and halogen-free flame retardants. Halogen-containing flame retardants act in the gas phase and contribute to incompletely burned substances like black smoke and toxic CO. Thus, there is a propaganda from environmental activist organizations which claims that halogenated systems, notably brominated systems, play an important role for the increasing percentage of people killed by smoke inhalation in North America. In a real fire many toxic gases are found. The most serious one is carbon monoxide, CO; it is a

highly toxic and non-irritating gas. As CO blocks the oxygen transport of the blood, it can disturb the respiration process immediately. Even though traditional solutions based on halogens have some advantages like low loadings and good retention of mechanical properties, they have also disadvantages compared to mineral flame retardants. Figure 2.13 depicts a comparison of flame retardant materials (Weber, 1999).

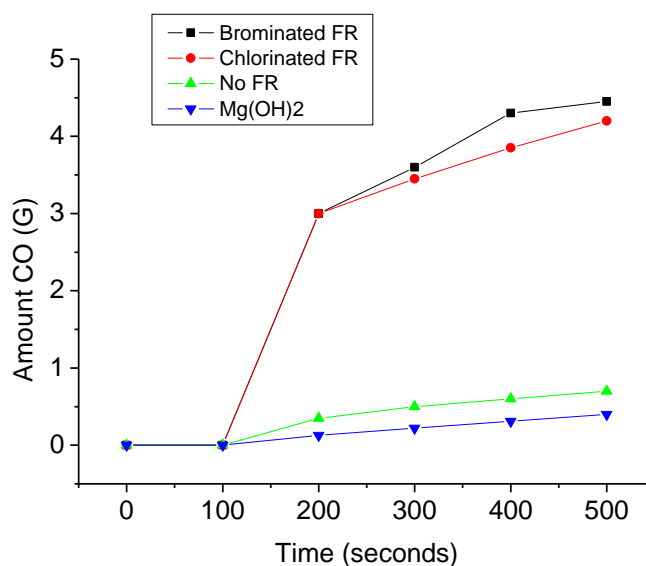


Figure 2.13 CO formation of different flame retardants (Weber, 1999)

2.1.2.5 Basic Flame Retardant Materials

2.1.2.5.1 Halogenated Flame Retardants (Containing Chlorine or Bromine Atoms). Halogenated flame retardants act by effectively removing the H^+ and OH^- radicals in the gas flame phase. This considerably slows or prevents the burning process, thus reducing heat generation and so the production of further gaseous flammable material. In fact, the mechanism is as follows. When exposed to high temperatures, the flame retardant molecule releases bromine (Br) or chlorine (Cl), as free radicals (Br^- or Cl^-) which react with hydrocarbon molecules (flammable gases) to give HBr or HCl. These then react with the high-energy H^+ and OH^- radicals to give water and the much lower energy Br^- or Cl^- radicals, which are then available to begin a new cycle of H^+ and OH^- radical removal. The effectiveness of halogenated

flame retardants thus depends on the quantity of the halogen atoms they contain (eg. 10 bromine atoms in one molecule of deca-DBP) and also, very strongly, on the control of the halogen release. Inasmuch as chlorine is released over a wider range of temperatures than bromine, it is then present in the flame zone at lower concentrations, and so is less effective. Bromine is released over a narrow temperature range, thus resulting in optimal concentrations in the flame zone. Many different bromine containing flame retardants have been developed, with bromine atoms bound into different organic molecules. These offer different properties, in terms of how the bromine is bound into the flame retardant molecule (aliphatically, aromatically), and of how the flame retardant molecule interacts with different plastics. Different specific brominated compounds can thus be added to or chemically bound into different plastics without deteriorating their properties (flexibility, durability, colour, etc.). The many varying brominated products available thus offer high flame retardancy effectiveness solutions for all plastics currently on the market and for most of their varied applications. Similarly, several chlorinated flame retardants are also available, and are effective flame retardants in standard and technical plastics, thermosets, textiles and rubbers materials (Efra, 2012).

2.1.2.5.2 Antimony Trioxide (Sb_2O_3). Antimony trioxide does not have flame retarding properties on its own, but is an effective synergist for halogenated flame retardants. It acts as a catalyst, facilitating the breakdown of halogenated flame retardants to active molecules. It also reacts with the halogens to produce volatile antimony halogen compounds, which are themselves directly effective in removing the high energy H^+ and OH radicals which feed the flame phase of the fire, thus reinforcing the flame suppressing effect of the halogenated flame retardants. When added to PVC, antimony trioxide acts to suppress flames by activating the chlorine present in the plastic itself materials (Efra, 2012).

2.1.2.5.3 Phosphorus Flame Retardants. Phosphorus containing flame retardants usually act in the solid phase of burning materials. When heated, the phosphorus reacts to give a polymeric form of phosphoric acid (PO_3). This acid causes the

material to char, inhibiting the “pyrolysis” process (break down and release of flammable gases) which is necessary to feed flames.

Different phosphorus containing flame retardants can be either simply mixed into plastics (and then held in the material when the plastic sets) or be reactive, and chemically bind into the plastic molecules at polymerisation. This will depend on the properties required of the plastic in terms of finished product performance, facility of processing (melting, extrusion, and moulding) and flame retardancy (temperature of onset of the charring process).

Phosphorus based flame retardants vary from elemental red phosphorus (P), which is oxidised to phosphoric acid with heat, through to complex P-containing organic molecules offering specific performance properties. Certain products contain both phosphorus and chlorine or nitrogen, thus combining the different flame retarding mechanisms of these elements (Efra, 2012).

2.1.2.5.4 Nitrogen Flame Retardants. The mechanisms of nitrogen containing flame retardants are not fully understood, but it is thought that they have several effects: formation of cross-linked molecular structures in the treated material. These are relatively stable at high temperatures, thus physically inhibiting the decomposition of materials to flammable gases (needed to feed flames) release of nitrogen gas which dilutes the flammable gases and thus reduces flames synergy with phosphorus containing flame retardants by reinforcing their function. To be effective, nitrogen based flame retardants are used at high concentrations, or in conjunction with other flame retardants. They can be either simply added to plastics, or reacted into the plastic molecules. Melamine-based products are the most widely used type of nitrogen flame retardant today, used in foams, nylons, but other products are also available or being developed materials (Efra, 2012).

2.1.2.5.5 Intumescent Coatings. Intumescent coatings are fire protection systems which are used to protect materials such as wood or plastic from fire (prevent burning), but also to protect steel and other materials from the high temperatures of

fires (thus preventing or retarding structural damage during fires). The coatings are made of a combination of products, applied to the surface like paint, which are designed to expand to form an insulating and fire-resistant covering when subject to heat. The products involved contain a number of essential interdependent ingredients: spumific compounds, which (when heated) release large quantities of non-flammable gas (such as nitrogen, ammonia, CO₂) a binder, which (when heated) melts to give a thick liquid, thus trapping the released gas in bubbles and producing a thick layer of froth an acid source and a carbon compound. On heating, the acid source releases phosphoric, boric or sulphuric acid which charrs the carbon compound, causing the layer of bubbles to harden and giving it a fire-resistant coating. Often the binder can also serve as this carbon compound.

In a fire, the coating expands to a thick non-flammable layer of bubbles, offering good insulation protection to the material coated. As well as being used to protect flammable materials and structural elements, intumescent systems are now being incorporated into certain plastics, thus providing an inherent fire protection capacity materilas (Efra, 2012).

2.1.2.5.6 Inorganic Flame Retardants. A number of inorganic compounds are used as flame retardants, interfering by various hysical processes with the burning process: release of water or non-flammable gases which dilute the gases feeding flames, absorption of heat energy (in these gas-release reactions) thus cooling the fire, production of a non-flammable and resistant layer on the surface of material. These mechanisms of inorganic compounds are however of a relatively low efficiency and the products having to be used often in relatively large concentrations, or more usually, in combination with other types of flame retardants. Specific application forms of these products (for instance, within organic coatings) can enable such high concentrations to be added to plastics without modifying their performance properties (Efra, 2012). Those inorganic flame retardants include aluminium trihydrate (ATO), magnesium hydroxide, boron compounds, zinc borate and other zinc and tin compounds.

-Aluminium trihydrate (ATO): This simple inorganic compound acts with all three of the mechanisms as indicated above. At around 200°C, it is decomposed to aluminium oxide (which forms a protective, non-flammable layer on the material surface) and water. The water (as steam) forms a layer of non-flammable gas near the material's surface, inhibiting flames. The reaction is endothermic (absorbs heat energy), thus cooling the material and slowing burning.

-Magnesium hydroxide: This acts with the same three mechanisms as aluminium trihydrate, but is only decomposed at somewhat higher temperatures (around 300°C), meaning that it can be used in plastics which are moulded or processed at relatively higher temperatures.

-Boron compounds: These also act by releasing water, in a heat absorbing reaction, and forming a protective glassy layer on the material's surface. They can release boric acid, which also acts by causing charring of the material, reducing the release of flammable gases.

-Zinc borate: This is a multifunctional flame retardant, which can function as a flame retardant (synergist of halogen), smoke suppressant (promote char formation), after glow suppressant. In some halogen-containing systems, it can display synergy with antimony oxide. In certain halogen-free systems, it can also promote ceramic char formation.

-Other zinc and tin compounds: These materials act to reduce smoke emission from PVC, to promote charring, or as synergists to increase the effectiveness of halogenated or nitrogen (melamine) flame retardants materials (Efra, 2012).

The flame retardant materials in Table 2.1 are seen to cover a wide range of decomposition temperatures, and to include release of carbon dioxide as well as water (Rothon, 2003, Yılmaz Atay & Çelik, 2008). Those materials remove a good deal of the heat evolved in degradation and thus can prevent further degradation. Nonetheless, to be effective, they must be used at very high loadings, which lead in

some instances to the loss of mechanical properties of interest. Nanocomposites are formed when a small amount of organically-modified aluminosilicate clay is added to a polymer. The presence of only a small amount of clay can give a significant reduction in the peak heat release rate. The difference between the microcomposite and the nanocomposite is the dispersion of the material in the polymer. In a nanocomposite, the clay, or the nano-filler/additive, is well dispersed throughout the polymer (Bras, Wilkie & Bourbigot, 2005, Yılmaz Atay, 2008).

Table 2.1 Principle candidate flame retardant fillers (Rothon, 2003)

Candidate material (common names and formula)	Approximate onset of decomposition (°C)*	Approximate enthalpy of decomposition (kJ.kg ⁻¹)	Volatile content % w/w		
			H ₂ O	CO ₂	Total
Nesquehonite MgCO ₃ .3H ₂ O	70-00	1750	39	32	71
Calcium sulfate dihydrate, Gypsum CaSO ₄ .2H ₂ O	60-130	Not available	21	0	21
Magnesium phosphate octahydrate, Mg ₃ (PO ₄) ₂ .8H ₂ O	140-150	Not available	35.5	0	35.5
Alumina trihydrate, Aluminium hydroxide, Al(OH) ₃	180-200	1,300	34.5	0	34.5
Basic magnesium carbonate, Hydromagnesite 4MgCO ₃ .Mg(OH) ₂ .4H ₂ O	220-240	1,300	19	38	57
Dawsonite (sodium form) NaAl(OH) ₂ CO ₃	240-260	Not available	12.5	30.5	43
Magnesium hydroxide , Mg(OH) ₂	300-320	1,450	31	0	31
Magnesium carbonate sub- hydrate (MCS), MgO.CO ₂ (0.96)H ₂ O(0.30)	340-350	Not available	9	47	56
Boehmite, AlO(OH)	340-350	560	15	0	15
Calcium hydroxide, Ca(OH) ₂	430-450	1,150	24	0	24

* The decomposition temperatures are only approximate, as they are usually determined under dynamic conditions and depend on heating rate and sample conditions.

Nanocomposite formation may have for fire retardancy purposes is the improvement in mechanical properties that usually occurs through the formation of the nanocomposite. Many fire retardants are used at very high loadings, which can significantly impact the physical properties of the polymer (Bras, Wilkie & Bourbigot, 2005, Yılmaz Atay, 2008).

2.1.2.5.7 Huntite/hydromagnesite Mineral. Huntite/hydromagnesite mineral is used in the polymer application for its flame retardancy properties. This mineral was introduced to the market in the late 1980s, as one of the magnesium containing sources for mineral flame retardants (Kirschbaum, 2001, Yılmaz Atay, Çelik, 2010). At present, the commercially used deposits are located in Greece and Turkey. The deposit normally consists of physical blends of two minerals huntite and hydromagnesite with varying ratios in between 40-30% huntite and 60-70% hydromagnesite. The level of impurities is very low; the most important ones are other white carbonate minerals such as aragonite, calcite, and dolomite. Physical densities of huntite ($\text{Mg}_3\text{Ca}(\text{CO}_3)_4$) and hydromagnesite ($\text{Mg}_4(\text{OH})_2(\text{CO}_3)_3 \cdot 3\text{H}_2\text{O}$) minerals are $2,70 \text{ g/cm}^3$ and $2,24 \text{ g/cm}^3$ respectively (Kirschbaum, 2001). The advantages of this mineral can be arranged in order such as being non-corrosive to processing equipments, low smoke generation, no acid gas emission, halogen free, environmentally safe, recyclable, no combustion gas corrosion, no limitation in colouring and low combustion. In addition, huntite/hydromagnesite offers a good cost/performance relationship in flame retardant applications (Weber, 1999).

2.1.3 Radar Absorbing Behaviour

Radar is one of the most important technological developments resulting from World War II. This technology revolutionized air and naval warfare. It has grown to significance not only in military and law-enforcement applications, but also for aerospace maneuvering and sensing, meteorological data collection and forecasting, and even lifestyle convenience (e.g. automatic doors) applications (Trujillo & Thurman, 2004). This is an object detection system that uses electromagnetic waves to identify the range, altitude, direction, or speed of both moving and fixed objects

such as aircraft, ships, motor vehicles, weather formations, and terrain. The term *RADAR* was coined in 1940 by the U.S. Navy as an acronym for: **R**Adio, **D**etection, **A**nd **R**anging (Gerhard, 2012, The History, 2003).

The basic idea behind radar is very simple: a signal is transmitted, it bounces off an object and it is later received by some type of receiver. This is like the type of thing that happens when sound echo's off a wall. However radars do not use sound as a signal. Instead they use certain kinds of electromagnetic waves called radio waves and microwaves (How radar, 2012).

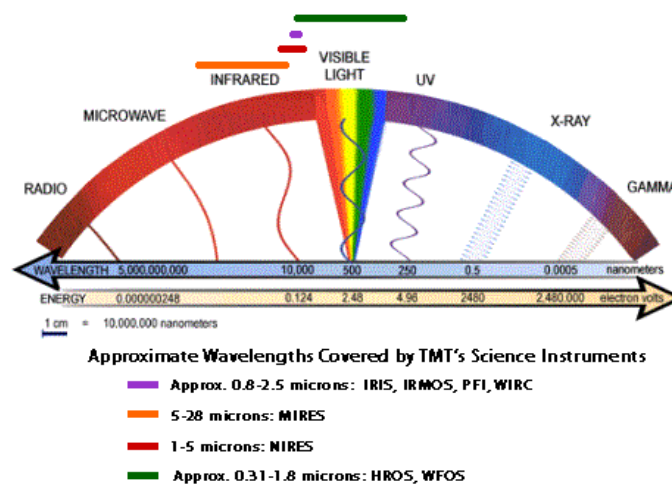


Figure 2.14 Electromagnetic waves (Range, 2012).

The fundamental operation of radar is transmission and reception of electromagnetic waves. Electromagnetic waves (Radio waves and microwaves) like all waves transport energy but can do so through a vacuum. Sound waves and ocean waves require matter to transport energy but electromagnetic waves can do so without the presence of matter. Because of this, satellites can use radars to work on projects outside of the Earth's atmosphere and on other planets. Another useful thing about electromagnetic waves is that they travel at a constant speed through a vacuum called the speed of light abbreviated by the letter "c" (292,792,458 meters per second). This is very useful to know to when doing ranging calculations (How radar, 2012). Radio waves have wavelengths that are 10 cm and greater and microwaves

have wavelengths that range from 10 cm to 1/10 of a mm (Figure 2.14) (Range, 2012).

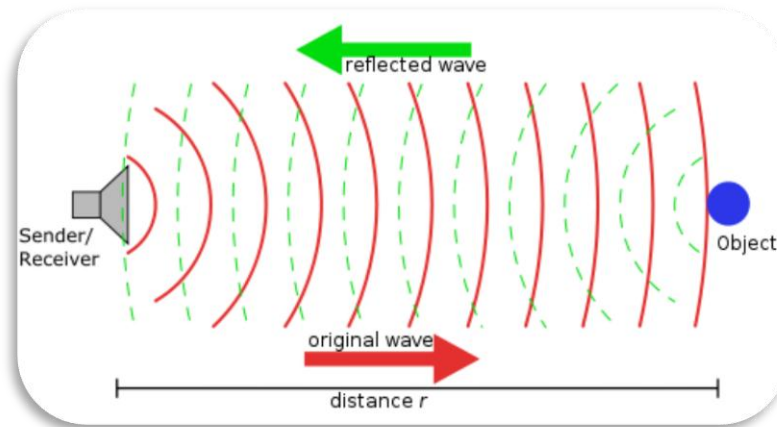


Figure 2.15 Incoming and reflected radar waves (Tushar, 2010).

Once radio waves strike an object, some portion is reflected, and some of this reflected energy is returned to the radar set, where it is detected. The location and other information about these reflective objects, targets, can be determined by the reflected energy (Varshney, (2002). Some useful information is calculated from this energy such as the time taken for it to be received, the strength of the returned signal, or the change in frequency of the signal. This information is then translated to reveal useful data: an image, a position or the velocity of your speeding car (Figure 2.15) (Trujillo & Thurman, 2004, Tushar, 2010).

The amount of reflection and refraction depends on the properties of the surface and the properties of the matter which the wave was originally traveling through. This is what happens to radar signals when they hit objects. If a radar signal hits a surface that is perfectly flat then the signal gets reflected in a single direction. If the signal hits a surface that is not perfectly flat then it gets reflected in all directions, only a very small fraction of the original signal is transmitted back in the direction of the receiver (Trujillo & Thurman, 2004).

In general, there are four methods of reducing reflection; shaping, active loading, passive loading and distributed loading. Shaping is the primary method of reducing

the backscattered signal as mentioned above. In spite of the fact that shaping is very important, it redirects the radiation through specular reflection hence increasing the probability of detection from bistatic radars. Active and passive loading aims to reduce the scattering from hotspot regions through the application of patches. Active materials detect the incident radiation and emit signals of equal amplitude and opposite phase to cancel the signal, while passive materials are designed to modify the surface impedance so as to cancel the scattered signal. The fourth method, distributed loading involves covering the surface with a radar absorbing material that has imaginary components of permittivity and/or permeability (ie the electric or magnetic fields of the radiation couple with the material properties and energy is consumed) (Saville, 2005).

2.1.3.1 Minimising The Reflection

Before passing to the reflection calculations, it will be useful to understand the electromagnetic waves fundamentals. Electromagnetic waves are created by time-varying currents and charges. They can be guided by structures (transmission lines) or by free space (Figure 2.16). E and H are the electric and magnetic field vectors.

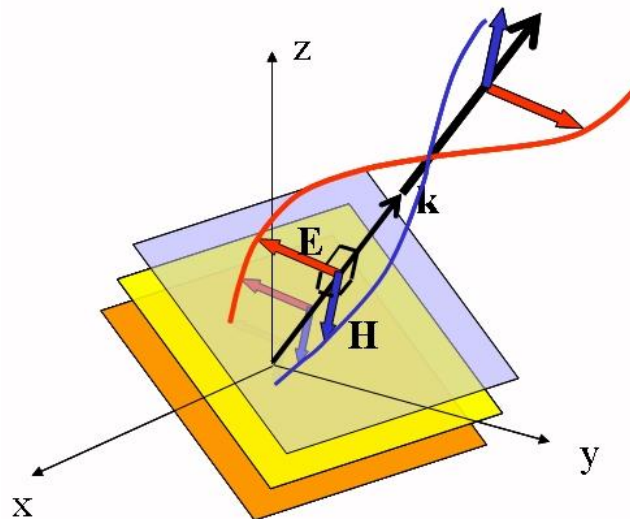


Figure 2.16. Electromagnetic waves (Diaz, 2012).

An antenna is a material structure that directs EM fields from a source into space, or, by reciprocity, from space to a receiver. The shape and size of the antenna controls the transition from the near field to the far field (Diaz, 2012). As it can be seen from Figure 2.17 that near-field behavior is most clearly seen surrounding small antennas; the electric dipole is a capacitive object (Diaz, 2012).

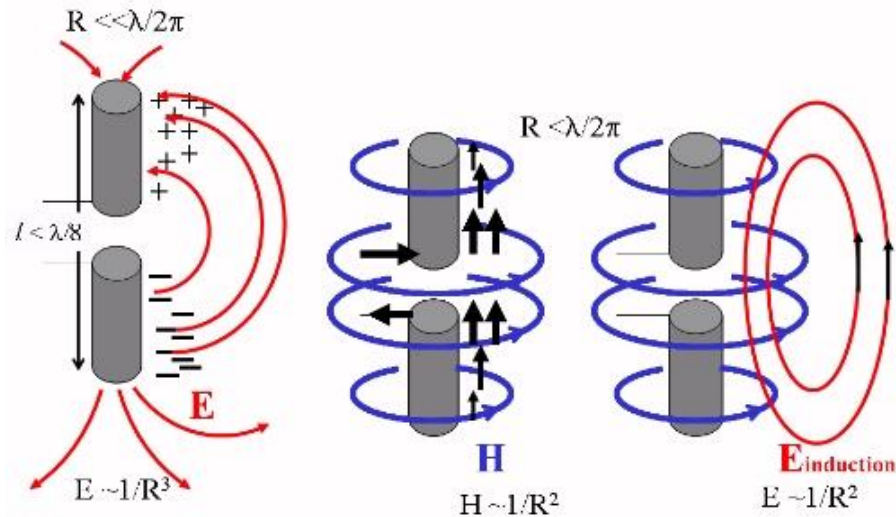


Figure 2.17 Near-field behaviour (Diaz, 2012).

The near field consists of the reactive near field, also known as the quasi-static near field, and the radiating near field also known as the Fresnel zone or Fresnel region. In the quasi-static near field we see fields that strongly resemble the electrostatic fields of a charge dipole for a dipole antenna and the fields of a magnetic dipole for a loop antenna. In large antennas the quasi-static field can be seen near edges (Figure 2.18) (Diaz, 2012).

In the Fresnel zone the waves are clearly not plane and may have phase shifts that do not vary linearly with distance from a (fictitious) phase center. From the near field to the far field, electromagnetic radiation changes from spherical waves to plane waves. The far-field is sometimes called the Fraunhofer region (Figure 2.18) (Diaz, 2012).

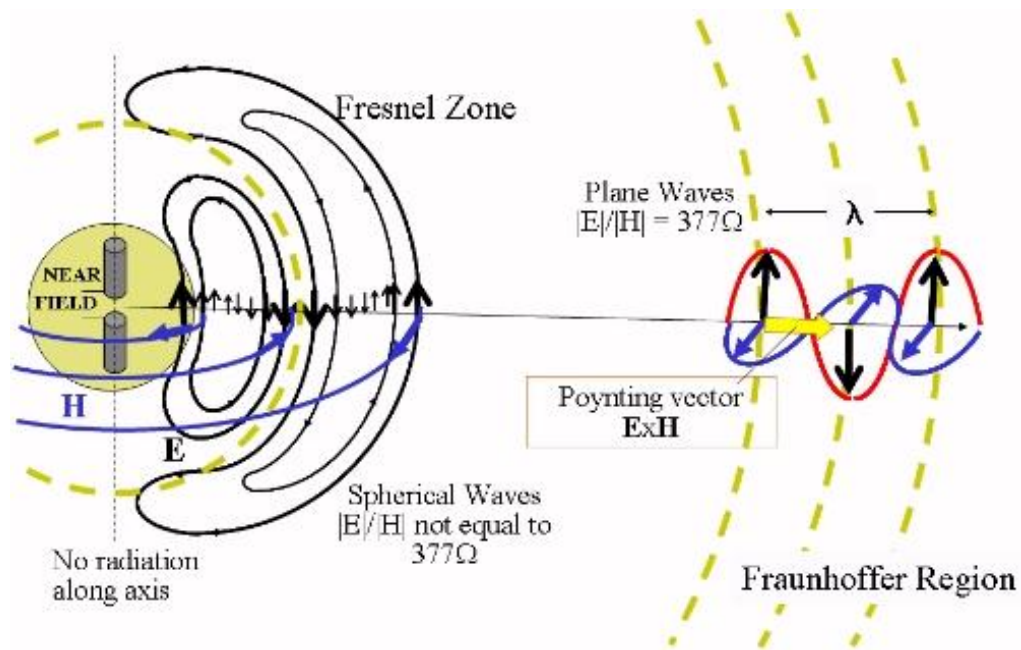


Figure 2.18 Fresnel zone and Fraunhofer region (Diaz, 2012).

2.1.3.2 Calculations For Minimising Reflection

In an attempt to minimise the reflection from a surface it is useful to consider the physical equations that represent the reflection process. There are three conditions that result in a minimum reflectivity. The first equation of interest is that describing the reflection coefficient at an interface (Saville, 2005).

$$r = \frac{\eta_M - \eta_o}{\eta_M + \eta_o} = \frac{Z_M - Z_o}{Z_M + Z_o} \quad (2.2)$$

where r is the reflection coefficient and η the admittance of the propagating medium (subscript “o” for incident medium or air and “M” for the substrate). The admittance in this equation can be replaced with the intrinsic impedance ($Z = 1/\eta$). The reflection coefficient falls to zero when the material in the layer is impedance matched to the incident medium. The intrinsic impedance of free space is effectively given by (Saville, 2005).

$$Z_o = \frac{E}{H} = \frac{\mu_o}{\epsilon_o} \approx 377 \text{ohms} \quad (2.3)$$

where \mathbf{E} and \mathbf{H} are the electric and magnetic field vectors and μ_o and ϵ_o are the permeability and permittivity of free space. Thus a material with an impedance of 377 ohms will not reflect microwaves if the incident medium is free space (Figure 2.18). Perfect impedance matching can also be realised if the electric permittivity and the magnetic permeability are equal. This gives the second condition that results in a minimum in the reflection coefficient. In this case Equation 2.2 is rewritten as (Saville, 2005):

$$r = \frac{(Z_M / Z_o) - 1}{(Z_M / Z_o) + 1} \quad (2.4)$$

The normalized intrinsic impedance is (Saville, 2005):

$$\frac{Z_M}{Z_o} = \sqrt{\frac{\eta_r^*}{\epsilon_r^*}} \quad (2.5)$$

in which $\epsilon_r^* = \frac{\epsilon' - i\epsilon''}{\epsilon_o}$ and $\mu_r^* = \frac{\mu' - i\mu''}{\mu_o}$ the prime and double prime superscripts

represent the real and imaginary components of the complex numbers, respectively. If the incident medium is free space and the reflectivity is zero, then it follows that $\mu_r^* = \epsilon_r^*$. The implication is if both the real and imaginary parts of the permittivity and permeability are equal, then the reflectivity coefficient is zero (Saville, 2005)

The third consideration is the attenuation of the wave as it propagates into the absorbing medium. The power of the wave decays exponentially with distance, x , by the factor $e^{-\alpha x}$. The α is the attenuation constant of the material and can be expressed as (Saville, 2005)

$$\alpha = -\sqrt{\varepsilon_o \mu_o} \omega (a^2 + b^2)^{1/4} \sin\left(\frac{1}{2} \tan^{-1}\left(-\frac{a}{b}\right)\right) \quad (2.6)$$

where $a = (\mu_r^* \varepsilon_r^* - \mu_r^* \varepsilon_r^*)$, $b = (\mu_r^* \varepsilon_r^* + \mu_r^* \varepsilon_r^*)$.

To get a large amount of attenuation in a small thickness, α must be large, which implies that must be large. It is noted here that this condition must be tempered with the first condition (Equation 2.2), where large values of permittivity and permeability would result in a large reflection coefficient (Saville, 2005).

2.1.3.3 Radar Absorbing Materials

There has been a growing and widespread interest in radar absorbing material technology. Those materials are developed from the coating whose electrical and/or magnetic properties have been altered to allow absorption of radar energy at discrete or broadband frequencies (Ting, Wu, Hsu, Chuang, & Yang, 2008). The coating's absorbency at a given frequency of radar wave depends upon its composition (Zhou, Ma, Zhong, Xu, Yue, & He, 2006). The goal of the coating manufacturer is to balance electrical performance, thickness, weight, mechanical properties and cost (Figure 2.19) (RF Products, 2004).

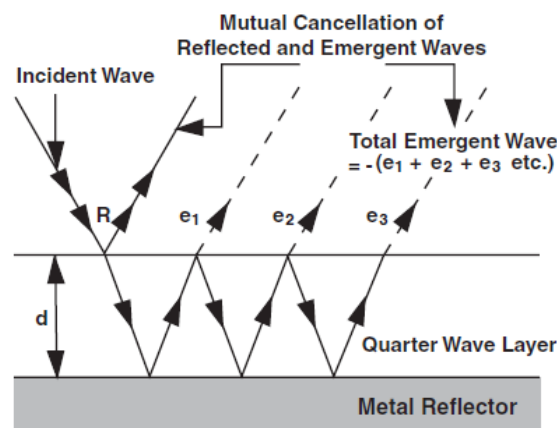


Figure 2.19 Out-of-phase condition existing between reflected and emergent waves (RF Products, 2004).

The earliest forms of radar absorbing materials were the materials called *Sumpf* and *Schornsteinfeger*, a coating used by Germans during the World War II for the snorkels (or periscopes) of submarines, to lower their reflectivity in the 20-centimeter radar band the Allies used. The material had a layered structure and was based on graphite particles and other semiconductive materials embedded in a rubber matrix (Figure 2.20) (RF Products, 2004, Kojima, 1982, Gambit, 2011).

As given in the example, radar absorbing materials can be produced by altering dielectric and magnetic properties of existing materials. For purposes of analysis, the dielectric properties of a material are categorized as its permittivity and the magnetic properties as its permeability. Common dielectric materials used for absorbers, such as foams, plastics and elastomers, has no magnetic properties. Magnetic materials, such as ferrites, iron and cobalt-nickel alloys are used to alter the permeability of the base materials. High dielectric materials, such as carbon, graphite and metal flakes, are used to modify the dielectric properties (RF Products, 2004, Kojima, 1982).

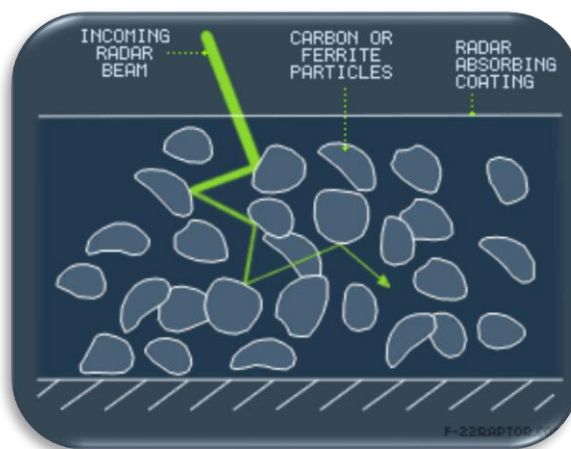


Figure 2.20 Radar absorbing mechanism (Gambit, 2011)

2.1.3.3.1 Radar Absorbers. Most known absorbers are carbon, metal and metal particles, conducting polymers, polypyrrole–polymer composites, polyaniline and so on.

Carbon: Absorbers for anechoic chambers were originally made, by coating mats of curled animal hair with carbon black impregnated neoprene. The front surface has then been moulded into geometric forms (ie pyramids) or the amount of lossy material was increased as a function of depth into the mat by dipping. Carbon black and fibrous carbon has been incorporated into layers (Saville, 2005).

Metal and metal particles: Broad band absorbers have been made from solid aluminum metallic particles or dielectric filled metallic shells in the shape of spheroids (oblate or prolate) dispersed in a matrix. Iron oxide, powdered iron, powdered aluminum and copper, steel wool, water, powdered “Advance” and “Constantin”, evaporated metal or nickel chromium alloy and metal wires (Saville, 2005).

Conducting polymers: In a polymer such as polypyrrole, partial oxidation of the polymer (doping) causes it to become conducting through the formation of polarons and bipolarons; the charge carriers along the chains. The conductivity of a conducting polymer is modelled by phonon assisted hopping between the randomly distributed localized states (that result from the partial oxidation) (Saville, 2005).

Polypyrrole–polymer composites: Polypyrrole by itself does not have great physical properties and so most of the useful materials are composites of polypyrrole and other materials such as latex, fibres or polymer blends. Polypyrrole finds great use due to its relative stability in air (Saville, 2005). Several materials have been formed by polymerising pyrrole in the presence of a fabric or fibres. Pyrrole has been oxidatively polymerised with ferric chloride in the presence of paper (cellulose) to form a polypyrrole coated paper composite. Through manipulation of the chemistry and deposition time, the electrical conductivity of the composite could be carefully controlled. Absorbers were fabricated from these materials and measured (Saville, 2005).

Polyaniline: Polyaniline, PANI, is another inexpensive, simple to make, readily available conducting polymer that has suitable properties for the fabrication of an

absorber. Polyaniline is slightly soluble and there are many derivatives of its monomer. Thus there is a large potential for tuning absorber properties with this material (Saville, 2005).

Other conducting polymers: One of the first calculations showing that conducting polymers could be used for Salisbury Screens and Jaumann layers used the permittivities at 9.89 GHz of poly-pphenylene-benzobis-thiazole and polyacetylene. Bithiophene has been electropolymerised into a latex matrix deposited onto a conducting plate. It was also noted that the latex could contain magnetic particles and other polymers such as pyrrole would be effective (Saville, 2005).

Tubules and filaments: Radar absorbing materials can be formed by loading an insulating polymer matrix with conducting filaments or tubules. The length of the filaments should be less than $\frac{1}{2}\lambda$ of the median frequency to be absorbed. For these materials, ϵ' reaches a maximum as the loading increases and starts to fall off at the percolation threshold, where the composite becomes macroscopically conducting. ϵ'' increases with loading around the percolation threshold and continues to increase to a saturation value at high loading (Saville, 2005).

Chiral materials: A reasonable amount of work has been conducted on chiral inclusions in a matrix as a radar absorbing material. Materials made with these chiral inclusions have been shown to be effective microwave absorbers and have been patented (Saville, 2005).

Shielding: Many of the materials discussed above can be used for shielding. For instance PET and PE fabrics coated with polypyrrole or metal show utility as electromagnetic interference shielding, giving between 20 and 80 dB depending on thickness and conductivity (Saville, 2005).

2.1.3.3.2 Barium Hexaferrite ($BaFe_{12}O_{19}$). Barium hexaferrite powders have been investigated as a material for permanent magnets, microwave absorber devices and recording media (Haijun, Zhichao, Chengliang, Xi, Liangying & Mingzhong, 2002).

Barium hexaferrite is widely used due to its high stability, excellent high frequency response, narrow switching field distribution and the temperature coefficient of the coercivity in various applications (Mendoza-Suarez, Rivas- Vazquez, Fuentes, Escalante-Garcia, Ayala-Valenzuela & Valdez, 2002). Barium ferrite with hexagonal molecular structure has fairly large magneto crystalline anisotropy, high Curie temperature and relatively large magnetization as well as chemical stability and corrosion stability (Figure 2.21) (Aksit, Onar, Ebeoglugil, Birlik, Celik & Ozdemir, 2009, Zhou, Ma, Zhong, Xu, Yue & He, 2006).

Ferrites are non-metal magnetic materials. Their composition can be expressed by the formula: $(M_2^{k+}O_k^{2-})_{m/2} \cdot (Fe_2^{3+}O_3^{2-})_n$ where M-a characterizing metal; k - his valency; m, n – integer numbers. The name of ferrite is determined by the characterizing ion of metal. Therefore, if M is an ion of nickel, then a ferrit is named nickeliferous (Zhuravlev & SuslyaeV 2006, Nejezchleba, Simaan & Zhvzta, 1997).

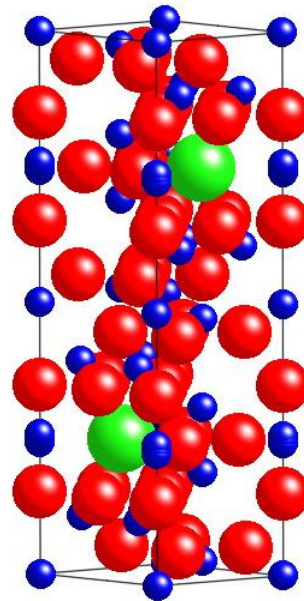


Figure 2.21 $BaFe_{12}O_{19}$ (Fe blue, Ba green, O red) (Pullar, 2012)

Properties of ferrites are largely determined by their structure. Distinguish a few types of structures ferrits. Most application in a technique was found:

-Ferrospinelns are ferrites with the structure of natural mineral spinel: MgAl_2O_4 .

-Ferrogarnets are ferrites with the structure of mineral garnet: $\text{Ca}_3\text{Al}_2(\text{SiO}_4)_3$.

-Geksaferrites are ferrites with a hexagonal structure, isomorphic structure of mineral magnetoplumbite: $\text{PbFe}_{7.5}\text{Mn}_{3.5}\text{Al}_{0.5}\text{Ti}_{0.5}\text{O}_{19}$.

-Ortoferries are ferrits with the rhombic distorted structure of mineral perovskite: CaTiO_3 (Zhou, Ma, Zhong, Xu, Yue, & He, 2006).

Hexaferrites are generated in the system of $\text{M}'\text{O} - \text{M}''\text{O} - \text{Fe}_2\text{O}_3$, where M are elements (Ba^{2+} , Ca^{2+} , Pb^{2+} or Sr^{2+}) with atomic by a radius (1,06...1,43 Å), near to the atomic radius of ion of oxygen (~1,32 Å) as given in Figure 2.22 (Magnetic ceramics, 2012).

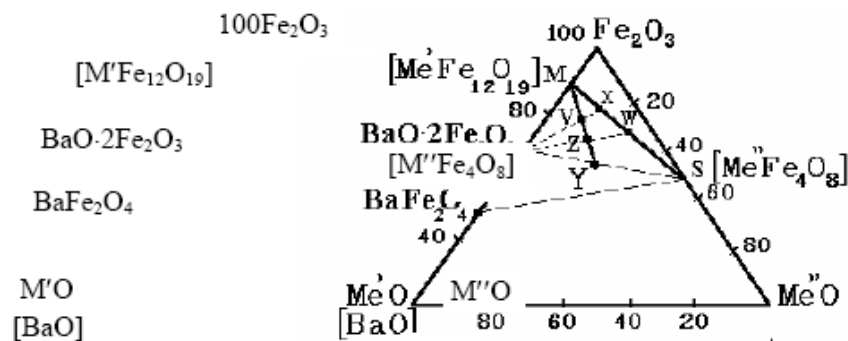


Figure 2.22 Compositions (mole %) of ferrites of hexagonal structure (Zhuravlev & Suslyayev, 2006).

In the past decade, there has been an increasing interest in methods for the preparation of fine particles of barium hexaferrites, because of its emerging application in perpendicular magnetic recording media. The synthesis method strongly determines its homogeneity, particle size, shape, and magnetic characteristics (Benito, Morales, Requena, Raposo, Vazquez, & Moya, 2001, Mali &

Ataie, 2004). Some production methods to obtain barium hexaferrite are as follows: Traditional ceramic process, chemical coprecipitation method, the sol-gel method, the supercritical water crystallization method, the gel self-combustion method, self-propagated high-temperature synthesis, microwave induced combustion synthesis, RF sputtering technique, the aerosol pyrolysis technique, the sono-chemical approach, pulsed laser deposition, freeze-dried technique, glass crystallization method can be used for this purpose (Aksit, Onar, Ebeoglugil, Birlik, Celik & Ozdemir, 2009, Ghasemi, Saatchi, Salehi, Hossienpour, Morisako & Liu, 2006).

2.1.4 Self-Healing Property

A self-healing material is a material that has the built-in ability to partially repair damage occurring during its service life time. Usually, certain properties of any engineering material degrade over time due to environmental conditions or fatigue, or due to damage incurred during operation. This damage is often on a microscopic scale, requiring periodic inspection and repair to avoid them growing and causing failure (Zwaag, 2007).

Self-healing materials are a class of smart materials that have the structurally incorporated ability to repair damage caused by mechanical usage over time. The inspiration comes from biological systems, which have the ability to heal after being wounded. Initiation of cracks and other types of damage on a microscopic level has been shown to change thermal, electrical, and acoustical properties, and eventually lead to whole scale failure of the material. Usually, cracks are mended by hand, which is difficult because cracks are often hard to detect. A material (polymers, ceramics, etc) that can intrinsically correct damage caused by normal usage could lower production costs of a number of different industrial processes through longer part lifetime, reduction of inefficiency over time caused by degradation, as well as prevent costs incurred by material failure (Zang, 2008).

Studies on self-healing materials focus on the dependence of their ability to heal on the extent of damage at both the micro- and mesoscale. Pre-emptive self-healing processes on such scales can prevent the development of catastrophic damage by suppressing the escalation of chemical bonds dissociation. Such escalation normally leads to the formation of microcracks or microcavities, eventually causing the macroscopic damage, which would require welding or relamination to repair. Hence, many of developed self-healing systems focus on molecular level interactions regardless of whether the study involves covalent or noncovalent bonds. In practice, reversible interactions are of particular interest due to their capability to heal repeated damage at the same position. Examples of reversible interactions include dynamic covalent bonds, metal-ligand interactions, multiple hydrogel bonding, ionic interaction, and π - π interactions. However, many of these systems are still limited in practice due to the requirement for external stimuli, e.g., heat, UV irradiation, or acid/base to trigger the healing response (Yoon, Kamada, Koynov, Mohin, Nicola, Zhang et al., 2012).

Self-healing materials address this degradation through the inclusion of an "active" phase that responds to the micro-damage by initiating a repair mechanism. Several mechanisms have been proposed for a range of engineering materials, e.g. metals, polymers, ceramics, cementitious, elastomeric and fibre-reinforced composite materials (Zwaag, 2007).

Different strategies and approaches to devise self-healing materials in metals, ceramics and polymers have been investigated. These materials possess different intrinsic properties and self-healing is based on the same common general principle in all of them. Self-healing can take place on the microscopic to macroscopic level. The prerequisite for a self-healing of a (mechanical) damage is the generation of a mobile phase and the mobile phase can close the crack (Figure 2.23). If a material is damaged (Figures 2.23.a and 2.23.b), a crack can occur. Then subsequently a "mobile phase" (Figure 2.23.c) which is triggered either by the occurrence of damage (in the ideal case) or by external stimuli was generated. Following the mobile phase generation, the damage can be removed due to the directed mass transport towards

the damage site and the subsequent local mending reaction (Figure 2.23.d). The latter assures the (re)connection of the crack planes by physical interactions and/or chemical bonds. After the healing of the damage the previously mobile material is immobilised again, resulting in the best case in fully restored mechanical properties (Figure 2.23.e) (Hager, Greil, Leyens, Zwaag & Schubert, 2010).

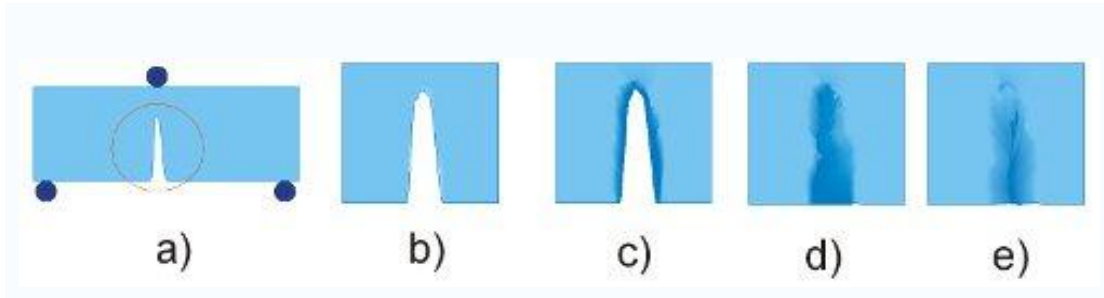


Figure 2.23 Generation of the mobile phase and closing the crack (Hager, Greil, Leyens, Zwaag & Schubert, 2010).

In general, self-healing is the ability of a material to restore mechanical properties, which were earlier perturbed by a plastic deformation or failure involving cracks and voids. Investigation of possible self-healing mechanisms is an important emerging field of nanotechnology (Ajayan, Schadler & Braun, 2003).

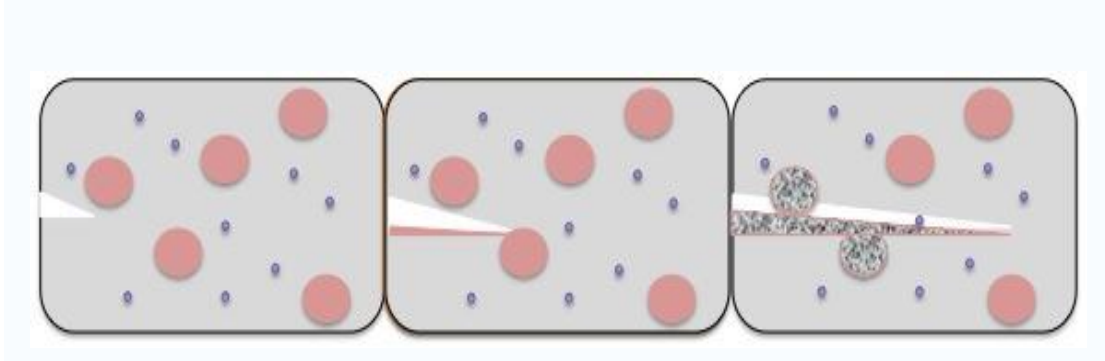


Figure 2.24 Depiction of crack propagation through microcapsule-embedded material. Monomer microcapsules are represented by pink circles and catalyst is shown by purple dots (Trask, Williams, & Bond, 2007).

The first report of a completely autonomous man-made self healing material was an epoxy system containing microcapsules. These microcapsules were filled with a (liquid-thermosetting) monomer. If a microcrack occurs in this system, the microcapsule will rupture and the monomer will fill the crack as given in Figure 2.24 (White, Sottos, Geubelle, Moore, Kessler, Sriram, et al., 2001, White, 2007).

Subsequently it will polymerise, initiated by catalyst particles that are also dispersed through the system. This model system of a self healing particle proved to work very well in pure polymers and polymer coatings (Trask, Williams, & Bond, 2007).

Other materials, such as SiC/C/SiC model composites and Si-Ti-C-O fiber-bonded ceramics are the examples that show self-healing features under heating at high temperatures (Bansal, 2005). In addition, semiorganic and ceramic protective coatings, silicate nanocomposites, and SiC/SiC fibrous composites may reveal chemical mechanisms of self-healing on exposure to oxygen (Liu, Karpov & Park, 2006). Generally speaking, very high local temperatures are required to repair most current ceramics, due to the high activation energies of the diffusive mass transport in the covalent or ionic structures of ceramics (*e.g.* SiC/Al₆Si₂O₁₃ composite: 1300 °C). In Figure 2.25, the healing reaction is initiated by the heat of combustion and a self-healing oxidation and corrosion protection coating on SiC-ceramic (burner nozzle) occur. A reactive filler (MoSi₂) embedded in a SiOC-matrix is oxidized by permeating oxygen and the formed SiO₂ closes the crack completely (Figure 2.25) (Hager, Greil, Leyens, Zwaag & Schubert, 2010).

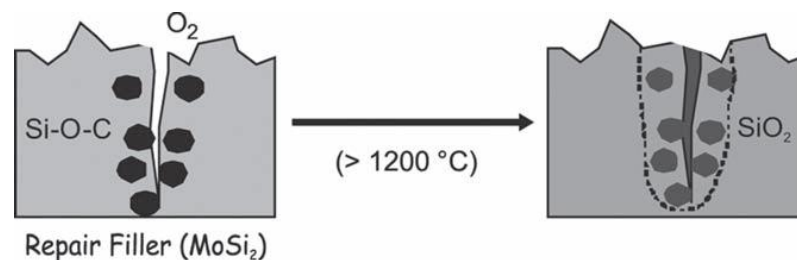


Figure 2.25 Self-healing of cracks in SiOC/MoSi₂ oxidation protection coatings on SiC ceramics (Hager, Greil, Leyens, Zwaag & Schubert, 2010).

Even though metals and ceramics have been investigated for self healing studies, polymers (and composites) are by far the most studied material class in the context of self-healing behaviour. This may be due to easy achievement of functionalisation and modification of the polymeric systems that require low temperatures to induce mobility and need the large volume of mobile molecules in comparison to the volume of mobile atoms (Hager, Greil, Leyens, Zwaag & Schubert, 2010).

2.1.4.1 Chitosan

Chitosan is a linear polysaccharide obtained by extensive deacetylation of chitin. It is mainly composed of two kinds of (1 → 4) linked structural units *viz.* 2-amino-2-deoxy-d-glucose and *N*-acetyl-2-amino-2-deoxy-d-glucose. The chemical structure of a completely deacetylated chitosan is represented in Figure 2.26. Nonetheless, inasmuch as it is virtually impossible to completely deacetylate chitin, what is usually known as chitosan is a family of chitins with different but always low degrees of acetylation. The capacity of chitosan to dissolve in dilute aqueous solutions is the commonly accepted criterion to differentiate it from chitin (Belgacem & Gandini, 2008, Raafat, 2008).

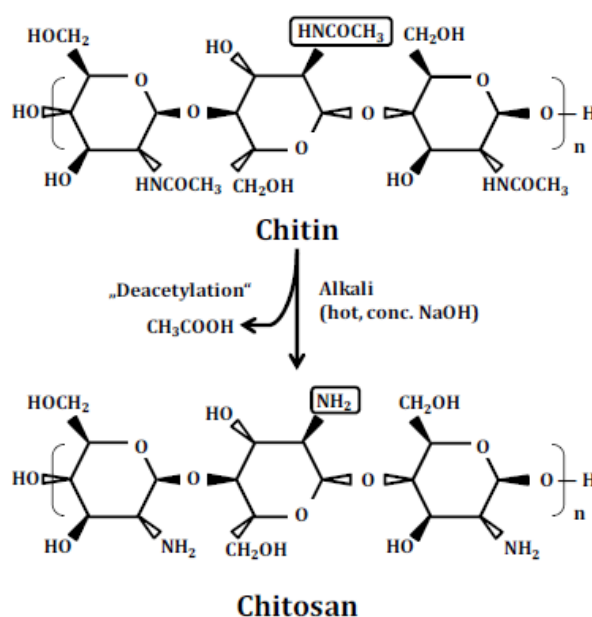


Figure 2.26 Chemical structures of chitosan and its production from chitin (Raafat, 2008).

Chitosan is also found in nature, such as in cell walls of fungi of the class *Zygomycetes*, in the green algae *Chlorella* sp., yeast and protozoa as well as in insect cuticles. Recent advances in fermentation technology suggest that the cultivation of fungi (*Aspergillus Niger*) can provide an alternative source of chitosan. However, chitosan from both sources differs slightly: whereas the acetyl groups in chitosan

produced from crustacean chitin are uniformly distributed along the polymer chain, a chitosan of similar degree of deacetylation isolated from fungal cell walls would possess acetyl residues that are grouped into clusters (Raafat, 2008).

In contrast to most of the naturally-occurring polysaccharides, e.g. cellulose, dextran, pectin, alginic acid, agar, agarose and carragenans, which are neutral or acidic in nature, chitosan is an example of a highly basic polysaccharide. Its nitrogen content varies from 5 to 8% depending on the extent of deacetylation; it is mostly in the form of primary aliphatic amino groups (Raafat, 2008).

The molecular weight distribution of a raw chitosan preparation is influenced by variable conditions employed in the deacetylation process, such as time, temperature, concentration and nature of starting material as well as atmospheric conditions. Weight-average molecular weights of several hundreds to over one million Dalton are common, with a mean molecular mass of up to 1 MDa, corresponding to a chain length of approximately 5,000 U (Raafat, 2008).

Pure, native chitosan ($pK_a \cong 6.3$) is insoluble in water, in alkaline medium and even in organic solvents. However, water-soluble salts of chitosan may be formed by neutralization with organic acids (e.g. 1-10% aqueous acetic, formic, succinic, lactic, glutamic and malic acids) or inorganic acids such as hydrochloric acid. The pH-dependent solubility of chitosan is attributed to its amino groups ($-\text{NH}_2$), which become protonated upon dissolution at pH 6 or below to form cationic amine groups ($-\text{NH}_3^+$), increasing intermolecular electric repulsion and resulting in a polycationic soluble polysaccharide, with a large number of charged groups on a weight basis. On the other hand, chitosan tends to lose its charge at higher pH, and may therefore precipitate from solution due to deprotonation of the amine groups (Raafat, 2008).

One of the most characteristic properties of many polymers, including chitosan, is their ability to form viscous solutions; they could therefore function as thickeners, stabilizers, or suspending agents. Chitosan solutions show pseudoplastic and viscoelastic properties; their viscosity is affected by chitosan's degree of

deacetylation, molecular weight and concentration, concentration and types of solvents, the prevailing solution pH and ionic strength, as well as temperature. The viscosity range of commercial chitosans (1% [wt/vol] in 1% acetic acid at 25°C) is from 10 to 1000 mPa·s (Raafat, 2008).

2.1.4.2 Working Mechanism

In spite of the fact that the underlying chemical and physical effects of some of the applications of chitosan and its derivatives are still not known in detail, considerable evidence has been gathered indicating that most of their physiological activities and functional properties depend on their molecular weight and the purity (Raafat, 2008).

Chitosan possesses three types of reactive functional groups: an amino group at the C-2 position of each deacetylated unit, as well as primary and secondary hydroxyl-groups at the C-6 and C-3 positions, respectively, of each repeat unit (Figure 2.26). These reactive groups are readily subjected to chemical derivatization under mild conditions, to allow for the manipulation of mechanical and physicochemical properties (Raafat, 2008). Figure 2.27 shows the complexation between metal ions and the $-NH_2$ groups of chitosan in the structure of $LiMn_2O_4$ film deposition; lithium/manganese acetates–chitosan precursor is proposed (Shih & Fung, 2006). Furthermore, the presence of free amino groups in chitosan permits its conjugation with some drugs, as well as complexing agents such as ethylenediaminetetraacetic acid and EDTA (Raafat, 2008).

Chitosan is a biological product with cationic (positive electrical charge) properties. It is of great interest, all the more so because most polysaccharides of the same types are neutral or negatively charged. By controlling the molecular weight, the degree of deacetylation and purity, it is possible to produce a broad range of chitosans and derivatives that can be used for industrial, dietary, cosmetic and biomedical purposes (Beaulieu, 2005). Moreover as the superior solubility makes chitosan easily manageable, it could be easily processed into a variety of useful

forms such as gels, membranes, sponges, films, fibers and beads, by controlling factors such as acid solvent, degree of deacetylation and molecular weight, to address a variety of applications (Raafat, 2008).

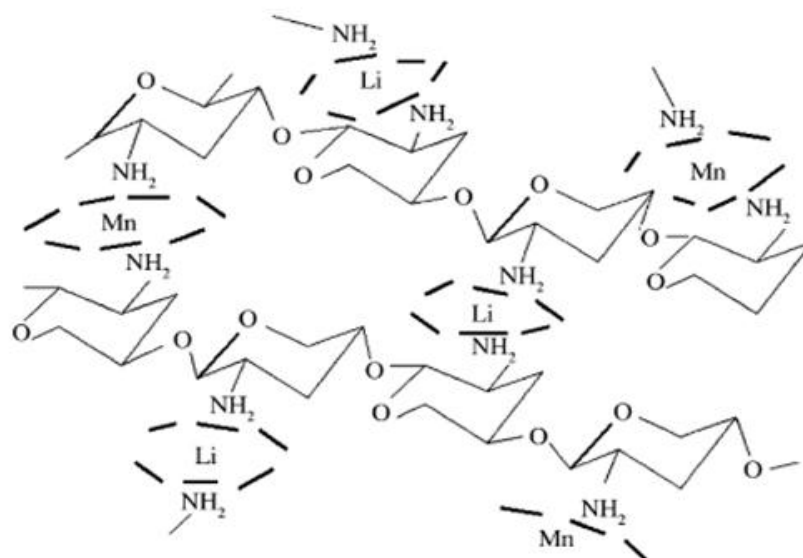


Figure 2.27 Schematic illustration of the chelate mechanism between chitosan and Li/Mn ions (Shih & Fung, 2006).

2.1.4.3 Applications

Chitosan has a very wide application range every where of life. It is a very useful polymer for biomedical applications in terms of its biocompatibility, biodegradability and low toxicity (Peniche, Argüelles-Monal & Goycoolea, 2008). The well-established antimicrobial properties of chitin and chitosan against a wide spectrum of bacteria, fungi and viruses can lead to a potentially large reduction in the amount of synthetic food preservatives currently used (Rabea, Badawy, Stevens, Smagghe & Steurbaut, 2003).

As mentioned above, the purity of the product is vital particularly for high-value product (biomedical or cosmetic area). This purity is quantified as the remaining ashes, proteins, insolubles, and also in the bio-burden (microbes, yeasts and moulds, endotoxins). Even in the lower value chitosan such as that used for the wastewaters treatment, the purity is a factor because the remaining ashes or proteins tend to block

active sites, the amine grouping. Being not available to bind, a greater amount of chitosan is needed to be effective (Raafat, 2008).

Applications of chitosan can be classified mainly in 3 categories according to the requirement on the purity of the chitosan (Beaulieu, 2005):

- Technical grade for agriculture and water treatment,
- Pure grade for the food and cosmetics industries, and
- Ultra-pure grade for biopharmaceutical uses.

In agriculture, chitosan offers a natural alternative to the use of chemical products that are sometimes harmful to humans and their environment. Chitosan triggers the defensive mechanisms in plants (acting much like a vaccine in humans), stimulates growth and induces certain enzymes (synthesis of phytoalexins, chitinases, pectinases, glucanases, and lignin). This new organic control approach offers promise as a biocontrol tool. In addition to the growth-stimulation properties and fungi, chitosans are used for: Seed- coating, Frost protection, Bloom and fruit-setting stimulation, Timed release of product into the soil (fertilizers, organic control agents, nutrients), Protective coating for fruits and vegetables (Beaulieu, 2005).

For water treatment, at the present time, physicochemical-type treatment is widely used at potable and wastewater treatment plants. The major disadvantage of using synthetic chemical products is the risk of resulting environmental pollution. Treating wastewater using "greener" methods has become an ecological necessity. Chitosan, due to its natural origin and being biodegradable, has proven to be a most interesting alternative from several points of view. Integrating a natural polymer made of crustacean residue into an existing system achieves a two-fold purpose: it improves the effectiveness of water treatment while reducing or even eliminating synthetic chemical products such as aluminum sulphate and synthetic polymers. Here are a few characteristics of chitosan that offer an ecological solution: Natural and biodegradable, A powerful competitor for synthetic chemical products, Potentially reduces the use of alum by up to 60% and eliminates 100% of the polymers from the

treated water, Improves system performance (suspended solids and chemical oxygen demand), Significantly reduces odor (Beaulieu, 2005).

In food, chitosan is already used as a food ingredient in Japan, in Europe and in the United States as a lipid trap, an important dietetic breakthrough. Since chitosan is not digested by the human body, it acts as a fiber, a crucial diet component. It has the unique property of being able to bind lipids arriving in the intestine, thereby reducing by 20 to 30% the amount of cholesterol absorbed by the human body. This raises the question: is chitosan really a "Fat Magnet"? In solutions, chitosan has thickening and stabilizing properties, both essential to the preparation of sauces and other culinary dishes that hold their consistency well. Finally, as a flocculating agent, it is used to clarify beverages. Owing to its phytosanitary properties, it can be sprayed in dilute form on foods such as fruits and vegetables, creating a protective, antibacterial, fungi static film. In Japan, a dilute solution of chitosan is commonly sprayed on apples and oranges as a protective measure. There are many other applications in the areas of nutraceutical and nutritional supplements, particularly for the broad range of chitosans that have been chemically or enzymatically modified. Principal commercial applications include: preservatives, food stabilizers, animal feed additives, anti-cholesterol additives (fat traps) (Beaulieu, 2005).

In cosmetics, chitosan forms a protective, moisturizing, elastic film on the surface of the skin that has the ability to bind other ingredients that act on the skin. In this way, chitosan can be used in formulating moisturizing agents such as sunscreens, organic acids, etc. to enhance their bioactivity and effectiveness. Today, chitosan is an essential component in skin-care creams, shampoos, and hairsprays due to its antibacterial properties. Many patents have been registered and new applications are just beginning to appear including the most highly prized moisturizing and antibacterial properties. Applications include: maintain skin moisture, treat acne, tone skin, protect the epidermis, reduce static electricity in hair, fight dandruff, and improve suppleness of hair (Beaulieu, 2005).

For biopharmaceutical uses, it is in the field of health that the many properties of chitosan (bacteriostatic, immunologic, antitumoral, cicatrizant, hemostatic and anticoagulant) are of interest. For example, because of its biocompatibility with human tissue, chitosan's cicatrizant properties have proven its effectiveness as a component, notably, in all types of dressings (artificial skin, corneal dressings, etc.), surgical sutures, dental implants, and in rebuilding bones and gums. Applications currently being developed include artificial skin, surgical sutures that are absorbed naturally after an operation, and corneal contact lenses. Finally, chitosan delivers and time-releases drugs used to treat animals and humans. There are many potential chitosan applications in the health field but their development calls for the use of components that comply with strict pharmaceutical-grade requirements. Possible applications include: ointments for wounds, surgical sutures, ophthalmology, orthopedics, pharmaceutical products (delivery agent), contact lenses (Beaulieu, 2005).

Applications of chitosan are growing rapidly. Not only due to its multitude of applications but due to increasing environmental awareness of the population, biodegradable, and non-toxic products from 'natural' sources such as chitin and chitosan are going to be more and more appealing for the replacement of synthetic compounds (Beaulieu, 2005).

On the other hand, besides those plenty of applications, it has been investigated chitosan's self healing property lately. In this sense, a completed research on a self-healing coating that can actually repair itself after a scratch occurs. After being exposed to sunlight, this amazing surface repairs small scratches. This material is a combination of polyurethane paint, chitosan molecules and a ring-shaped molecule called oxetane. The chitosan molecules are the same molecules found in shells of lobsters, crabs and other crustaceans. When a small scratch occurs in the surface of the paint, the oxetane rings are split and left with loose ends. The sunlight causes the chitosan molecules to react with split oxetane rings, which in turn closes the split, essentially healing the surface (Trask, Williams, & Bond, 2007).

Polyurethane networks that exhibit self-repairing characteristics upon exposure to ultraviolet light. The network consists of an oxetane-substituted chitosan precursor incorporated into two-component polyurethane. Upon mechanical damage of the network, four-member oxetane rings open to create two reactive ends. When exposed to ultraviolet light, chitosan chain scission occurs, which forms crosslinks with the reactive oxetane ends, thus repairing the network. These materials are capable of repairing themselves and can be used in many coatings applications, ranging from transportation to packaging or fashion and biomedical industries (Ghosh, & Urban, 2009).

CHAPTER THREE

EXPERIMENTAL PROCEDURE

3.1 Purpose

The aim of this thesis is to design a material to accomplish multiple performance objectives in a single system to respond the required needs as mentioned above; antibacterial, flame retardant, radar absorbing and self-healing. As there is no any literature knowledge regarding this kind of multifunctional material having those four properties, it is important to produce this type of material in this study. From this point of view, in this research, the new approach is to explore both the science and technology of how reinforced materials affect structures of polyurethane and epoxy dyes as composite coatings and connect the results to materials properties, and show the engineering concepts that can be used to produce or improve multifunctional paints by several applications. This work will be a guide for the future researches followed by the researches. In this respect, the structural, microstructural, thermal, adhesion, antibacterial, flame retardant, radar absorbing and self-healing properties of the produced reinforced materials and composite coatings/paints were determined in this chapter in details.

3.2 Materials

3.2.1 Substrate Materials

Glass, metal and plastic substrates were used in this research. The substrate types were chosen according to the characterization technical requirements. The surface of the substrate were suitably polished and become stable. Prior to coating process, the substrates were cleaned in an ultrasonic bath using acetone in order to eliminate impurities from the sample surface. Afterwards, substrate surfaces were dried at room temperature in air.

3.2.2 Starting Materials

All precursor materials used in production of composite coatings/paints are listed in Table 3.1 in details. For the multifunctional properties such as antibacterial, flame retardant, radar absorbing and self-healing, the materials are classified in Table 3.1. Polyurethane and epoxy dyes purchasing from DYO Inc., Izmir were used as main materials. In order to prepare antibacterial solutions, silver nitrate (AgNO_3 , Merch), glucose ($\text{C}_6\text{H}_{12}\text{O}_6$, Merch) and distilled water were utilized to produce Ag nanoparticles with the help of a chemical synthesis technique.

Table 3.1 All precursor materials and their descriptions for multifunctional properties

Functions	Materials	Paint matrix
Antibacterial	-Silver nitrate (AgNO_3 , Merch) -Glucose ($\text{C}_6\text{H}_{12}\text{O}_6$, Merch) -Distilled water	Polyurethan/Epoxy
Flame retardant	-Huntite hydromagnesite ($\text{Mg}_3\text{Ca}(\text{CO}_3)_4$, $4\text{MgCO}_3.\text{Mg}(\text{OH})_2.4\text{H}_2\text{O}$, Lidya Minelco Inc.) -Boric acid (H_3BO_3) -Antimony oxide (Sb_2O_3 , Aldrich, 99.99%) -Distilled water	Polyurethan/Epoxy
Radar absorbing	-Barium nitrate ($\text{Ba}(\text{NO}_3)_2$, Aldrich, 99.99%) -Ferric citrate mono hydrate ($\text{C}_6\text{H}_5\text{FeO}_7.\text{H}_2\text{O}$, Fluka) - Citric acid monohydrate ($\text{C}_6\text{H}_8\text{O}_7.\text{H}_2\text{O}$, Sigma, >99.50%) -Ammonium hydroxide (NH_4OH , Merch, 25%)	Polyurethan/Epoxy
Self-healing	-Chitosan (Poly-(D)glucosamine, Sigma) - Acidic acid (CH_3COOH , 1%)	Polyurethan/Epoxy
Multifunctional	-Antibacterial components -Flame retardant components -Radar absorbing components -Self-healing components	Polyurethan/Epoxy

As for flame retardant properties, huntite, hydromagnesite ($\text{Mg}_3\text{Ca}(\text{CO}_3)_4$, $4\text{MgCO}_3.\text{Mg}(\text{OH})_2.4\text{H}_2\text{O}$, Likya Minelco Inc., Denizli), boric acid (H_3BO_3) and

antimony oxide (Sb_2O_3 , Aldrich, 99.99%) were used as reinforced materials. For radar absorbing characteristics, barium nitrate ($\text{Ba}(\text{NO}_3)_2$, Aldrich, 99.99%), ferric citrate mono hydrate ($\text{C}_6\text{H}_5\text{FeO}_7 \cdot \text{H}_2\text{O}$, Fluka), citric acid monohydrate ($\text{C}_6\text{H}_8\text{O}_7 \cdot \text{H}_2\text{O}$, Sigma, >99.50%) and ammonium hydroxide (NH_4OH Merch, 25%) were utilized to synthesize barium hexaferrite ($\text{BaFe}_5\text{O}_{19}$) using sol-gel technique. In addition, chitosan (Poly-(D) glucosamine, Sigma) and acetic acid (CH_3COOH , 1%) were used to possess self-healing properties. After an optimum production of antibacterial, flame retardant, radar absorbing and self-healing compounds, they were used in polyurethane/epoxy matrix as reinforced materials.

3.3 Production Technique

3.3.1 Multifunctional Component Production

3.3.1.1 Antibacterial Ag Nanoparticles

Before producing antibacterial polymeric composite coatings/paints on plastic and glass substrates, Ag nanoparticle was synthesized from AgNO_3 , $\text{C}_6\text{H}_{12}\text{O}_6$ and distilled water with the aid of chemical synthesis technique which is related with chemical reactions during the process. As can be seen from Figure 3.1, a flow chart regularly clarifies production of Ag nanoparticles as from starting step to final one. In this section of the thesis, AgNO_3 and $\text{C}_6\text{H}_{12}\text{O}_6$ powder based precursors were separately dissolved using distilled water using ultrasonic bath/cleaning machine (Wise Circu) which accelerates the reaction process with vibration as shown in Figure 3.2 and then transparent solutions were prepared before producing Ag nanoparticles. After this process, an aqueous solution of AgNO_3 and an aqueous solution of a non-ammonia reducing agent were mixed to form an Ag nanoparticle-containing solution at room temperature for 15 minutes in air. $\text{C}_6\text{H}_{12}\text{O}_6$ was used as a reducing agent in this study wherein AgNO_3 and $\text{C}_6\text{H}_{12}\text{O}_6$ was at a ratio of about 2:1 by weight. End of this procedure, Ag particles with Nano scale were produced for antibacterial coating applications.

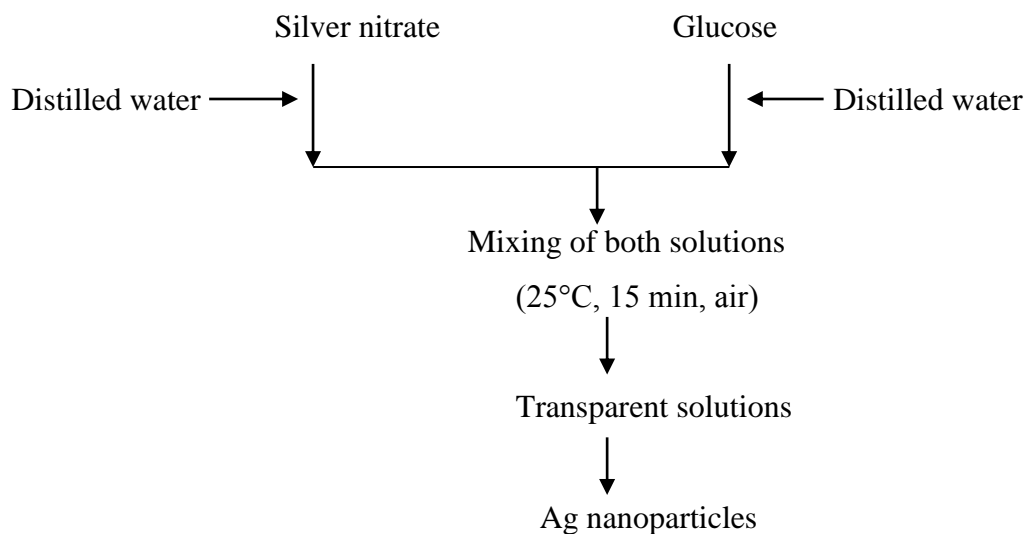


Figure 3.1 Flow chart for production of Ag nanoparticles by means of chemical synthesis method



Figure 3.2 The ultrasonic bath/cleaning machine (Chemistry Lab., DEU)

3.3.1.2 Flame Retardant Nano powders

Huntite/hydromagnesite ($\text{Mg}_3\text{Ca}(\text{CO}_3)_4/4\text{MgCO}_3 \cdot \text{Mg}(\text{OH})_2 \cdot 4\text{H}_2\text{O}$), boric acid (H_3BO_3) and antimony oxide (Sb_2O_3) powders were utilized in the polyurethane and epoxy polymeric coating/paints as flame retardant materials. In order to obtain synergetic effects of these flame retardant materials, Nano powder systems with one, two or three components were prepared in this experiment.

Inasmuch as huntite/hydromagnesite is very effective flame retardant, first of all it was chosen in polymeric composite materials. Figure 3.3 signifies a flow chart for production of flame retardant powders. After the huntite/hydromagnesite minerals is crushed and ground to get finer fractions, 10 μm size huntite/hydromagnesite minerals were ground at room temperature for 0, 15, 30, 60 hours in air by means of a standard ball mill machine as seen from Figure 3.4. Then these powders were ground from micron-scale powders to Nano size particles in a High Energy Ball milling machine (Fritsch Premium line Pulverisette 7 model) in Figure 3.5. The flame retardant powders were ground at rate of 800 rpm at room temperature for 15 minutes in air.

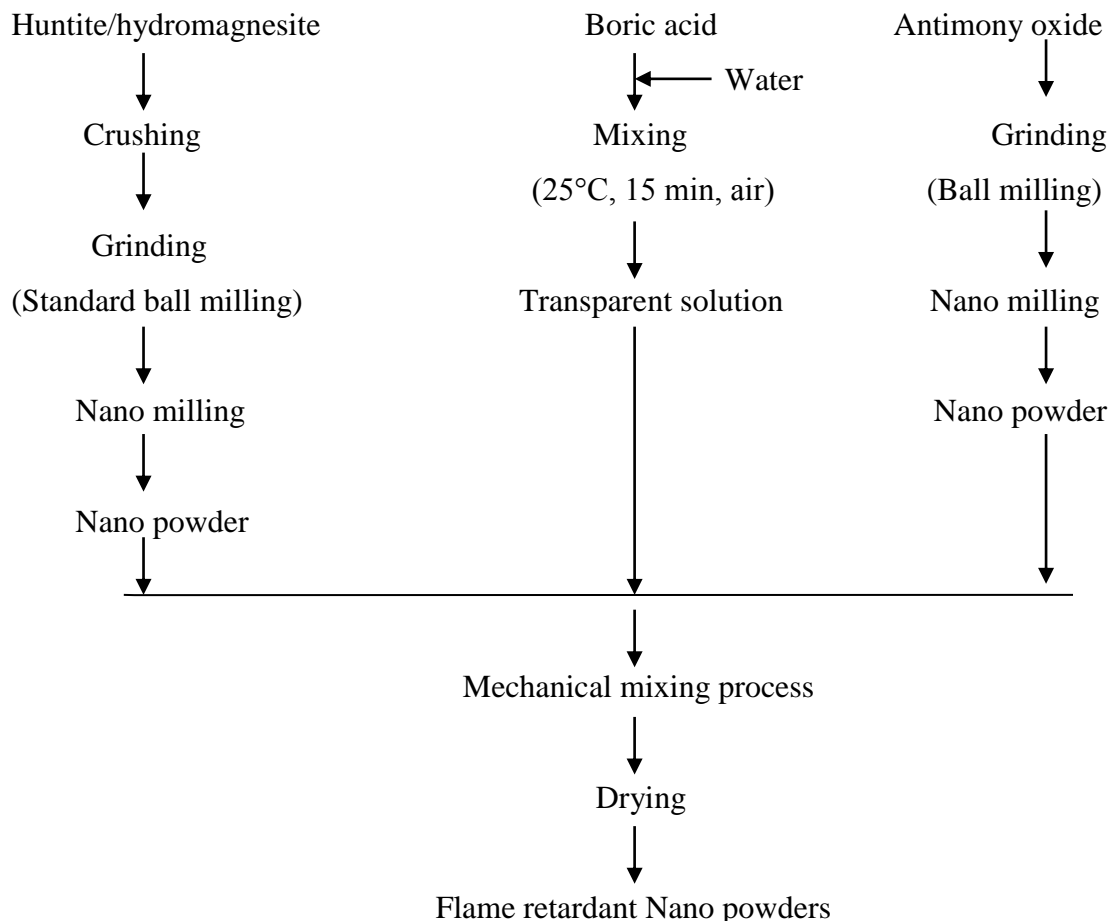


Figure 3.3 Flow chart for production of flame retardant powders

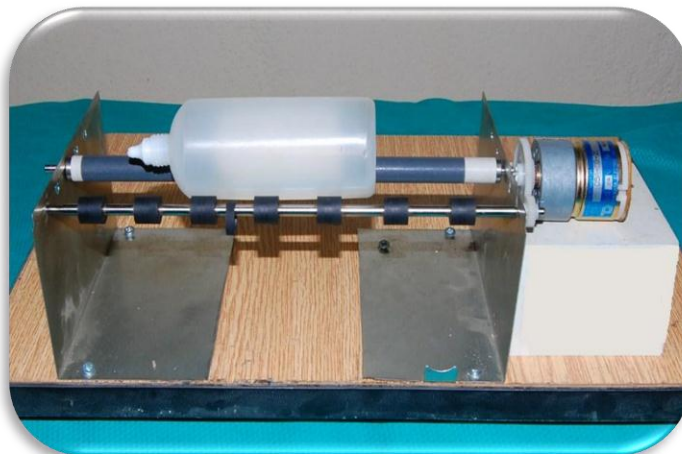


Figure 3.4 The ball milling machine (Electronic Materials Lab., DEU)

As in the case of the production of boron based flame retardant materials, boric acid was used to incorporate into the polymeric composite coatings. For this, boric acid powders were dissolved in distilled water at room temperature for 15 minutes in air using ultrasonic bath/cleaning machine (Wise Circu) and then transparent solutions were prepared for flame retardant materials. On account of the fact that water based solutions containing boron sometimes have problems in coating/painting process, they were added into flame retardant powders in certain concentrations in order to obtain their beneficial effects.



Figure 3.5 The high energy ball milling machine (Nanotechnology Lab., EMUM-DEU)

As for the production of antimony oxide Nano powder, the micron scale powder was purchased from Aldrich Company. These powders were ground from micron-scale powders to Nano size particles in a ball milling machine (Fritsch pulverisette 7). After separately producing Nano powders from huntite/hydromagnesite, boric acid and antimony oxide, they were mechanically mixed and subsequently dried at room temperature for 1 day in air as a last product for flame retardant composite coatings/paints.

3.3.1.3 Radar Absorbing Powder

Barium hexaferrite powders were synthesized by sol-gel method (Aksit et al. 2009). Preprocessing and synthesis of the powders were described in Ref. (Zhuravlev & Suslyayev 2006) in detail and briefly summarized in Figure 3.6. In this research this technique was slightly modified for multifunctional composite materials. The used precursors are barium nitrate ($\text{Ba}(\text{NO}_3)_2$, Aldrich) and ferric citrate mono hydrate ($\text{C}_6\text{H}_5\text{FeO}_7 \cdot \text{H}_2\text{O}$, Fluka), chelating agent is citric acid monohydrate ($\text{C}_6\text{H}_8\text{O}_7 \cdot \text{H}_2\text{O}$) and pH regulator is ammonium hydroxide (NH_4OH). Ferric citrate and barium nitrate were separately dissolved of in citric acid using molar ratios of citric acid: metal=3 and Fe: Ba=11. The solutions were vigorously mixed by magnetic stirrer until the transparent solution was obtained. Ammonium hydroxide was added until reaching of the pH value of the solution to 7 at room temperature and then mixed by magnetic stirrer. Thus, it was aimed to provide homogenous suspension and stable pH condition in the solution after whole solution preparation. The solution was kept in water bath at 80°C for 15 hours in air. Therefore the water in the solution was gradually removed and wet gel with high viscosity was obtained. The wet gel was treated at 180°C for 15 hours in Nüve KD400 oven to prepare dry gel. The dry gel was exposed to pre-sintering process at 550°C for 6 hours to evaporate impurities and then was sintered at 1000°C for 5 hours in air in a Protherm electrical tube furnace (Figure 3.7).

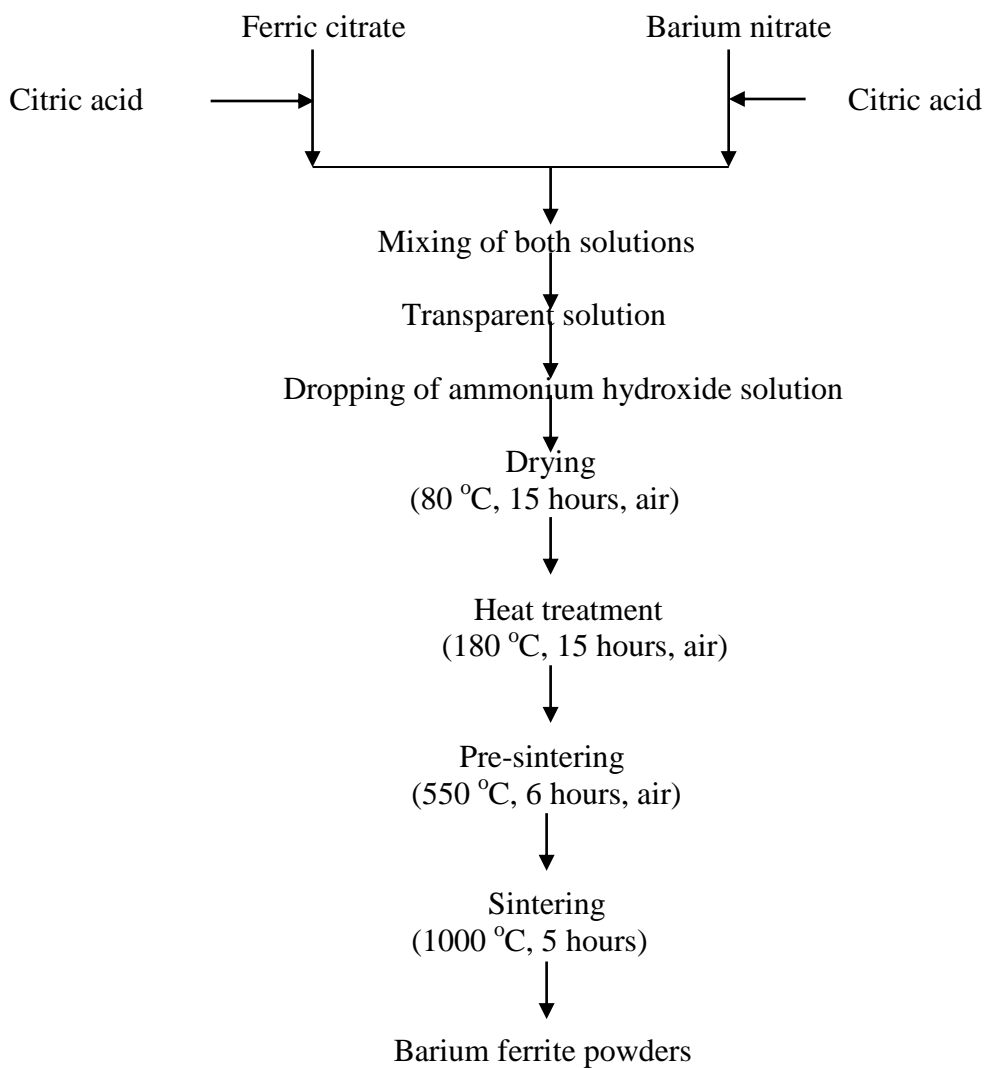


Figure 3.6 The flow chart for producing barium ferrite powders (Onar, 2009).



Figure 3.7 Protherm tube furnaces (Heat Treatment Lab. DEU)

3.3.1.4 Self-healing Solution

Chitosan (Poly-(D) glucosamine, Sigma) and acidic acid (CH_3COOH , 1%) were used for self-healing coatings. In this case, two different solutions containing 1% and 3% chitosan in the acetic acid were prepared as presented in Figure 3.8. Different amount of chitosan powder was dissolved with stirring in each acid solution at different concentrations. After complete mixing, firstly they were stirred in ultrasonic cleaner, and then stirred at 25°C for 20 minutes in air by using magnetic balls. Finally homogeneous chitosan colloids were obtained in the solutions.

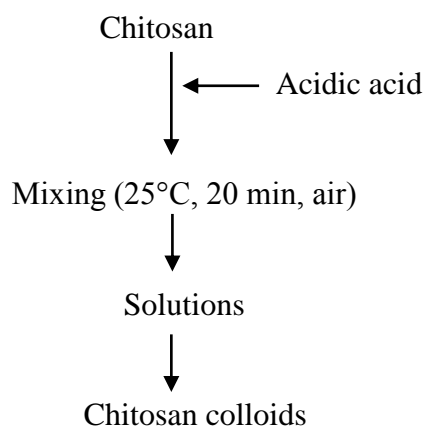


Figure 3.8 Flow chart for production of chitosan colloids

3.3.2 Composite Coating Production

3.3.2.1 Antibacterial Coatings

Polymeric paint composites were prepared by adding Ag nanoparticles at different ratios into the polyurethane matrix. Before adding Ag nanoparticles, polyurethane paint and its hardener were mixed with a 1:1 weight ratio. First coating was carried out with this mixture to a glass base. This was called 0% Ag nanoparticle including coating. Then, it was started to add Ag nanoparticles into coating composite with different ratio. By concentrating the composite matrix with Ag nanoparticles, each

coated sample of different concentration was used to see the concentration dependence of Ag nanoparticles' antibacterial effects.

Table 3.2 First group samples and their descriptions of the composite coatings

Sample codes	Ag nanoparticle content in the solution (%)	Solution content in the composite (%)
NAG 00	0	-
NAG 01	0.10	33.33
NAG 10	1.00	33.33
NAG 50	5.00	33.33
NAG 100	10.00	33.33
NAG 200	20.00	33.33
NAG 301	30.00	20.00
NAG 302	30.00	33.33
NAG 303	30.00	42.85
NAG 304	30.00	50.00

Three different sample groups were prepared for this purpose and different test types were performed to them. In the first group, as listed in Table 3.2, which shows the sample codes and their descriptions of antibacterial coatings, inhibition test was performed with those samples. As for the second group, as shown in Table 3.3, the second group sample codes and their descriptions of antibacterial coatings can be seen in detail.

Table 3.3. The sample codes and descriptions of Ag nanoparticle reinforced polymeric composites

Sample name	Sample description
D 0001	0.001 % Nano Ag added dye
D 01	0.1 % Nano Ag added dye
D 0	Pure dye
D 1	1 % Nano Ag added dye
D 5	5 % Nano Ag added dye
D 10	10 % Nano Ag added dye

Here diffusion test was performed to those samples by parallel cultivations method with different types of bacteria (S.Aureus, E.Coli, P. Aeruginosa, K. Pneumonie, and C. Albicans) and yeast-Fongüs. In addition percent decreasing tests was also performed to these samples. In the third group, Table 3.4 shows those sample codes and their descriptions of antibacterial coatings. After obtaining good results, different types of samples were prepared to estimate the effect of dye amount. Only percent decreasing tests were performed to those samples.

Table 3.4 Sample codes and descriptions of Ag nanoparticle reinforced composites

Sample name	Sample description
D 00	0.05 g pure dye
D 01	0.1 g pure dye
D 02	0.2 g pure dye
D 03	0.3 g pure dye
D 04	0.4 g pure dye
D 05	0.5 g pure dye
DAG 103	1% Ag nanoparticle added, 0.3 g composite
DAG 105	1% Ag nanoparticle added, 0.5 g composite
DAG 503	5% Ag nanoparticle added, 0.3 g composite
DAG 505	5% Ag nanoparticle added, 0.5 g composite

3.3.2.2 Flame Retardant Coatings

Polymeric paint composite coatings were prepared by reinforcing flame retardant nanoparticles at different ratios into the polyurethane and epoxy matrixes. Prior to the reinforcement of flame retardant nanoparticles, polyurethane and epoxy paints and their hardeners were mixed with a 1:1 weight ratio respectively. After this procedure, two types of polymeric composites were prepared for flame retardant performance.

One of the flame retardant materials was only huntite/hydromagnesite mineral in the dye matrix. The code of the ground huntite/hydromagnesite materials are listed in Table 3.5. The sample name was called according to grinding periods including 0,

15, 30 and 60 hours at room temperature in air. Then ground minerals were blended to the epoxy dye with different size and different loading level. Afterwards, the plastic substrates are coated with those composite dyes. More details for the coated sample descriptions and codes about flame retardant composite coatings are presented in Table 3.6.

Table 3.5 The codes of the ground huntite/hydromagnesite materials

Sample names	Grinding periods
HM00	0 hour grinding
HM15	15 hours grinding
HM30	30 hours grinding
HM60	60 hours grinding

Table 3.6 Sample codes and descriptions of composite coatings

Sample code	Description
V00	Pure
VS 15-25	15 hours ground, % 25 added
VS 15-65	15 hours ground, % 65 added
VS 15-50	15 hours ground, % 50 added

The other flame retardant mixture contains huntite/hydromagnesite, boric acid solution and antimony oxide. Fine and coarse huntite and hydromagnesite minerals were blended with boric acid solution and antimony oxide with the ratio of 1%, 5%, 10%, 15%, 20% and 30% separately. This flame retardant mixture was then blended to a dye material with the ratio of 30%. The glass substrates were coated with this dye-mineral composite. Sample codes and descriptions of the flame retardant composite coatings were given in Table 3.7.

Table 3.7 Sample codes and descriptions of flame retardant composite coatings

Sample code	Description
A1%N	1% antimony and standard huntite /hydromagnesite reinforced coating
A1%O	1% antimony and ground huntite /hydromagnesite reinforced coating
A5%N	5% antimony and standard huntite /hydromagnesite reinforced coating
A5%O	5% antimony and ground huntite /hydromagnesite reinforced coating
A10%N	10% antimony and standard huntite /hydromagnesite reinforced coating
A10%O	10% antimony and ground huntite /hydromagnesite reinforced coating
A15%N	15% antimony and standard huntite /hydromagnesite reinforced coating
A15%O	15% antimony and ground huntite /hydromagnesite reinforced coating
A30%N	30% antimony and standard huntite /hydromagnesite reinforced coating
A30%O	30% antimony and ground huntite /hydromagnesite reinforced coating
A50%N	50% antimony and standard huntite /hydromagnesite reinforced coating
A50%O	50% antimony and ground huntite /hydromagnesite reinforced coating
B1%N	1% boric acid and standard huntite /hydromagnesite reinforced coating
B1%O	1% boric acid and ground huntite /hydromagnesite reinforced coating
B5%N	5% boric acid and standard huntite /hydromagnesite reinforced coating
B5%O	5% boric acid and ground huntite /hydromagnesite reinforced coating
B10%N	10% boric acid and standard huntite /hydromagnesite reinforced coating
B10%O	10% boric acid and ground huntite /hydromagnesite reinforced coating
B15%N	15% boric acid and standard huntite /hydromagnesite reinforced coating
B15%O	15% boric acid and ground huntite /hydromagnesite reinforced coating
B30%N	30% boric acid and standard huntite /hydromagnesite reinforced coating
B30%O	30% boric acid and ground huntite /hydromagnesite reinforced coating
B50%N	50% boric acid and standard huntite /hydromagnesite reinforced coating
B50%O	50% boric acid and ground huntite /hydromagnesite reinforced coating
SFBoya	Coating with pure dye
SFPlast	Uncoated plastic substrate

N: Standard huntite/hydromagnesite minerals having 10 micron size

O: Ground in Nano grinding machine

3.3.2.3 Radar Absorbing Coatings

Epoxy dye has been used as a composite matrix that is known as polyepoxide, a thermosetting copolymer formed from reaction of an epoxide "resin" with polyamine "hardener". The resin consists of short chain polymers with an epoxide group at

either end. Epoxy resin is produced from a reaction between epichlorohydrin and bisphenol-A. The hardener consists of polyamine monomers, triethylenetetramine (Chem424, 2012, Ebert, 1991).

Produced barium hexaferrite powders were added to this epoxy matrix with different loading levels such as 0%, 5%, 10% and 20% to evaluate the concentration dependence of particles' radar absorbing effects. Then metal and glass substrates were coated with those polymer composites and subsequently dried at room temperature in air (Figure 3.9). The sample codes and descriptions of the radar absorbed composites are listed in Table 3.8.



Figure 3.9 Photographs of the as-coated samples before any tested.

Table 3.8 Sample codes and descriptions of barium hexaferrite reinforced composite coatings

Sample code	Description
BF00	0% barium hexaferrite reinforced coating
BF05	5% barium hexaferrite reinforced coating
BF10	10% barium hexaferrite reinforced coating
BF20	20% barium hexaferrite reinforced coating

3.3.2.4 Self-healing Coatings

As mentioned above that the epoxy dye a thermosetting copolymer formed from reaction of an epoxide resin with polyamine hardener has been used as a composite matrix for obtaining self-healing property. Epoxy resin is produced from the reaction between epichlorohydrin and bisphenol-A and the hardener consists of polyamine monomers, triethylenetetramine (Chem424, 2012, Ebert, 1991).

The obtained chitosan colloids were incorporated into epoxy dye as a polymer matrix with different loading levels to assess the concentration dependence of material's self-healing effect. Then glass substrates were coated with those polymer composites. The sample codes and descriptions of self-healing coatings are indicated in Table 3.9. After the composite coatings are obtained, they were subsequently dried for 24 hours at the room temperature in the air, no more curing process were performed. After the coated samples are obtained, they were scratched by a very thin pin to get thin splits/cracks and then observed in scanning electron microscopy (SEM) as shown in Figure 3.10.

Table 3.9 Description and sample codes of the self-healing composite coatings

Sample codes	Chitosan percentage in the composites (%)
1	0.0005
2	0.0049
3	0.0237
4	0.0452
5	0.0119
6	0.0119
7	Pure

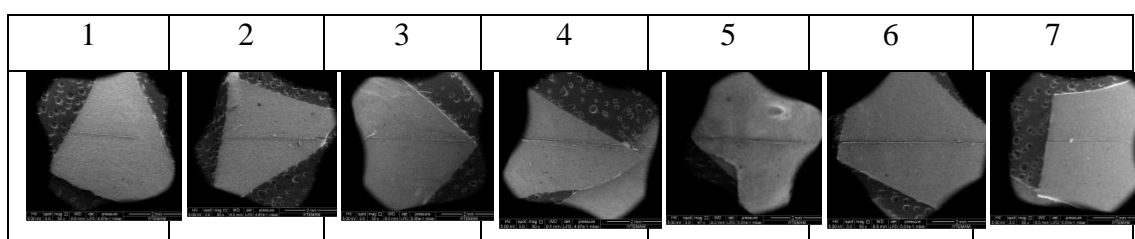


Figure 3.10 SEM micrographs of the coated samples.

3.3.2.5 Multifunctional Coatings

For multifunctional properties, epoxy composite dyes were prepared by adding Ag nanoparticles, which are for antibacterial characteristics, huntite/hydromagnesite powders which are for flame retardant property, barium hexaferrite powders which are for the radar absorbing behavior and chitosan colloids which are for the self-healing property at different ratios into the paint matrix. Additive amounts and the ratio of the multifunctional composites are given in Tables 3.10 and 3.11.

Table 3.10 Description of the multifunctional composite samples by percentage

Code of the samples	Ag nanoparticles (%)	Huntite/hydromagnesite (%)	Barium hexaferrite (%)	Chitosan (%)
AMF 0	-	-	-	-
AMF 1	-	10	5	0.05
AMF 2	0.05	10	5	0.05
AMF 3	0.1	20	10	0.1
AMF4	0.2	30	20	0.2
BMF 1	-	10	-	0.01
BMF 2	0.05	10	5	0.01
BMF 3	0.1	20	5	0.05
BMF 4	0.2	30	-	0.1

According to the characterization tests, different types of substrates such as plastic, glass and metal were used for multifunctional composite coatings. First of all pure dye coating was obtained as a control sample. Then, it was started to add different kind of additives with different amount. By concentrating the composite matrix with the powder additives, each composite sample of different concentration was utilized to scrutinize the concentration dependence.

Table 3.11 Descriptions of the multifunctional composite samples by weight

Code of the samples	Ag nanoparticles (g)	Huntite/hydromagnesite (g)	Barium hexaferrite (g)	Chitosan (g)
AMF 0	-	-	-	-
AMF 1	-	1	0.5	0.005
AMF 2	0.005	1	0.5	0.005
AMF 3	0.01	2	1	0.01
AMF4	0.02	3	2	0.02
BMF 1	-	1	-	0.001
BMF 2	0.005	1	0.5	0.001
BMF 3	0.01	2	0.5	0.005
BMF 4	0.02	3	-	0.01

3.4 Characterization

3.4.1 Ag⁺ ion Determination

Ag⁺ ion determination testing is carried out by atomic absorption spectroscopy with Analytic Jena AG-NovAA® 300. This is a technique for determining the concentration of a particular metal element in a sample. In short, the electrons of the atoms in the atomizer can be promoted to higher orbitals for a short amount of time by absorbing a set quantity of energy (i.e. light of a given wavelength). This amount of energy (or wavelength) is specific to a particular electron transition in a particular element, and in general, each wavelength corresponds to only one element. This gives the technique its elemental selectivity. As the quantity of energy (the power) put into the flame is known, and the quantity remaining at the other side (at the detector) can be measured, it is possible calculate how many of these transitions took place, and thus get a signal that is proportional to the concentration of the element being measured (Figure 3.11) (Welz & Sperling, 1999).

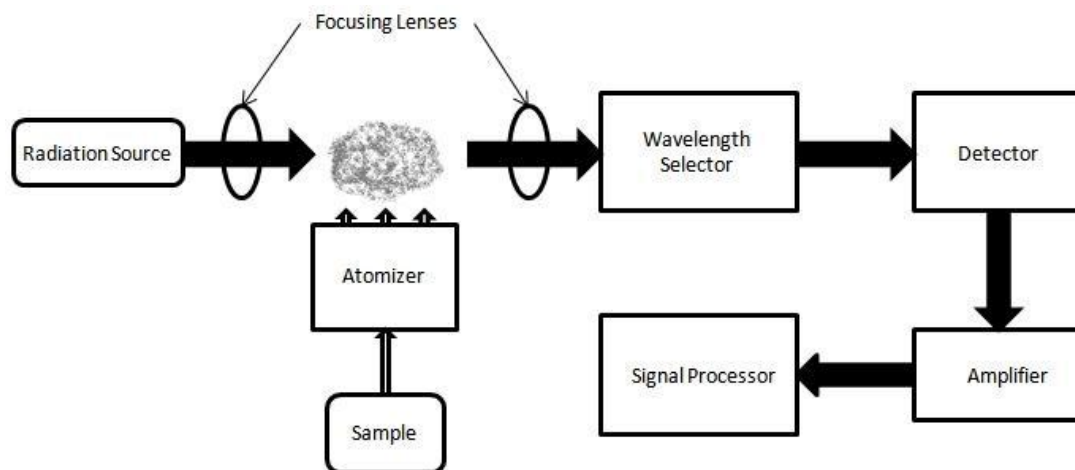


Figure 3.11 Atomic absorption spectrometer block diagram (Welz & Sperling, 1999).

3.4.2 Glucose Determination

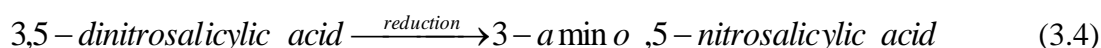
Glucose determinations were performed to prepare Ag nanoparticles by means of Fehling Reactive and DNS method.

3.4.2.1 Fehling Method

Fehling's solution is a chemical test used to differentiate between water-soluble carbohydrate and ketone functional groups, and as a test for monosaccharaides. Fehling's is always prepared fresh in the laboratory. It is made initially as two separate solutions, known as Fehling's A and Fehling's B. Fehling's A is a blue aqueous solution of copper (II) sulfate, while Fehling's B is a clear solution of aqueous potassium sodium tartrate (also known as Rochelle salt) and a strong alkali (commonly sodium hydroxide). Equal volumes of the two mixtures are mixed to get the final Fehling's solution, which is a deep blue color. In this final mixture, aqueous tartrate ions from the dissolved Rochelle salt chelate to Cu^{2+} (aq) ions from the dissolved copper (II) sulfate, as bidentate ligands giving the bistartratocuprate(II)⁴⁻ complex. The tartrate ions, by complexing copper prevent the formation of $\text{Cu}(\text{OH})_2$ from the reaction of $\text{CuSO}_4 \cdot 2\text{H}_2\text{O}$ and NaOH present in the solution (Fehling, 1849).

3.4.2.2 DNS Method

This method tests for the presence of free carbonyl group (C=O), the so-called reducing sugars. This involves the oxidation of the aldehyde functional group present in, for example, glucose and the ketone functional group in fructose. Simultaneously, 3,5-dinitrosalicylic acid (DNS) is reduced to 3-amino,5-nitrosalicylic acid under alkaline conditions:



Now that dissolved oxygen can interfere with glucose oxidation, sulfite, which itself is not necessary for the color reaction, is added in the reagent to absorb the dissolved oxygen.

The above reaction scheme shows that one mole of sugar will react with one mole of 3,5-dinitrosalicylic acid. However, it is suspected that there are many side reactions, and the actual reaction stoichiometry is more complicated than that previously described. The type of side reaction depends on the exact nature of the reducing sugars. Different reducing sugars generally yield different color intensities; thus, it is necessary to calibrate for each sugar. In addition to the oxidation of the carbonyl groups in the sugar, other side reactions such as the decomposition of sugar also competes for the availability of 3,5-dinitrosalicylic acid. As a consequence, carboxymethyl cellulose can affect the calibration curve by enhancing the intensity of the developed color (Wang, 2012).

3.4.3 The pH Determination

The pH fundamentally represents the value of hydrogen ion activity in solutions. Pure water has a pH very close to 7 at 25°C. Solutions with a pH less than 7 are said

to be acidic and solutions with a pH greater than 7 are basic or alkaline. The pH of the Ag nanoparticle based solutions was measured using Mettler Toledo Inlab 412 pH meter of a glass electrode.

A typical pH meter consists of a special measuring probe (a glass electrode) connected to an electronic meter that measures and displays the pH reading. The pH value is defined by the equation given below. This value well accords with the logarithm of the reciprocal of hydrogen ion concentration in dilute solutions (General, 2012):

$$pH = pH_s + (E - E_s) / (2.302RT / F) \quad (3.5)$$

where pH_s =pH value of a pH standard solution, E =electromotive force (volt) on the combination of glass and reference electrodes in a sample solution; the constitution of the cell is expressed by the following:

glass electrode | sample solution | reference electrode

E_s =electromotive force (volt) on the combination of glass and reference electrodes in a pH standard solution, the constitution of the cell is expressed by the following:

glass electrode | pH standard solution | reference electrode

R = gas constant, T = absolute temperature and F = Faraday constant.

3.4.4 Turbidity Measurement

Turbidity (or the relative cloudiness of a liquid) measurement gives the optical characteristics of suspended particles in a liquid. Light is passed through the sample and is scattered in all directions. The light that is scattered at a 90° angle to the incident light is then detected by a photo diode and is converted into a signal linearized by the analyzer and displayed as an NTU (Nephelometric Turbidity Units)

value. The more suspended particles there are in a liquid, the more light will be scattered, resulting in a higher NTU value. In the experiment, turbidity measurements of the prepared precursor solutions were performed by using TB1 Turbid meter just like in Figure 3.12.



Figure 3.12 TB1 Turbid meter, VELP, Scientifics Srl, Italy (Chemistry Lab., DEU)

The sample was placed in the vessel with a dimension of Ø25 mm and height of 50 mm. Formazin is recognized throughout the world as a primary standard. Formazin solution was used to calibrate the turbidity measurements. It was determined whether AgNO_3 powder precursors are well-dissolved in the used solvent.

3.4.5 Particle Size Measurement

The particle size distribution of Ag nanoparticles was determined using particle size analyzer which uses light scattering techniques to measure hydrodynamic size of nanoparticles. The particle zeta potential was determined using Malvern Zetasizer Nano Z (Malvern Instruments Ltd., UK) whereas the particle size distribution was measured using Malvern Zeta Sizes Nano S90 (Figure 3.13.a). In both cases at

temperature of 25°C at least five measurements were made in order to eliminate random errors.



(a)



(b)

Figure 3.13 (a) Malvern Zeta Size Nano S90 and (b) Mastersizer 2000 particles size distribution system (Malvern Instruments, EMUM-DEU).

A laser diffraction machine from Malvern Instruments, Mastersizer 2000 (Figure 3.13.b) was used to obtain the particle size distribution of ceramic powder reinforced materials for composite materials. This method depends upon analysis of the "halo" of diffracted light produced when a laser beam passes through a dispersion of particles in air or in a liquid. The angle of diffraction increases as particle size decreases, so that this method is particularly good for measuring sizes below 1 μm .

3.4.6 Differential Thermal Analysis-Thermogravimetry (DTA-TG)

Thermal methods are based upon the measurement of the dynamic relationship between temperature and some property of the system such as mass and heat absorbed by or evolved from it. Differential Thermal Analysis (DTA) and Thermogravimetry (TG) are the most important thermal methods used in characterization of materials. In DTA the heat absorbed or emitted by a system is observed by measuring the temperature difference ΔT between the sample and an inert reference material (generally alumina powder), as the temperature of both is increased at a constant rate. TG analysis is concerned with the change in weight of a material as its temperatures changes. Many series of thermal analysis techniques can be combined with other non-thermal technique for valuable multiple-parameter information as in our DTA/TG system. The thermal behaviors of hydromagnesite/huntite mineral were evaluated to observe decomposition and phase formation at a heating rate of $10^{\circ}\text{C}/\text{min}$ in the temperature range of $25\text{-}700^{\circ}\text{C}$ under air atmosphere by using DTA/TG machine (DTG-60H Shimadzu) (Figure 3.14).



Figure 3.14 Shimadzu DTG-60H/TA-60WS simultaneous thermal analyzer (Ceramics Lab, DEU)

3.4.7 Fourier Transform Infrared Spectroscopy (FTIR)

FTIR is a powerful tool for identifying types of chemical bonds in a molecule by producing an infrared absorption spectrum that is like a molecular "fingerprint". Each different material is a unique combination of atoms, so two different compounds never produce the exact same infrared spectrum. Therefore, infrared spectroscopy can result in qualitative analysis of every different kind of material. By interpreting the infrared absorption spectrum, the chemical bonds in a molecule can be determined. In principle, molecular bonds vibrate at various frequencies depending on the elements and the type of bonds. For any given bond, there are several specific frequencies at which it can vibrate. According to quantum mechanics, these frequencies correspond to the ground state (lowest frequency) and several excited states (higher frequencies). One way to cause the frequency of a molecular vibration to increase is to excite the bond by having it absorb light energy. For any given transition between two states the light energy (determined by the wavelength) must exactly equal the difference in the energy between the two states. The energy corresponding to these transitions between molecular vibrational states is generally 1-10 kilocalories/mole which corresponds to the infrared portion of the electromagnetic spectrum. The results are generally plotted as a function transmittance or absorbance versus wavelength. The conversion between transmittance to absorbance data is:

$$A = \log (1/T) \quad (3.6)$$

where A is absorbance and T is transmittance.

In addition to qualitative analysis, the size of the peaks in the spectrum is a direct indication of the amount of material present. With suitable software algorithms, infrared is also an excellent tool for quantitative analysis.

The technique of Attenuated Total Reflectance (ATR) has in recent years revolutionized solid and liquid sample analyses because it combats the most challenging aspects of infrared analyses namely sample preparation and spectral reproducibility. An ATR accessory operates by measuring the changes that occur in a

totally internally reflected infrared beam when the beam comes into contact with a sample as indicated in Figure 3.15.

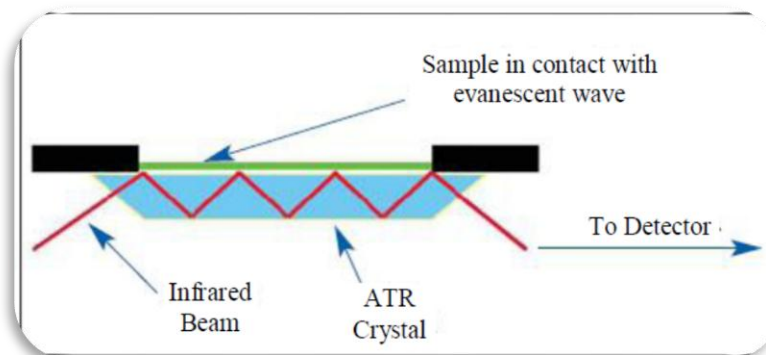


Figure 3.15 Schematic representation of an ATR system (Birlik, 2011)

The infrared spectra of the samples were recorded with a Perkin Elmer Spectrum BX instrument equipped with ATR apparatus (Figure 3.16) in the spectra range between 4000 and 650 cm^{-1} with a resolution of 4 cm^{-1} . All of the samples were characterized by FTIR by which % transmittance as a function of wavelength and % absorbance as a function of wavenumber curves can be obtained.



Figure 3.16 Schematic illustration of FTIR system having ATR apparatus (Electronic Materials Lab., DEU).

3.4.8 X-Ray Diffractometer (XRD)

XRD is one of the primary techniques to analyze all kinds of materials such as powders and coatings. XRD can provide information about crystalline structure and structural phases. It is extensively used to investigate the structural properties of all powders and composite coatings on substrates. All materials were analyzed by means of XRD in Figure 3.17 with a grazing angle attachment and an incident angle of 1° (Rigaku, D/Max-2200/PC). X-Ray radiation of CuK_α was set at 40 kV and 36 mA with a scanning speed of $2^\circ 2\theta/\text{min}$, from 15° to 80° .



Figure 3.17 X-Ray Diffractometer, Rigaku, D/Max-2200/PC (X-Ray Lab., DEU)

3.4.9 Scanning Electron Microscopy-Energy Dispersive Spectroscopy (SEM-EDS)

SEM, as depicted in Figure 3.18, is one of the most common analytical methods to examine surface morphology of the solid-state specimen. In SEM, a tiny high-energy electron beam is scanned across the sample surface. Series of radiations can be produced in terms of the interaction between the electron beam and the sample.

Normally, two types of radiation are utilized for image formation: primary backscattered electrons and secondary electrons. Backscattered electrons reveal the compositional and topographical information of the specimen.

The secondary electron images produce a depth of field which shows the surface topography. The signal modulation of the two types of radiation is viewed as images in the CRT and provides the morphology, surface topology and composition of the specimen surface. EDS is often attached to the SEM. The X-rays generated from the interaction between the electron beam and the specimen is used to identify and measure quantitatively the elemental composition of the specimen. Therefore, SEM/EDS can detect the elemental composition and obtain the morphology of the specimen simultaneously. In this study, the surface and elemental composition of the particles and the composite samples were examined by using JEOL JSM-6060 instrument operating at an accelerating voltage of 15 kV.

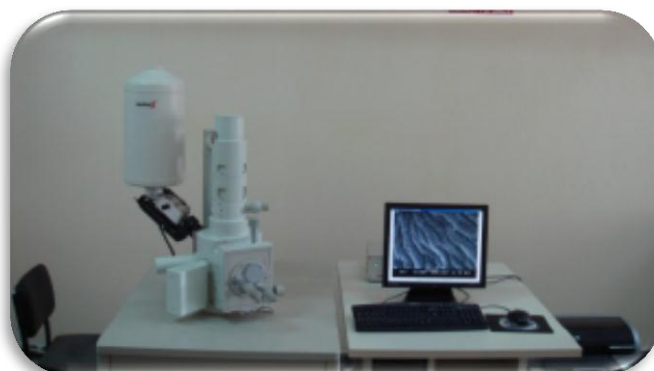


Figure 3.18 JEOL JSM-6060 (SEM Lab., DEU)

3.4.10 Atomic Force Microscopy (AFM)

As shown in Figure 3.19, AFM is a useful tool for assessing the morphological quality of films. A Digital Instruments Nanoscope III was used in tapping mode to obtain AFM images of at least one film in each batch measured. In “Tapping Mode” technique the probe is oscillated at a constant frequency as the AFM head scans across the surface. The amplitude of oscillation of the tip varies as it moves nearer to

the surface of the film, this change is used as feedback to control the sample-tip distance and deduce the surface height of the film.



Figure 3.19 Nanoscope III AFM machine (Metallography Lab., DEU)

In general AFM measurements revealed that it was difficult to obtain vicinal films with as high a quality as the best *c*-axis films. Even the best films exhibited pin-hole defects or outgrowths. The AFM employed was well calibrated in the *z*-axis, a maximum error of ± 2 nm was observed imaging 180 nm deep pits on a calibration sample. The AFM could therefore be used to obtain film thickness by measuring the height of chemically etched steps the information is gathered by "feeling" the surface with a mechanical probe. Piezoelectric elements that facilitate tiny but accurate and precise movements on (electronic) command enable the very precise scanning.

AFM was used to investigate the surface morphologies of the polymeric composite coatings. All measurements were performed at a 20 μm imaging area, 1 second time/line speed and 1024 points/line resolution.

3.4.11 Vibrating Sample Magnetometer (VSM)

A VSM is used to measure the magnetic behavior of magnetic materials. It operates on Faraday's Law of Induction, which shows the changing magnetic field will produce an electric field. This electric field which gives the information about

the changing magnetic field can be measured. The sample to be studied is kept in a constant magnetic field. If the sample is magnetic, this constant magnetic field will magnetize the sample by aligning the magnetic domains, or the individual magnetic spins, with the field (Figure 3.20).

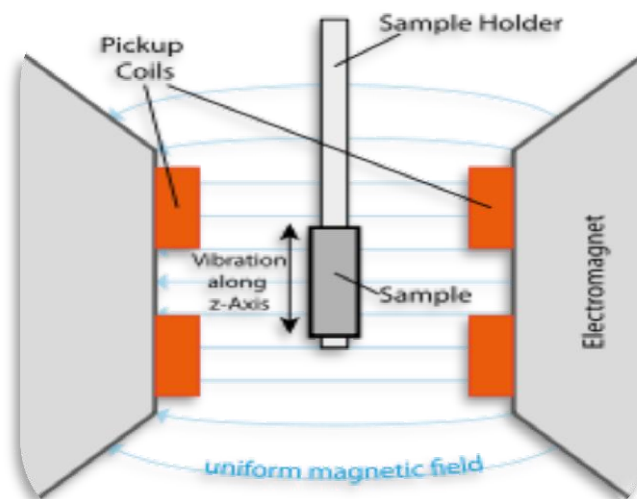


Figure 3.20 Vibrating Sample Magnetometer - sample holder and detection mechanism (Foner, 1959).

The stronger the constant field, the larger the magnetization will be. The magnetic dipole moment of the sample will create a magnetic field around the sample, sometimes called magnetic stray field. As the sample is moving up and down, magnetic stray field is changing as a function of time and can be sensed by a set of pick-up coils. The alternating magnetic field which causes an electric current in the pick-up coils according to Faraday's Law of Induction. This current will be proportional to the magnetization of the sample. The greater the magnetization, the greater the current induced. The induction current is amplified by a transimpedance amplifier and lock-in amplifier (Phil, 2009).

The magnetic properties of the barium hexaferrite powders were measured at room temperature on VSM (Lakeshore 736, 7400 Series) in a maximum applied field of 20000 Gauss. Hysteresis loops of the samples were obtained using VSM.

3.4.12 Scratch Testing Machine

Adhesion properties of the composite coatings were measured by using Shimadzu Scanning Scratch Tester SST-W101 in Figure 3.21 (Instruction Manual, Shimadzu Scanning Scratch Tester SST-W101, 2002, Shimadzu Corporation.) equipped with a standard off-line Zeis metallographic microscope. In this technique, the load on a Rockwell C diamond with tip radius of stylus (R) of 15 μm was linearly increased from 0 mN to 98 mN at loading speed of 1 $\mu\text{m/s}$ and scratch speed of 1-5 $\mu\text{m/s}$ as the diamond is drawn across the coating surface. The testing temperature and humidity percentage are 20.3 $^{\circ}\text{C}$ and 50 %, respectively. During the test, a stylus was drawn on coating surface with a sliding speed of 5 $\mu\text{m.s}^{-1}$ keeping scanning amplitude of 10 μm which perpendicular to the scratching direction at the same time. Friction on the stylus increases with increasing load, which causes a delay in movement between cartridge body and stylus. This delay is defined as a cartridge output. As a result of tests, test force versus cartridge output (%) curves are obtained and compared results.

The scratch was examined with an optical microscope and critical force (W_c) value at which the coating is removed from substrate was determined. After micro hardness value of metal substrate was converted to Brinell Hardness (H) from Vickers Micro hardness by using Standard Hardness Conversion Tables for Metal (Ebeoglugil, 2011, Culha, 2009), the adhesion strength (F) of the coatings was calculated as MPa unit by using Equation 3.7 (Culha, 2009).

$$F = \frac{H}{\left[\frac{\pi R^2 H - W_c}{W_c} \right]^{1/2}}$$

(3.7)

where H is Brinell hardness value in kg/mm^2 of the Si substrate and R is radius of stylus in μm . In addition, it is possible to evaluate adhesion of coatings using Equation (3.7). As the test force applied to coating increases, speeling of coating occurs. At this time peeled pieces of coating cause a high frequency noise in a

cartridge output signal. Detecting this noise makes it possible to determine a critical force. Normally, this critical force can be used the adhesion value of coating. Nonetheless, in the case that a hardness of the substrate has been known, Equation (3.7) can show adhesion strength. As a result of this, test force–cartridge output graph is obtained from this measurement. Cartridge output (%) represents percentage of indentation of the stylus as a function of loading during the test. The percentage increases with a increasing load, that applied by stylus, due to the adhesion resistance of the coating to substrate (Ebeoglulil, 2011, Culha, 2009).



Figure 3.21 Schimadzu, SST-W101 scratch testing machine (Metallography Lab., DEU)

3.4.13 Surface Profilometer

Composite samples surface's profiles were investigated with a surface profilometer Mitutoyo SJ-301 (Figure 3.22), in order to quantify the roughness. Whilst the historical notion of a profilometer was a device similar to a phonograph that measures a surface as the surface is moved relative to the contact profilometer's stylus, this notion is changing with the emergence of numerous non-contact profilometer techniques.



Figure 3.22 Mitutoyo SJ-301 surface (Tribology Lab., DEU)

3.4.14 Antibacterial Test

There are two types of antibacterial test used in this study; Inhibition zone test and percent decreasing test.

3.4.14.1 Inhibition Zone Test

The agar disc diffusion method was employed for the determination of antimicrobial activity of silver-loaded coating specimens (in size of 2.4×2.4 mm) against *S. aureus* ATCC 6538P, a Gram-positive bacterium and *E. coli* ATCC 12228, a Gram-negative bacterium (NCCLS, 1997). Briefly, test microorganisms were activated in Müller Hinton Broth (MHB) at 37°C for 18 hours and a suspension of the test bacteria was spread on solid media plates containing MHA. After duration of two hours, polymer coatings were placed in the center of inoculated plates and incubated at 37°C for 24 hours. At the end of the incubation period, the plates were inspected for growth on and under coating samples, as well as for the presence or absence of growth in a halo around the samples (NCCLS, 1977). The width of the halo was measured across the center line of the sample, both horizontally and vertically. An average of these two values was then taken to give an estimate of the

antimicrobial activity of the samples as shown in Equation 3.8 (Figure 3.23). Each experiment was repeated for three times.

$$\text{Inhibition radius} = \frac{r_1 + r_2}{2} \quad (3.8)$$

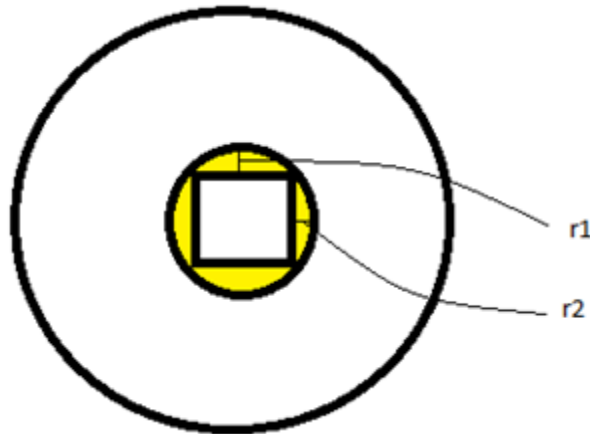


Figure 3.23 Estimation of antimicrobial activity and inhibition zone.

For the first samples (mentioned above) E.Coli and S.Aureus bacteria are used with square sample substrates. But for the second time samples, S.Aureus, E.Coli, P. Aeruginosa, K. Pneumoniae bacteria, and C. Albicans yeast and Fungus were used with rectangular substrates.

3.4.14.2 Percent Decreasing Test

A plate counter agar solid culture medium was poured into the plates that were subsequently incubated at 37 °C for 24 hours so that the *Vital* cells, eventually present, could grow into colonies. The microorganisms' colony presence was then evaluated, by counting the colony-forming units per Petri plate (CFU/mL). Used bacteria were E.coli (ATTC 11228). The difference between the number of the bacteria obtained after 0 hour and after 24 hour will give the antibacterial performance (Equation 3.9).

$$\% \text{ decrease} = \left[\frac{A - B}{A} \right] \times 100 \quad (3.9)$$

in which, A: Bacteria number after 0 hour and B: Bacteria number after 24 hours.

3.4.15 Flame Retardant Test

For retardant tests, there exist two types of flame retardant tests including Limiting Oxygen Index (LOI) and UL94.

3.4.15.1 Limiting Oxygen Index (LOI)

A LOI test machine with Asian Oxygen Index Tester Model, as presented in Figure 3.24, measures the minimum concentration of oxygen in a flowing mixture of oxygen and nitrogen that will just support flaming combustion of a material initially at room temperature.



Figure 3.24 LOI test machine (Electronic Material Production Lab., EMUM-DEU)

The flame retardant composite coatings on plastic substrates are ignited and burns from the top downwards. The rating or oxygen index is expressed in terms of this volume percent oxygen concentration. The classification specifications are shown in Table 3.12 (Xanthus, 2004).

Table 3.12 LOI classification specifications (Xanthos, 2004).

Grouping of test procedures	LOI Classifications	
Fire propagation	<24	Flammable
Fire resistance	24-28	Limited flame resistance
Fire gases	29-34	Flame resistance
Integrity of service	>34	Extra flame resistance

3.4.15.2 UL94 Classification

This technique is used in plastic industry according to UL94 standardization. The material is conducted to the flame in a specific angle and distance. Extinguishing time of the flame and dripping ability are measured (Figure 3.25) (Stec, 2010).

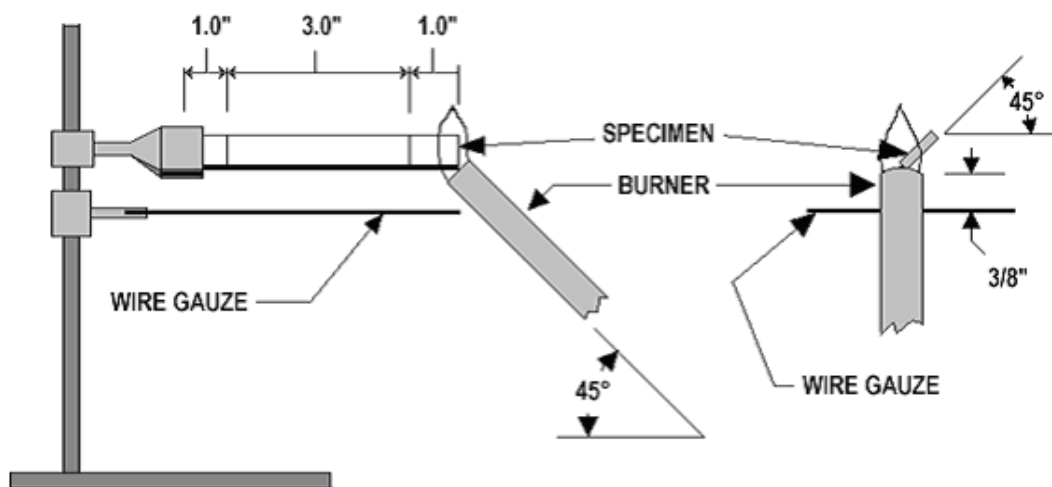


Figure 3.25 Horizontal burning test for 94HB classification (Stec, 2010).

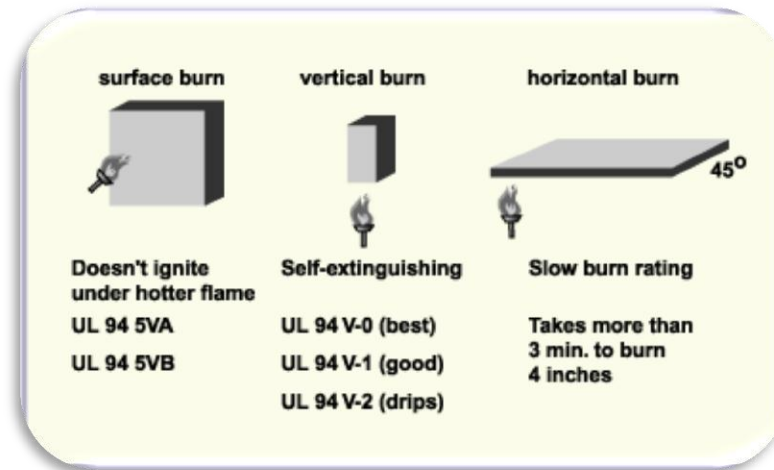


Figure 3.26 Schematic of UL94 test requirements (Tarr, 2011).

The UL94 test standard is a generally-used indicator of the acceptability of plastic for general use with regard to its flammability. There are three different tests, and several different levels, as indicated schematically in Figure 3.26 and Table 3.13. Also needle flame test machine is shown in Figure 3.27.

The testing for the 94V-0 rating involves two separate applications of a flame for 10 s to each sample from two sets of five specimens, and meeting the criteria that:

- All specimens must self-extinguish within 10 s after each flame application.
- The total flaming combustion for all five specimens of any set must be less than 20 seconds.
- No samples are to drip flaming particles or have glowing combustion lasting beyond 30 seconds after the second flame test.

Table 3.13 UL94 flammability ratings (Tarr, 2011).

UL94 5VA	Burning must stop within 60 seconds after five applications of five seconds each of a flame to a test bar, and there must be no burn-through hole. The flame is larger than that used in Vertical Burn testing. This is the highest (most flame retardant) UL94 rating.
UL94 5VB	As for 94 5VA, but a burn-through hole is allowed.
a) Surface Burn tests	
UL94 V-0	Specimens must extinguish within 10 seconds after each flame application and a total combustion of less than 10 seconds after 10 flame applications. No samples are to drip flaming particles or have glowing combustion lasting beyond 30 seconds after the second flame test.
UL94 V-1	Specimens must extinguish within 30 seconds after each flame application and a total combustion of less than 250 seconds after 10 flame applications. No samples are to drip flaming particles or have glowing combustion lasting beyond 60 seconds after the second flame test.
UL94 V-2	Specimens must extinguish within 30 seconds after each flame application and a total combustion of less than 250 seconds after 10 flame applications. Samples may drip flame particles, burning briefly; and no specimen will have glowing combustion beyond 60 seconds after the second flame test.
UL94 VTM	Thin material version of the vertical burning test applied to thin or flexible materials which may distort, shrink or flex during the 94 V test. A specimen 200 × 50 mm is rolled longitudinally around a 12.7 mm diameter mandrel and taped on one end. When the mandrel is removed the specimen forms a cone shape, which gives it longitudinal rigidity. Has the same three classifications as 94 V. Differences are that a flame is applied twice for only three seconds, and no specimens may have flaming or glowing combustion beyond a point 125 mm from the bottom of the specimen.
b) Vertical Burn tests	
UL94 HB	Slow horizontal burning on a 3 mm thick specimen with a burning rate is less than 75 mm/min or stops burning before a mark 125 mm away from the point of flame application. HB rated materials are considered 'self-extinguishing'. This is the lowest (least flame retardant) UL94 rating
c) Horizontal Burn test	



Figure 3.27 Needle flame test machine (Electronic Material Production Lab., EMUM-DEU)

3.4.16 Radar Absorbing Test

The electromagnetic parameters of the radar absorbing composite coatings were measured with transmission/reflection method in the region of 8–12 GHz. with a Network Analyzer HP8720D as indicated in Figure 3.28. Figure 3.29 shows schematically the setup of this system. The network analyzer and coaxial line fixture have been calibrated. The incident power, delivered by the network analyzer, and the reflected and transmitted power, measured by the network analyzer, is depicted in Figure 3.30 (Aksit et al., 2008).



Figure 3.28 Network analyzer test machine (Electronic Material Production Lab., EMUM-DEU)

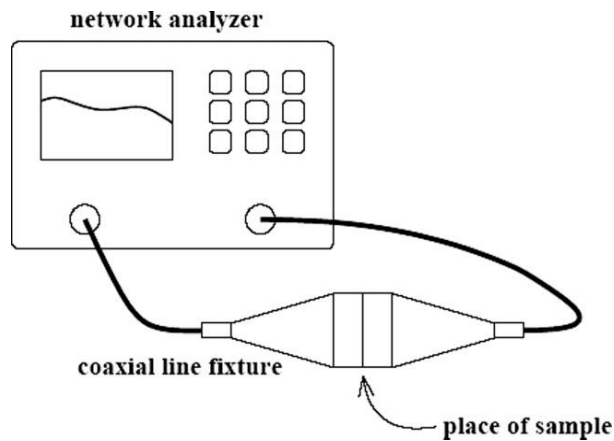


Figure 3.29 Measurement setup with network analyzer and coaxial line fixture (Aksit et al., 2008).

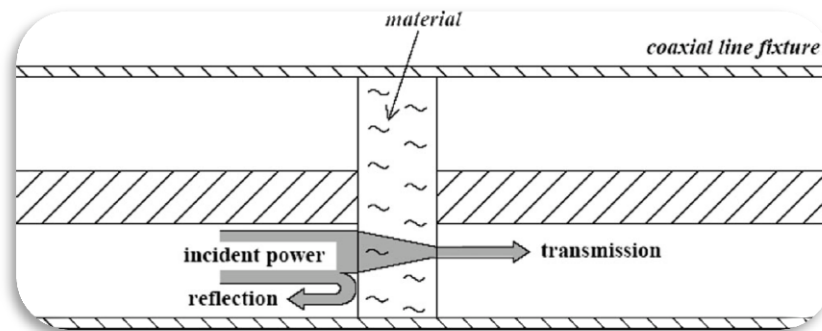


Figure 3.30 Incident, reflected, and transmitted power at the sample material (Aksit et al., 2008).

3.4.17 Self-healing Test

Self healing property is followed by using a JEOL JJM 6060 SEM. As mentioned above, SEM can produce very high resolution images of a sample surface. The micrographs have a large depth of field yielding a characteristic three-dimensional appearance useful for understanding the surface structure of a sample because of very narrow electron beam. A wide range of magnifications can be possible till 300000 times. Therefore, first of all SEM photographs were taken from all composite samples before any scratching treatment. Then, after the coated samples are scratched by a very thin pin and the cracks are obtained, they were examined using SEM again. Even if the cracks are too small, they can be investigated by this high

resolution technique method. The surface morphologies of the composite samples were observed with SEM imaging periodically. By obtaining the micrographs in different times, cracks can be followed in detail. Thus by this way it can be investigated if any closing behaviour or any different kind of improvements related with the self healing in the cracks.

CHAPTER FOUR

RESULTS AND DISCUSSION

4.1 Ag Nanoparticle Added Polymeric Coatings

Ag nanoparticles added polyurethan composite coatings/paints were extensively characterized before and after deposition process. Comparative studies of the structural, mechanical and antibacterial performance of the composite/paints were performed as solution and coating characteristics in this section in details.

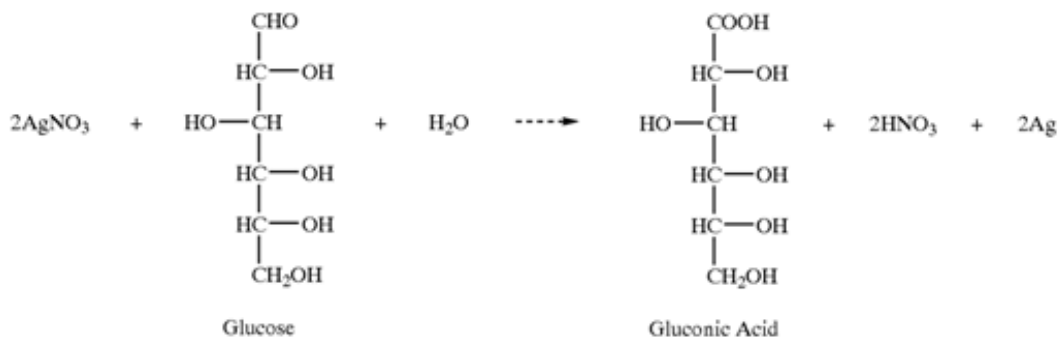
4.1.1 Solution Characteristics

Prior to coating process, Ag ions, glucose, Ag nanoparticle and solutions were characterized with the aid of atomic absorption spectroscopy, Fehling Reactive and DNS methods, pH meter, turbidimeter and particle size analyzer.

4.1.1.1 Production of Ag Nanoparticles

Ag nanoparticles have been extensively used in various fields. Widespread studies are being conducted on Ag nano-sized particles for their antibacterial efficiency and they may potential commercial application in several areas (Lkhagvajav et al., 2011). Now that Ag nanoparticle added polymeric composite coatings/paints on a variety of substrates are important, some researches were reported on different synthesis techniques in the literature. It is reported in elsewhere (Yan & Cheng 2005) that with this method the fabricated Ag nanoparticles have diameter between 1 and 100 nm. On the other hand according to Binitha et al. (2009), glucose reductant together with urea stabilizer makes size of silver particles low in the range of 4–5 nm for better antibacterial activity.

Briefly again, a nitrate solution was mixed with a 10 mL aqueous solution of glucose. As shown from Reaction 4.1;



(4.1)

the silver nitrate was reduced to metallic silver by interacting with glucose where the glucose itself was oxidized to gluconic acid which is its oxidation product. In our case, water used for solutions was distilled. After stirring was performed for 15 min at room temperature in air, Ag ions were reduced to produce the nanoparticles in the liquid matrix. Additionally gluconic acid and nitric acid were formed as the other products of the reaction. The solution had been stirred repeatedly until it became stabilized and approximately after an hour some dark color appeared. At this point Ag nanoparticle were chemically stable in the solution. Because of this, we have a good agreement with literature (Binitha et al. 2009).

4.1.1.2 Ag⁺ Ion Determination

Ag⁺ ion determination is important in antimicrobial coatings. Using atomic absorption spectroscopy Ag⁺ ion concentration in the obtained solution was estimated as 10 %, which agrees with our estimation at the beginning. Depending on this result, correct AgNO₃ amount was calculated very well before preparation of nano Ag.

4.1.1.3 Glucose Determination

Due to the fact that microorganisms live glucose materials as a food, their residue in solutions and coatings is not desired. Such a residue influences antibacterial activities in the coatings. Thanks to this reason, glucose determinations were performed to prepare Ag nanoparticles through Fehling Reactive and DNS method. With Fehling Reactive method, glucose concentration in the solutions was found to be 10 % and 8,5 % which are not acceptable for further processing. Nevertheless, using DNS method it was estimated as 0 % which is very good for further processing. By taking DNS method as a base, the experiments were gone on to be produce antibacterial coatings.

4.1.1.4 Asidic/Basic Characteristics

The pH measurement refers to determination of the activity of hydrogen ions in Ag nanoparticle based solution. Many important properties of the solution can be determined from an accurate measurement of pH, including the acidity of a solution and the extent of a reaction in the solution. Many chemical processes and properties, such as the speed of a reaction and the solubility of a compound, can also depend greatly on the pH of the solution. The pH value of the obtained solution was determined as 4.80. While ramified structure having Ag nanoparticle is randomly formed in acidic conditions, separated clusters are formed from the solutions showing basic characters. The nanoparticle with bigger size is generally produced with the ramified structure. Owing to this reality, the size of Ag nanoparticle can be changed by altering pH values of the solutions. Upon decreasing the size of Ag nanoparticle, its antibacterial activities dramatically increase in the coatings.

4.1.1.5 Turbidity

With turbidity experiments, whether AgNO₃ powder precursor materials are dissolved very well in solutions is understood by looking ntu values before coating

process. As mentioned before, the turbidity values of the solutions vary in the range of 0 ntu and 1,000 ntu. It is interpreted that powder based precursors are completely dissolved as turbidity value approaches to 0 ntu and they are not dissolved and some powder particles are suspended in a solution as it approaches to 1000 ntu. In this experiment, turbidity value of the solutions was measured as 58.80 ntu. Based on the turbidity value, it can be pointed that AgNO_3 powder is completely dissolved in the solutions.

4.1.1.6 Particle Size Analyzer

The size and particle size distribution of Ag nanoparticles were determined using particle size analyzer which uses light scattering techniques to measure hydrodynamic size of nanoparticles. Particle size distribution of the produced Ag nanoparticles was represented in Figure 4.1.

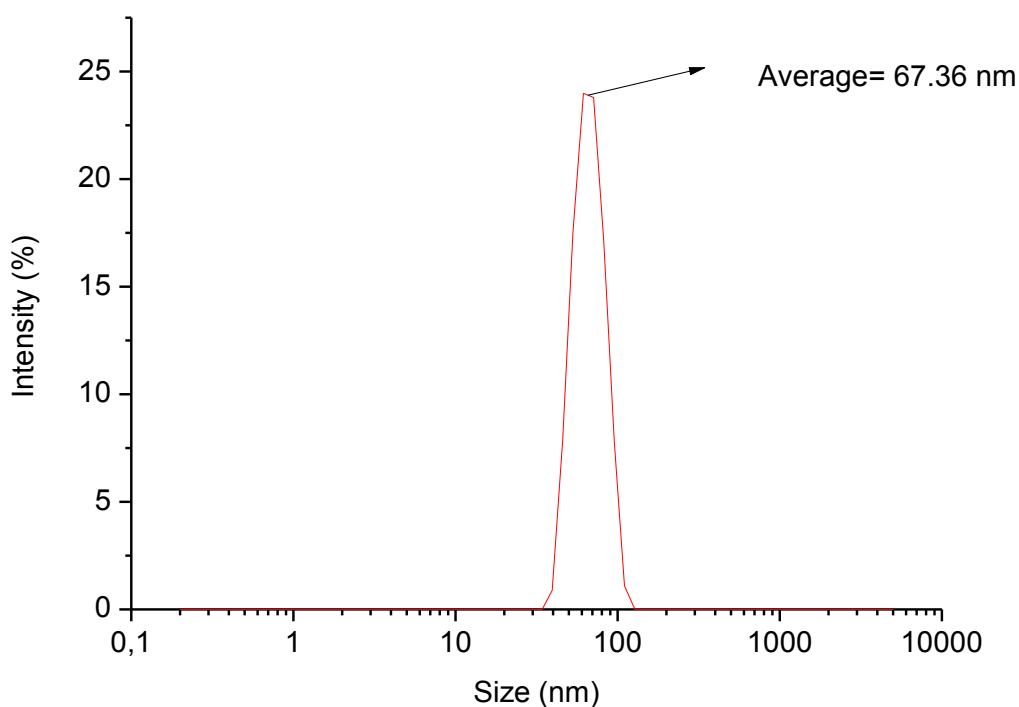


Figure 4.1 Particle size distribution of Ag nanoparticles

According to size distribution approximate, particle size was found to be in the range of 39 nm and 128 nm, and the average particle size was about 67.36 nm which is acceptable for antibacterial activities. The produced Ag nanoparticles can be identified as monodispersed due to small particle size distribution range.

4.1.2 Coating Characteristics

After coating process, 0%, 5%, 10%, 15% and 20% Ag nanoparticle added polyurethan composites were characterized through FTIR, XRD, SEM-EDS, AFM, scratch tester and antibacterial tests and comparatively discuss with literature.

4.1.2.1 FTIR Analysis

FTIR spectra of 0%, 5%, 10%, 15% and 20% Ag nanoparticle added antibacterial polyurethan composites are shown in Figure 4.1. It is clear from this figure that the polymer composite does not include any Ag nanoparticles. This is because the coatings possess a very low content Ag. Note that four IR bands observed at 452, 557 and 836 cm^{-1} , they might be vibrations of C-H bonds. The band located at 1006 cm^{-1} may be of N-H bonds owing to polyurethan paints. Worth nothing here is that the intense and sharp band located at 1272 cm^{-1} can be related to the C=C or C-O bonds. The band observed at 3861 may be vibrations of O-H bonds in the polymer matrix. In the spectra of the composite coatings, the band at $\approx 500 \text{ cm}^{-1}$ may be assigned to the vibration of some oxide bands, as might be expected, appear from the structure because of pigments in the polymer matrix.

As in the case of Ag metallic nanoparticles in the coatings, metallic bonds can not be seen from FTIR results in details. Therefore, it can be easily seen in Figure 4.2 that by increasing the loading level of Ag, there is no any difference in the graphs. It can be expressed that Ag nanoparticles do not affect the organic bonds in the composite coatings. It should be kept in mind that this behaviour strongly influences antibacterial activities of the coatings. If Ag has an interaction with polymeric

structure, microorganisms such as microbes, bacteria and viruses do not die after application of paints. It is believed that Ag nanoparticles affect enzymatic structure of microorganisms when they separately stay without making any organic group in the polymeric coatings. This makes it easy to use in antibacterial coatings and meets the requirements of hygienic environments.

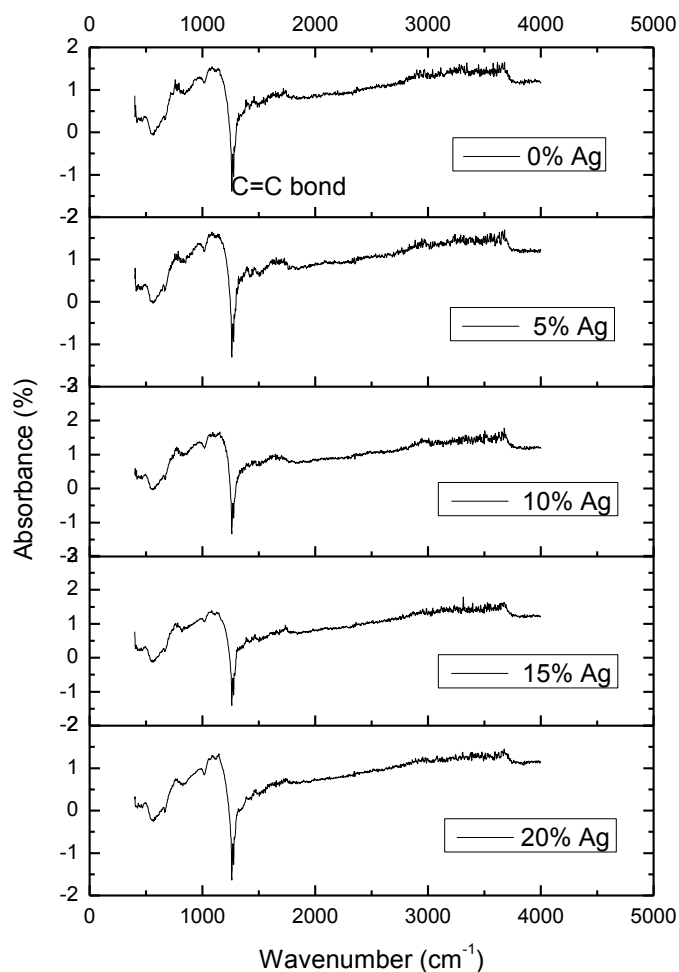


Figure 4.2 FTIR spectra of 0%, 5%, 10%, 15% and 20% Ag nanoparticles reinforced polymeric composite/paints

4.1.2.2 Phase Analysis

XRD patterns of antibacterial polymeric polyurethan composite coatings/paints are denoted in Figure 4.3. It is obviously found that the main phase is SiO_2 in the composite coatings. More importantly, MgO and TiO_2 can be found from these

results because polyurethan paint has these kinds of pigments. Except for this, it can be seen from the patterns that after Ag nanoparticle is incorporated into the polyurethan polymer matrix a peak appears at 37.5° and its intensity increases when additive level increases. The results demonstrate that neither XRD pattern nor FTIR graphs show any change in the intensities by increasing or decreasing of the concentrate of Ag nanoparticles. It means that Ag nanoparticles do not change the phase or band structure of the polymeric dye considerably.

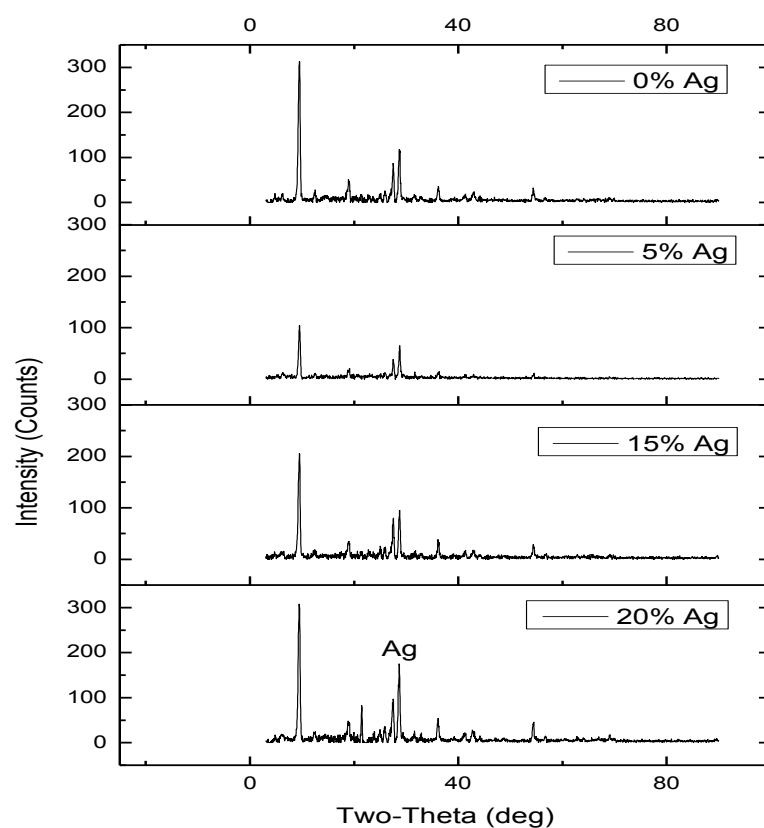
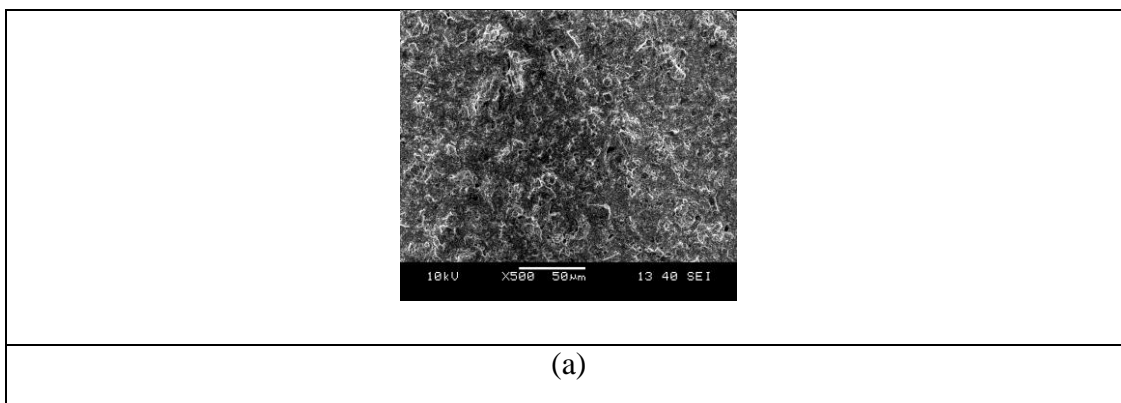


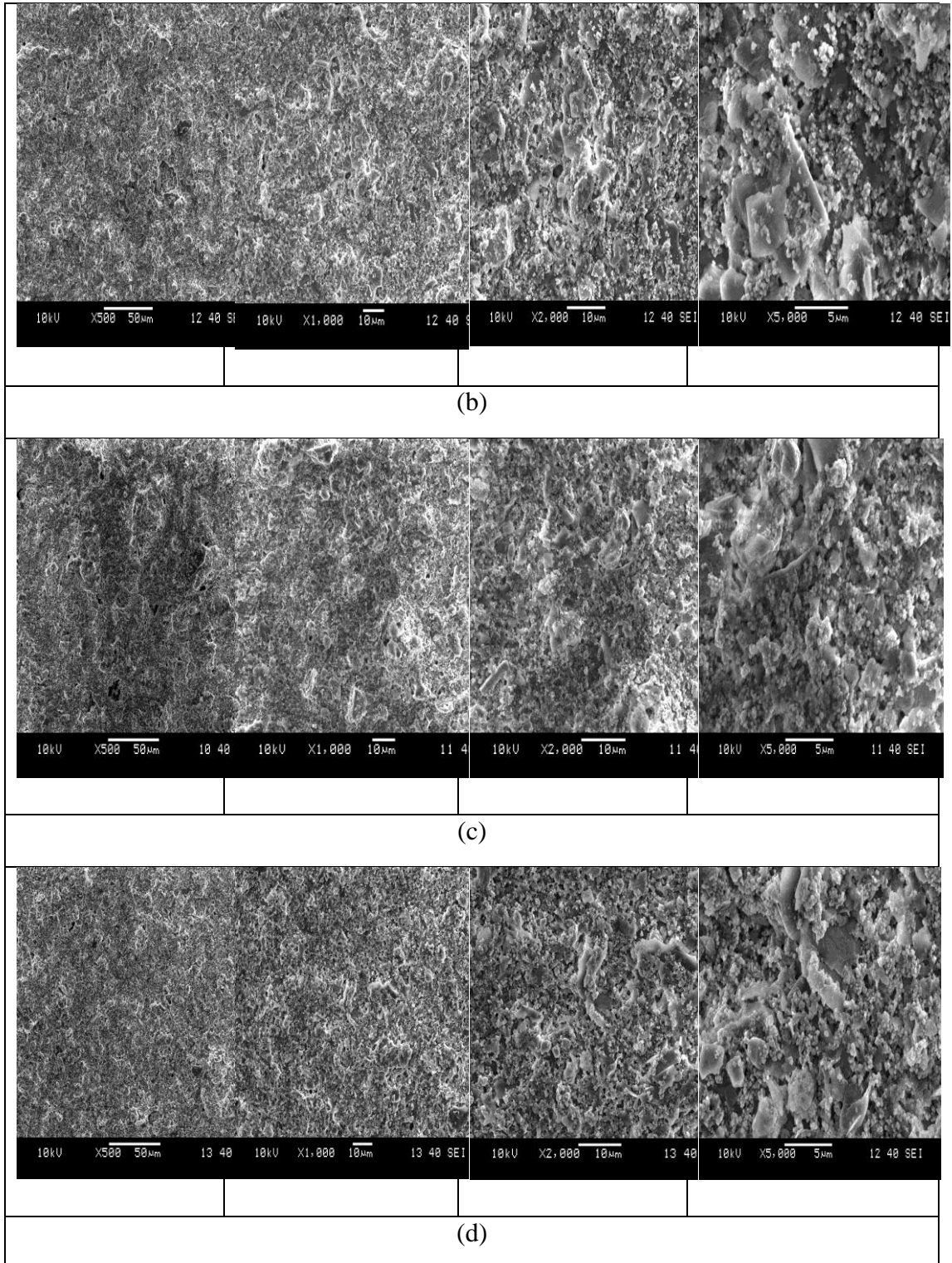
Figure 4.3. XRD patterns of 0%, 5%, 10%, 15% and 20% Ag nanoparticles added polyurethan composite coatings/paints

It is interesting to note here that they just settle into the empty places between the polymer chains. This limits the movement ability of the chains and leads to rigidity in the polymer structure. Due to this, diffusion ability of polymer composite or Ag nanoparticles is limited. Therefore, increasing the Ag nanoparticle amount increases the limitation.

4.1.2.3 SEM-EDS Analysis

SEM micrographs and EDS analysis of 0%, 5%, 10%, 15% and 20% Ag nanoparticle added polyurethane composite coatings Ag nanoparticle added polyurethane composite coatings/paints are denoted in Figure 4.4. When Ag nanoparticle content is increased in the coatings, the microstructure regularly changed as shown in Figure 4.4. In spite of the fact that smooth surface is obtained at low content of Ag nanoparticle in the coating, some defects such as porosity, rough surface and so on are produced at high ones. The SEM micrographs were taken at different magnifications including at 500X, 1000X, 2000X and 5000X. It is important to emphasize here that surface coverage and quality are good because it can be seen from SEM micrographs at low magnifications. In SEM micrographs, it can be seen especially the micrographs at 5000X that by adding Ag nanoparticles, the concentration of small particles increased and Ag nanoparticles have the size of smaller than 70 nm.





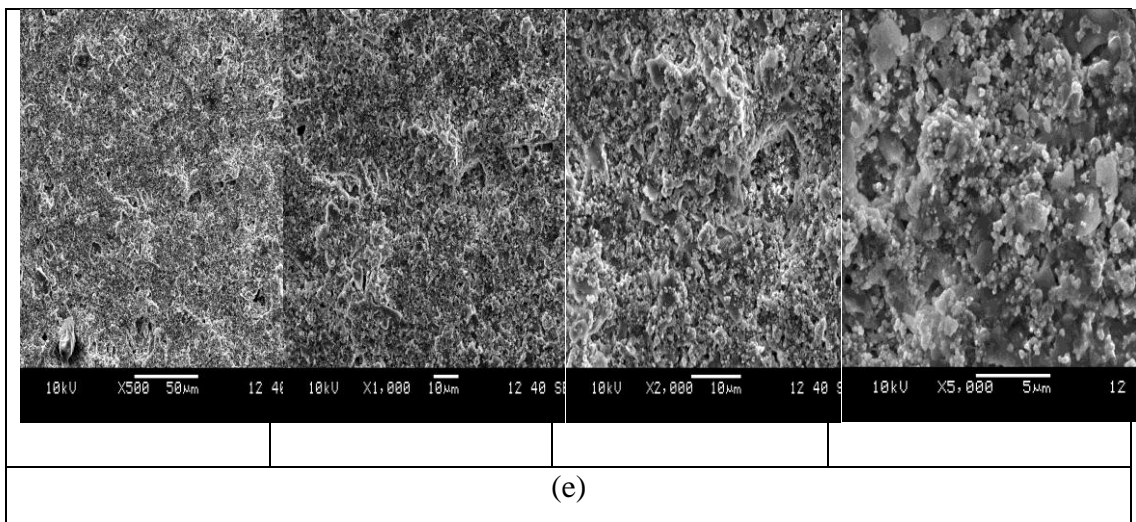
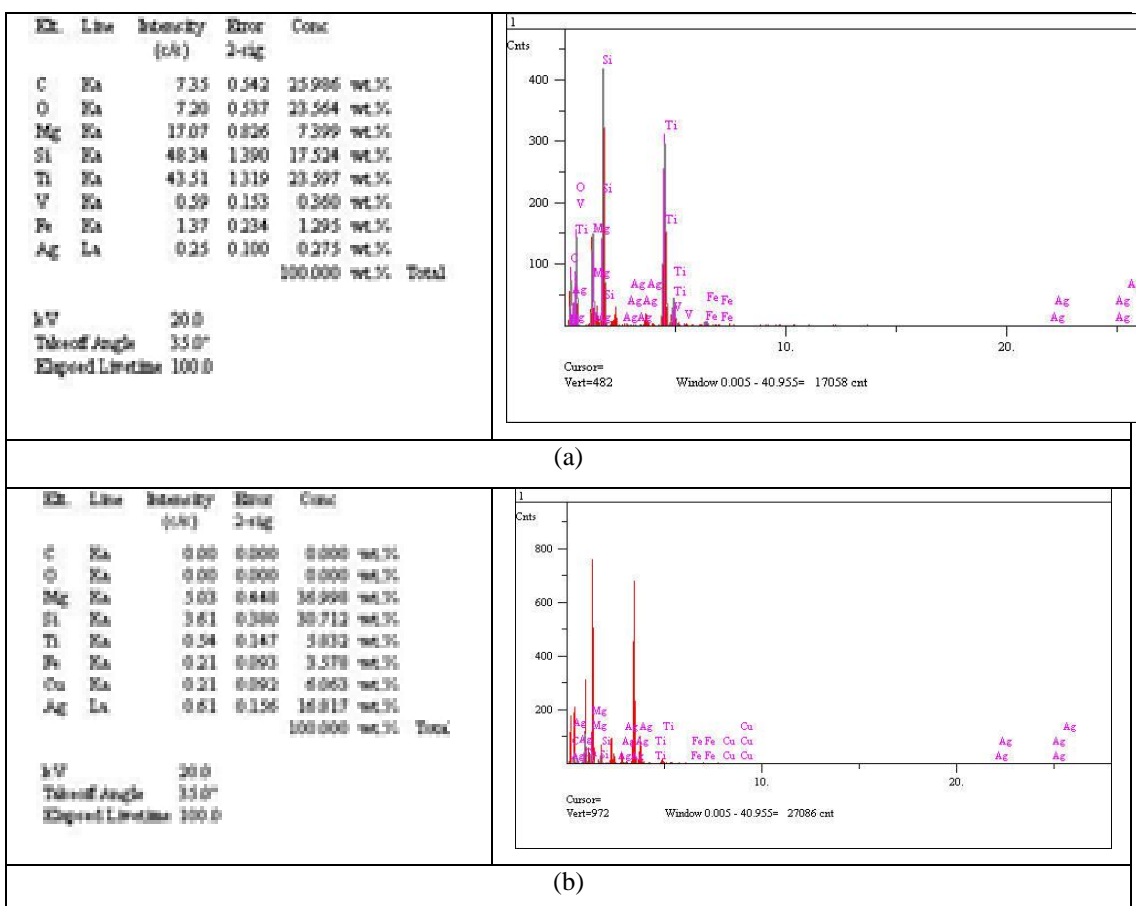


Figure 4.4 SEM micrographs of (a) 0%, (b) 5%, (c) 10%, (d) 15% and (e) 20% Ag nanoparticle added polyurethane composite coatings



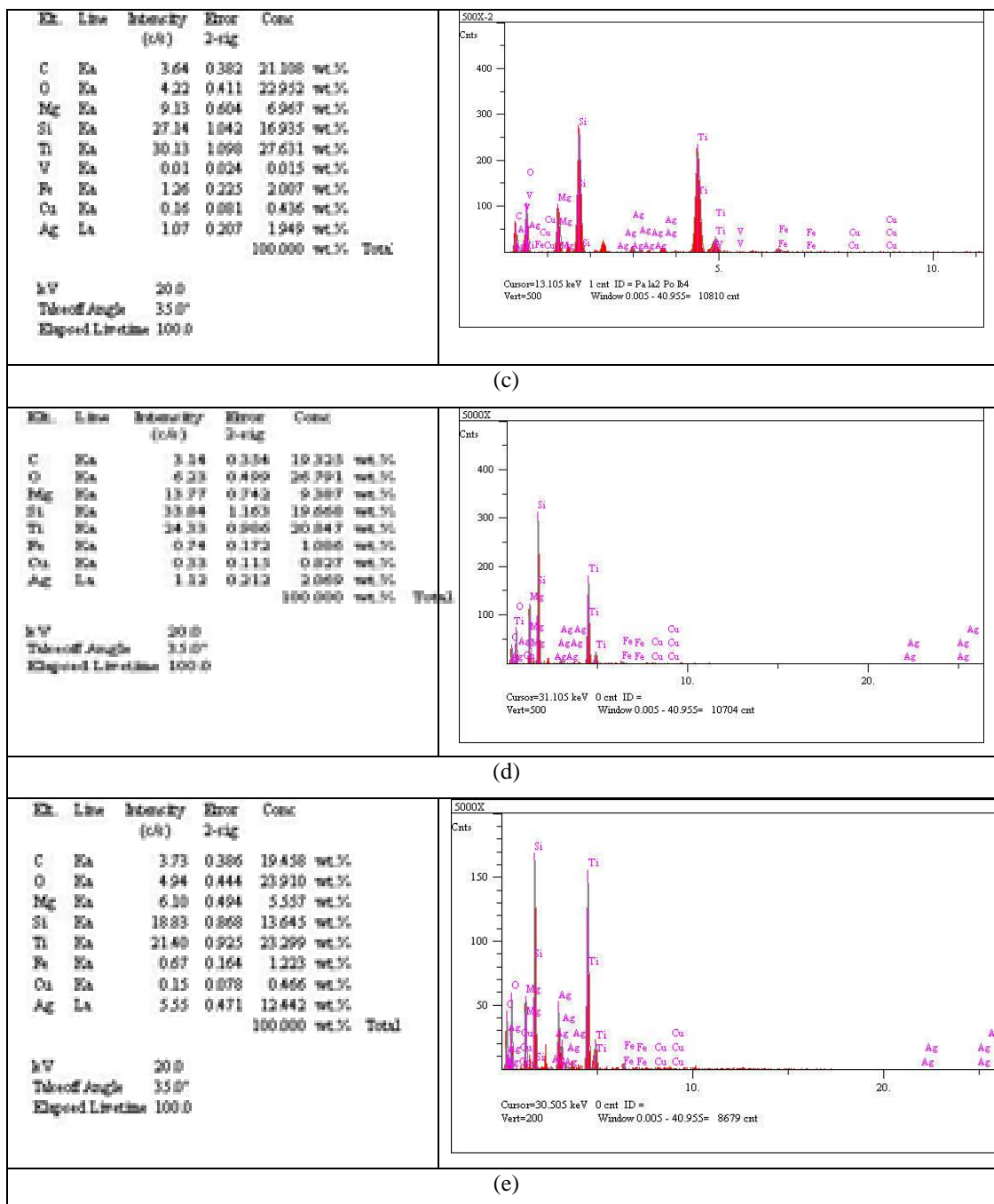


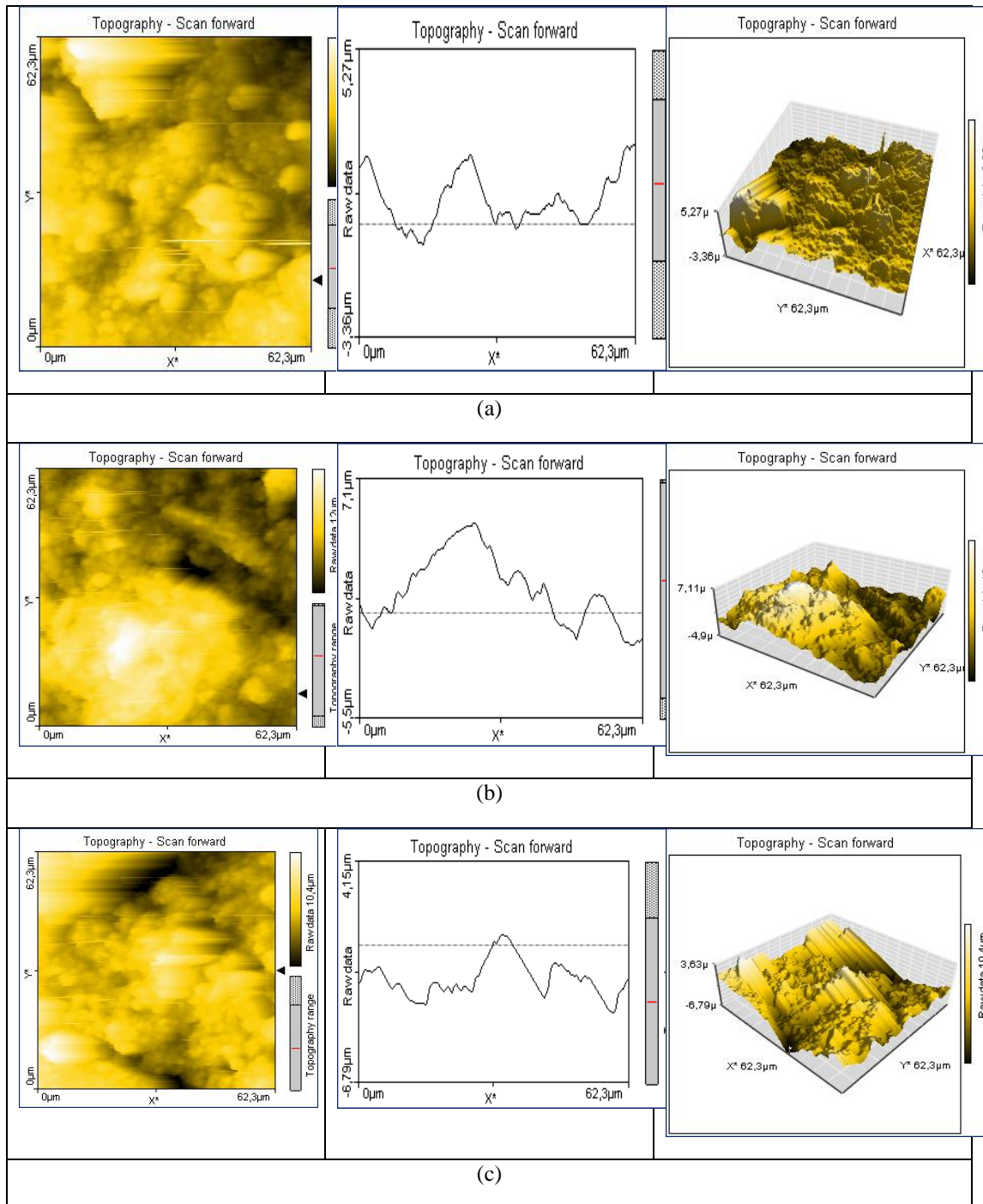
Figure 4.5 EDS analysis of (a) 0%, (b) 5%, (c) 10%, (d) 15% and (e) 20% Ag nanoparticle added polyurethan composite coatings

In EDS analysis of Figure 4.5, C, O, Ag, Mg, Si and Ti elements are observed in the polymer matrix. As explained previously, due to the fact that polyurethan matrix is equipped with C, O, Mg, Si and Ti elements as oxide and polymeric structures, it is normal to determine them in the composite coatings. This result agrees the FTIR

spectra and XRD patterns as stated just before that the polyurethan matrix has already have Mg, Si and Ti. On the other hand, it can be easily seen that by adding Ag nanoparticles and increasing loading level Ag quantities increase regularly in the EDS results.

4.1.2.4 AFM Analysis

AFM results of 0%, 5%, 10%, 15% and 20% Ag nanoparticle added polyurethan composite coatings are shown in Figure 4.6. Interesting observations have emerged from the AFM studies on surface morphologies of the composite coatings. View from the top, 2D and 3D images of the composite coatings are depicted to decide the quality of the surface topography. Surface roughness, which is represented by the arithmetic mean value, R_a and the maximum roughness height, R_t values can be estimated from cross-section graphs that raw data are given. R_a values of 0%, 5%, 10%, 15% and 20% Ag nanoparticle added composite coatings are calculated as 2, 4, 3, 2 and 4.5 μm and R_t values are calculated as 2.6, 6, 4, 3.5 and 5.5 μm for the samples in Figures 4.6.a, 4.6.b, 4.6.c, 4.6.d and 4.6.e, respectively. Generally speaking, once increasing Ag content in the coating, the values of surface roughness increases. These AFM results comply with SEM ones. It can be said that the coating surfaces are not well smooth in terms of rough samples and it might be due to poor coating quality which is acceptable for technological applications.



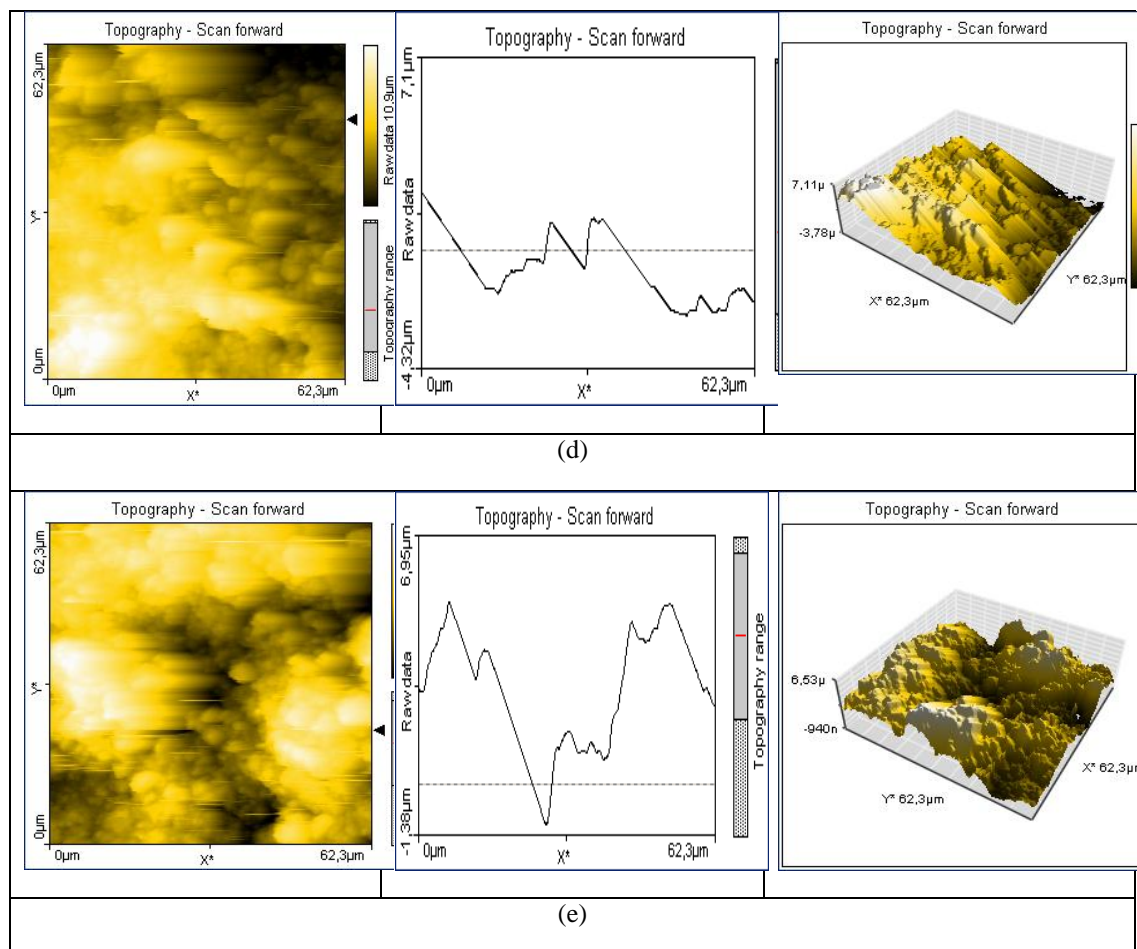


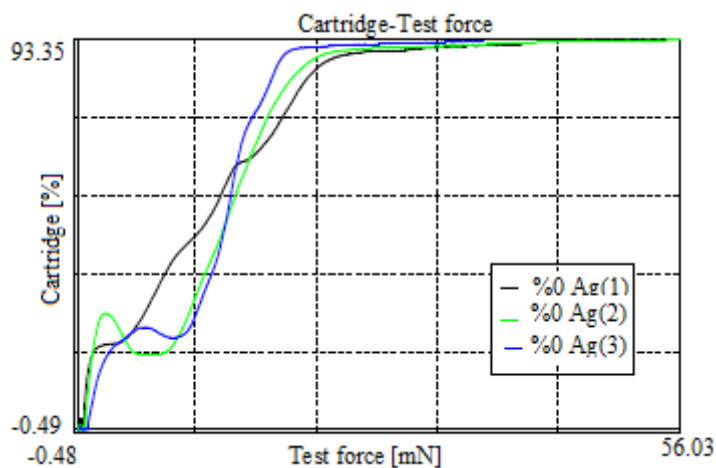
Figure 4.6 AFM images of (a) 0%, (b) 5%, (c) 10%, (d) 15% and (e) 20% Ag nanoparticle added polyurethane composite coatings/paints

4.1.2.5 Adhesion Properties

Scratch test results of the Ag nanoparticle added polymer composite coatings are depicted in Figure 4.7. It was found that average critical forces of 0%, 5%, 10%, 15% and 20% Ag nanoparticle added composite coatings are 20.11 mN, 17.83 mN, 18.53 mN, 9.89 mN, and 14.11 mN, respectively. It can be seen that the critical forces are small values comparing with the metal coating which may have 120 N critical force (Fox, Renevier, Teer, Hampshire & Rigato, 1999). Moreover, it is worth noting that critical values of 0%, 5%, 10%, 15% and 20% Ag nanoparticle added composite coatings are 20.11 mN, 17.83 mN, 18.53mN, 9.89 mN and 14.11 mN, respectively. And corresponding adhesion strengths are 72.41 MPa, 67.28 MPa, 68.87 MPa, 47.98 MPa and 58.62 MPa.

No	Critical Force[mN]	Corrected Critical Force[mN]	Data Name
1	21.16	21.16	%0 Ag(1)
2	20.24	20.24	%0 Ag(2)
3	18.93	18.93	%0 Ag(3)
Average	20.11	20.11	
Standard Deviation	1.12	1.12	
Coefficient of Variation	5.59	5.59	

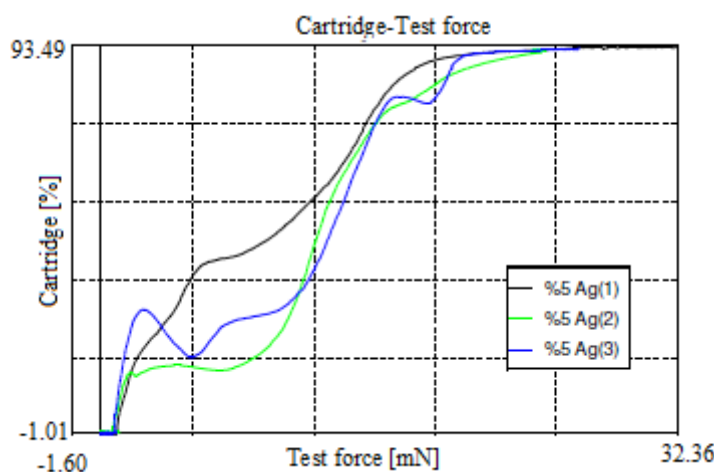
Data File Name %0 Ag
Test Condition
Sample Name %0 Ag
Sample No. %0 Ag
Tip Radius of Stylus[um] 15
Cartridge No. 028
Full Test Force 98[mN]
Loading Speed[um/s] 1
Amplitude[um] 10
Scratch Speed[um/s] 2
Number of Test 3
Correction Coefficient 1.00
Automatic Start OFF
Temperature[C.] 20
Humidity[%] 60
Comment



(a)

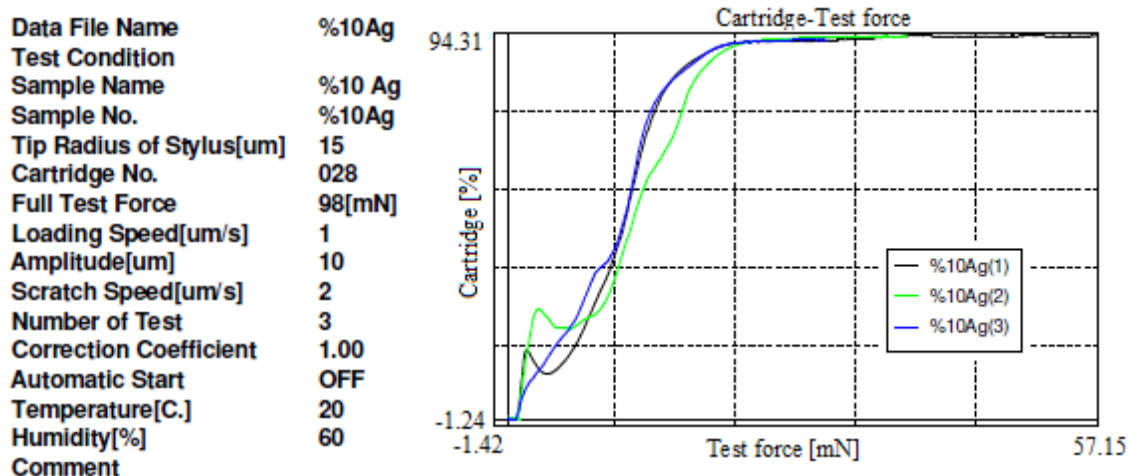
No	Critical Force[mN]	Corrected Critical Force[mN]	Data Name
1	17.36	17.36	%5 Ag(1)
2	18.36	18.36	%5 Ag(2)
3	17.76	17.76	%5 Ag(3)
Average	17.83	17.83	
Standard Deviation	0.51	0.51	
Coefficient of Variation	2.84	2.84	

Data File Name %5 Ag
Test Condition
Sample Name %5 Ag
Sample No. %5 Ag
Tip Radius of Stylus[um] 15
Cartridge No. 028
Full Test Force 98[mN]
Loading Speed[um/s] 1
Amplitude[um] 10
Scratch Speed[um/s] 2
Number of Test 3
Correction Coefficient 1.00
Automatic Start OFF
Temperature[C.] 20
Humidity[%] 60
Comment



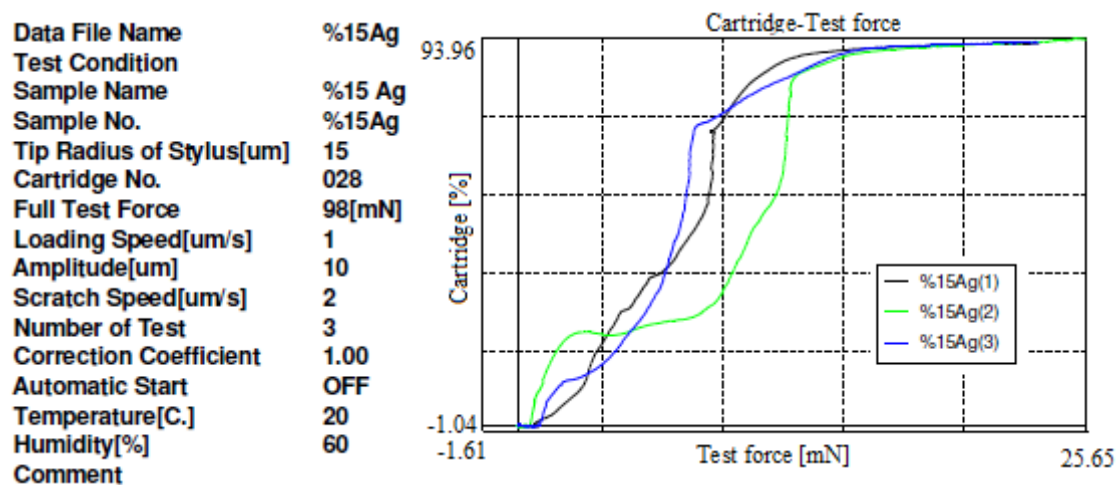
(b)

No	Critical Force[mN]	Corrected Critical Force[mN]	Data Name
1	17.51	17.51	%10Ag(1)
2	20.12	20.12	%10Ag(2)
3	17.96	17.96	%10Ag(3)
Average	18.53	18.53	
Standard Deviation	1.40	1.40	
Coefficient of Variation	7.53	7.53	



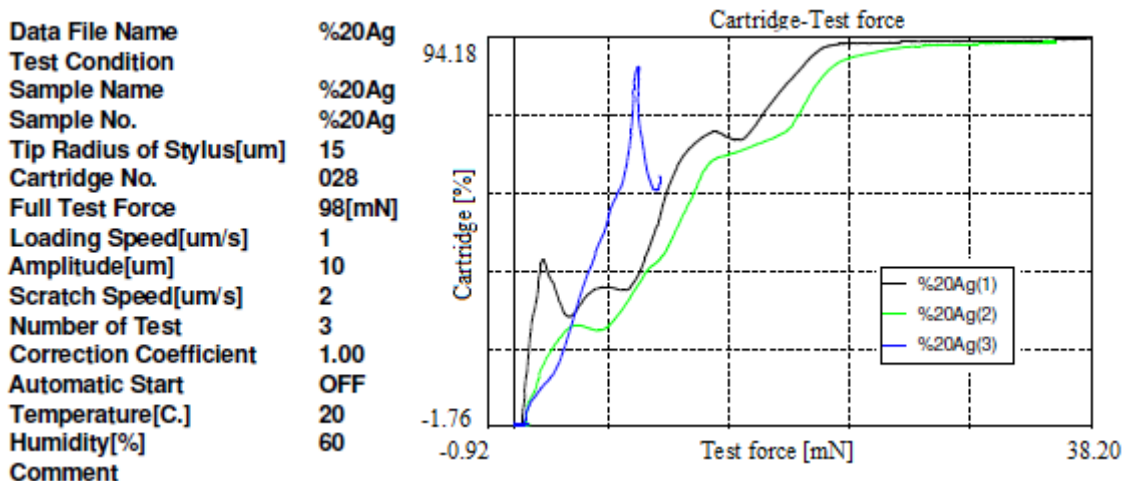
(c)

No	Critical Force[mN]	Corrected Critical Force[mN]	Data Name
1	9.79	9.79	%15Ag(1)
2	12.19	12.19	%15Ag(2)
3	7.68	7.68	%15Ag(3)
Average	9.89	9.89	
Standard Deviation	2.26	2.26	
Coefficient of Variation	22.83	22.83	



(d)

No	Critical Force[mN]	Corrected Critical Force[mN]	Data Name
1	15.10	15.10	%20Ag(1)
2	19.60	19.60	%20Ag(2)
3	7.63	7.63	%20Ag(3)
Average	14.11	14.11	
Standard Deviation	6.04	6.04	
Coefficient of Variation	42.83	42.83	

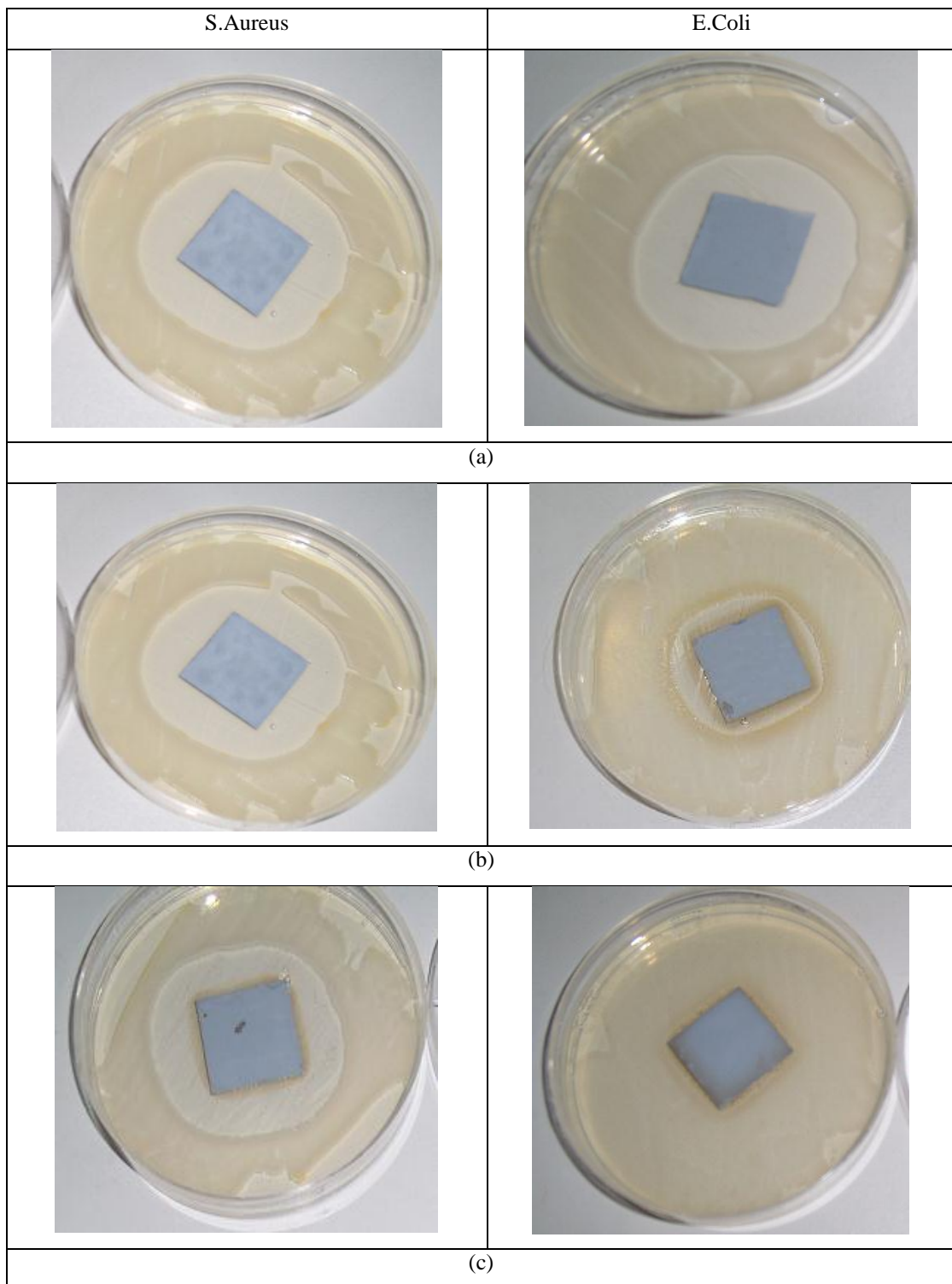


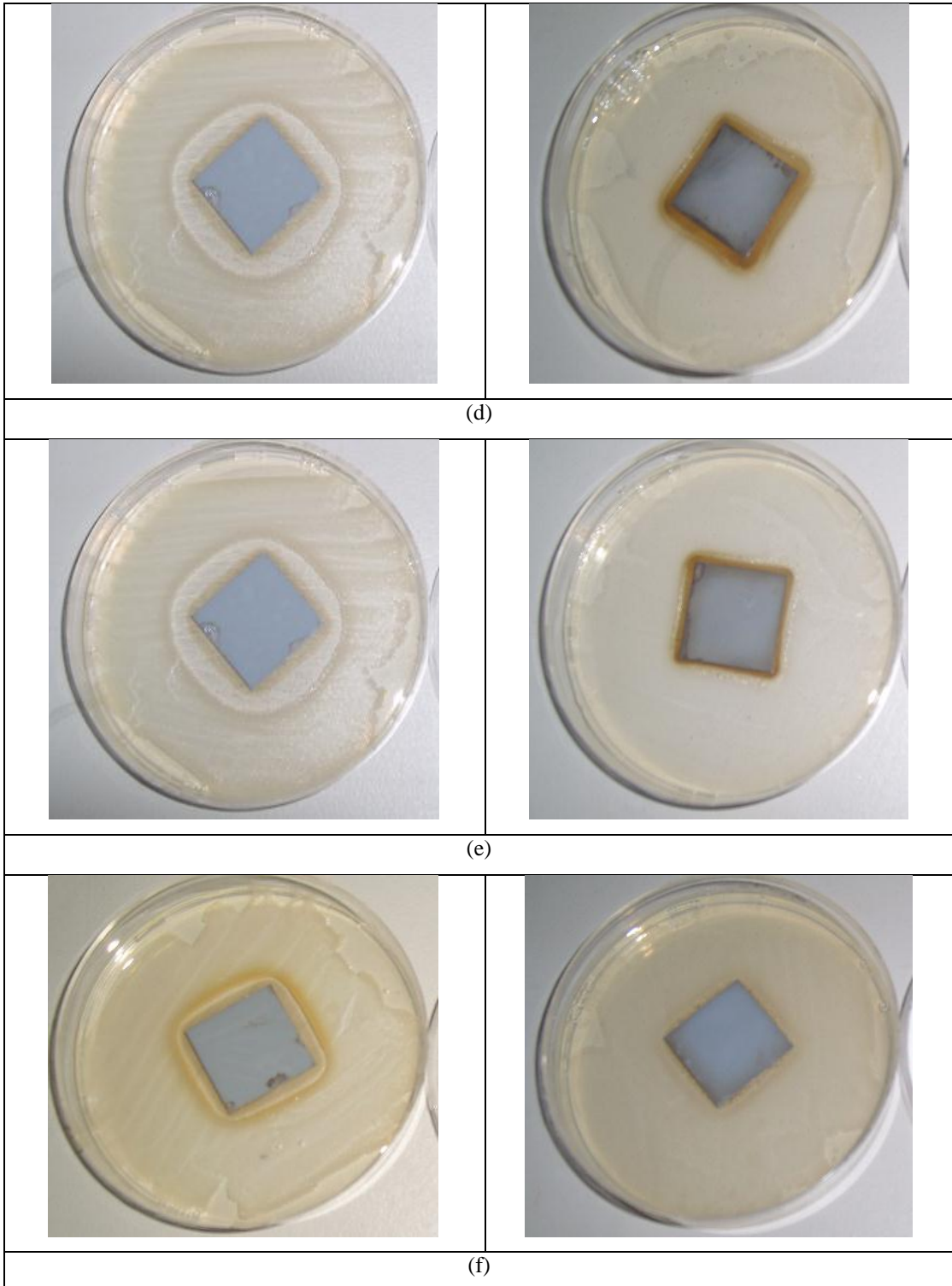
(e)

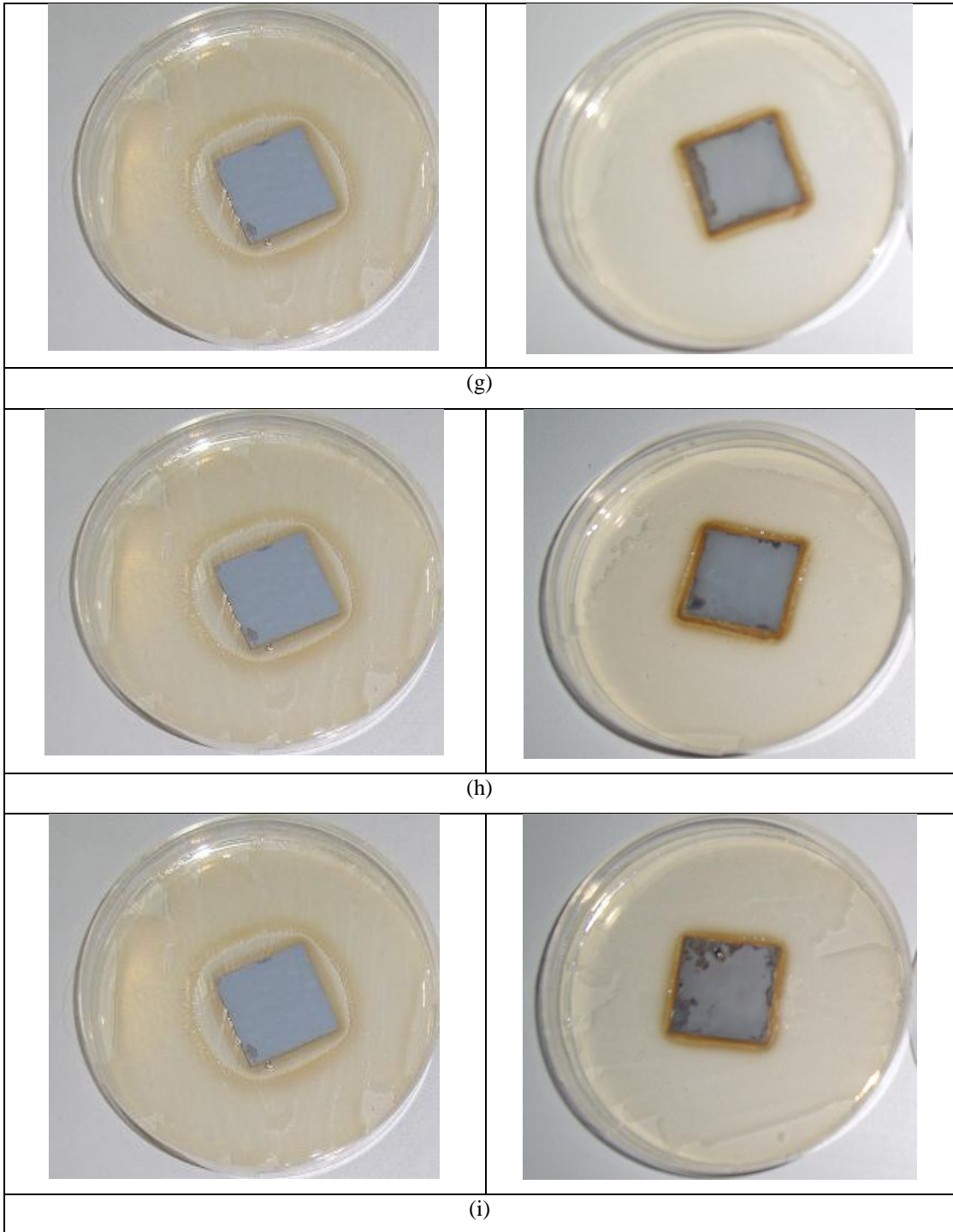
Figure 4.7 Adhesion properties of (a) 0%, (b) 5%, (c) 10%, (d) 15% and (e) 20% Ag nanoparticle added polyurethan composite coatings

4.1.2.6 Antibacterial Behaviour

Hygienic protection is a major concern for food and drink manufacturers, kitchens, hospitals, pharmaceutical companies and operators in the leisure industry. Meeting demanding new hygiene regulations and customer demands for the highest standards of cleanliness requires a hygienic operating environment as well as sterile equipment and hygiene focussed methods and procedures. Due to these reason, surface protection against bacterias and viruses is a significant issue using antibacterial coatings/paints. As mentioned before, three different sample groups were prepared for antibacterial properties.







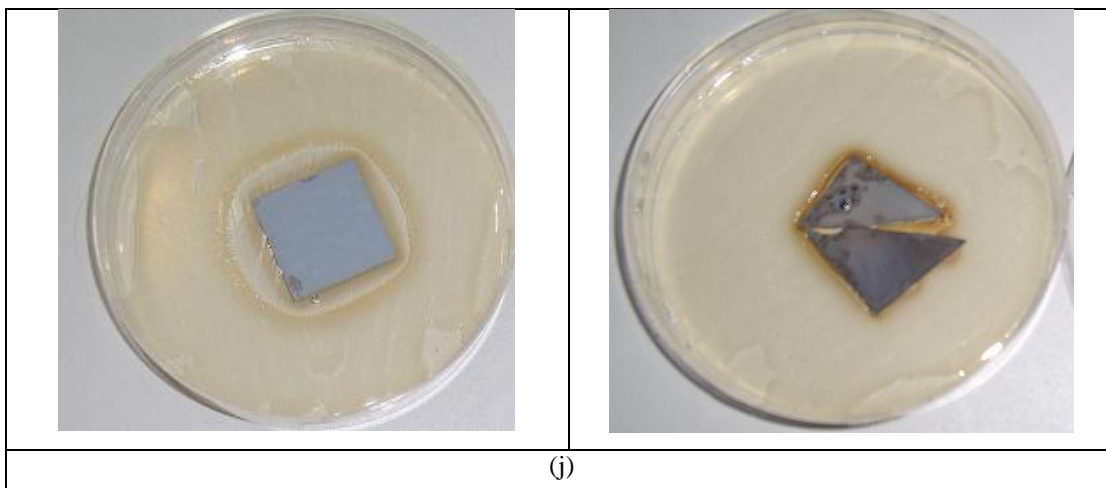


Figure 4.8 Antibacterial test results of (a) NAG00, (b) NAG01, (c) NAG10, (d) NAG50, (e) NAG100, (f) NAG200, (g) NAG301, (h) NAG302, (i) NAG303 and (j) NAG304 samples

In the first group samples presented in Table 3.2, only inhibition test was performed (see Figure 4.8 for details). While *S. Aureus* bacteria was used for left side samples, *E. Coli* was used for right side ones. From these figures, the inhibition zones can be seen easily. Zone of inhibition is produced by Ag nanoparticle added polymer coating against *S. Aureus* and *E. Coli*, representing its antibacterial effect. This antibacterial activity of silver is thought that it results from the interaction of silver and thiol groups in bacteria proteins. We have a good agreement with a research of Baoli (2008). The photographs of the agar plates in which antibacterial tests applied are shown in Figure 4.8. Table 4.1 shows the measured zones of inhibition (ZOI) in diameters as a function of Ag loading concentrate. According to Table 4.4, it can be pointed out that for NAG 50, 100, 200 and 301 samples increasing loaded Ag nanoparticles, increases antimicrobial property.

In the second group samples given in Table 3.3, diffusion test was performed by parallel cultivations method. Figure 4.9 shows antibacterial effect of second group samples. In addition, percent decreasing test also performed to these samples. Ag nanoparticle added (from 0,0001 % to 10 %) composite dye coatings were held in different bacteria regions including *S. Aureus*, *E. Coli*, *P. Aeruginosa*, *K. Pneumonie* and *C. Albicans* yeast-Fongus. It is clear from Figure 4.9 that bacteria were died at diffusion zone of the samples. Pure dye and Ag nanoparticle added composite dye

coatings were held in E.Coli region, the percent decreasing test results are shown in Table 4.2. It can be seen that very good results were obtained after 24 hours in Ag nanoparticle added coatings for all of all bacterias.

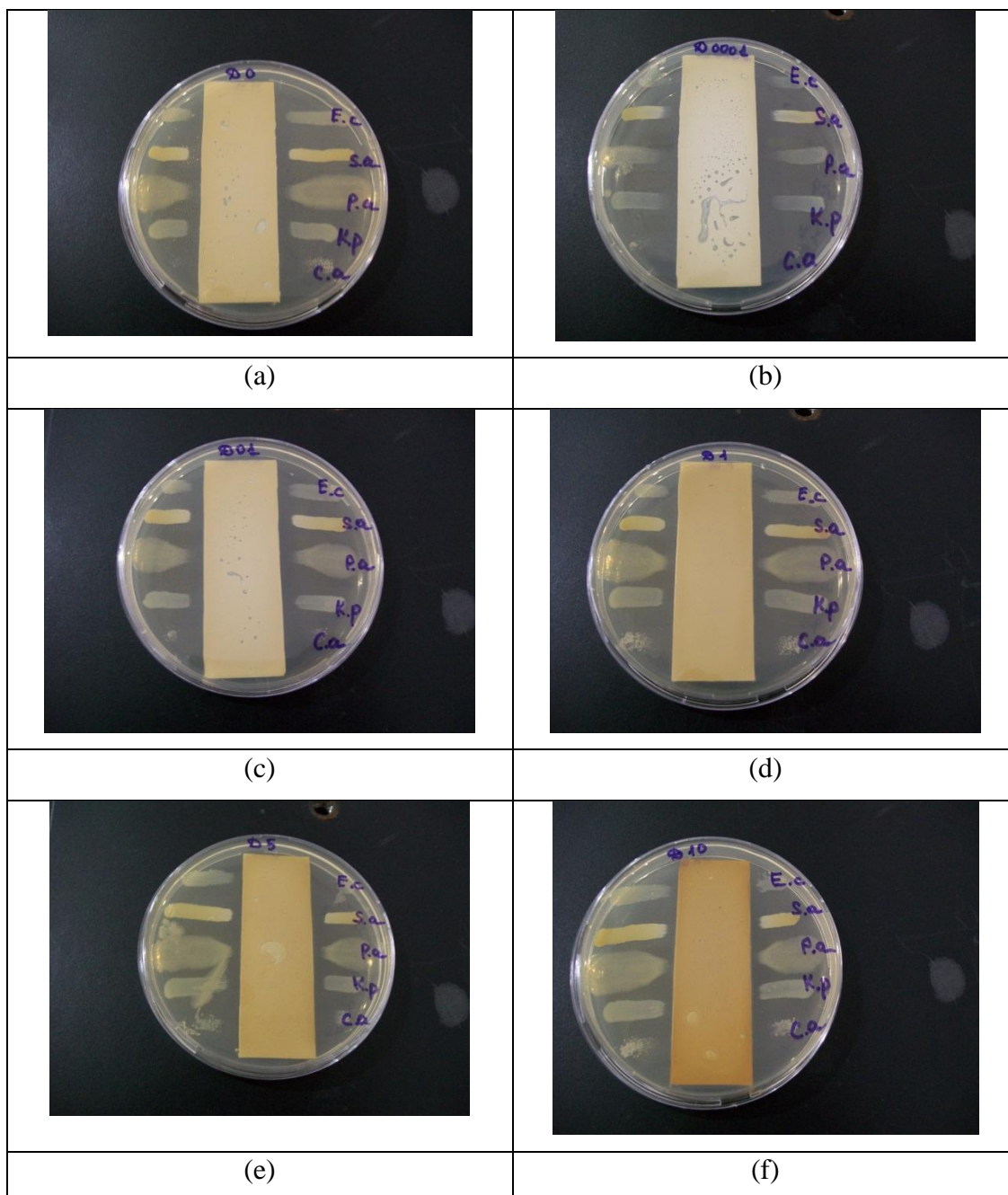


Figure 4.9 (a) 0 %, (b) 0.001 %, (c) 0.1 %, (d) 1 %, (e) 5 % and (f) 10 % Ag nanoparticle added polyurethan composite coatings

Table 4.1 Inhibition radius of Ag nanoparticle added composite coatings

Samples	S.Aureus	E.Coli
NAG 00	1.200	-
NAG 01	1.250	0.125
NAG 10	1.150	0.175
NAG 50	0.225	0.325
NAG 100	0.450	0.225
NAG 200	0.363	0.225
NAG 301	0.600	0.275
NAG 302	0.500	0.275
NAG 303	0.375	0.200
NAG 304	0.250	0.125

Table 4.2 Percent decreasing test results of the antibacterial samples

Sample code	0 hour	24 hours
D 0001	1.01×10^4	0
D 001	0.99×10^4	0.03×10^4
D 01	1.06×10^4	0
D 0	0.87×10^4	2.63×10^4
D 1	0.86×10^4	0.02×10^4
D 5	1.44×10^4	0
D 10	1.25×10^4	0

Table 4.3 Percent decreasing test results of Ag nanoparticle added composite coatings

Sample codes	0 hour	24 hours	Decrease, %
Bactery number at the beginning	16.6×10^4	-	-
D 005	15.9×10^4	9.0×10^4	43.39
D 01	20.4×10^4	1.1×10^4	94.61
D 02	13.2×10^4	0.55×10^4	95.83
D 03	16.4×10^4	5.6×10^4	65.85
D 04	13.9×10^4	2.2×10^4	84.17
D 05	13.7×10^4	0.6×10^4	95.62
DAG 103	19.9×10^4	0	100
DAG 105	15.3×10^4	0	100
DAG 503	20.0×10^4	0	100
DAG 505	17.5×10^4	0	100

Only percent decreasing tests were performed in the third group samples presented in Table 3.4. The results of this test are given in Table 4.3. According to those results, all samples having Ag nanoparticles make all bacteria death/destroyed. On the other hand, it can be explained from the estimations that this does not seem to be depending of the dye amount.

4.2 Flame Retardant Reinforced Composite Coatings

Since huntite/hydromagnesite, boric acid and antimony oxide were used as flame retardant materials, powders and composite coatings/paints were characterized before and after deposition process. The structural, microstructural, thermal and flame retardant properties of the composite/paints were scrutinized in this section. With this concept, this section was divided to two parts as powder and coating characteristics.

4.2.1 Powder Characteristics

Now that the main flame retardant material is huntite/hydromagnesite powder, its powder characteristics were evaluated before coating process. The powders were characterized by DTA-TG, XRD and SEM-EDS.

4.2.1.1 DTA-TG Analysis

Inasmuch as exothermic and endothermic reactions are significant in regard to flame retardancy properties, DTA-TG analysis are carried out to investigate the huntite/hydromagnesite minerals which were ground at different times such 0, 15, 30 and 60 hour(s). DTA-TG analyses are performed by heating up at the rate of 10 °C/min at temperatures between 25°C and 600°C in air. DTA analysis of huntite/hydromagnesite mineral is demonstrated in Figure 4.10, showing that there are three thermal reactions. Huntite and hydromagnesite possess $\text{Mg}_3\text{Ca}(\text{CO}_3)_4$ and $\text{Mg}_4(\text{OH})_2(\text{CO}_3)_3 \cdot 3\text{H}_2\text{O}$ chemical formulas respectively. Note that decomposition occurred in these minerals at temperatures between 25°C and 600°C. The first

thermal phenomenon starts at 219.86°C and ends at 331.89°C and then heat absorption is -3,61 J, corresponding to removal of water and OH groups. After removal of water from hydromagnesite, $Mg_4(CO_3)_3$ decomposes to MgO and CO_2 . It is estimated that the decomposition of $Mg_4(CO_3)_3$ occurs at temperatures between 376.29°C and 490,76°C. This is the second thermal behaviour and heat absorbed at -5,49 J. It is difficult to separately state decomposition phenomena of the individual components of huntite/hydromagnesite because it is a mixture of $Mg_4(OH)_2(CO_3)_3 \cdot 3H_2O$ and $Mg_3Ca(CO_3)_4$. Finally the third thermal effect starts at 503.94°C and ends at 598.29°C. In this case, heat absorption is -1,43 J. MgO and CaO are formed by the end of this process.

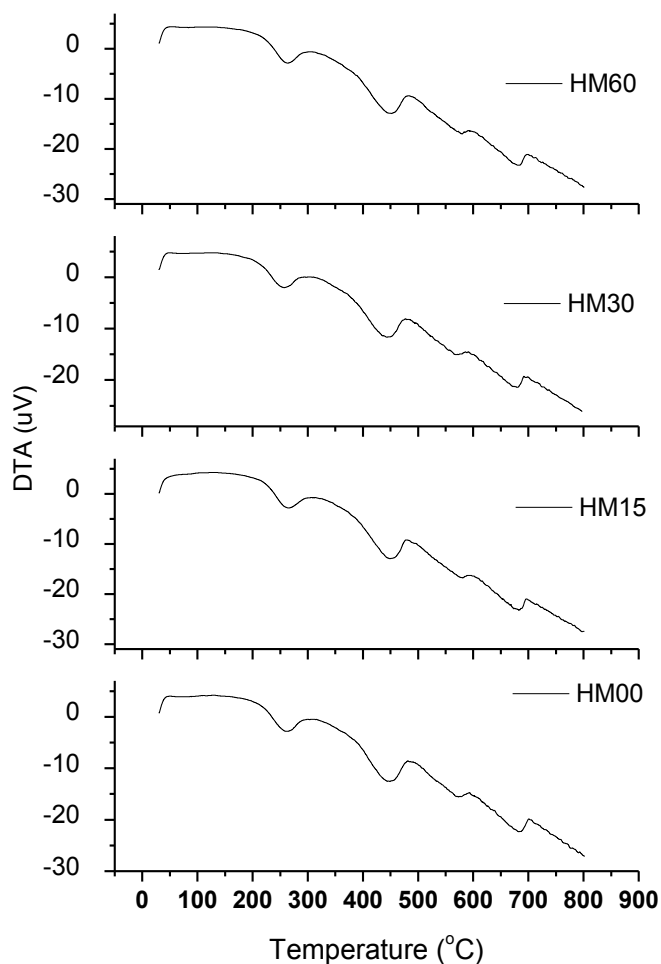


Figure 4.10 DTA curves of huntite/hydromagnesite minerals which were ground at different times such 0, 15, 30 and 60 hour(s).

The similar results can be found in Ref. (Schmidt, 1999). According to Equations 4.2 and 4.3, $\text{Mg}_4(\text{OH})_2(\text{CO}_3)_3 \cdot 3\text{H}_2\text{O}$ and $\text{Mg}_3\text{Ca}(\text{CO}_3)_4$ starts to decompose at high temperatures.

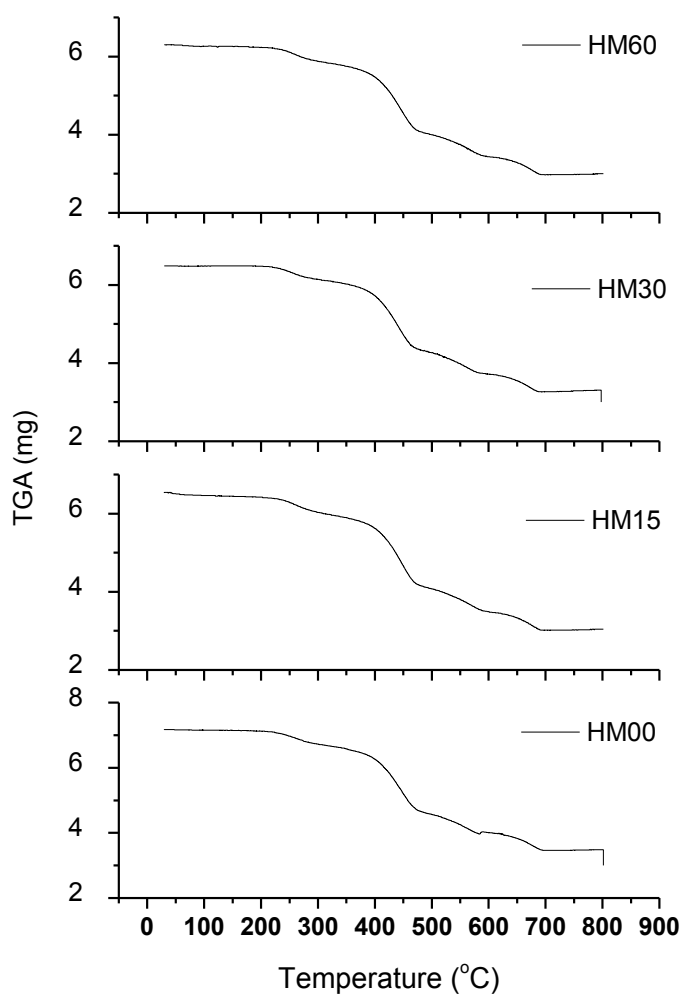
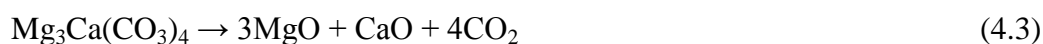


Figure 4.11 TGA curves of huntite/hydromagnesite minerals ground with different time such 0, 15, 30 and 60 hour(s).

As for TGA analysis, as depicted in Figure 4.11, the weight losses occur in huntite/hydromagnesite minerals as a function of temperature from room temperature

to 800°C. It is indicated that the decomposition of huntite/hydromagnesite mineral occurs at temperatures between 400°C and 500°C. Total weight losses of huntite/hydromagnesite mineral were found to be 56 wt %. Rothon (1994) indicated the decomposition temperatures of $\text{Mg}(\text{OH})_2$ and $\text{Al}(\text{OH})_3$ are 300-400°C and 250-350°C, respectively. Therefore it can be explained that huntite/hydromagnesite or even mineral reinforced composite sample have higher decomposition temperatures than $\text{Mg}(\text{OH})_2$ and $\text{Al}(\text{OH})_3$. The fact that decomposition temperature of huntite/hydromagnesite minerals is high and MgO and CaO ceramic materials are formed after burning process are quite likely to be a key area for development of flame retardant polymeric composite coatings. In the context of thermal properties of huntite/hydromagnesite minerals, it can be used as a flame retardant material.

4.2.1.2 Phase Analysis

The XRD pattern of huntite/hydromagnesite mineral powder is shown in Figure 4.12. It is found from this result that the basic minerals are hydromagnesite ($\text{Mg}_4(\text{OH})_2(\text{CO}_3)_3 \cdot 3\text{H}_2\text{O}$), huntite ($\text{Mg}_3\text{Ca}(\text{CO}_3)_4$) and dolomite ($\text{CaMg}(\text{CO}_3)_2$) in the raw huntite/hydromagnesite mineral. The most striking feature of the powder is that the main phases with high intensity are huntite and hydromagnesite.

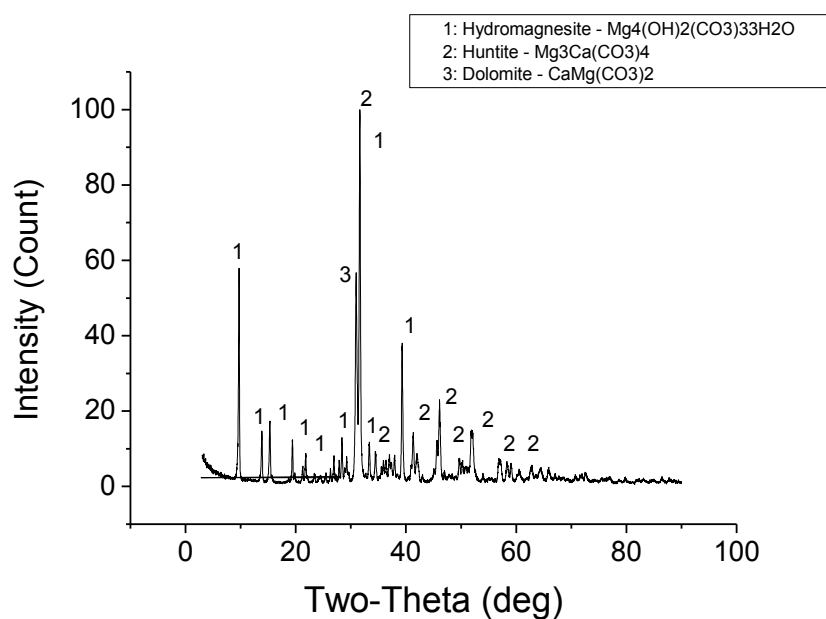
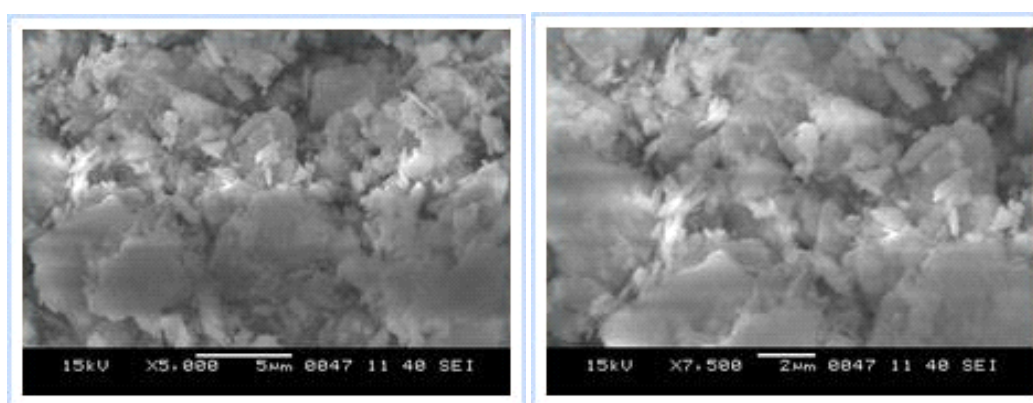


Figure 4.12 XRD pattern of huntite/hydromagnesite mineral powder

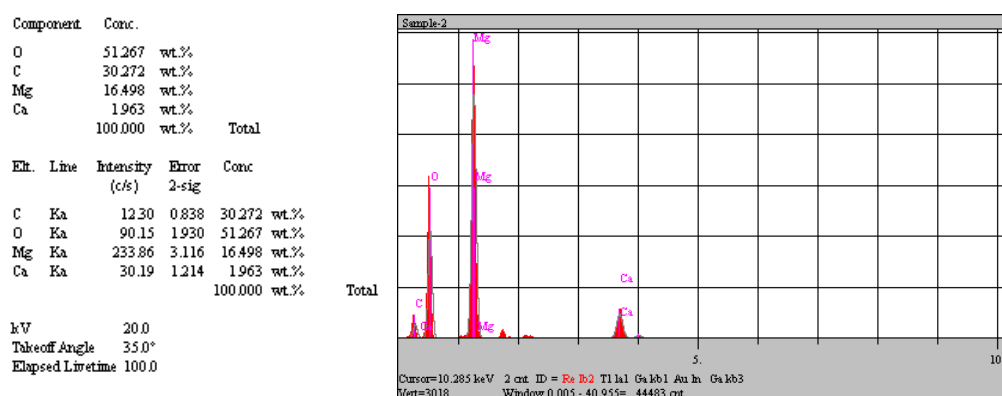
An average mineralogical composition, based on XRD and chemical analysis data of current ores is as follows huntite (46 %), hydromagnesite (46 %), magnesite (4 %), aragonite (3 %) and calcite (1 %). This finding in the current study is similar to Kirschbaum's research (2001).

4.2.1.3 SEM-EDS Analysis

Figure 4.13 demonstrates SEM micrographs and EDS analysis of huntite/hydromagnesite mineral particles. It is seen from Figure 4.13 that huntite/hydromagnesite mineral particles of 20 μm size possess irregular shapes after the grinding process. EDS analysis proved XRD result because Mg, Ca, C and O elements were found in the huntite and hydromagnesite minerals and there are some elements from ores as impurities.



(a)



(b)

Figure 4.13. SEM micrographs and EDS analysis of huntite/hydromagnesite mineral powders with 20 μm before grinding process

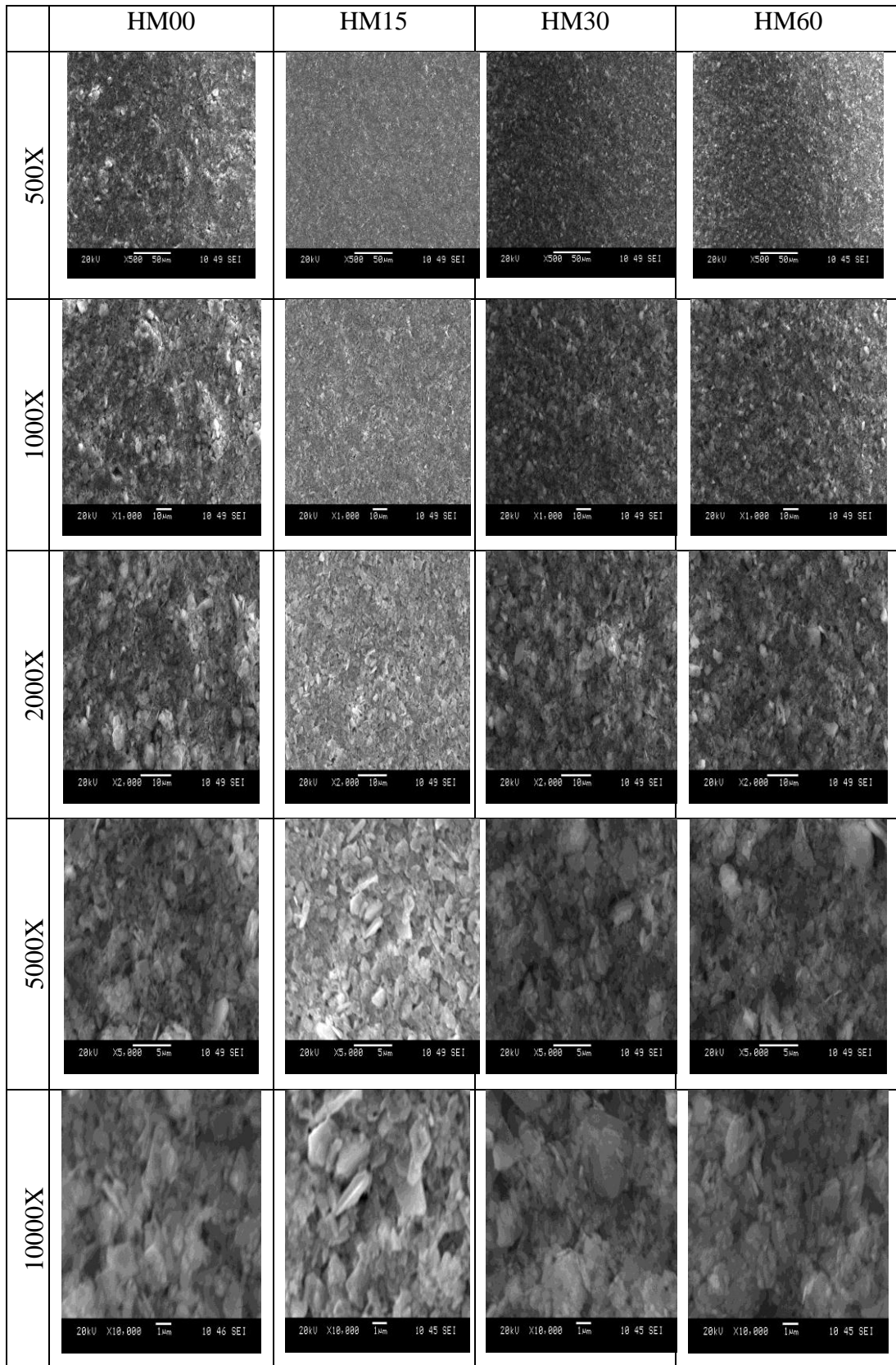


Figure 4.14 SEM micrographs of ground huntite/hydromagnesite mineral powders at different magnifications

SEM micrographs of ground huntite/hydromagnesite mineral powder samples at different magnifications such as 500X, 1000X, 2000X, 5000X and 10000X are denoted in Figure 4.14. The powders in Figure 4.14 were ground at different times including 0, 15, 30 and 60 hours at room temperature in air. The grinding process of the minerals provides outstanding final flame retardant properties. While giving the anticipated benefits in grinding process of the powders, their mechanical and flame retardant properties are affected. With increasing grinding time from 0 hour to 60 hours, finer particles are obtained. These effects can be seen from SEM micrographs. Naturally, it can be stated that smaller the size of the mineral denser the composite coating/paint material. Note that this behaviour increases the flame retardancy property of the material. As SEM micrographs are comparatively examined, the size of the powder ground of 0 hour is bigger than that at 60 hours.

4.2.2 Coating Characteristics

Flame retardant reinforced composite coatings/paints were characterized after deposition process. Within the framework of the present study, experimental investigations were performed to characterize structural, microstructural and flame retardant properties of the composite/paints.

4.2.2.1 Huntite/hydromagnesite Reinforced Polymeric Coatings

Huntite/hydromagnesite reinforced composite coatings/paints were specially characterized using FTIR and candle flame tester.

4.2.2.1.1 FTIR Analysis. Figure 4.15 presents FTIR spectra of huntite/hydromagnesite mineral epoxy dye matrix composite coatings. The minerals used in the coatings were ground with different times containing 0, 15, 30 and 60 hour(s). Their effects were evaluated with this respect. It should be noted that there is no any influence of grinding process to organic bonding in order to form a new structure. In these experiments, the analysis was carried out in 500- 4000 cm^{-1} band range. It is important to realize that the high intensity band at 1500 cm^{-1} may related

with C=C bonds in the matrix, and the weak bands at 600-700 cm^{-1} may be related with C-H bonds. More specifically, those weak bands may be related with calcium carbonate bonds. The other interesting point is that there does not exist interaction between huntite/hydromagnesite mineral and epoxy dye. Thanks to this reason, the composite coatings/paints were formed instead of a new polymeric material.

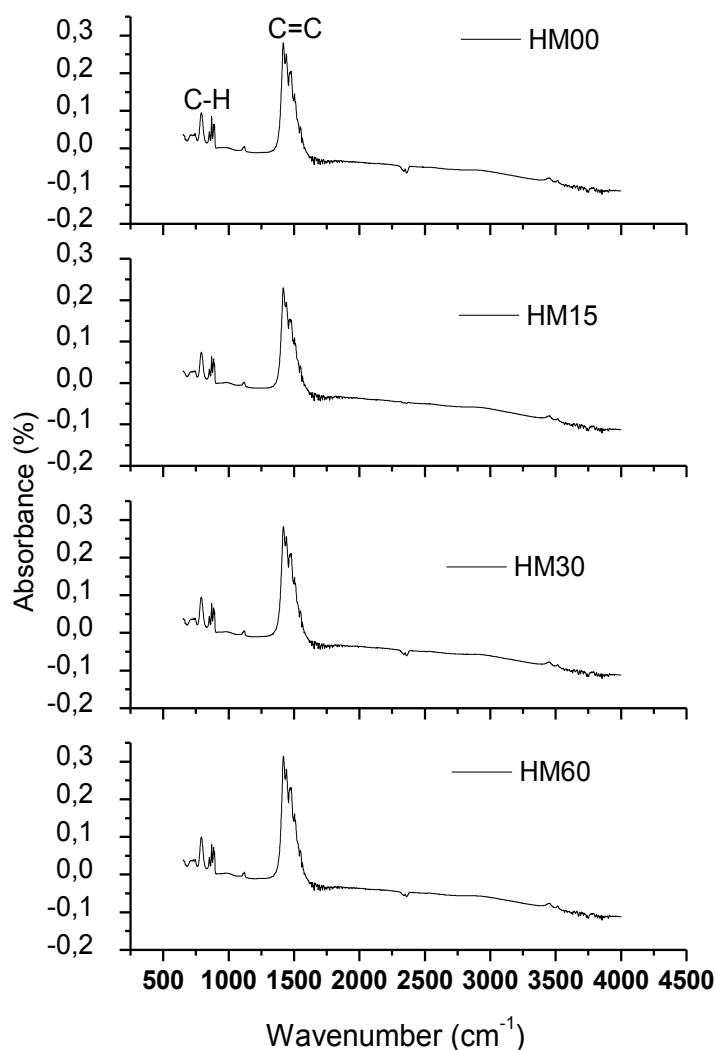


Figure 4.15 FTIR spectra of huntite/hydromagnesite reinforced epoxy dye matrix composite coatings.

In the composite coatings/paints, structural modification did not alter in material chemistry. Only huntite/hydromagnesite mineral was embedded in the epoxy structure. In preparing composite materials with flame retardant content, it is

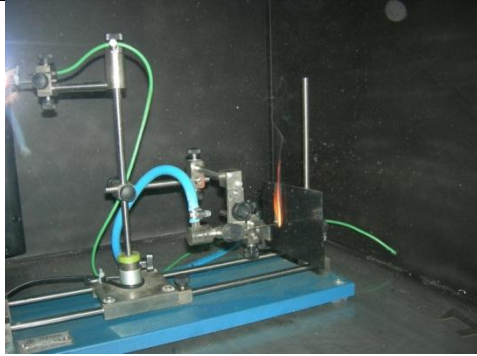

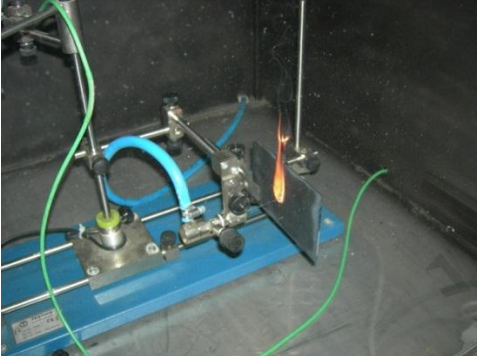

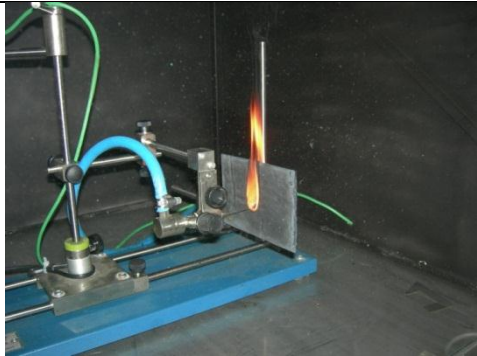

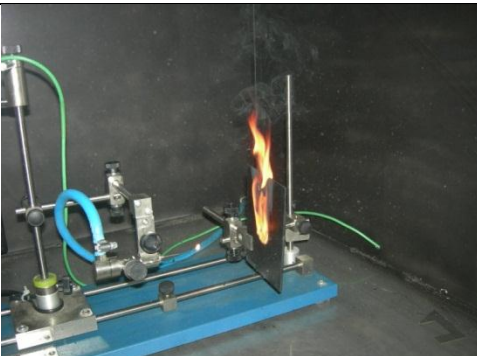

necessary to achieve a homogeneous distribution of huntite/hydromagnesite mineral. To overcome this, the grinding process is a significant issue and consequently powder size of the mineral is an important factor. Even if there is any interaction between them, the powder with small size means homogenous mixture and strong mechanical strength and high flame retardancy in the composite coatings/paints.

4.2.2.1.2 Flame Retardant Properties. Huntite/hydromagnesite reinforced epoxy dye matrix composite coated plastic samples were subjected to flame retardancy tests as indicated beforehand, and the obtained results were presented in Table 4.4. The characteristic burning behaviours of huntite/hydromagnesite reinforced epoxy dye matrix composite coated samples including ground minerals are also shown in Figure 4.16.

It can be seen from Table 4.4 that the coatings are not enough to get required flame retardancy property. This was due to the thickness of the composite coatings. But at the same table, it can be seen that the composite with 30 hours-ground powder shows better flame retardancy property than that with 15 hours-ground because of small particle size of huntite/hydromagnesite. This result is similar our previous study performed with EVA polymers elsewhere (Yılmaz Atay & Celik, 2010).

Table 4.4 Flame starting time of the huntite/hydromagnesite reinforced composite samples

Sample name	Flame starts	After flame	Results
V00	110 sec.	>180 sec.	NOK
VS 15-25	100 sec.	>180 sec.	NOK
VS 15-50	120 sec.	>180 sec.	NOK
VS 15-65	120 sec.	>180 sec.	NOK
VS 30-25	180 sec.	>180 sec.	NOK
VS 30-50	180 sec.	>180 sec.	NOK

After 100 sec	End of the test
	
VS00	
	
VS15-50	
	
VS15-65	
	
VS30-25	

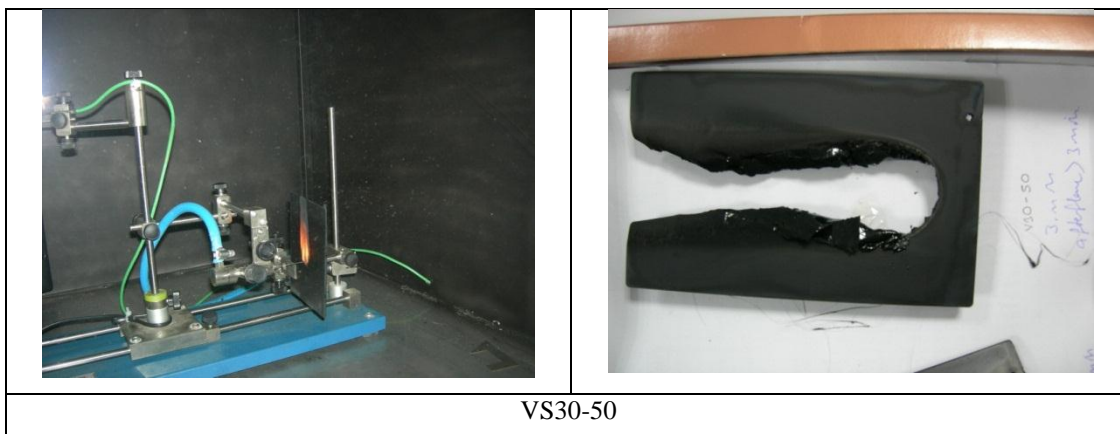


Figure 4.16 Burning behaviours of huntite/hydromagnesite reinforced epoxy dye matrix composite coated samples including ground minerals

4.2.2.2 Boric acid, Antimony Oxide and Huntite/hydromagnesite Reinforced Coatings

To see how synergistically effect is formed, let us use boric acid, antimony oxide and huntite/hydromagnesite in the polymeric composite together as flame retardant materials. These flame retardant powder reinforced composite coatings were characterized by DTA-TG, FTIR, SEM-EDS and candle flame tester.

4.2.2.2.1 DTA-TG Analysis. Since exothermic and endothermic reactions are significant in regard to flame retardancy properties, DTA-TG analysis are carried out to investigate the thermal behaviours of plastic substrate, pure paint and the boric acid, antimony oxide and huntite/hydromagnesite reinforced composites. DTA-TG analyses are performed by heating up at the rate of 10 °C/min at temperatures between 25°C and 900°C under air.

DTA curve of antimony oxide and huntite/hydromagnesite mineral reinforced paint is demonstrated in Figure 4.17 (Sample of A10N). It can be seen that there are four thermal reactions. The first thermal phenomenon starts at 125.06°C and ends at 136.26°C, heat absorption is -1.71 J/g, corresponds to removal of physical bonded water. The second thermal phenomenon starts at 219.86°C and ends at 331.89°C and then heat absorption is -3.61 J, corresponding to removal of chemical bonded water

and OH groups. At the temperatures between 376.29°C and 490.76°C the biggest thermal phenomenon is occurred and this refers to decompose of the minerals. Heat absorption is -5.49 J. It is difficult to separately state decomposition phenomena of the individual components of huntite/hydromagnesite because it is a mixture of $Mg_4(OH)_2(CO_3)_3 \cdot 3H_2O$, $Mg_3Ca(CO_3)_4$, and antimony oxide. Finally the last thermal effect starts at 653.94°C and ends at 727.29°C. In this case, heat absorption is -1.43 J. By TGA analysis of the sample, as depicted in Figure 4.18, the weight losses occur, it is indicated that the decomposition of mineral occurs at temperatures between 25 °C and 900 °C. Total weight loss was found to be 86 %.

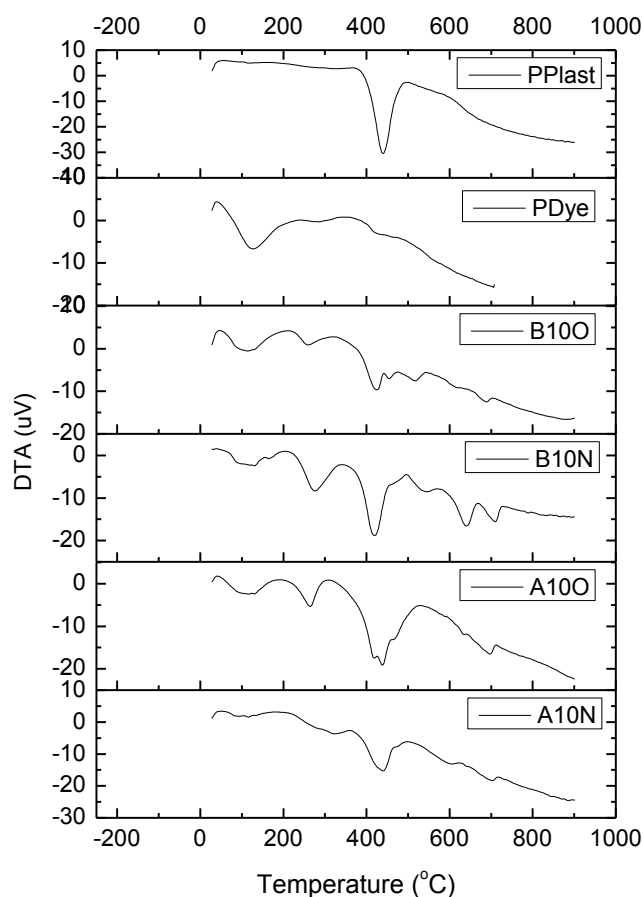


Figure 4.17 DTA curves of the composite coatings; (a) A10N, (b) A10Ö, (c) B10N, (d) B10Ö, (e) SFBO and (f) SFPL

For ground antimony oxide and huntite/hydromagnesite mineral reinforced paint, it can be seen from Figure 4.17 (Sample of A10Ö) that the thermal behaviours are

very similar with A10N. However, four thermal phenomenon started earlier than A10N and the heat absorptions increased for all those phenomenon. For TGA analysis of the samples, as denoted in Figure 4.18, it is indicated that the decomposition of minerals occurs at temperatures between 25 °C and 900 °C. Total weight loss was found to be 88 %.

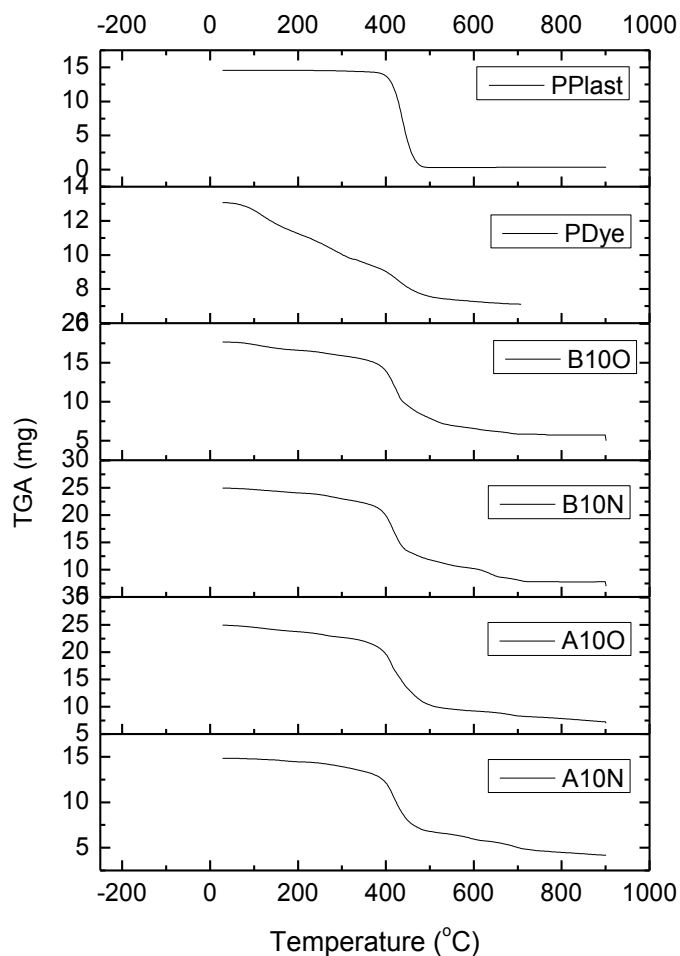


Figure 4.18 TG curves of the composite coatings; (a) A10N, (b) A10Ö, (c) B10N, (d) B10Ö, (e) SFBO and (f) SFPL

For huntite/hydromagnesite and boric acid reinforced composites (Samples of B10N and B10Ö), it can be seen from Figure 4.17 that there are three thermal phenomenon similar with antimony reinforced ones. Except for removing of water and OH groups, minerals decompositions occur at around 390 and 460 °C.

Comparing with B10N and B10Ö, it can be said that the heat absorptions at B10N are higher than B10Ö for all thermal reactions. This means decomposition on ground mineral is easier than the normal one.

According to TGA analysis of the samples, as given in Figure 4.18, it is indicated that the decomposition of mineral occurs at temperatures between 25 °C and 900 °C. Total weight loss was found to be 88 and 90 %, respectively.

DTA curve of the pure dye coated sample was shown in Figure 4.17. It is clear from the figure that apart from the removal of water and OH groups the big thermal phenomenon starts at 386.06°C and ends at 462.90°C, heat absorption is -13.24 J/g. For TGA analysis of the samples, as shown in Figure 4.18 at temperatures between 25 °C and 900 °C, total weight loss was found to be 90 %.

DTA curve of the pure plastic substrate was shown in Figure 4.17. It was found that there is one big thermal reaction that starts at 366.18°C and ends at 515.61°C, heat absorption is -49.76 J/g. This related with the melting of plastic substrate. For TGA analysis of the samples, as depicted in Figure 4.18 at temperatures between 25 °C and 900 °C, total weight loss occurred very sharply, and it was found to be 88 %.

4.2.2.2.2 FTIR Analysis. Figure 4.19 shows FTIR analysis of epoxy dye – mineral composites. The analysis was done in 500- 4000 cm^{-1} band range. In the pure plastic substrate, there is a characteristic band at 700 cm^{-1} may related with C-H bonds, in the pure dye coated composite there are bands at 1100-1200 cm^{-1} may related with C-C and O-H bonds. In addition, it can be seen that by adding minerals to the dye, there was no big change in the structure.

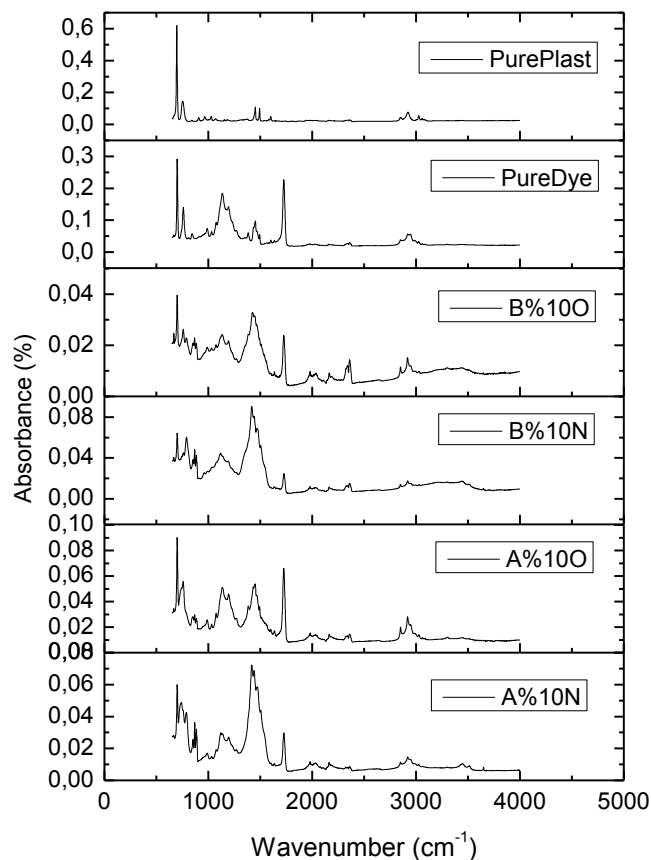
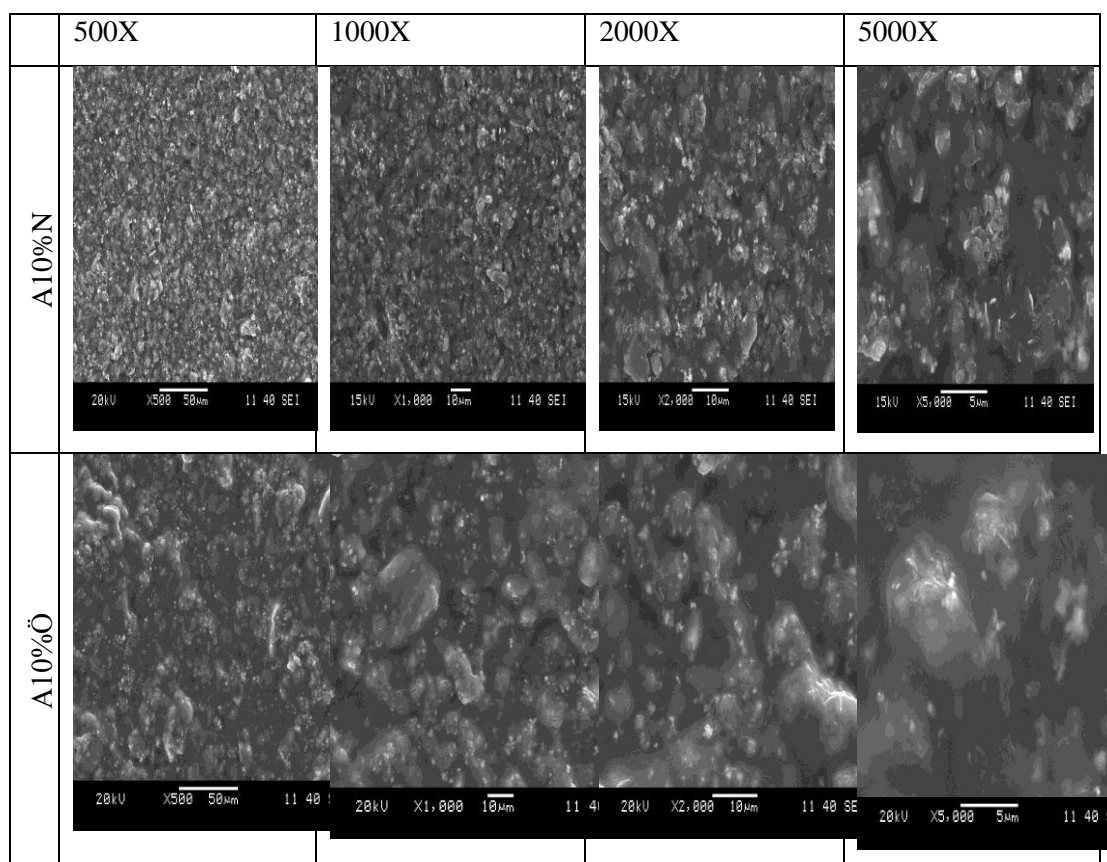


Figure 4.19 FTIR spectra of the samples

4.2.2.2.3 SEM-EDS Analysis. Figures 4.20 and 4.21 demonstrate SEM micrographs and EDS analysis of pure plastic substrate, pure epoxy paint, and boric acid-huntite/hydromagnesite and antimony oxide-huntite/hydromagnesite binary reinforced composite coatings/paints respectively. Reinforcement powders were used normally and groundly in this experiment.

Figure 4.20 signifies SEM micrographs of composite coatings coatings, including A%10N, A%10Ö, B%10N, B%10Ö, pure dye coating, and pure plastic substrate (PurePlastic) at different magnifications. The results of this investigation show that even though pure substrate and pure paint possess very smooth surfaces, boric acid-huntite/hydromagnesite and antimony oxide-huntite/hydromagnesite binary

reinforced composite coatings have rough surfaces on account of mineral particles. In the reinforced composite coatings, there exist two types of the compound powders containing normal and ground boric acid and antimony oxide in Figure 4.20. It can be said that smaller the size of the mineral denser and smoother the composite material. This can be clearly distinguishing in the results between boric acid-huntite/hydromagnesite and antimony oxide-huntite/hydromagnesite binary reinforced composite coatings on the plastic substrates. Note that boric acid-huntite/hydromagnesite reinforced composite coating is smoother than that of antimony oxide-huntite/hydromagnesite. This is due to the fact that boric acid can easily dissolve in solvents. Whereas antimony oxide does not dissolved in a solvent that have stable structure. As it was mentioned above, this will positively affect to increase the flame retardancy property of the material. Currently these attempts are being made to harmonies denser the composite coatings and to finalize a novel opportunity in the flame retardancy results.



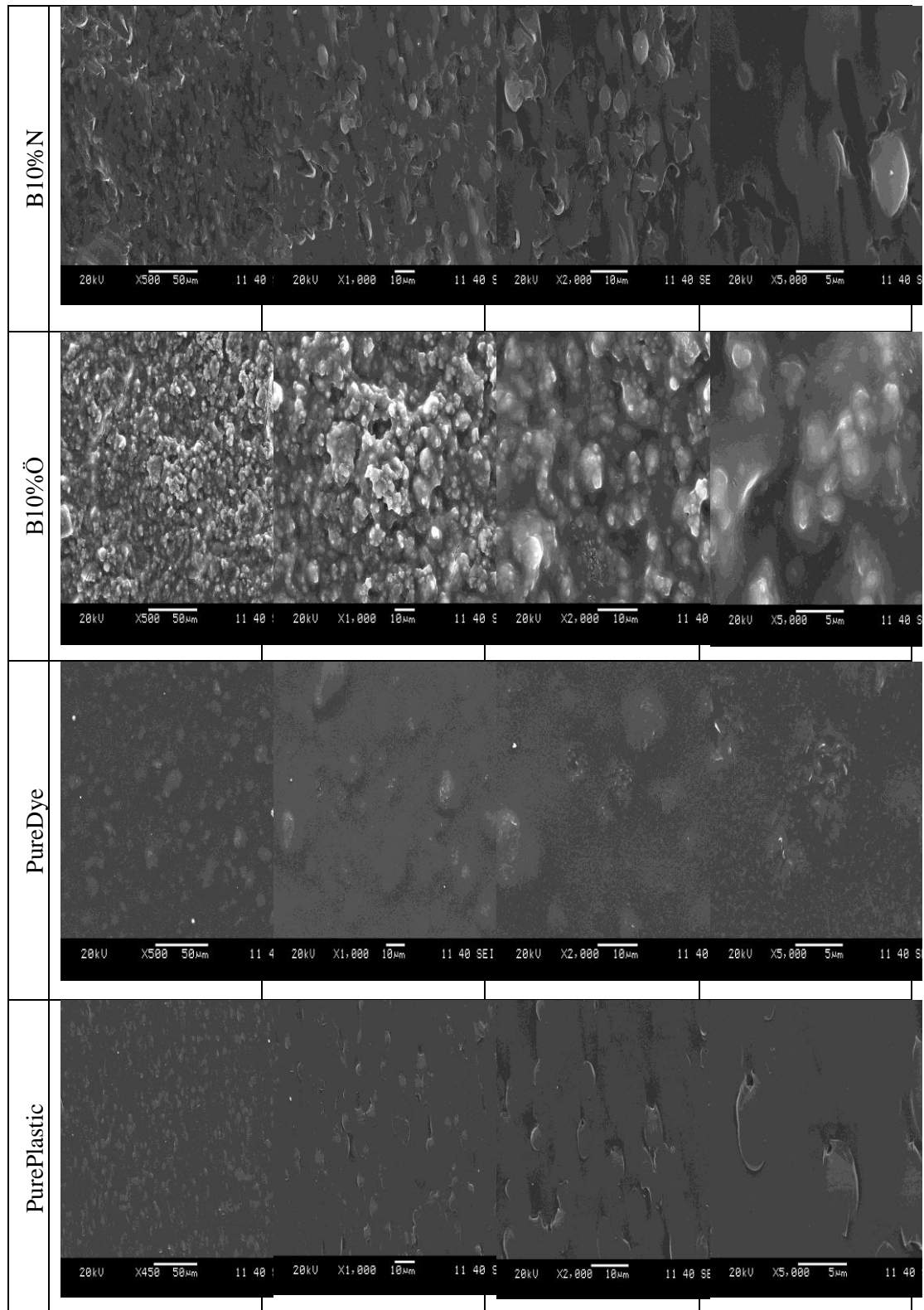
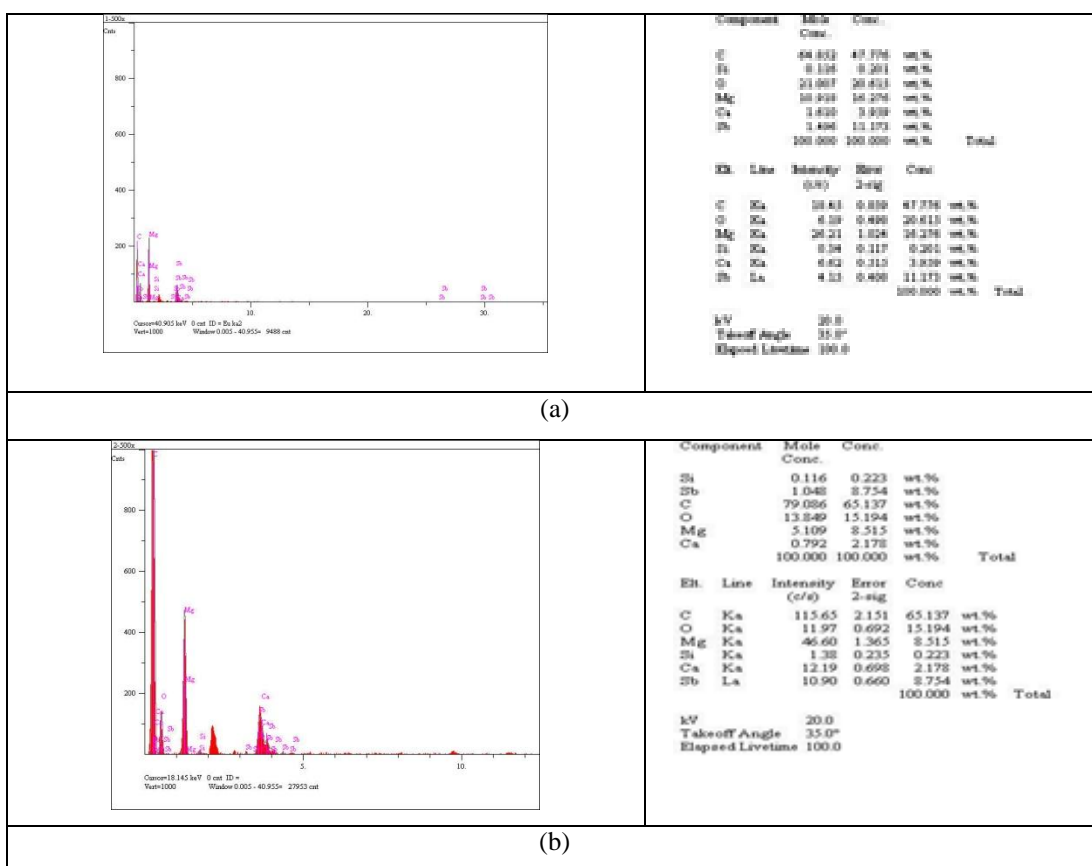


Figure 4.20. SEM micrographs of the composite coatings including A%10N, A%10Ö, B%10N, B%10Ö, PureDye, and PurePlastic. N:Normal and Ö:Ground powders.

Figure 4.21 depicts EDS analysis of boric acid-huntite/hydromagnesite and antimony oxide-huntite/hydromagnesite binary reinforced composite coatings/paints, pure epoxy paint and pure plastic substrate. In pure plastic substrate, C peak with high intensity was determined according to EDS analysis. Also Si and O elements were observed in the plastic structure in terms of SiO_2 pigment. As in the case of pure epoxy paint on the plastic substrate, Si, Mg, Ca, O and C elements were found from the samples. It is believed that the pure paint has Mg, Ca and O elements as oxide forms like MgO and CaO pigments and the plastic structure has C, Si and O elements were observed in the structure in terms of SiO_2 pigment. Upon investigating normal and ground boric acid-huntite/hydromagnesite reinforced composite coatings on the plastic substrate, C, Si, Mg, Ca, B, and O elements were observed in the samples.



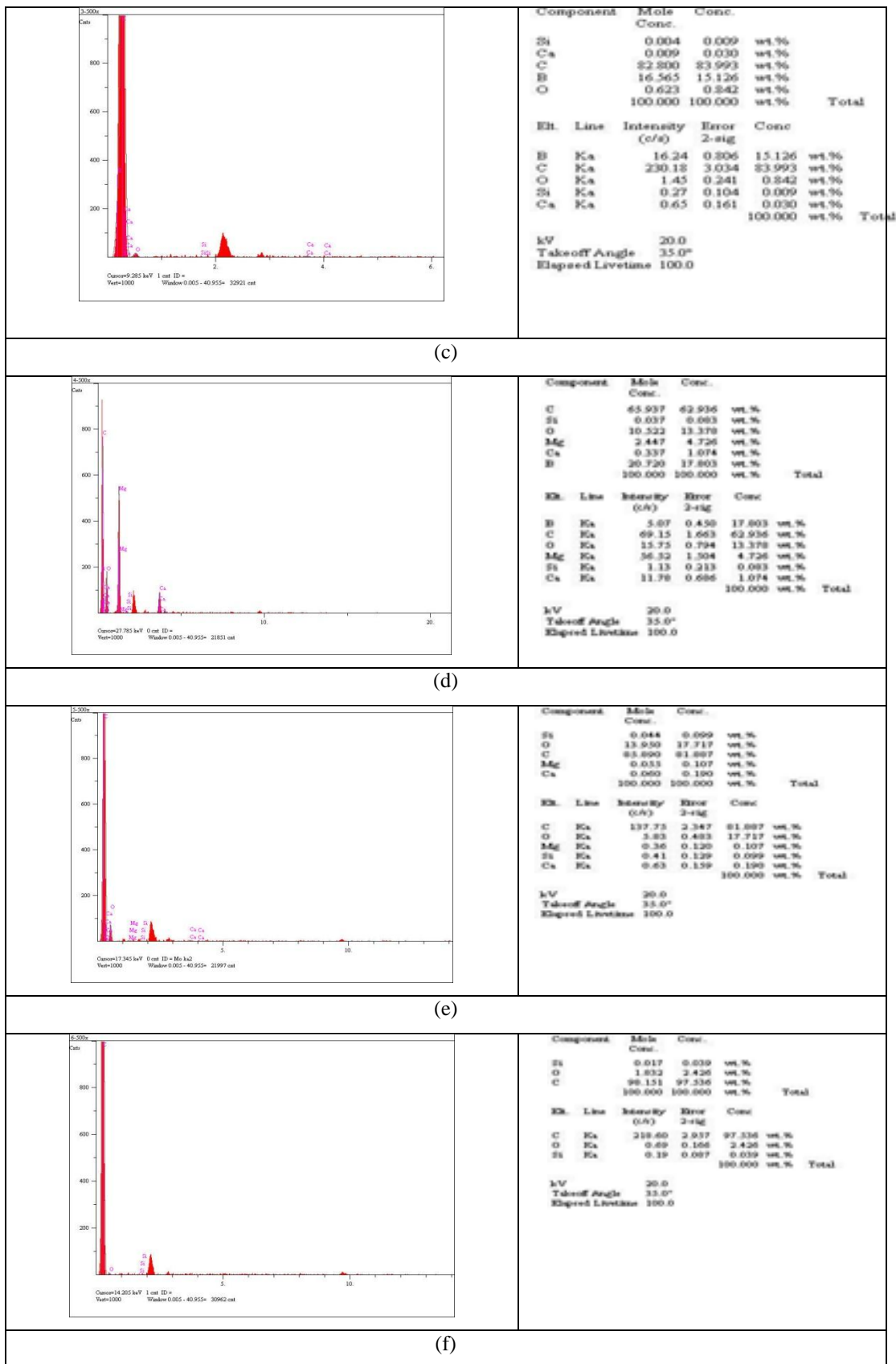


Figure 4.21 EDS analysis of the composite coatings including (a) A%10N, (b) A%10O, (c) B%10N, (d)B%10O, (e) PureDye, (f) PurePlastic

In addition to these, normal and ground antimony oxide-huntite/hydromagnesite reinforced composite coatings on the plastic substrate, C, Si, Mg, Ca, Sb, and O elements were found in the samples. In the specimens of boric acid-huntite/hydromagnesite and antimony oxide-huntite/hydromagnesite binary reinforced composite coatings/paints on the plastic substrate, the intensities of Mg and Ca elements increased because huntite/hydromagnesite mineral possesses $\text{Mg}_4(\text{OH})_2(\text{CO}_3)_3 \cdot 3\text{H}_2\text{O}$ and $\text{Mg}_3\text{Ca}(\text{CO}_3)_4$ as well as MgO and CaO pigments.

4.2.2.2.4 Flame Retardant Properties. The flame retardancy test results are shown in Figures 4.22-4.31. The figures show antimony oxide-huntite/hydromagnesite and boric acid-huntite/hydromagnesite reinforced composites. On the other hand Figure 4.30 shows the time testing process of the composite coatings/paints on plastic substrates. The samples are subjected to flame for 3 minutes after calibration process is completed (flame height: 12 mm, it is 23.5 s \pm 1 s to reach from T1:100 C to T2:700 C). The details regarding the tests are following: name of the test is needle flame test, the used equipment is apparatus for flame test and the used gas is propane with 99.5% of purity.

More specifically, Figure 4.22 depicts candle flame test results of 1% ground, 1% normal and 5% normal boric acid-huntite/hydromagnesite binary reinforced polymeric composite coated/painted plastic samples depending on different boric acid amount in the structure. As boric acid amount was increased in the structure, the performance of its flame retardancy increased as seen from Figure 4.22. Figure 4.23 shows candle flame test results of 1% ground and 1% normal antimony oxide-huntite/hydromagnesite binary reinforced polymeric composite coated/painted plastic samples. As may be expected, flame retardant properties of 1% ground antimony oxide-huntite/hydromagnesite reinforced polymeric composite coated/painted plastic samples is better than that of 1% normal sample after the tests. Grinding effects can easily be seen from Figure 4.23 showing the candle flame test results of 5% ground, 10% normal and 10% ground boric acid-huntite/hydromagnesite binary reinforced polymeric composite painted plastic samples.

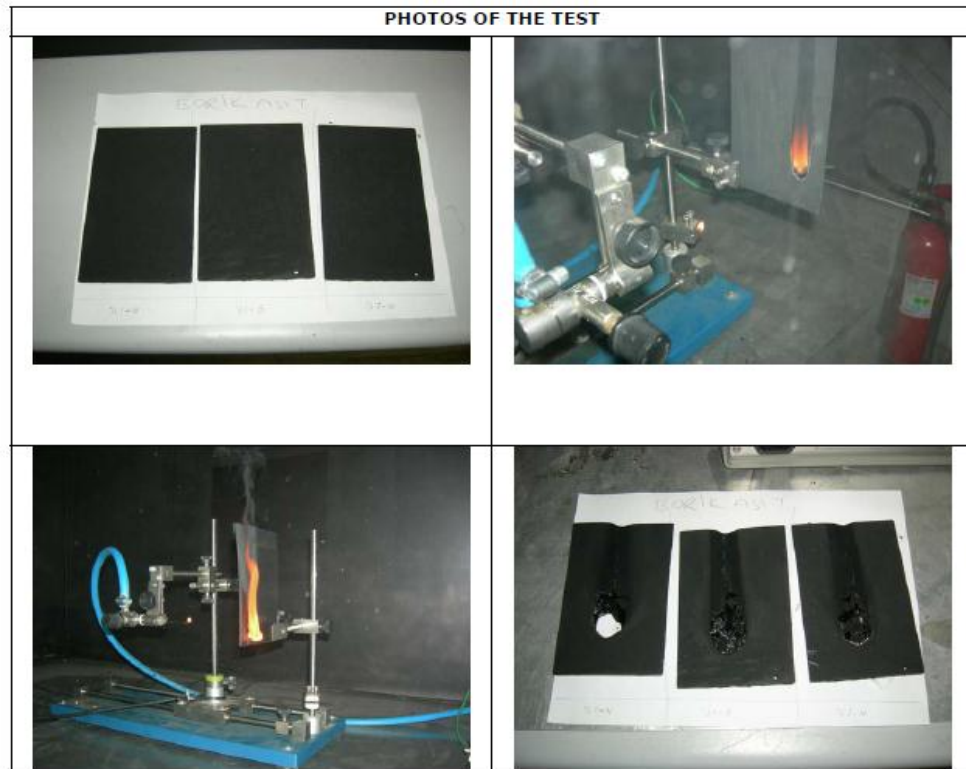


Figure 4.22 Candle flame test results of 1% ground, 1% normal and 5% normal boric acid-huntite/hydromagnesite binary reinforced polymeric composite painted plastic samples

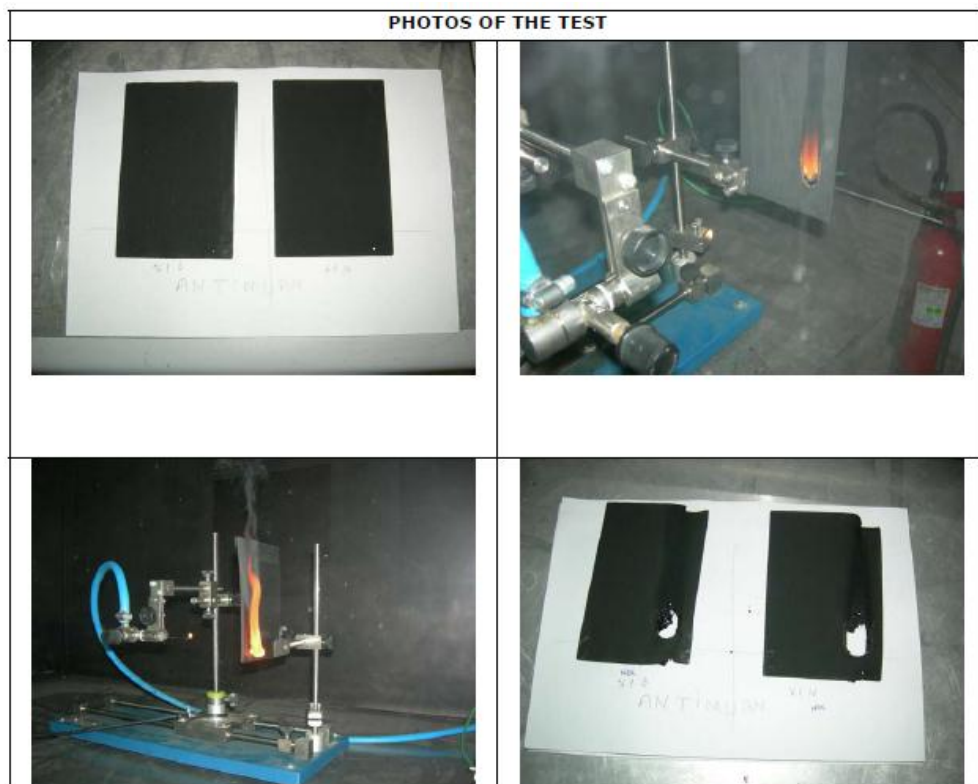


Figure 4.23 Candle flame test results of 1% ground and 1% normal antimony oxide-huntite/hydromagnesite binary reinforced polymeric composite coated/painted samples

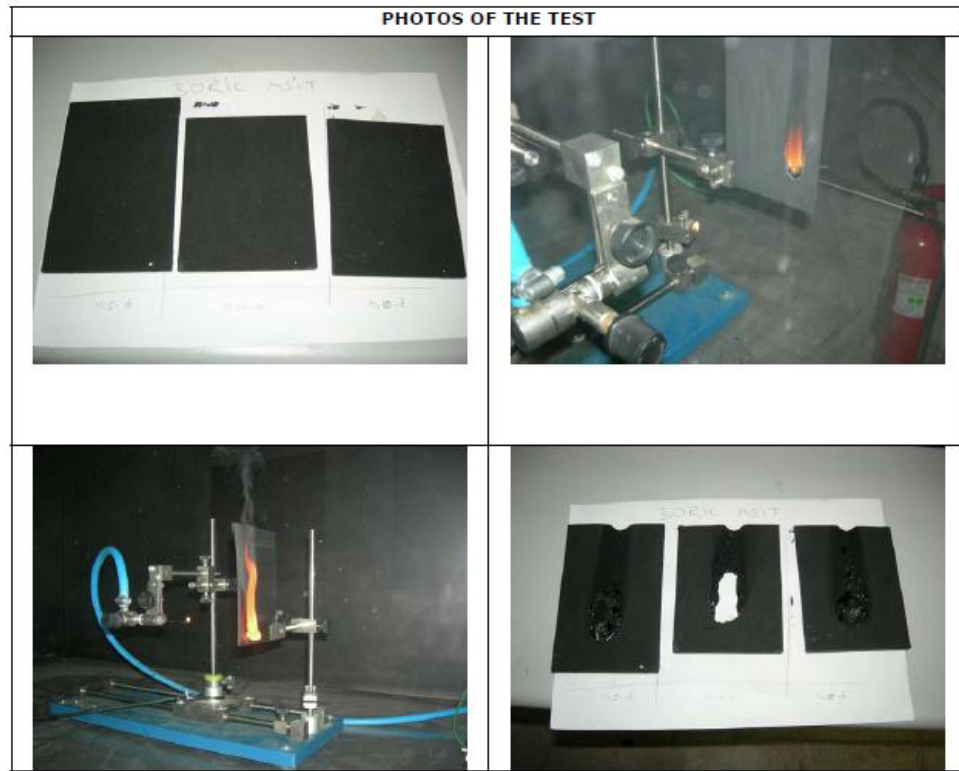


Figure 4.24 Candle flame test results of 5% ground, 10% normal and 10% ground boric acid-huntite/hydromagnesite binary reinforced polymeric composite painted plastic samples

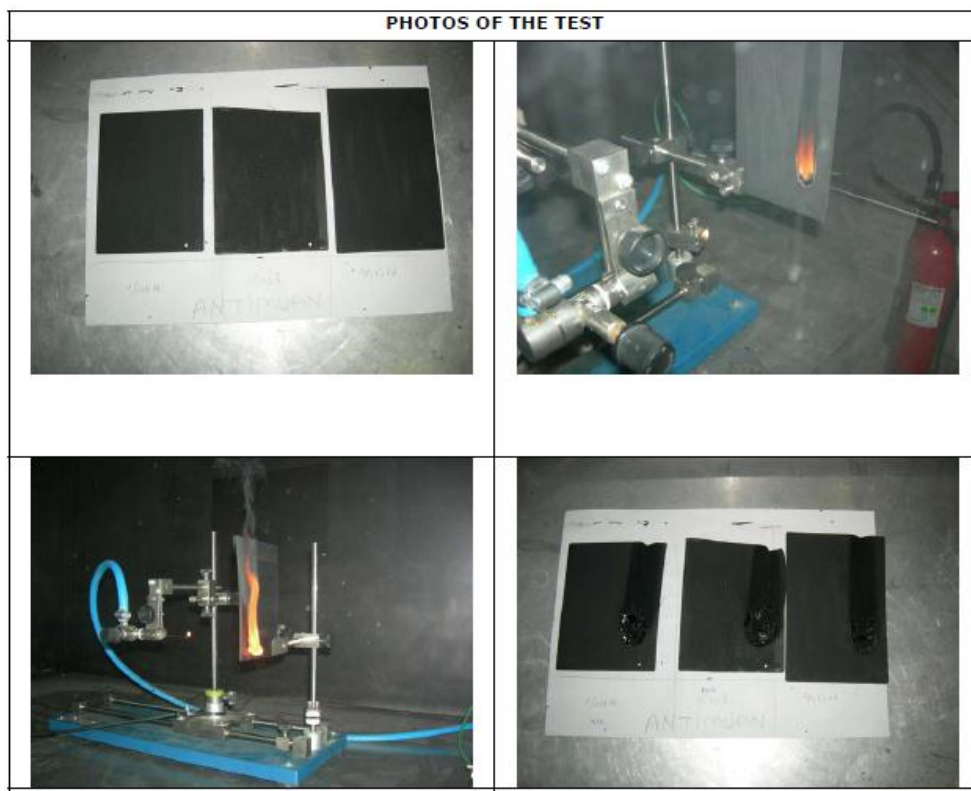


Figure 4.25 Candle flame test results of 10% ground, 10% normal and 15% normal antimony oxide-huntite/hydromagnesite binary reinforced polymeric composite samples

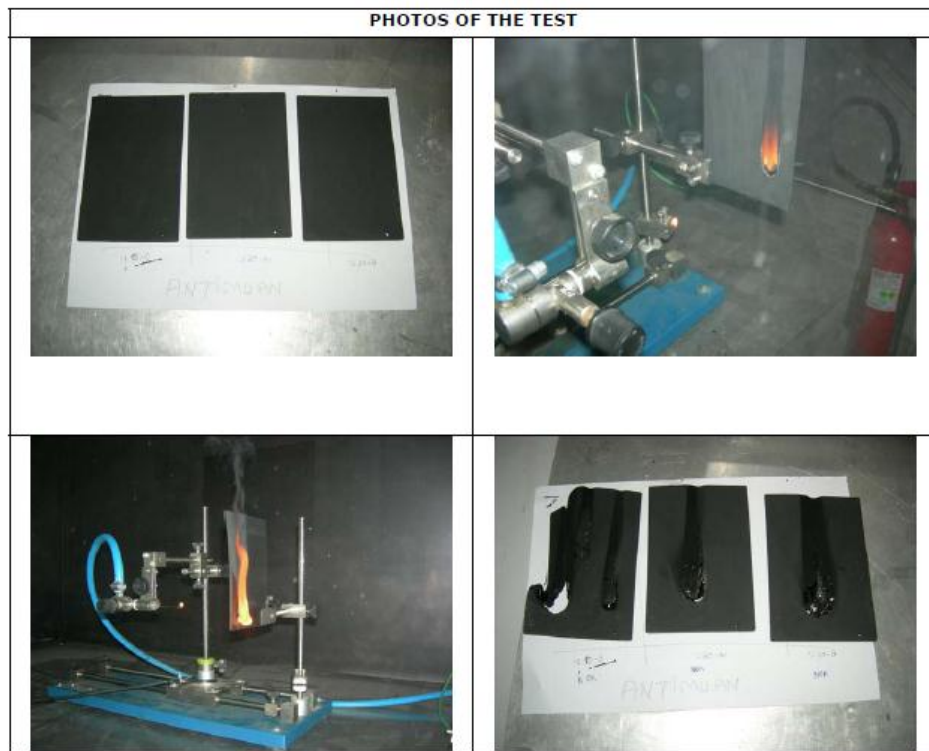


Figure 4.26 Candle flame test results of 15% ground, 30% normal and 30% ground antimony oxide-huntite/hydromagnesite binary reinforced polymeric composite samples

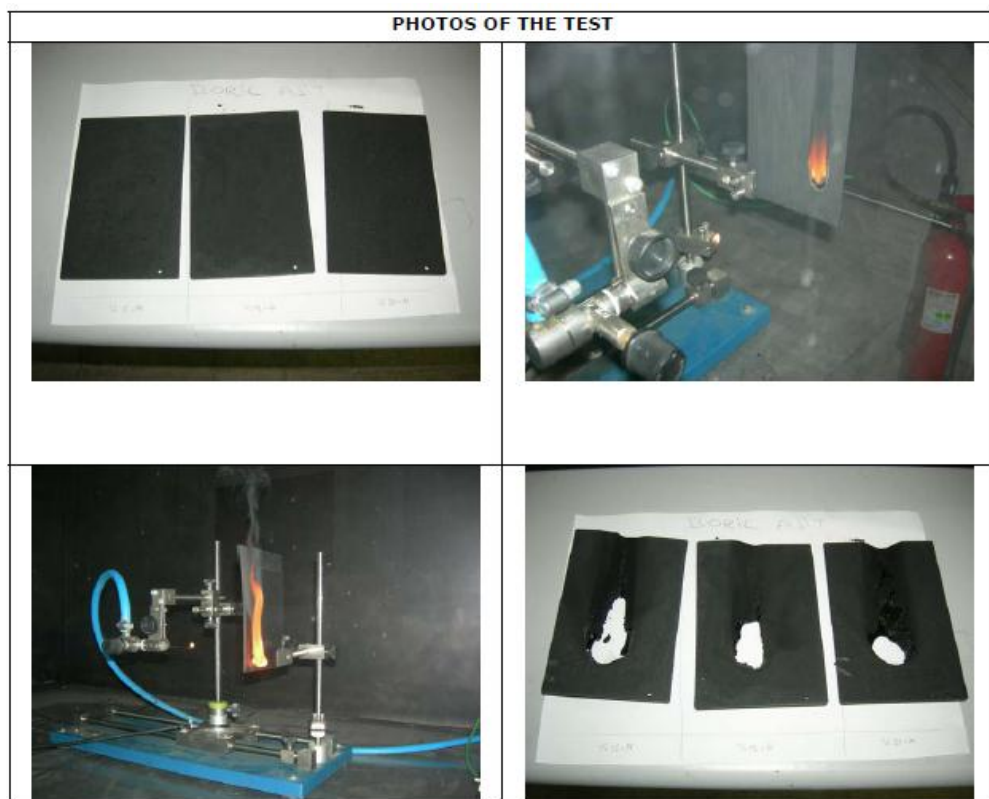


Figure 4.27 Candle flame test results of 15% normal, 15% ground and 30% normal boric acid-huntite/hydromagnesite binary reinforced polymeric composite painted plastic samples

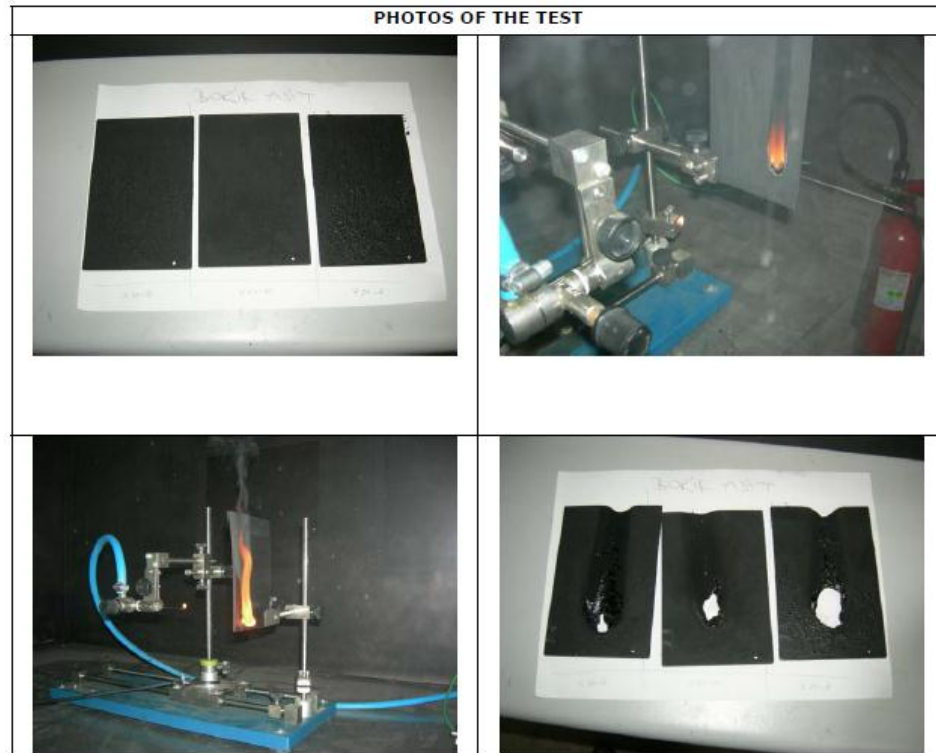


Figure 4.28 Candle flame test results of 30% ground, 50% normal and 50% ground boric acid-huntite/hydromagnesite binary reinforced polymeric composite painted samples

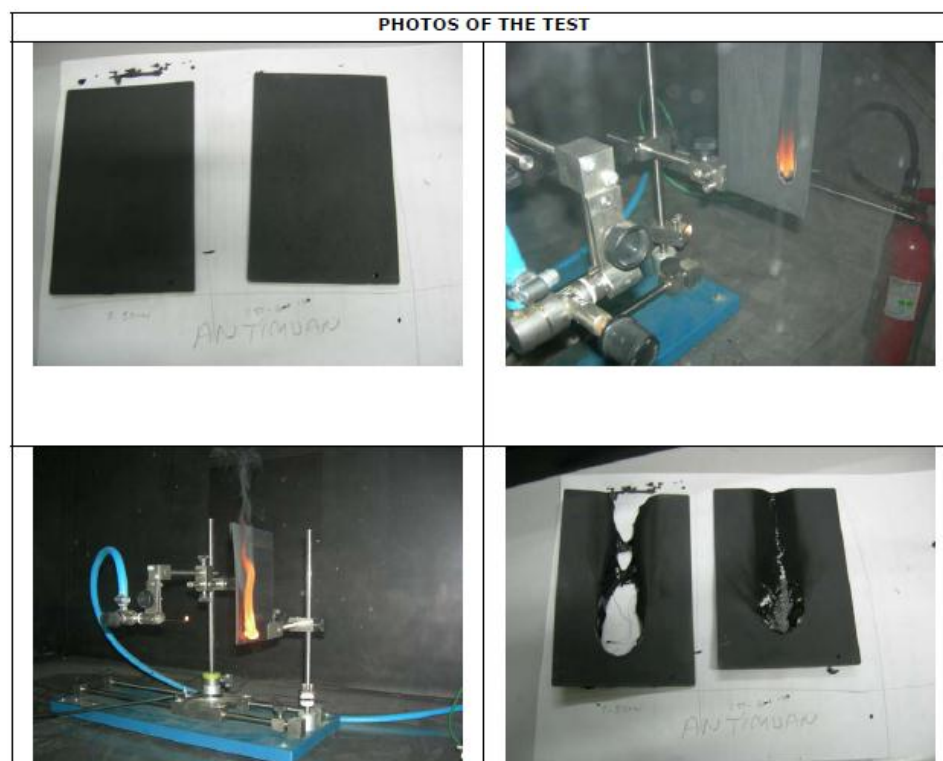


Figure 4.29 Candle flame test results of 50% normal and 50% ground antimony oxide-huntite/hydromagnesite binary reinforced polymeric composite painted plastic samples

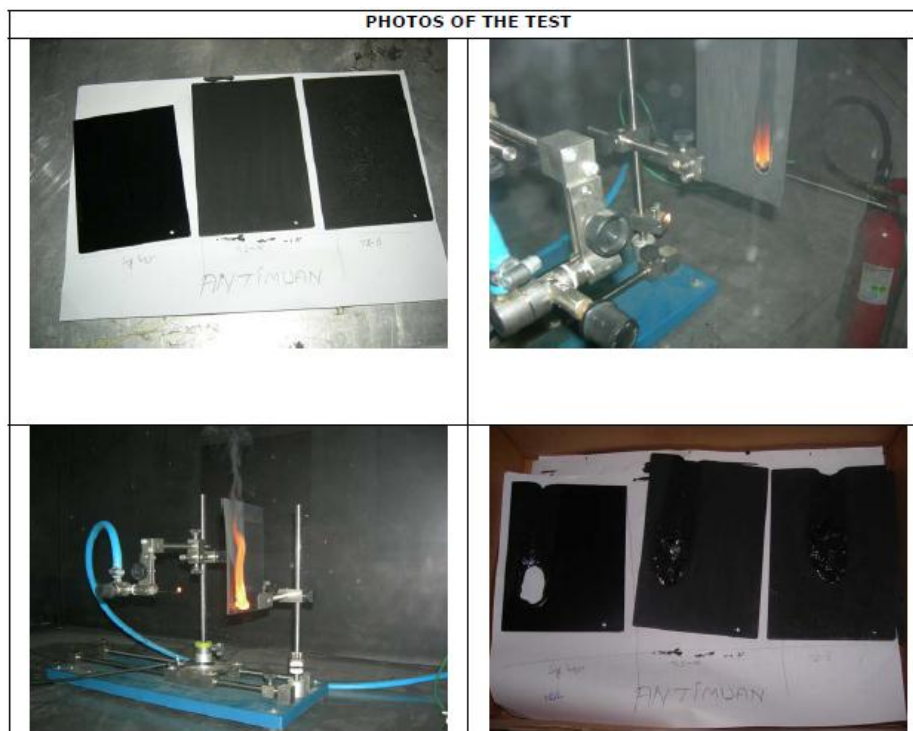


Figure 4.30 Candle flame test results of 5% normal, 5% ground antimony-huntite/hydromagnesite binary reinforced polymeric composite painted samples

With these samples, the outstanding improvements in flame retardancy were performed with the help of the grinding process. As the normal powder used as-received from Likya Inc. company was compared with the ground one as the flame retardant characteristics, it can be pointed out that the ground samples were much more better than that of normal one. Figure 4.25 indicates candle flame test results of 10% ground, 10% normal and 15% normal antimony oxide-huntite/hydromagnesite binary reinforced polymeric composite painted plastic samples. Figure 4.26 signifies candle flame test results of 15% ground, 30% normal and 30% ground antimony oxide-huntite/hydromagnesite binary reinforced polymeric composite painted plastic samples. Figure 4.27 shows candle flame test results of 15% normal, 15% ground and 30% normal boric acid-huntite/hydromagnesite binary reinforced polymeric composite painted plastic samples. Figure 4.28 demonstrates candle flame test results of 30% ground, 50% normal and 50% ground boric acid-huntite/hydromagnesite binary reinforced polymeric composite painted plastic samples.

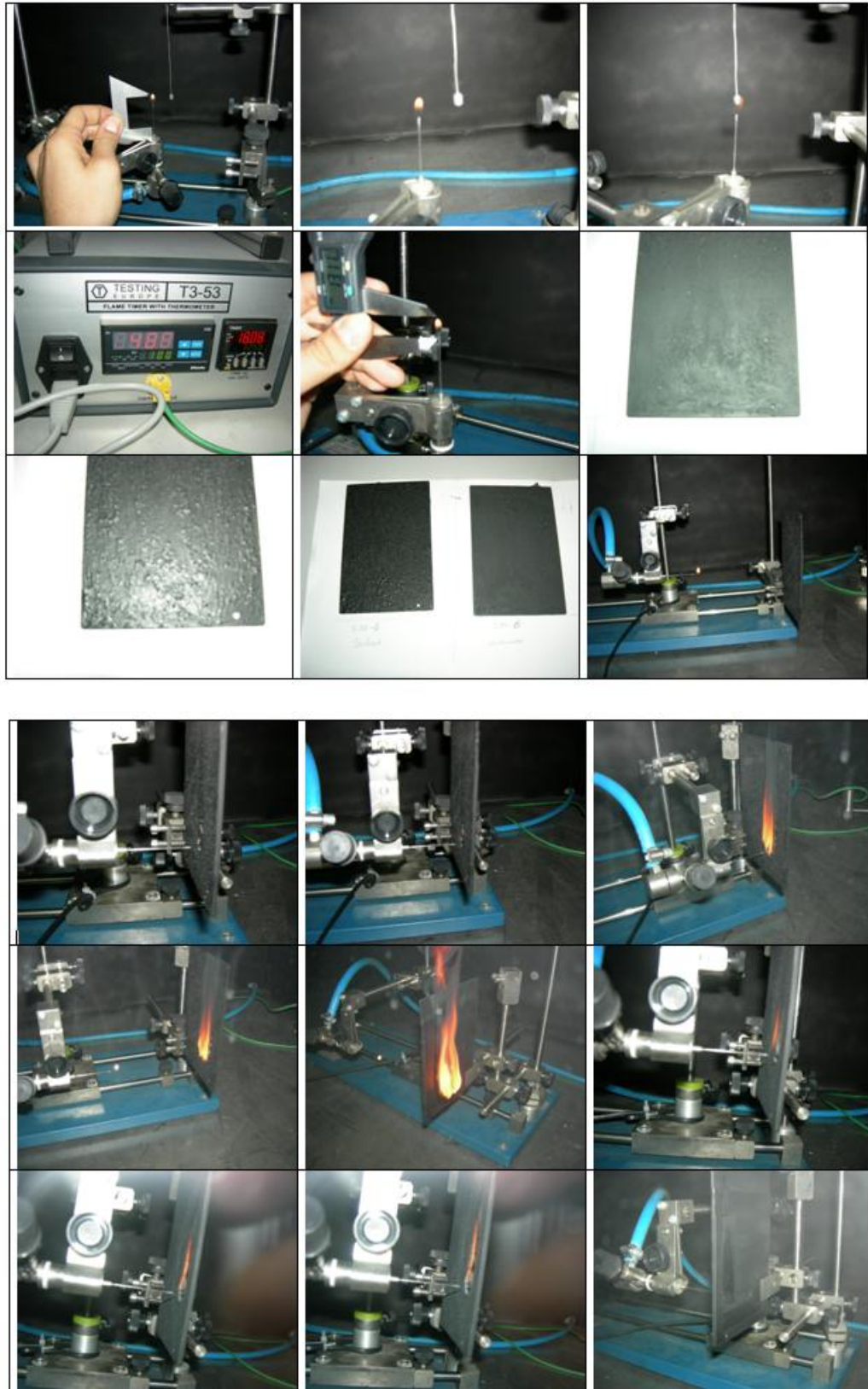


Figure 4.31 Flame retardant time values of the composite coatings on plastic substrates.

In addition to these, candle flame test results of 50% normal and 50% ground antimony oxide-huntite/hydromagnesite binary reinforced polymeric composite painted plastic samples are given in Figure 4.29. Furthermore, Figure 4.30 presents candle flame test results of 5% normal, 5% ground antimony-huntite/hydromagnesite binary reinforced polymeric composite painted plastic samples. Generally speaking, when the amounts of boric acid and antimony oxide were increased in huntite/hydromagnesite reinforced polymeric composite coatings, their flame retardant properties strongly improved as shown in the mentioned figures in details. What expected by using flame retardant in the paints as a binary system is to provide outstanding properties. The synergistic beneficial effects were obtained with binary flame retardant additives in the composite coatings.

Table 4.5 The comparison of flame retardant time values among huntite/ hydromagnesite one component and boric acid-hutite/hydromagnesite and antimony oxide-huntite/hydromagnesite binary component reinforced composite coatings on plastic substrates

Materials	Sample name	Flash over	After flame	Results
Pure dye coating	V00	110 sec	>180 sec	NOK
One componet huntite/hydromagnesite	VS 15-25	100 sec	>180 sec	NOK
	VS 15-50	120 sec	>180 sec	NOK
	VS 15-65	120 sec	>180 sec	NOK
	VS 30-25	180 sec	>180 sec	NOK
	VS 30-50	180 sec	>180 sec	NOK
Binary component boric acid- huntite/hydromagnesite	B50-Ö	170 sec	240 sec	OK
Binary component antimony oxide- huntite/hydromagnesite	A50-Ö	140 sec	200 sec	OK

As well as the improved flame retardant properties, the time can be indicated as another characteristic parameter. In Table 4.5, flame retardant time values of the huntite/hydromagnesite, boric acid-huntite/hydromagnesite and antimony oxide-huntite/hydromagnesite reinforced composite coatings are given in details after the tests. It can be seen from Table 4.5 that all reinforcement additives such as

huntite/hydromagnesite, boric acid and antimony oxide increase the flame retardancy properties of the coatings as just stated. Pure dye and one component huntite/hydromagnesite reinforcement composite coatings are not enough to assess their flame retardant times. Even if the huntite/hydromagnesite reinforcement composite coating is flame retardant, it is not sufficient as a time factor. Due to this reality, it is required to be incorporated into the composite coatings as new flame retardants such as boric acid and antimony oxide. It is important that these requirements should be satisfied to be able to select the suitable flame retardant configuration. Besides, boric acid is much more efficient to improve the flame retardancy property of the composite comparing with antimony oxide.

4.2.2.2.5. Surface Profilometer. Figure 4.32 depicts the surface roughness profiles of the composite coatings on plastic substrate. The optimum samples were boric acid-huntite/hydromagnesite and antimony oxide-huntite/hydromagnesite binary component reinforced composite coatings on plastic substrates. An understanding of the surface roughness is critical to the efficient design of the composite paints. The smooth surfaces are desirable in all paints. It can be seen that the surfaces can be considered to be rough. In this context, average surface roughness values were determined to be in the range of 100 μm and 150 μm in all the coating specimens. This might be due to blending much different kind of mineral particles to a liquid matrix and also manual coating. These can be improved by using spray method. More importantly, it should be noticed that there exists a beneficial effect in the samples produced by grinding the flame retardant powders.

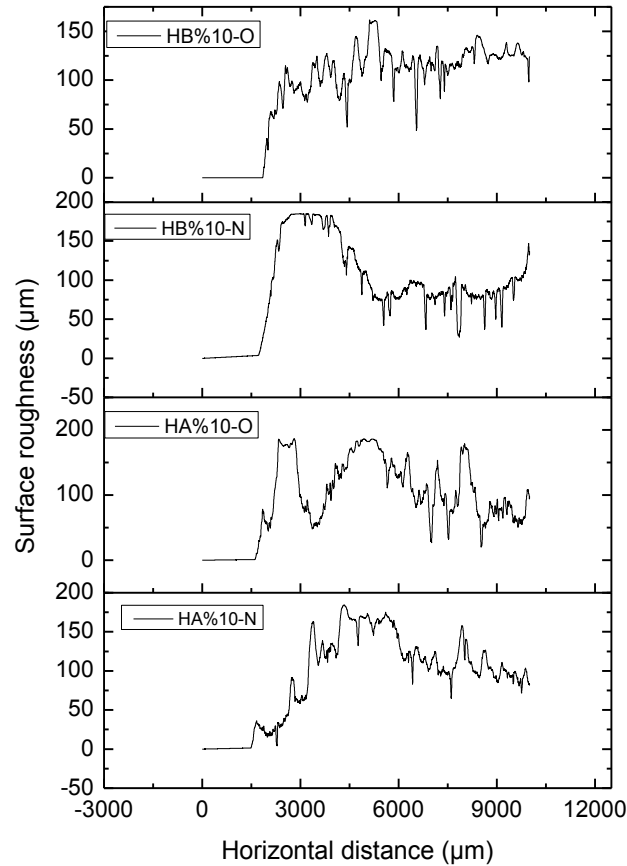


Figure 4.32 Surface roughness profiles of the composite coatings such as (a) normal (HA%10N) and (b) ground antimony oxide-huntite/hydromagnesite (HA10 \ddot{O}), (c) normal (HB%10N) and (d) ground (HB%10 \ddot{O}) boric acid-huntite/hydromagnesite reinforced materials.

4.3 Barium Hexaferrite Reinforced Composite Coatings

Inasmuch as barium hexaferrite were used as radar absorbing materials, powders and composite coatings/paints were characterized before and after deposition process. The structural, microstructural, magnetic and radar absorbing properties of the composite/paints were evaluated in this section. In this context, this section was divided to two parts as powder and coating characteristics.

4.3.1 Powder Characteristics

Since the main radar absorbing material is barium hexaferrite powder, its properties were evaluated before coating process. The powders were characterized by XRD and SEM.

4.3.1.1 Phase Analysis

Figure 4.33 clarifies XRD pattern of barium hexaferrite ($\text{BaFe}_{12}\text{O}_{19}$) powders produced by sol-gel process. The presence of barium ferrite phase as a major phase and also a little amount of iron oxide (Fe_2O_3) as a minor phase are observed in the powders. This result is enough to obtain its radar absorbing properties. It is anticipated that any amorphous phase is not indicated from the XRD pattern.

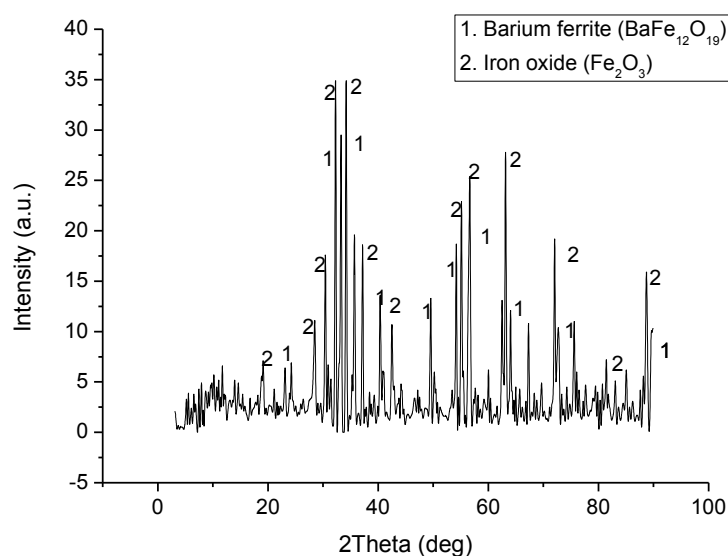


Figure 4.33 XRD pattern of $\text{BaFe}_{12}\text{O}_{19}$ powders produced by sol-gel process .

The similar results can be found elsewhere (Mali, 2004) that the reaction was sufficient for complete conversion of the metal compounds to metal oxides. This may be a result of high enough sintering temperature e.g. 1000 °C. On the other hand, as

increasing of heat leads to particle growth, it needs to be decided an optimum sintering temperature. The observed narrow diffraction peaks may give rise though an increase in the crystallite size (Mali, 2004, Mozaffari, 2009).

4.3.1.2 SEM Analysis

Figure 4.34 depicts an SEM image of $\text{BaFe}_{12}\text{O}_{19}$ powders produced by sol-gel process. The micrograph of the $\text{BaFe}_{12}\text{O}_{19}$ powders is illustrated the powders with platelet microstructure (Akşit, 2009, Mozaffari 2009) whose is a general characteristic. The size and thickness of the powders are approximately 5 μm and 0.2-0.5 μm , respectively. The platelet characteristic influences radar absorbing properties.

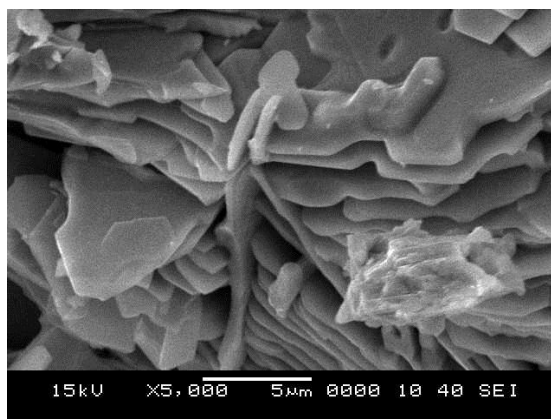


Figure 4.34 SEM micrograph of $\text{BaFe}_{12}\text{O}_{19}$ powders produced by sol-gel process.

4.3.2 Coating Characteristics

Barium hexaferrite reinforced composite coatings/paints were characterized after deposition process. In this scope of the present study, experimental results were given from structural, microstructural, magnetic and radar absorbing properties of the composite/paints.

4.3.2.1 FTIR Analysis

Figure 4.35 shows FTIR spectra of 0%, 5%, 10% and 20% BaFe₁₂O₁₉ reinforced epoxy composite coatings. The analysis was carried out in 500- 4000 cm⁻¹ band range. Note that the characteristic peaks of epoxy indicate the formation of Si-O, Si-O-Si and Si-C at 793, 1084 and 1170 cm⁻¹ respectively. These results can also be seen in a report of Castillo (2011). The observed peaks at 1450 cm⁻¹ can correspond to C-H bending and at 2900 cm⁻¹ to alkyl groups (-CH₃ and -CH₂) stretching. We have a good agreement with Ref. (Lin, 2006).

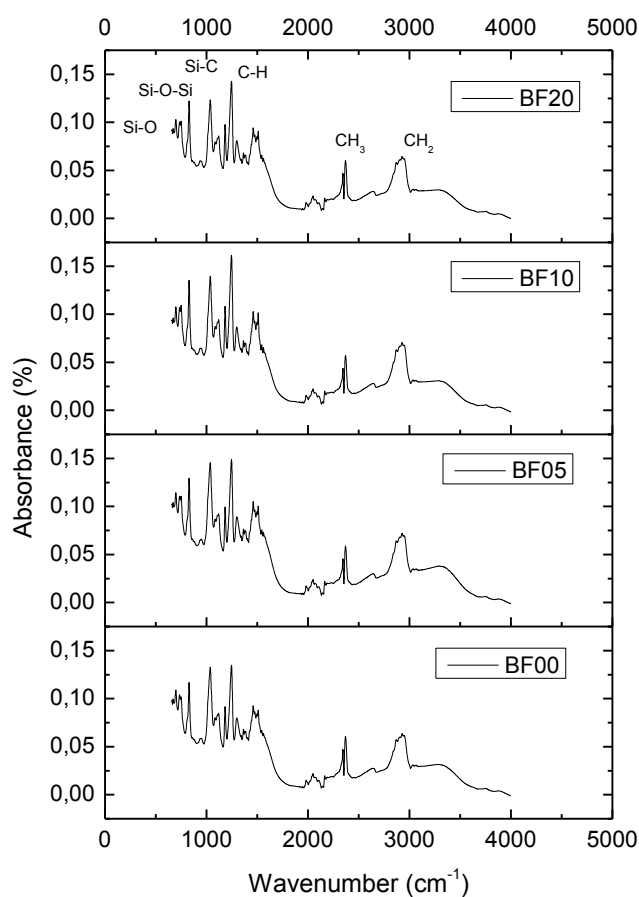


Figure 4.35. FTIR spectra of BaFe₁₂O₁₉ reinforced polymeric composite coatings/paints

It can be seen that by adding BaFe₁₂O₁₉ powders (from 0 wt.% to 20 wt.%) to the dye, there was no any significant change in the structure. Since the reinforced barium hexaferrite or ferrite particles may set in the gaps between the polymer chains, there is no any change in the intensity of organic bonds (FTIR shows only organic bond intensities). Therefore the results indicated that there was not any interaction between polymer chains and ferrite or barium hexaferrite particles (Li, 2007).

4.3.2.2 SEM-EDS Analysis

Figure 4.36 denotes SEM micrographs of 0 wt.%, 10 wt.% and 20 wt.% BaFe₁₂O₁₉ reinforced polymer composite coatings. The powders were incorporated into the coatings and it appeared as smooth and rough surfaces which could be visualized when the powder content increases. More importantly, a slight agglomeration was also observed, which is due to the high surface energy and the magnetic interactions of the nanoparticles (Li, 2008).

Upon increasing BaFe₁₂O₁₉ content in the composite coatings, the microstructure of the material varied regularly. It makes it possible to gradually increase radar absorbing performance of BaFe₁₂O₁₉ reinforced polymer composite coatings. For this reason, homogeneous mixture of BaFe₁₂O₁₉ powder is a significant issue in polymer composite coatings. In principle, this manner is the key feature of paint system.

Figure 4.37 shows EDS results of pure paint and 20 wt.% BaFe₁₂O₁₉ reinforced polymer composite coatings. It can be easily seen from EDS spectra that although there do not exist Ba and Fe elements in the pure dye coating, Ba and Fe elements appeared with increasing BaFe₁₂O₁₉ amount in the structure. Note that C peak with intensity was observed in the both composite coatings in terms of paint structure.

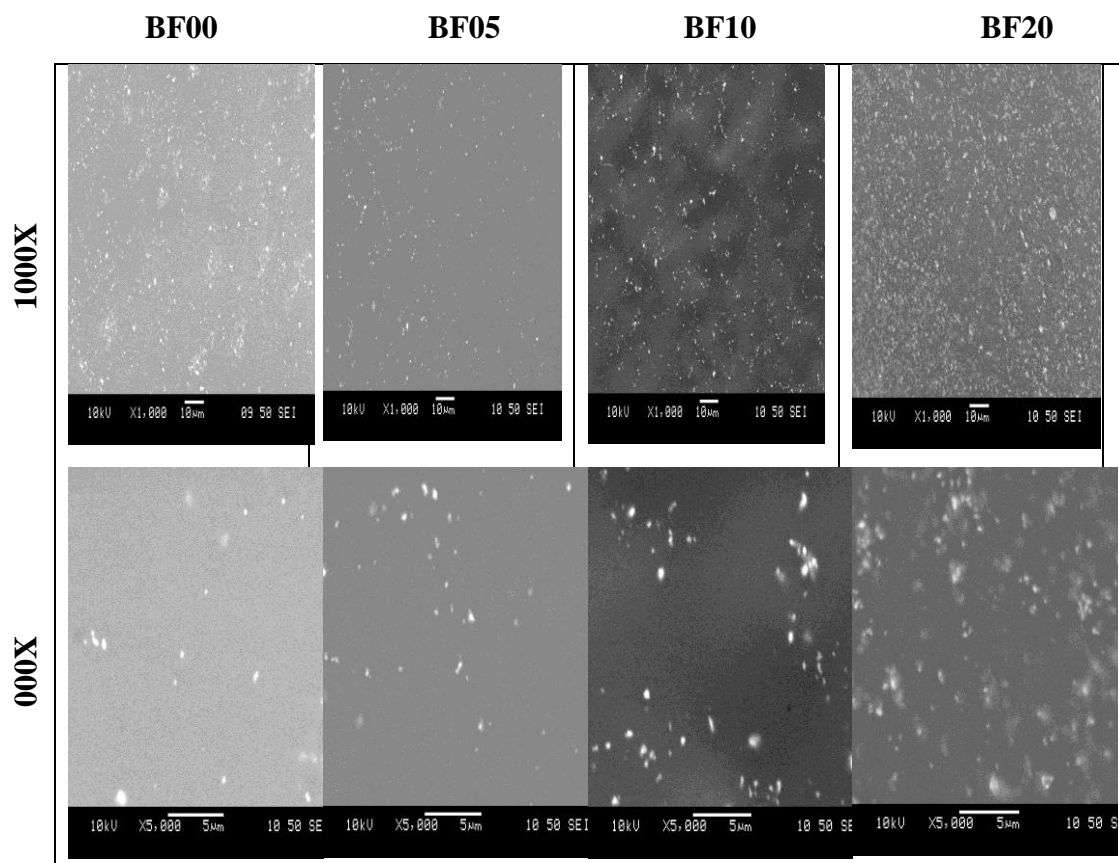
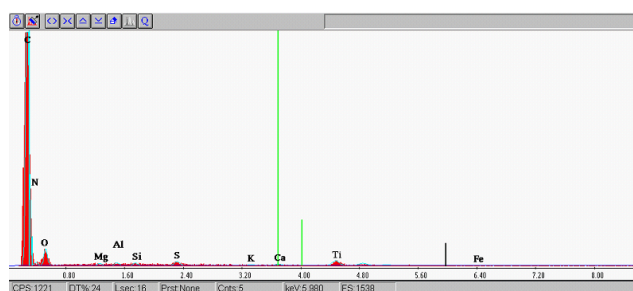
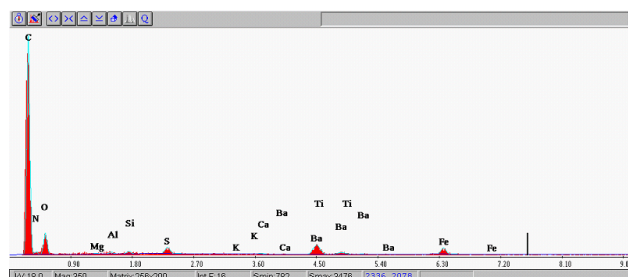


Figure 4.36 SEM micrographs of BaFe₁₂O₁₉ reinforced polymeric composite coatings/paints depending on BaFe₁₂O₁₉ content in the structure at different magnifications; X1000 and X5000.



(a)



(b)

Figure 4.37. EDS spectra of (a) pure dye and (b) 20 wt.% BaFe₁₂O₁₉ reinforced composite coatings

4.3.2.3 Magnetic Properties

The magnetization (M) as a function of the applied magnetic field (H) for pure epoxy dye and 0 wt. %, 5 wt.%, 10 wt.%, 20 wt.% $\text{BaFe}_{12}\text{O}_{19}$ reinforced composite coatings at room temperature are shown in Figure 4.38. It is worth noting that well-defined hysteresis loops are observed for all samples except for pure dye coating. Magnetic saturation (M_s) and coercivity (H_c) are 32.959×10^{-3} Emu and 1813.7 G respectively for 20 wt.% $\text{BaFe}_{12}\text{O}_{19}$ reinforced composite coatings (BF20). It can be seen from Figure 4.38 that the saturated magnetization values increased by increasing $\text{BaFe}_{12}\text{O}_{19}$ powders quantity in the composite coatings. This may be due to the existence of nonmagnetic epoxy and the interaction between magnetic nanoparticles and the nonmagnetic medium, which contributes to the magnetic anisotropy by the means of dipole–dipole interactions. For the epoxy–barium ferrite composite system, with the decrease of the surface anisotropy upon coating and the increase of the interparticle distances which will lead to weakening interparticle interaction, the decreases in coercivity and M_s are expected (Li, 2008).

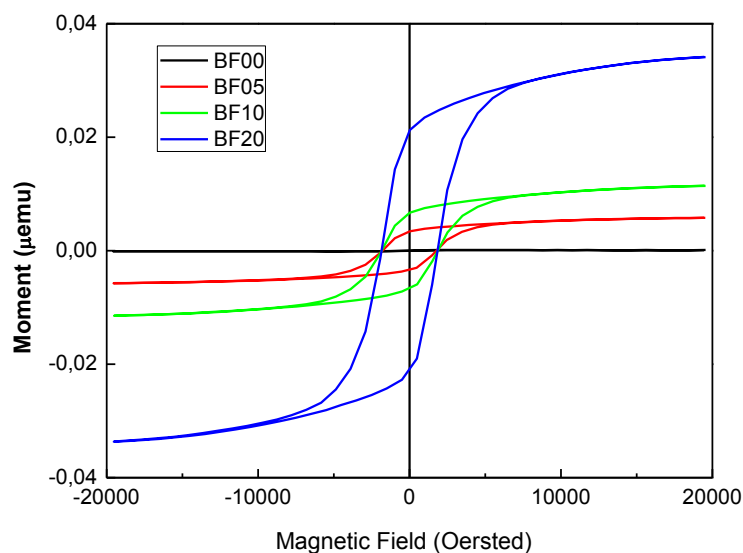


Figure 4.38 The hysteresis curves of $\text{BaFe}_{12}\text{O}_{19}$ reinforced polymeric composite coatings/paints

4.3.2.4 Radar Absorbing Behaviour

Figure 4.39 depicts microwave absorption characteristics of the pure epoxy coating and 0 wt. %, 5 wt.%, 10 wt.%, 20 wt.% BaFe₁₂O₁₉ reinforced composite coatings. Figure 4.39.b shows radar absorbing characteristics of all samples. However, as absorber is omitted in Figure 4.39.b, radar absorbing values of the composite coatings can be seen in detail. It is clear to see in Figure 4.39 that there was no any radar absorbing activity in pure epoxy coating. Whereas, BaFe₁₂O₁₉ reinforced composite coating has a significant absorbing activities. The radar waves absorbing properties of composites were substantially improved after the addition of barium hexaferrite particles; absorbing percentage increases with increasing additive content in the composite coatings (Singh, 1999). The highest absorbing peak reaches 12.13% at 11.86 GHz with the sample of BF20.

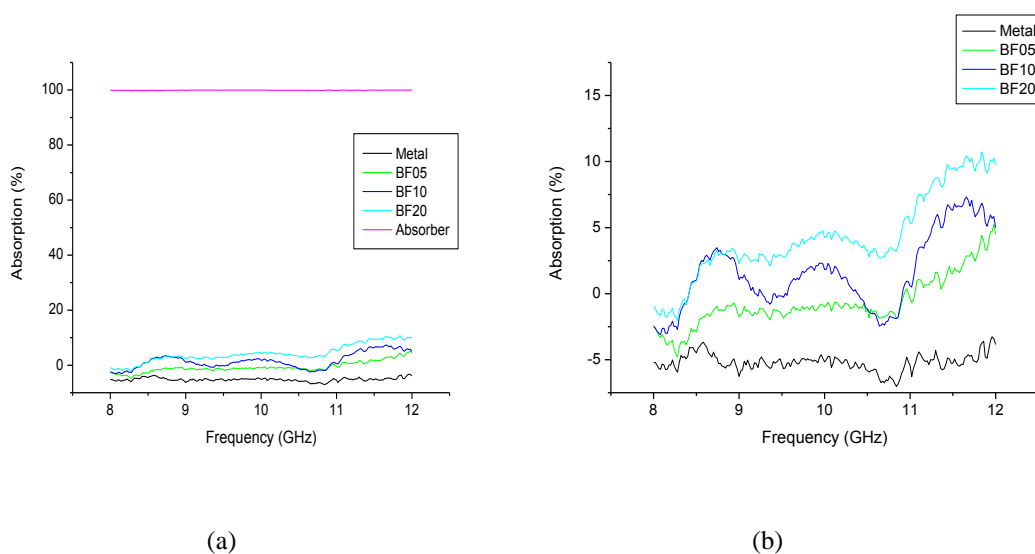


Figure 4.39 The absorption values (%) versus the frequency range of 8–12 GHz of the radar absorbing composite coated samples (a) all samples and (b) absorber omitted.

As mentioned above, BaFe₁₂O₁₉ has large magneto crystalline anisotropy. Due to the spin orientations of the Fe³⁺ ions, the numbers of unpaired electrons are occurred in their 4s and 3d shells. Those not fully filled shells lead to magnetic moment. On the other hand, the magnetic moments of barium hexaferrite particles are related with not only the unpaired electrons but even though angular momentum which represents the product of the body's rotational inertia and rotational velocity. These unique

characteristics enhance largely the microwave absorption performance of barium hexaferrite reinforced composites. The same manner can be seen in a report of Sun, Gao, Li and Wu (2011).

4.4 Chitosan Added Composite Coatings

Due to the fact that chitosan is used as self-healing materials, colloidal and composite coatings/paints were characterized before and after the deposition process as explained in other composite coatings. The structural, microstructural, self-healing properties of the composite/paints were evaluated in this section. Also here, this section was divided into two parts as colloid and coating characteristics.

4.4.1 Colloid Characteristics

Colloid is any substance consisting of particles substantially larger than atoms or ordinary molecules but too small to be visible to the unaided eye; more broadly, any substance, including thin films and fibres, having at least one dimension in this general size range, which encompasses about 10^{-7} to 10^{-3} cm (Colloid, 2012). The colloidal system consists of two separate phases: a dispersed phase (or internal phase) which is chitosan molecules in this study and a continuous phase (or dispersion medium) which is acid solution in which the colloid is dispersed. The colloids were obtained as irreversible and they were indicated as translucent, this may be because of the Tyndall effect, which is the scattering of light by particles in the colloid (Scattering, 2012). The gel network stabilization was obtained against sedimentation or flocculation.

4.4.2 Coating Characteristics

Chitosan added composite coatings/paints were characterized after the deposition process. In this section of the study, experimental results were explained as FTIR,

SEM-EDS analysis, self-healing and antibacterial properties of the composite/paints on the glass substrates.

4.4.2.1 FTIR Analysis

Figure 4.40 shows FTIR analysis results of the chitosan added composite coatings/paints. It is obviously clear from Figure 4.40 that chitosan exhibits main characteristic bands of carbonyl (C=O-NHR) and amine group (-NH_2) at 1450 cm^{-1} . However this band can correspond to C-H bending from epoxy matrix.

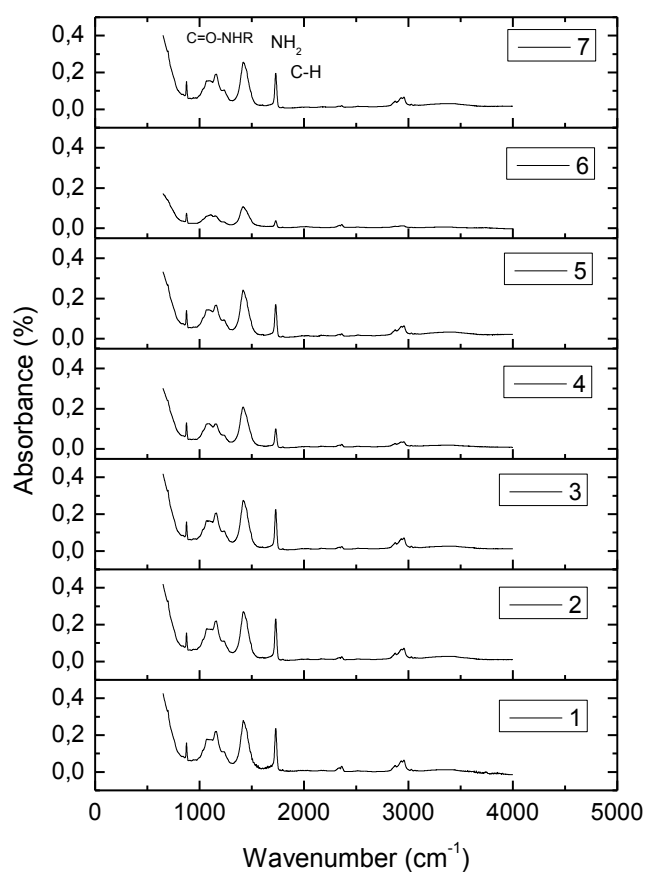


Figure 4.40 FTIR analysis results of the the chitosan added composite coatings/paints with chitosan content as given in Table 3.7.

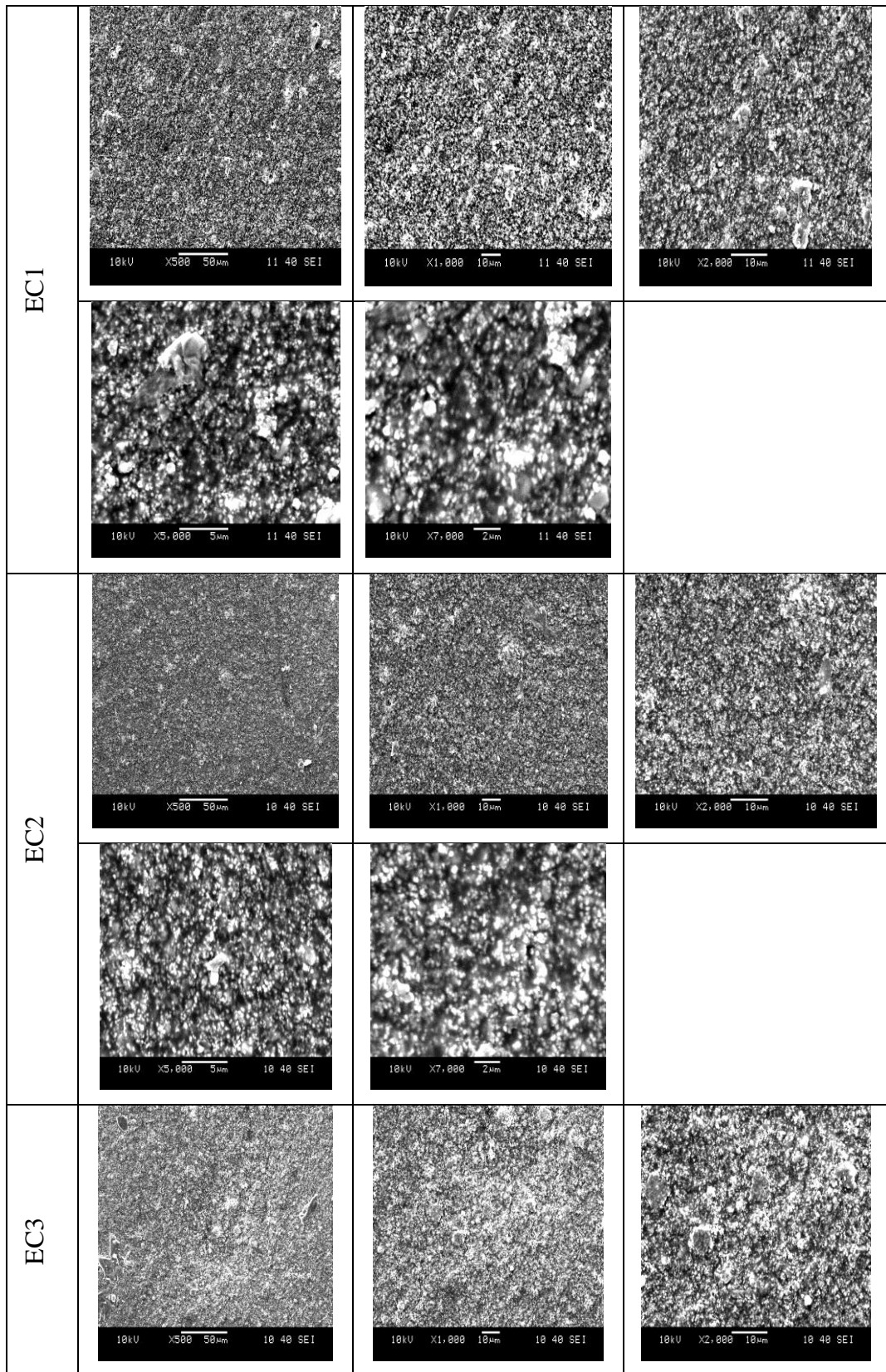
In the same way, CH_3COH group band can be observed at 748 cm^{-1} related with the chitosan but this may come from the epoxy also, because the characteristic peaks of epoxy indicate the formation of Si-O, Si-O-Si and Si-C at 751 , 1084 and 1270 cm^{-1} respectively. The broad band due to the stretching vibration of $-\text{NH}_2$ and $-\text{OH}$ group from chitosan can be observed at 2950 cm^{-1} but it may be related with epoxy alkyl groups ($-\text{CH}_3$ and $-\text{CH}_2$) stretching (Boonsongrit, Mueller, Mitrevej, 2008 and Osman, Arof, 2003).

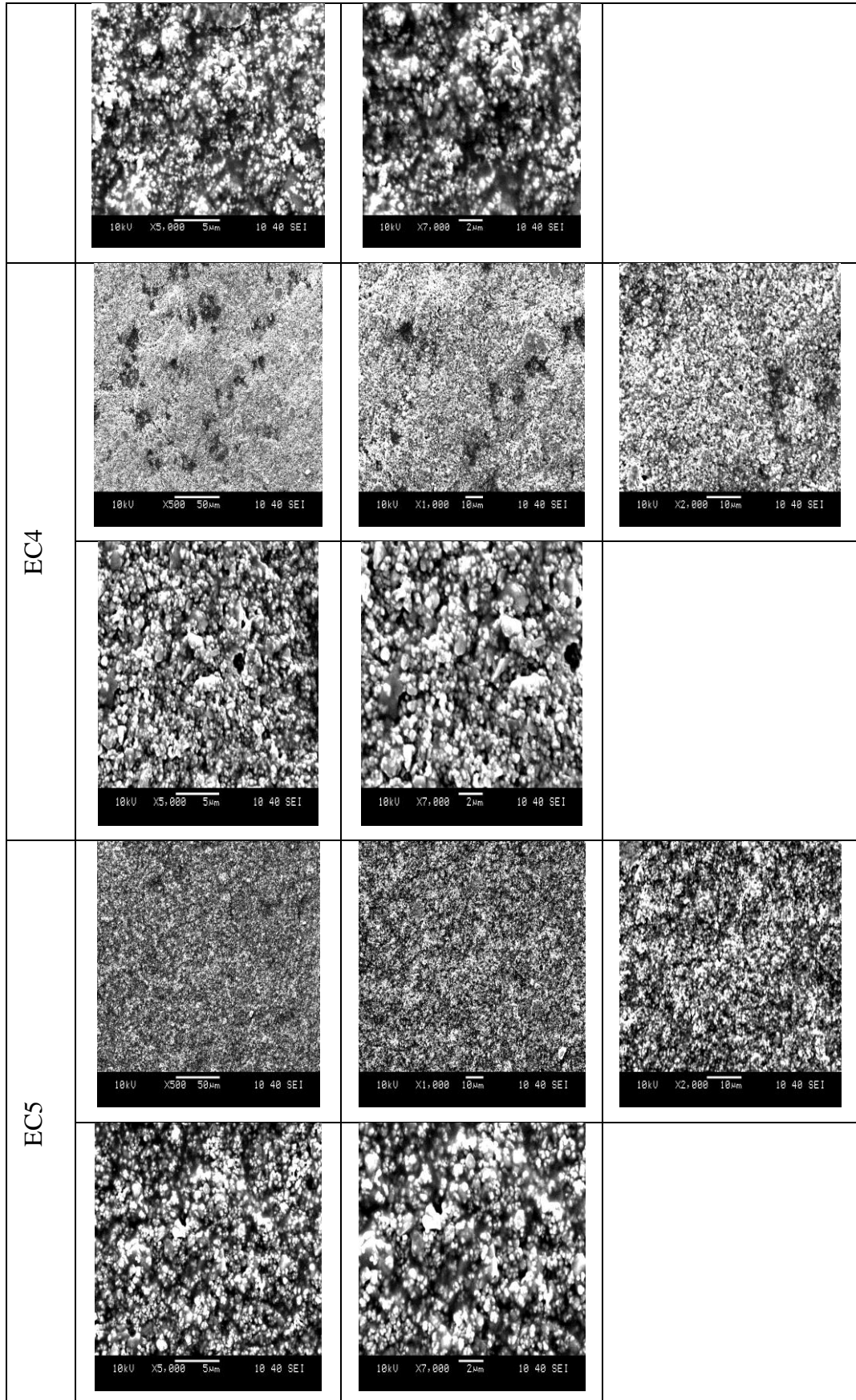
Since both chitosan and epoxy are polymers, they have organic bands. As epoxy dye is formed by different materials and having different bands, some of its bands can overlap with chitosan bands in the FTIR analysis. Therefore, sometimes it can be difficult to separate the peaks and their corresponding bands.

4.4.2.2 SEM-EDS Analysis

Figure 4.41 denotes SEM micrographs of chitosan added epoxy dye composite coatings. Chitosan were incorporated into the composite coatings in different concentrations including samples of EC1 (0.0005 %), EC2 (0.0049 %), EC3 (0.0237 %), EC4 (0.0452 %), EC5 (0.0119 %), EC6 (0.0019 %) and EC7 (0 % - pure). Generally homogeneous composites with smooth surfaces were produced with mixture of chitosan and epoxy dye. It can be seen from the figure that the sample 4 has not got a good surface compared with other coatings. The reason may be that that the sample EC4 has 0.0452 % chitosan in dye composite as a maximum percentage used in the experiment. Therefore, it can be stated out that 0.0452 % of quantity is too much for chitosan to use as an additive in the dye. To decide the exact value, it needs to be checked out the self healing test results.

On the other hand, as it was mentioned earlier, two different rate acid solutions were used for taking into account that different acid rates lead to different dissolution for chitosan. Acid rate is 3% for sample EC5 and 1% for sample EC6, the chitosan quantity were the same as 0.0119 %. As it can be seen from the Figure 4.41 that there is no any difference between the surfaces of samples of EC5 and EC6.





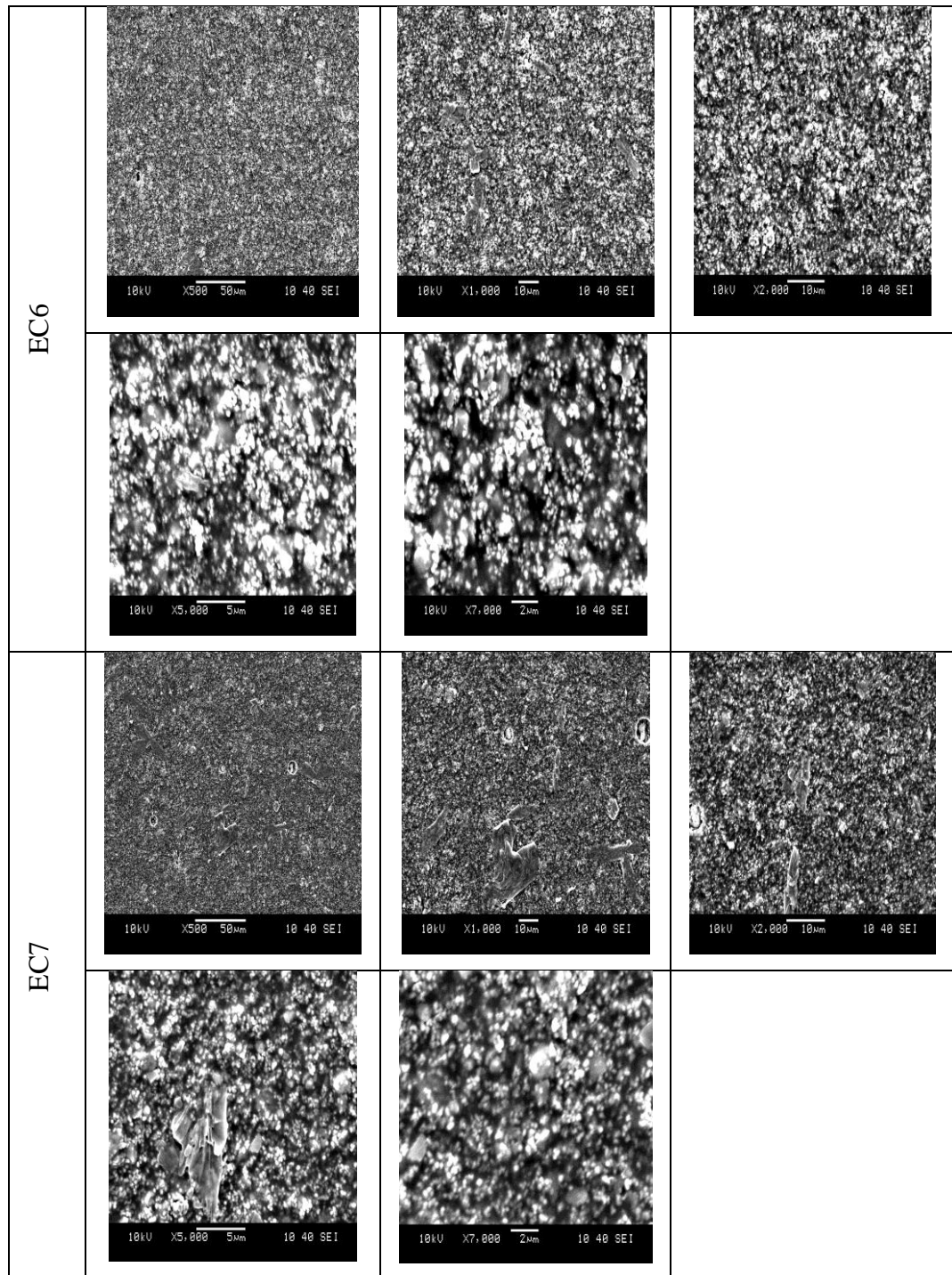
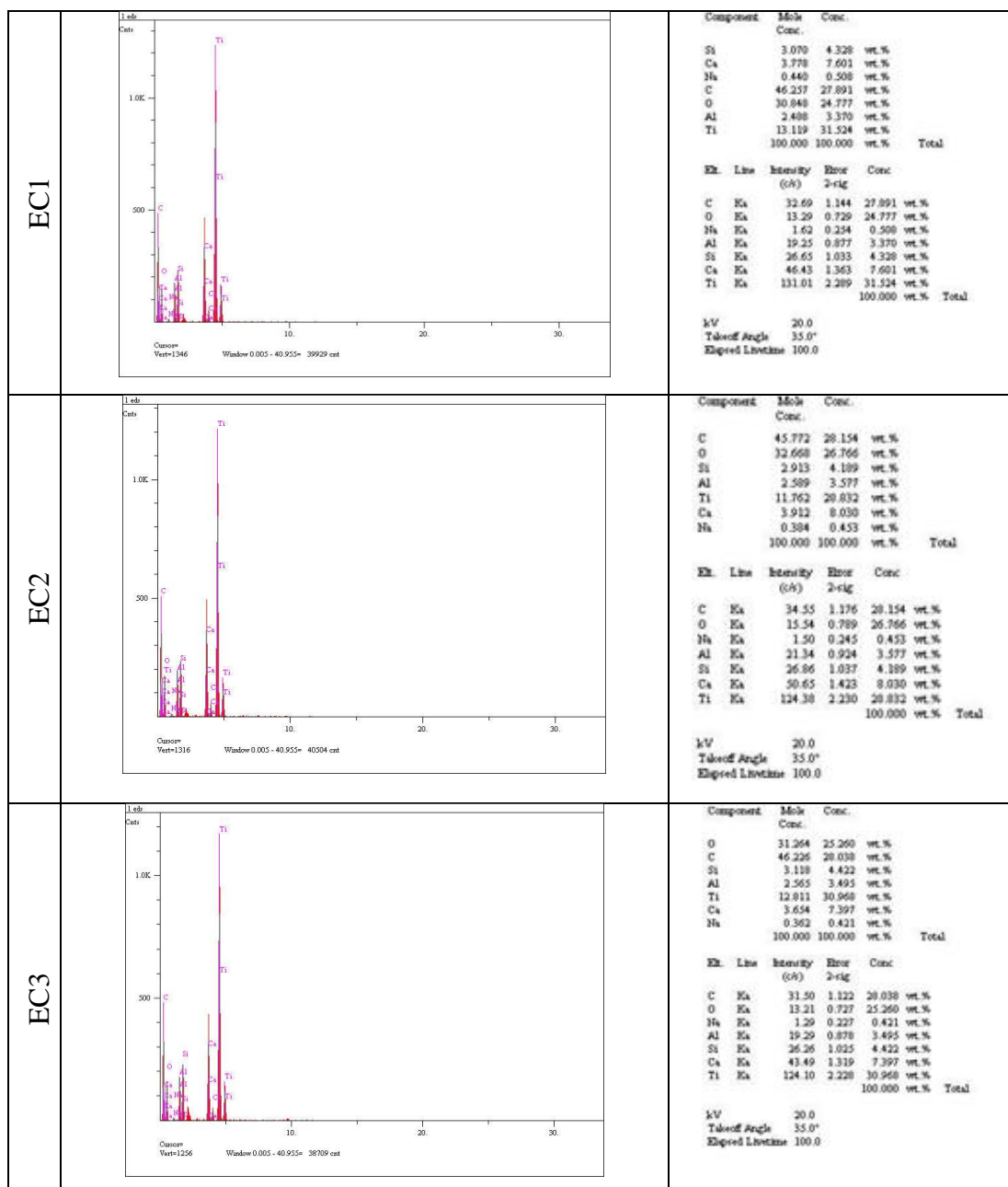


Figure 4.41. SEM micrographs of chitosan added composite coatings at different magnifications (X500, X1000, X2000, X5000 and X7000). The samples are coded as EC1, EC2, EC3, EC4, EC5, EC6 and EC7 according to chitosan contents 0.0005 %, 0.0049 %, 0.0237 %, 0.0452 %, 0.0119 %, 0.0019 % and 0 % chitosan respectively.

Figure 4.42 demonstrates EDS analysis of chitosan reinforced epoxy composite coatings. It can be seen from the figure that EDS results are similar for all coatings.

Chitosan and epoxy dye material both have polymer structure. The both materials were blended with different concentrations to produce the composite coatings. Thus all samples have the same elements with different quantity. From these results, Si, Ca, Na, C, Al, Ti and O elements were found from all samples. Because of this reason, it is normal to obtain similar EDS results from all samples.



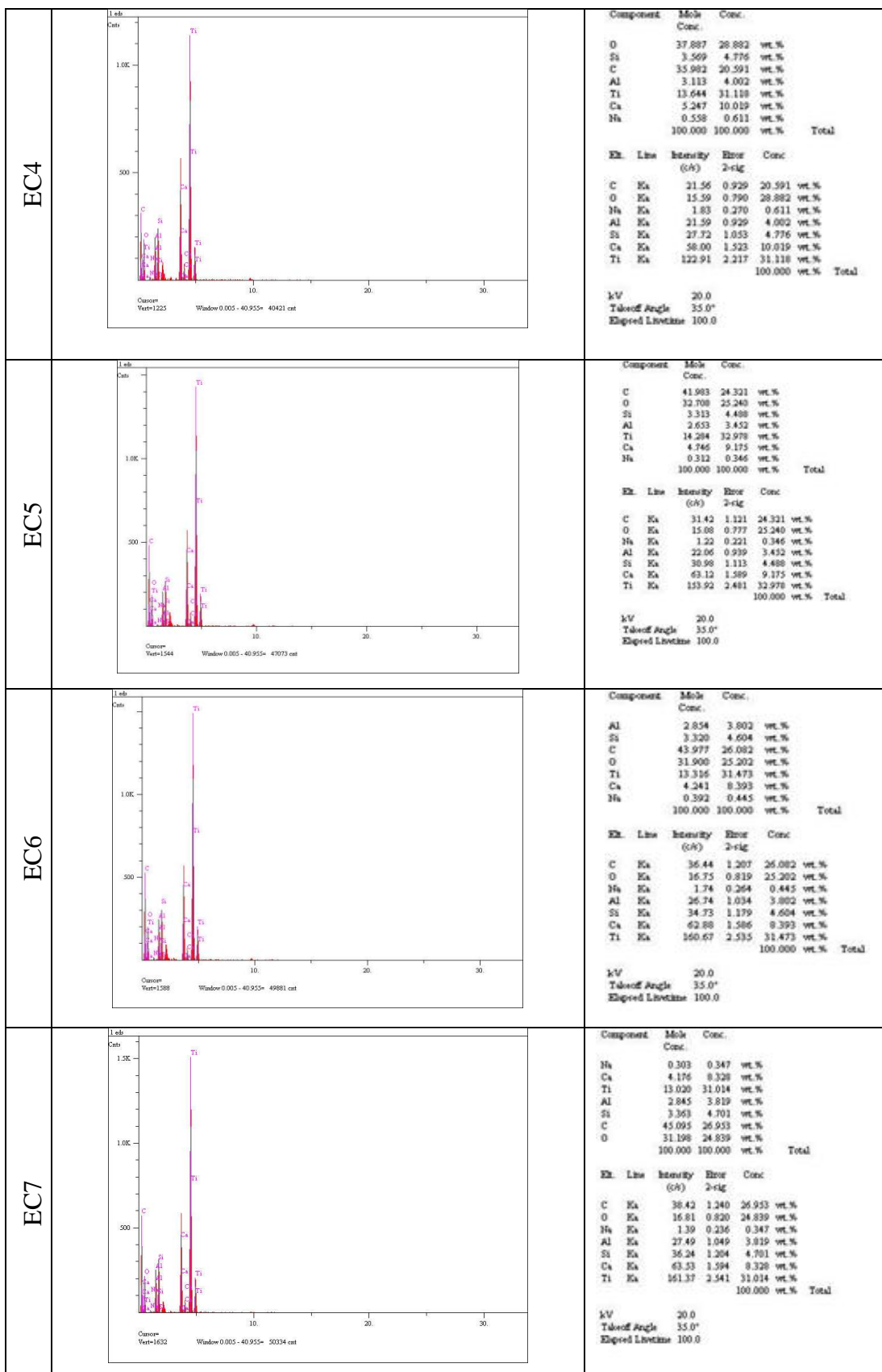


Figure 4.42 EDS analysis of chitosan added epoxy composite coatings

4.4.2.3 Self Healing Property

SEM micrographs of chitosan added epoxy composite coatings after scratch testing were given in Figures 4.43, 4.44, 4.45, 4.46, 4.47, 4.48 and 4.49. After scratch tests of the chitosan added composite coatings were performed, the SEM micrographs were taken after 1st, 8th, 20th and 35th days in order to see how to change their self healing properties.

Generally from all figures, self healing property can be determined as like putting forth branches like a tree, splits/caves are packed with the composite. It can be seen from Figure 4.43 that it can not be mentioned any self healing in sample EC7, as chitosan rate is 0 %. Except for sample EC7, all samples have dissolved chitosan and there are healing activities at all of them. Therefore it can be pointed out that chitosan's self healing effect appeared clearly.

In order to try to find self healing mechanism of chitosan and working principles of self healing, it needs to look at SEM micrographs again. Although the distinctions on the splits were measured and written on the micrographs, the self healing can not be determined according to those values.

As mentioned above, branches were developed like arms for a wound the heal. That is to say that self healing mechanism might be operated with those branches. For the comparing the samples by means of self healing, no need to measure the distances on the top of the splits, but it needs to look the branches numbers, shapes, orders or thicknesses of them.

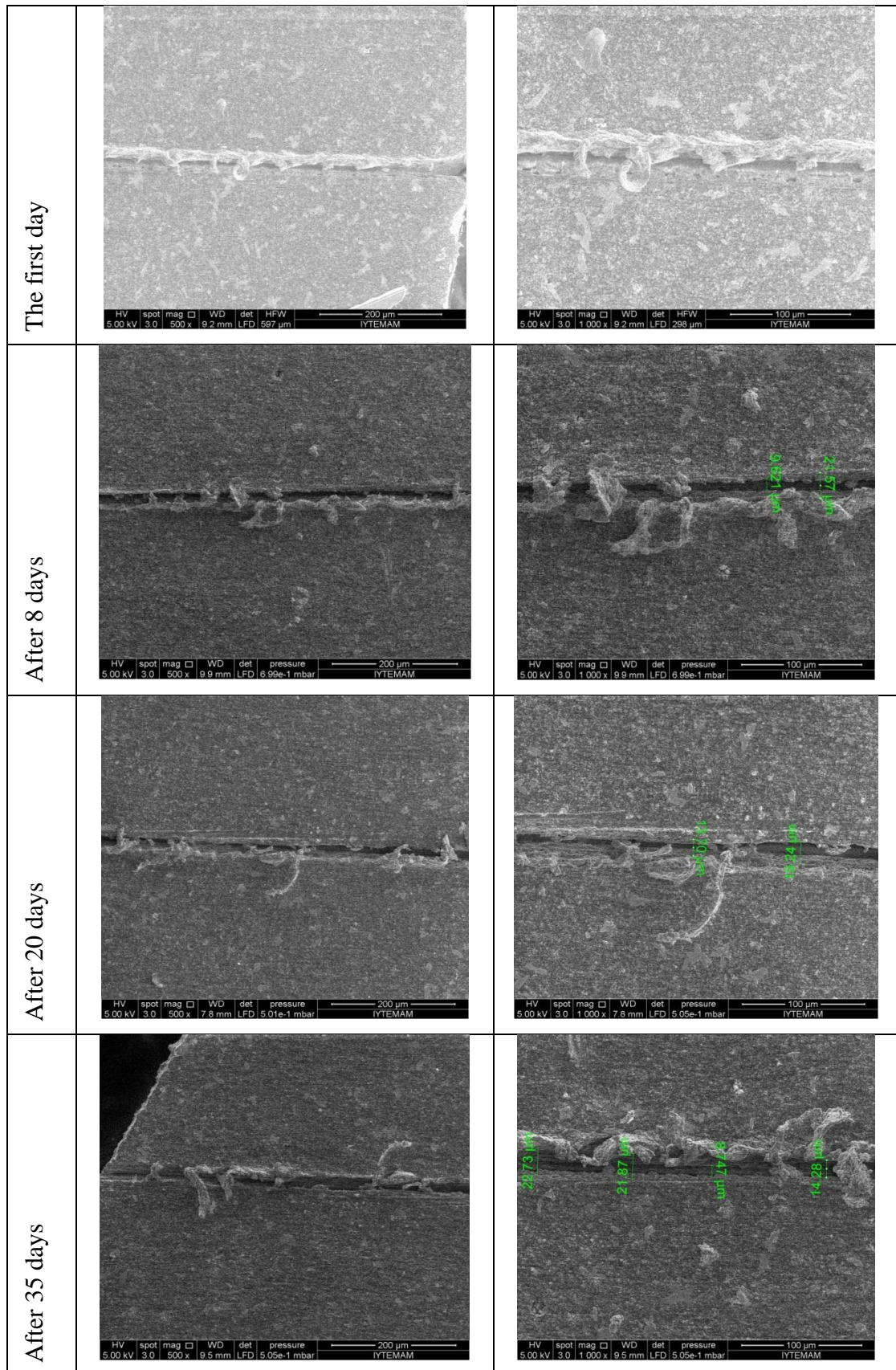


Figure 4.43 SEM micrographs of sample of EC1 0.0005 % chitosan added epoxy composite coatings after scratch testing

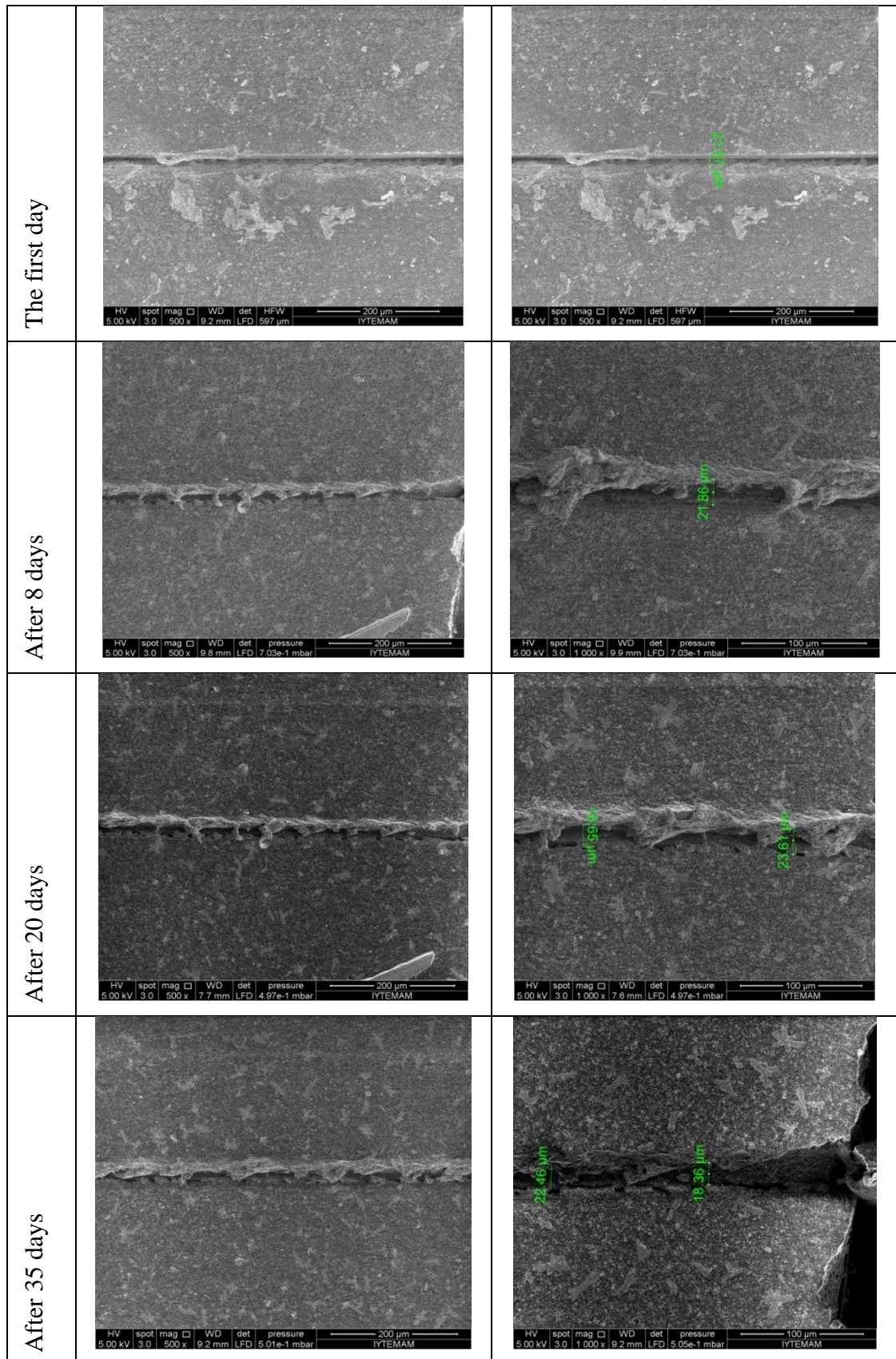


Figure 4.44 SEM micrographs of sample of EC2 0.0049 % chitosan added epoxy composite coatings after scratch testing

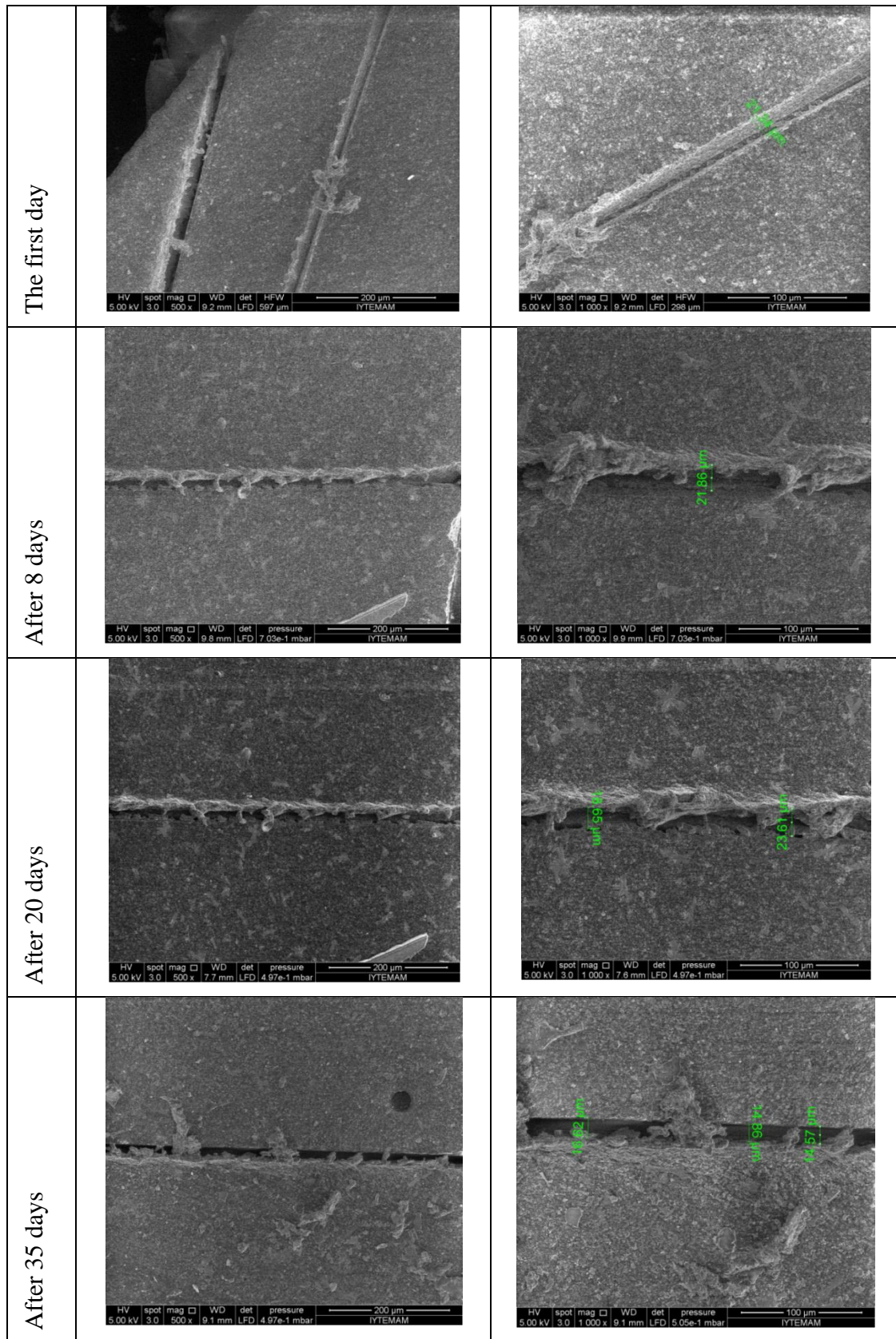


Figure 4.45 SEM micrographs of sample of EC3 0.00237 % chitosan added epoxy composite coatings after scratch testing

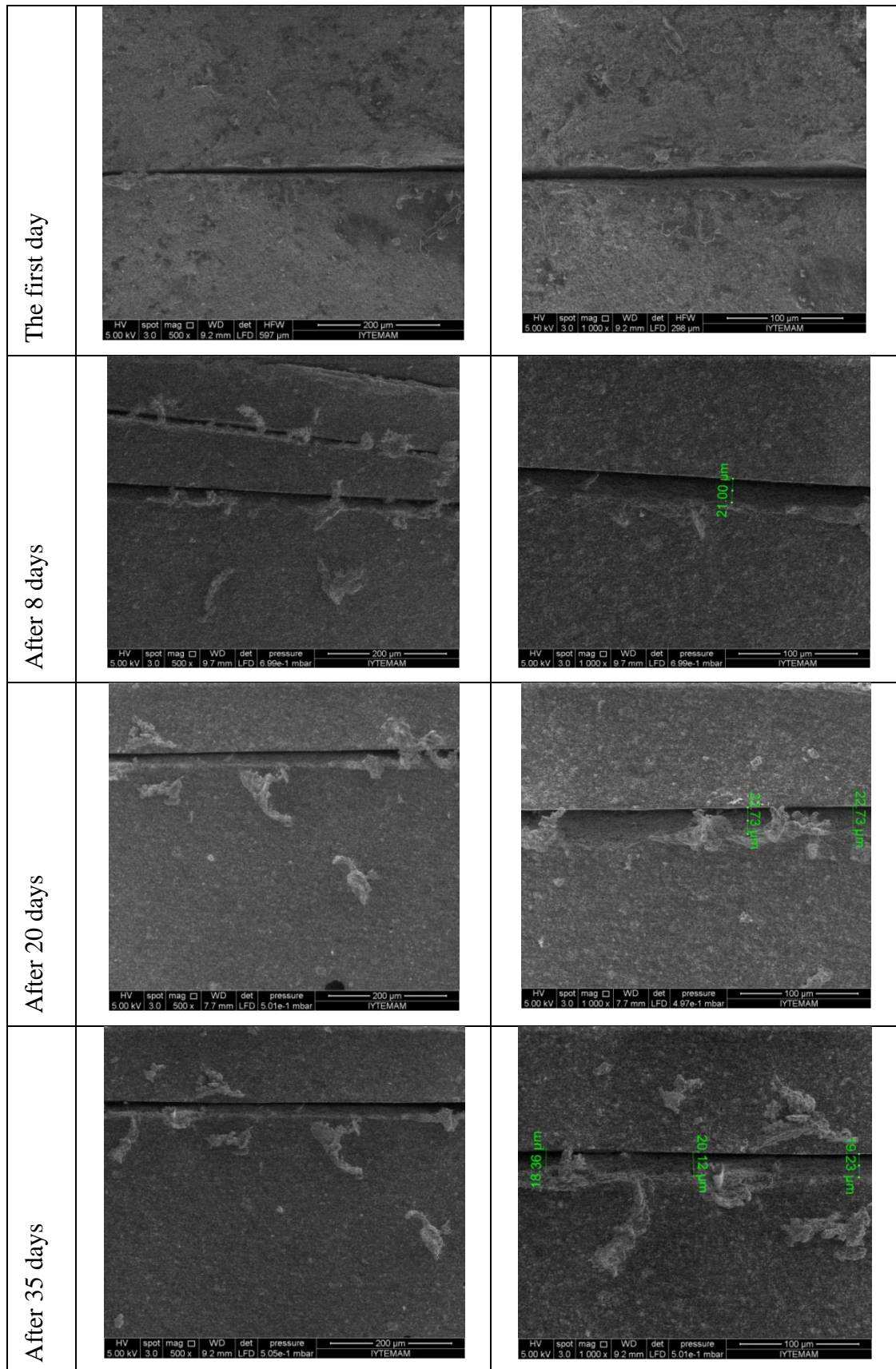


Figure 4.46 SEM micrographs of sample of EC4 0.00452 % chitosan added epoxy composite coatings after scratch testing

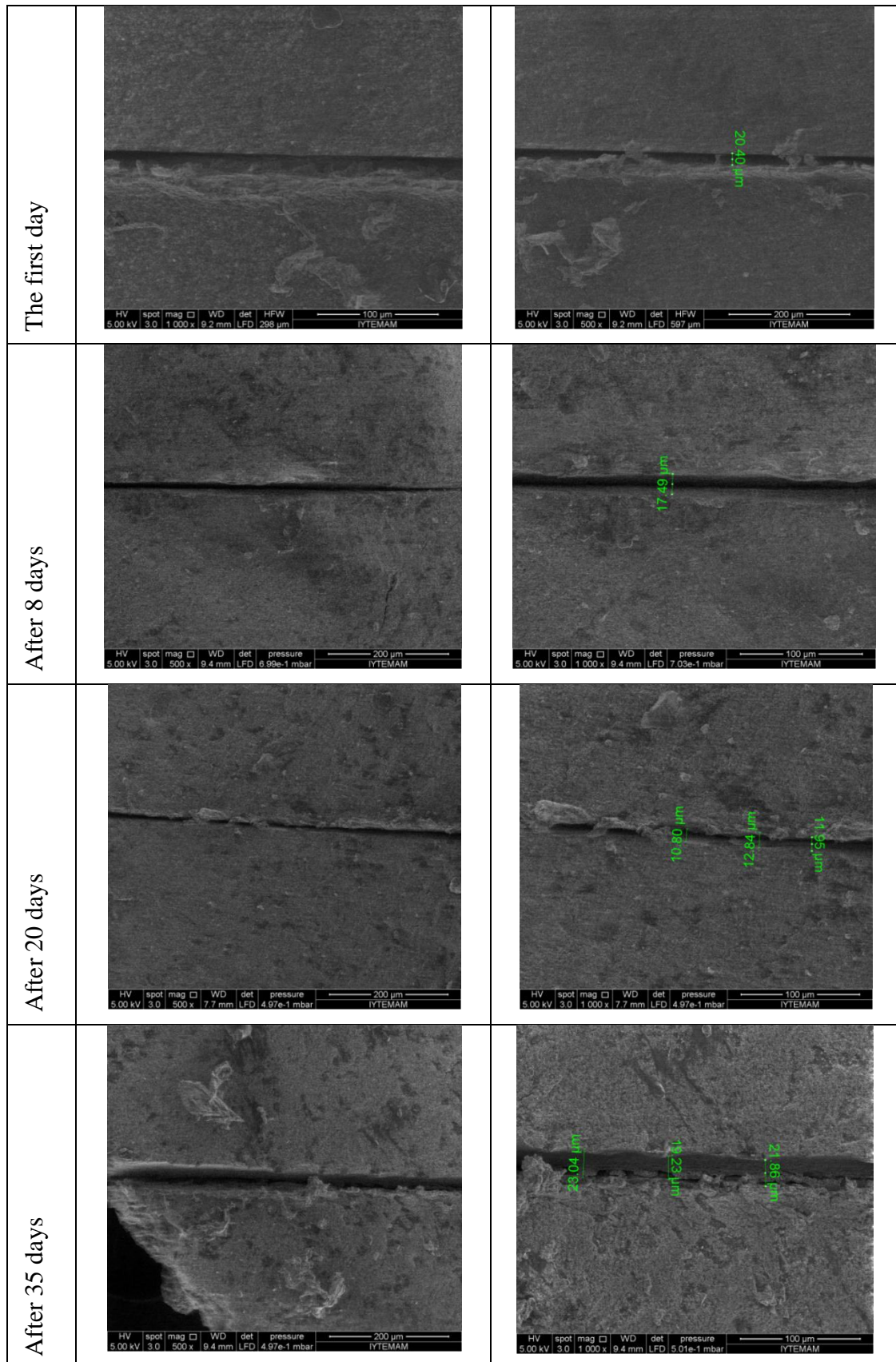


Figure 4.47 SEM micrographs of sample of EC5 0.0119 % chitosan added epoxy composite coatings after scratch testing

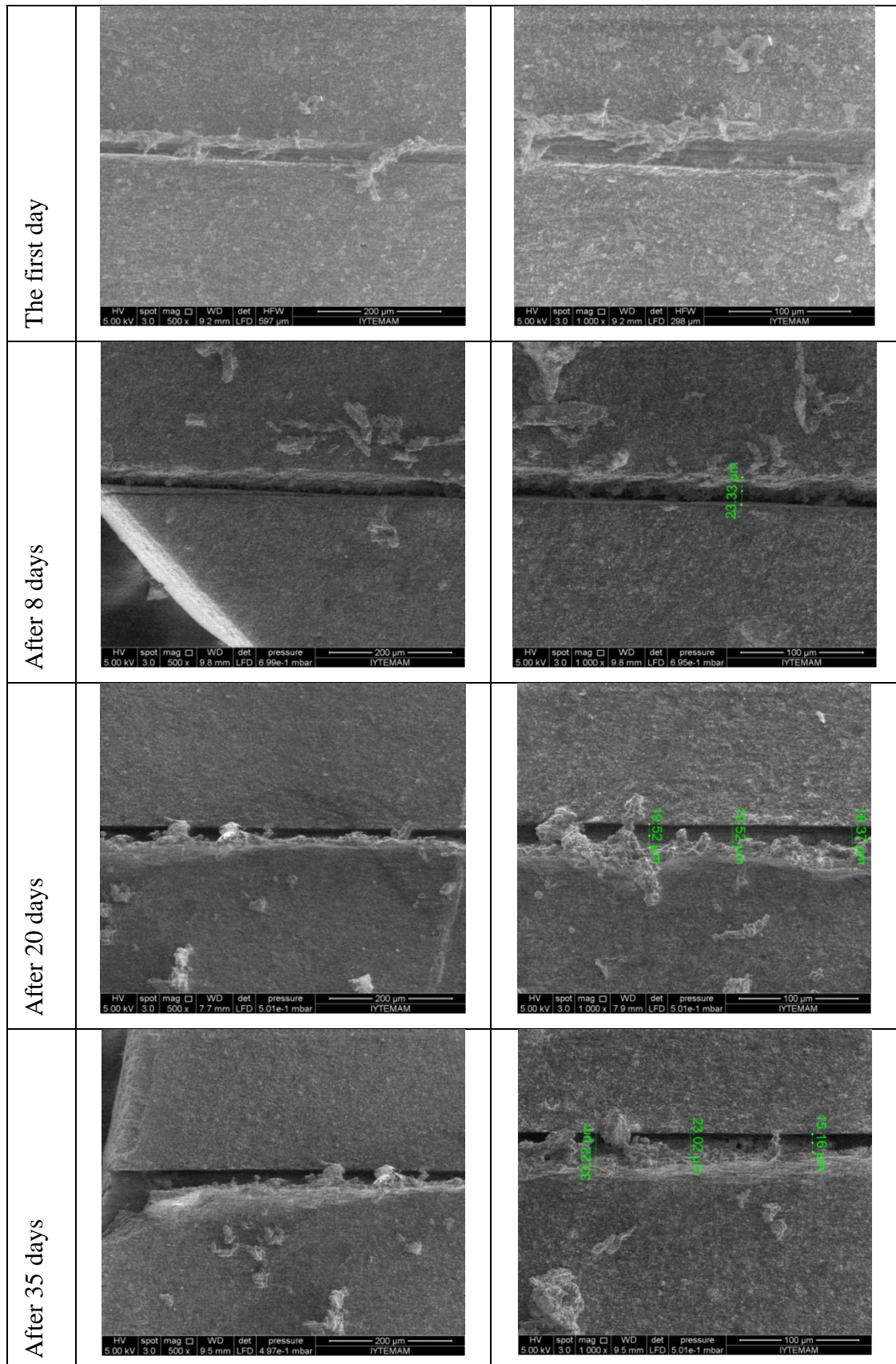


Figure 4.48 SEM micrographs of sample of EC6 0.0019 % chitosan added epoxy composite coatings after scratch testing

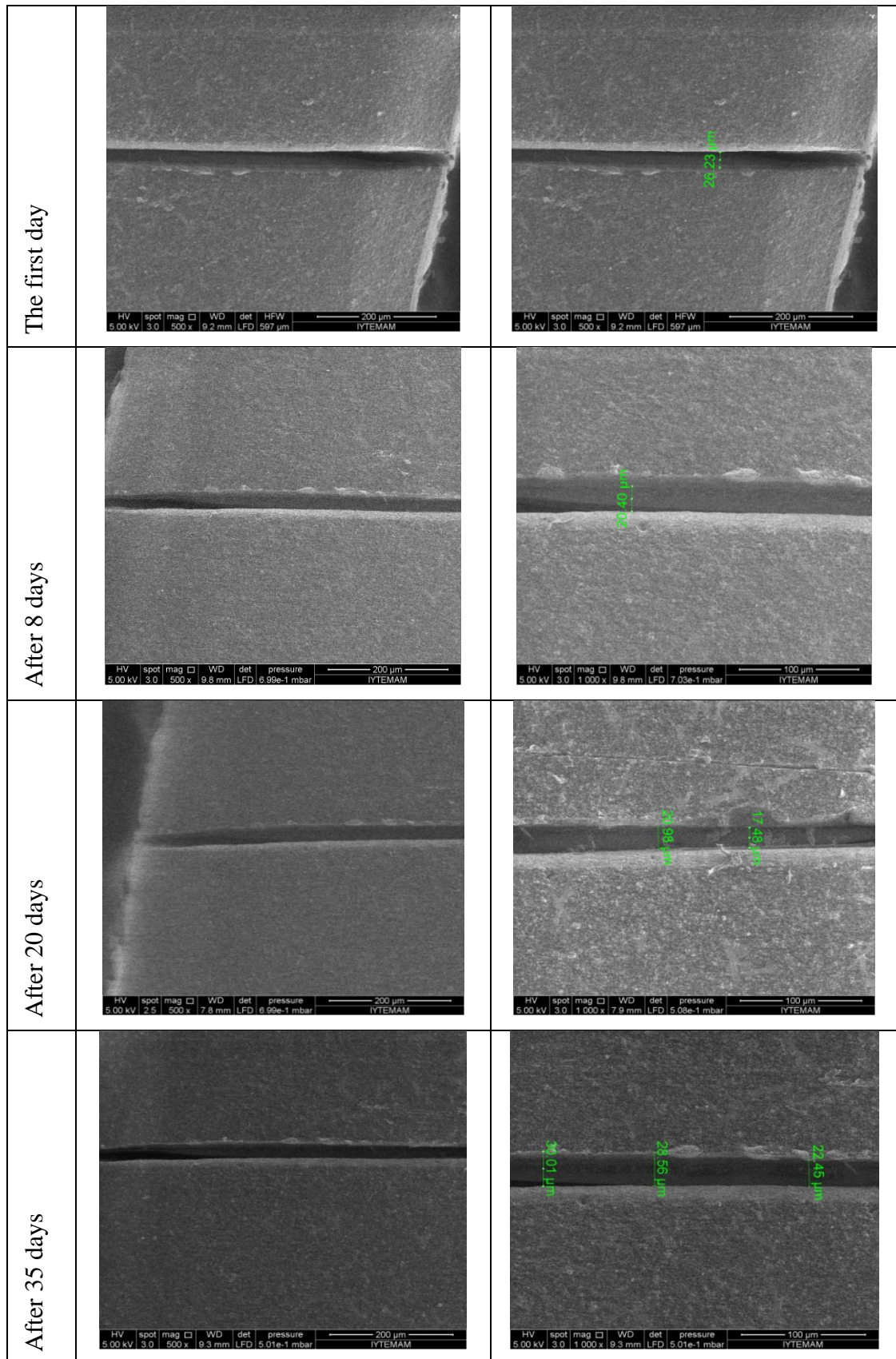


Figure 4.49 SEM micrographs of sample of EC7 0 % chitosan added epoxy composite coatings after scratch testing

4.4.2.4 Antibacterial Property

As mentioned above, chitosan is also known for its antibacterial activity. After coating preparation part, the chitosan added epoxy composite coated samples were subjected to antibacterial test. The test type was called “decreasing test”. At the beginning there were 2000 bacterias, then it was counted after 24 hours. The results are shown in Table 4.6 below. It can be expressed that chitosan reinforced dye coatings showed antibacterial property.

Table 4.6 Decreasing test results of the chitosan added epoxy composite coated samples

Code	Bacteria quantity after 24 hours
EC1	1800
EC2	342
EC3	1060
EC4	672
EC5	171
EC6	1512
EC7	612

4.4 Multifunctional Coatings

In this part, after optimum results were taken from each coating, multifunctional property was formed in antibacterial, flame retardancy, radar absorbing and self-healing. These multifunctional composite coatings/paints were characterized after deposition process. The structural, adhesion, antibacterial, flame retardant, radar absorbing and self-healing properties of the composite/paints were assessed with aid of FTIR, profilometer, scratch, antibacterial, flame retardant, radar absorbing and self-healing testers in detail.

4.4.1 FTIR Analysis

Figure 4.50 shows FTIR spectra of the multifunctional coated samples. It can be seen from the figure that the chitosan exhibits main characteristic bands of carbonyl (C=O-NHR) and amine group ($-\text{NH}_2$) at 1450 cm^{-1} . Nevertheless, this band can correspond to C-H bending from epoxy matrix. Huntite hydromagnesite and barium hexaferrite powders are not organic minerals and they can not be indicated for FTIR. In the same way, CH_3COH group band can be observed at 748 cm^{-1} related with the chitosan but this may come from the epoxy, because the characteristic peaks of epoxy indicate the formation of Si-O, Si-O-Si and Si-C at 751 , 1084 and 1270 cm^{-1} respectively. The broad band due to the stretching vibration of $-\text{NH}_2$ and $-\text{OH}$ group from chitosan can be observed at 2950 cm^{-1} but it may be related with epoxy alkyl groups ($-\text{CH}_3$, $-\text{CH}_2$) stretching. The similar results were reported elsewhere (Boonsongrit, Mueller, Mitrevej, 2008 and Osman, Arof, 2003).

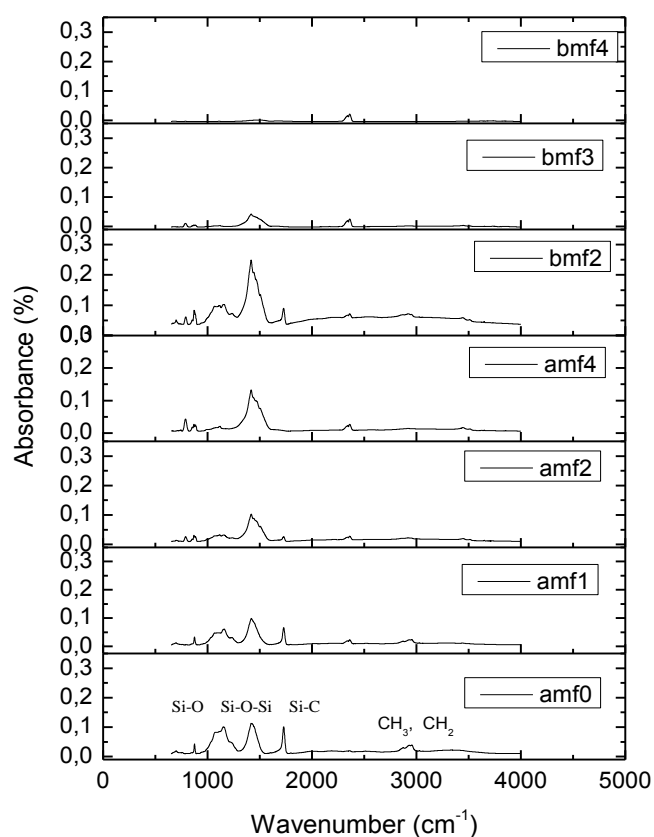


Figure 4.50 FTIR analysis of multifunctional composite samples

4.4.2 Surface Profilometer

Surface roughness of the multifunctional coatings represented by the arithmetic mean value R_a and the maximum roughness height R_t values were demonstrated in Table 4.7. These values can give the ideas regarding the surface profiles of the composite samples. It can be seen that the samples have not very good smooth surfaces. Furthermore some of the samples could not be tested. This may be due to adding different kind of materials and powders into a liquid material.

Table 4.7 Surface profilometer test results.

Surface roughness values	MF0	BMF1	BMF2
R_a	0.40	5.19	9.95
	0.39	4.96	12.71
	0.87		
R_t	4.27	46.35	82.95
	3.54	39.51	114.09
	6.53		

4.4.3 Adhesion Properties

Scratch test results of the multifunctional coatings are denoted in Table 4.8. It can be pointed out that the adhesion strength of the multimultional composite coating is higher than that of pure dye.

Table 4.8 Multifunctional composite coatings scratch test results

Sample codes	BMF1	BMF2	BMF3	BMF4	MF2	MF4	MF0
Critical Force (mN)	38,5	19,5	24,3	21,2	24,7	22,5	13,5
Adhesion Strenght (MPa)	67.04	43.39	49.16	45.98	49.79	45.34	35.16

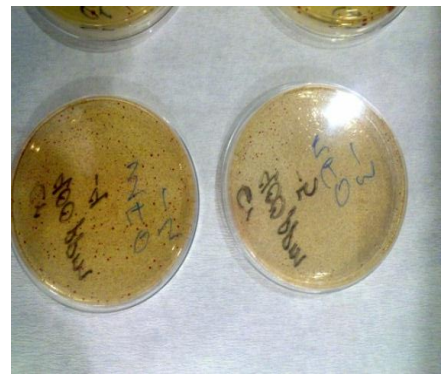
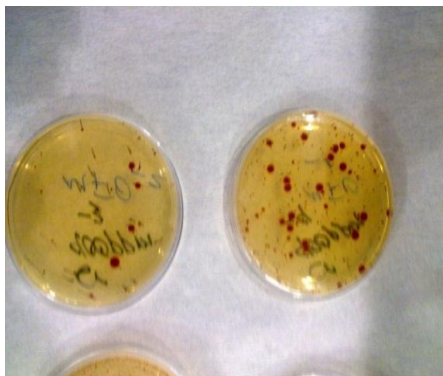
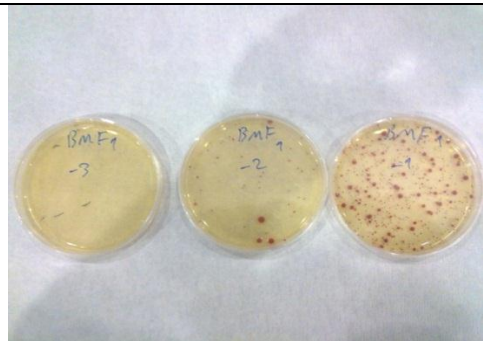
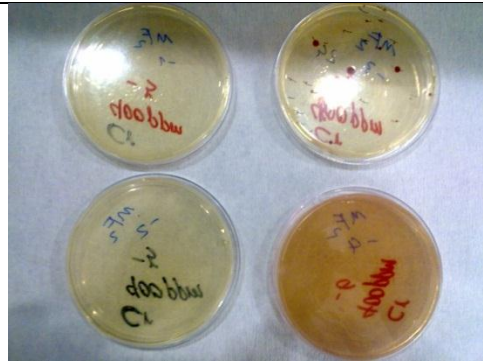
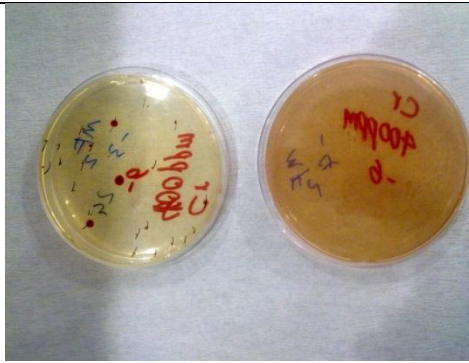
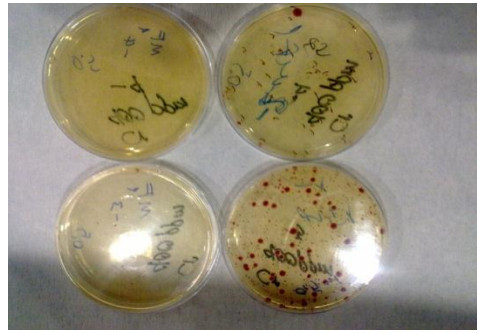
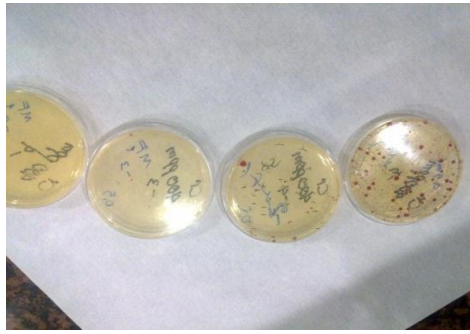
4.4.4 Antibacterial Behaviour

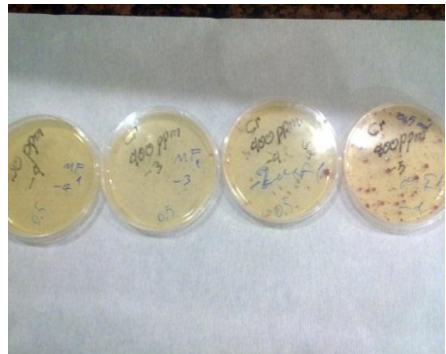
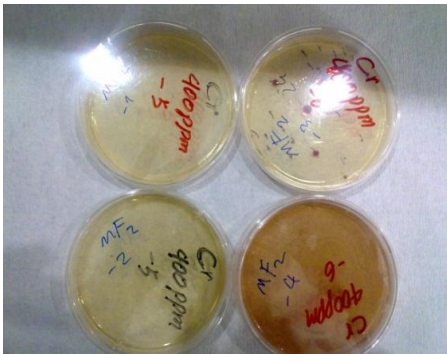
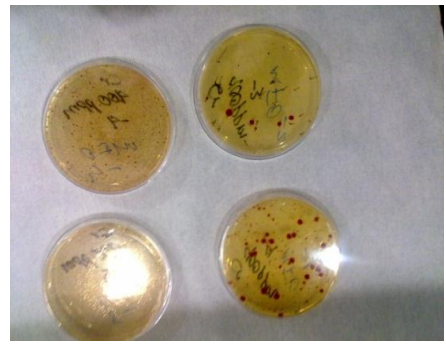
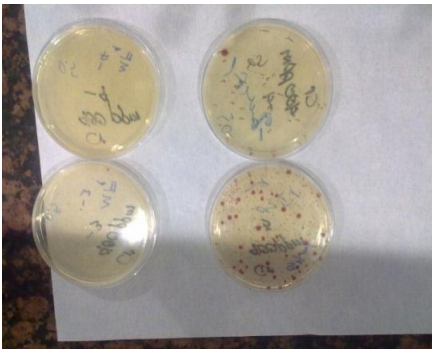
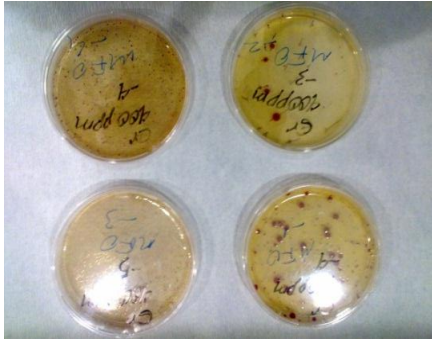
Decreasing percentage test results of multifunctional composite coatings as coded in Table 3.10 are given in Table 4.9. Ag nanoparticle content was in the range of 0.05 % and 0.2 % in the multifunctional coatings. The photographs of the tests are depicted in Figure 4.51.

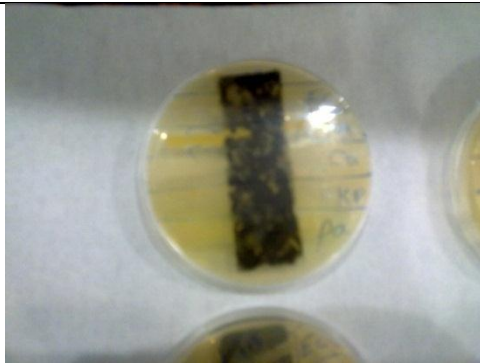
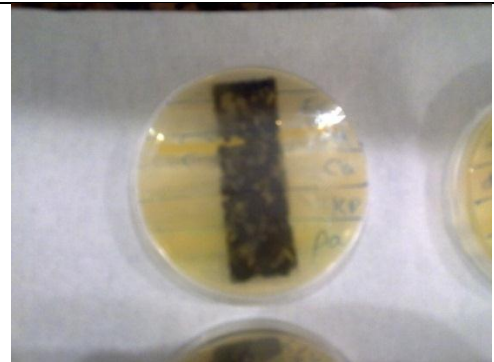
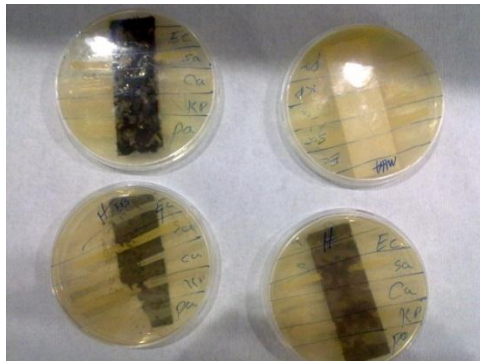
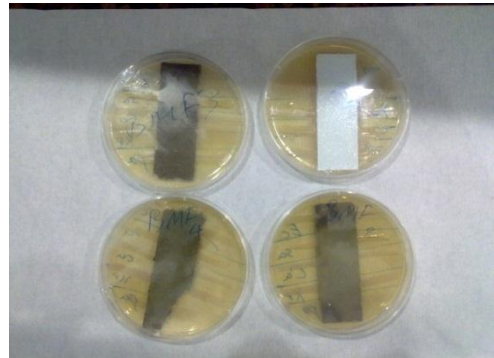
According to those results, all composites showed successful antibacterial behaviours. Notably AMF3, AMF4, BMF2, BMF3 and BMF4 specimens destroyed 100 % of the bacterias after 2 hours; all of those mentioned samples had Ag nanoparticles. It was observed that AMF1 and BMF1 samples destroyed some bacterias due to presence of chitosan.

Table 4.9 Decreasing percentage test results of multifunctional composite coatings

Sample codes	E. Coli amount at the beginning	E.Coli amount after 2 hours	% decreasing
AMF 0	9.10^5	79.10^4	12.2
AMF 1	9.10^5	75.10^4	16.66
AMF 2	9.10^5	68.10^4	24.44
AMF 3	9.10^5	-	100
AMF4	9.10^5	-	100
BMF 1	9.10^5	46.10^4	48.88
BMF 2	9.10^5	-	100
BMF 3	9.10^5	-	100
BMF 4	9.10^5	-	100







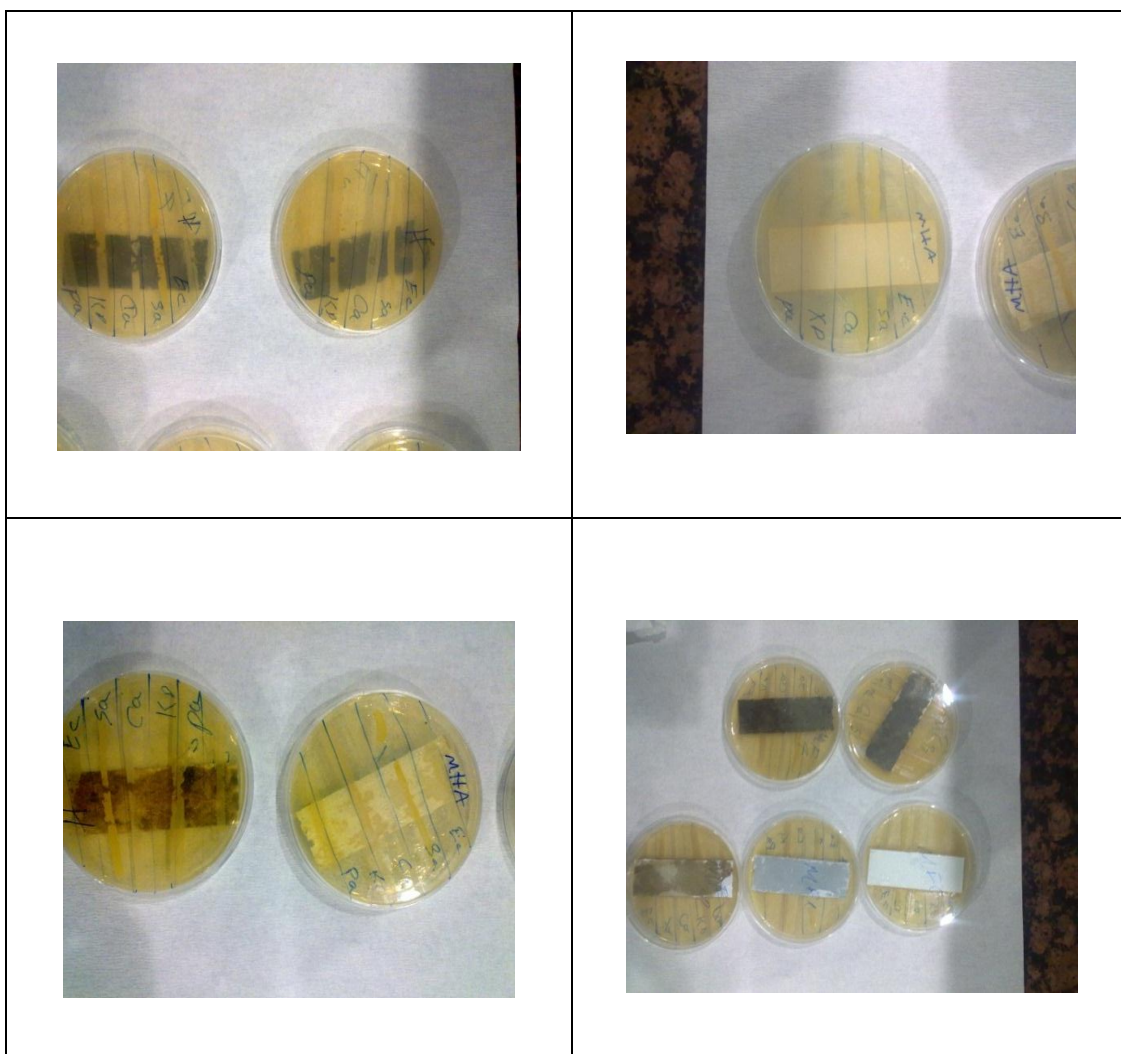


Figure 4.51 Antibacterial test results of multifunctional composite coatings as coded in Table 3.10

4.4.5 Flame Retardant Properties



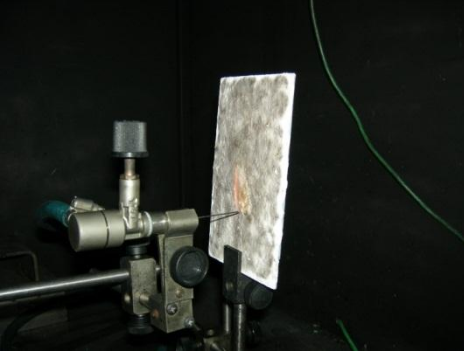
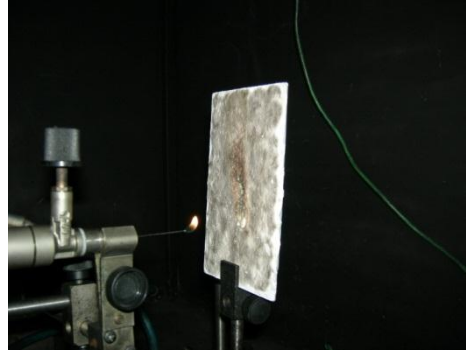
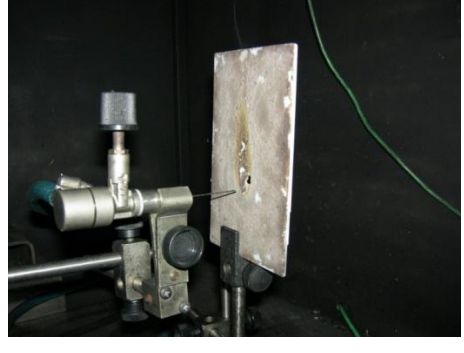
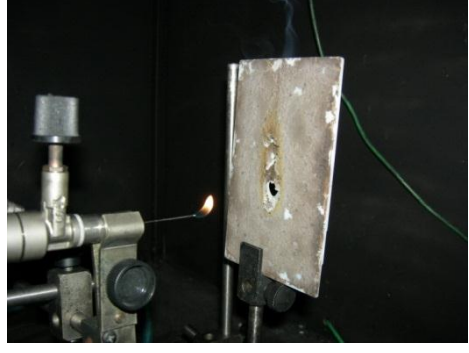
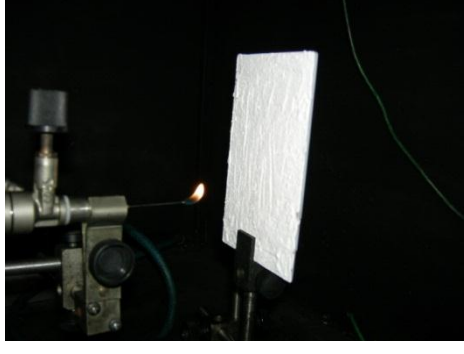
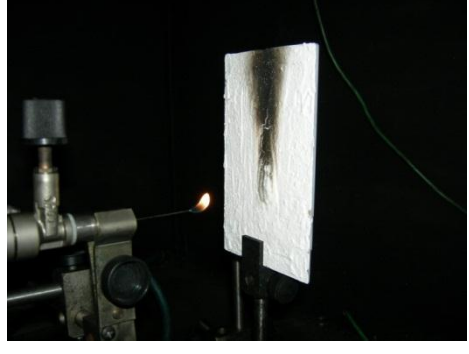
Flame retardant test results of multifunctional composite coatings as coded in Table 3.10 are shown in Table 4.10. As may be seen from Table 3.10, huntite/hydromagnesite content changed between 10 and 30 % in the multifunctional coatings. As shown, except for the control sample and BMF4, all composites seem to be flame retardant. Inasmuch as BMF1 and BMF2 samples possessed 10% huntite hydromagnesite, they were described as flame retardant but this amount might be not enough for the excellent flame retardancy that similar results were obtained from the earlier studies. Note that AMF4 and BMF4 samples had 30% huntite and

hydromagnesite. In spite of the fact that AMF4 sample was excellent flame retardant, BMF4 was failed for this application. This might be due to lack of barium hexaferrite. Thus it can be expressed that barium hexaferrite redounded flame retardancy with huntite hydromagnesite.

Table 4.10 Flame retardant test results of multifunctional composite coatings as coded in Table 3.10

Plastic material	Flame starts at	After flame	Result
AMF0	55 sec	>180 sec	NOK
AMF1	No flame	No after flame	OK
AMF2	No flame	No after flame	OK
AMF3	No flame	No after flame	OK
AMF4	No flame	No after flame	OK
BMF1	60 sec (only the paint) till 120 sec	No after flame	OK
BMF2	55 sec (only the paint) till 126 sec	No after flame	OK
BMF3	No flame	No after flame	OK
BMF4	160 sec	>180 sec	NOK

The photographs of multifunctional coatings before flame and after flame are shown in Figure 4.52 indicating that the multifunctional composites exhibit flame retardant behaviour. It is obviously clear from Figure 4.52 that even though pure dye coating (AFM0) burned easily, multifunctional coatings strongly showed flame retardant properties. As shown from Figure 4.52, AMF4 sample which contains 30 % huntite/hydromagnesite mineral was excellent flame retardant owing to the synergical effect of barium hexaferrite. This behavior could not observe in BMF4 sample which contain 30 % huntite/hydromagnesite mineral thanks to lack of barium hexaferrite.

	BEFORE FLAME	AFTER FLAME
AMF0		
AMF1		
AMF2		
AMF3		
AMF4		
BMF1		

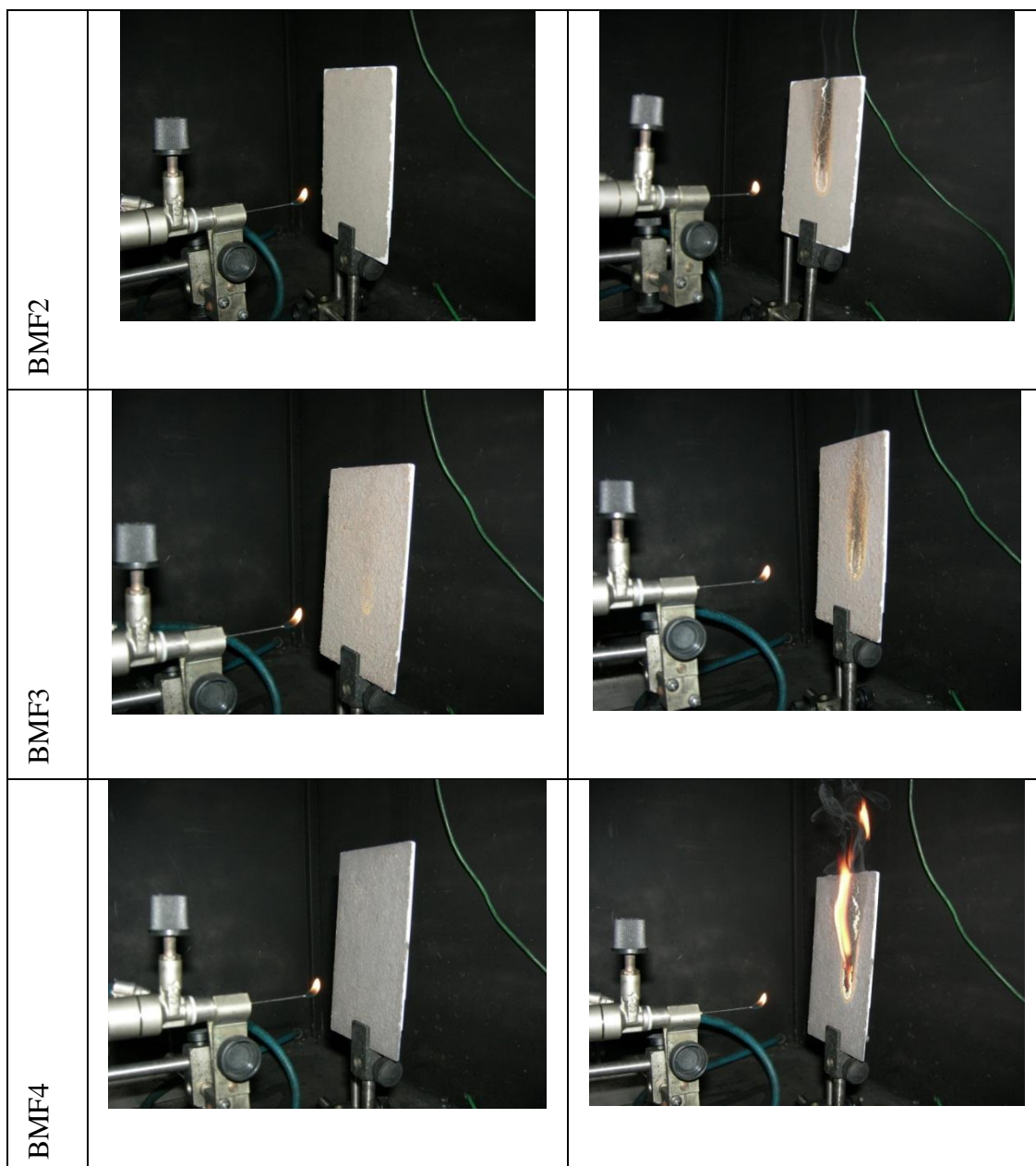


Figure 4.52 Flame retardant results of pure dye and multifunctional coatings before flame and after flame testing.

4.4.6 Radar Absorbing Behaviour

Figure 4.53 signifies the absorption values versus the frequency range of 6–14 GHz of the multifunctional coatings. Here, barium hexaferrite content altered between 5 and 20 % in the multifunctional coatings. Note that in this case the highest absorption was obtained from AMF4 which have the highest barium hexaferrite

amount (20%). The second one was AMF3 which have 10% barium hexaferrite as the radar absorbing properties. AMF1, AMF2, BMF2 and BMF3 (5%) are similar and again they have useful absorption values.

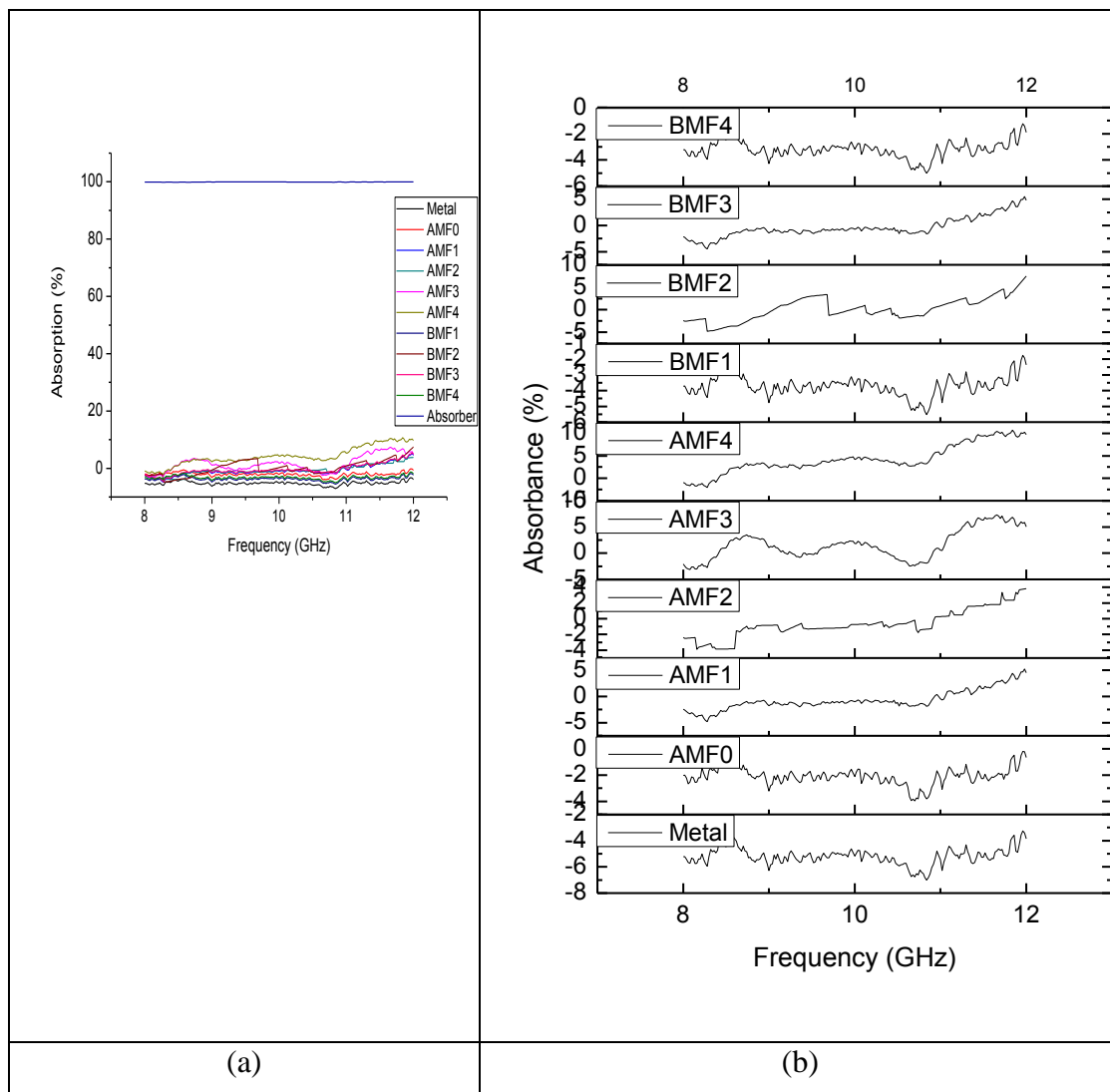


Figure 4.53 Network analyzer test results of the multifunctional coatings (a) with and (b) without absorber

As standart absorber is omitted in Figure 4.53.b, the composite coatings absorbtion values can be seen in detail. It can be normally seen that there was no any absorbing activity in pure epoxy coating due to lack of barium hexaferrite in the sample. However, in the $\text{BaFe}_{12}\text{O}_{19}$ reinforced coating there were significant

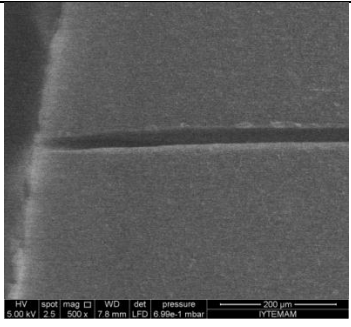
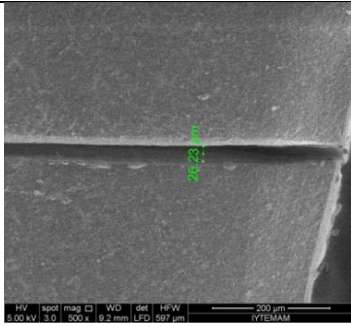
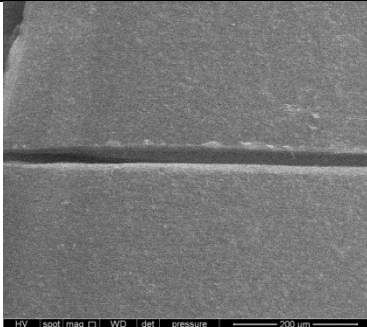
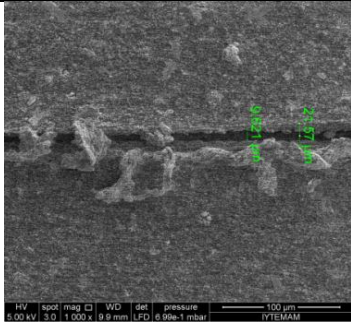
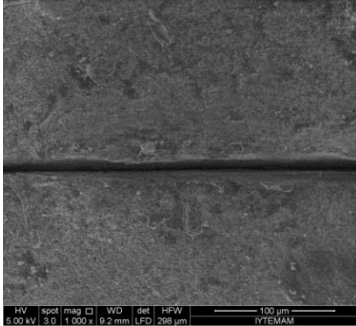
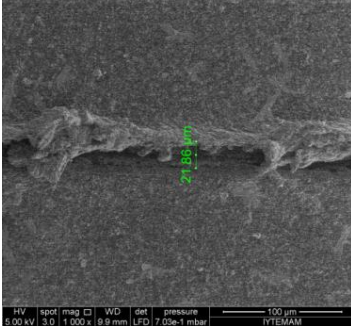
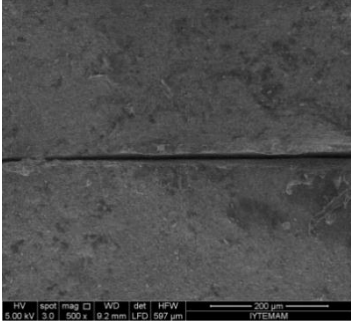
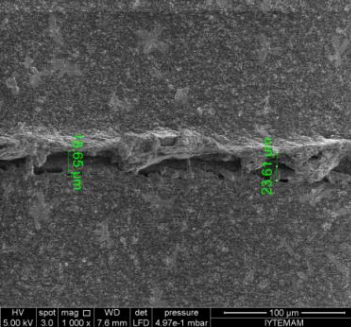
absorbing activities. The radar waves absorbing properties of composites were substantially improved after the loading of barium hexaferrite particles; absorbing percentage increases with increasing additive content in the composite coatings (Singh, 1999). The highest absorbing peak reaches 12.13% at 11.86 GHz with the sample of BF20.

As mentioned above, $\text{BaFe}_{12}\text{O}_{19}$ has large magneto crystalline anisotropy. Due to the spin orientations of the Fe^{3+} ions, the numbers of unpaired electrons are occurred in their 4s and 3d shells. Those not fully filled shells lead to magnetic moment. On the other hand, the magnetic moment of barium hexaferrite particles are related with not only the unpaired electrons but although angular momentum which represents the product of the body's rotational inertia and rotational velocity. These unique characteristics enhance largely the microwave absorption performance of barium hexaferrite reinforced composites (Sun, Gao, Li and Wu 2011).

4.4.7 Self Healing Properties

Figure 4.54 depicts SEM micrographs of the self-healed multifunctional coatings after scratch testing. In these experiments, chitosan content varied in the range of 0.01 and 0.2 % in the multifunctional coatings. As stated earlier, the micrographs were taken from the samples in 0 min, 30 min, 7 days, 20 days and 35 days after the scratching to examine the improvement on healing from SEM machine.

From all chitosan reinforced samples, self healing properties were obtained just after 30 min, and no more improvement has been found after that time. Therefore there were not any differences among the SEM micrographs taken 7, 20 and 35 days after scratching. Due to this they are not displayed.

	After 0 min	After 30 min
AMF0		
AMF1		
AMF2		
AMF3		

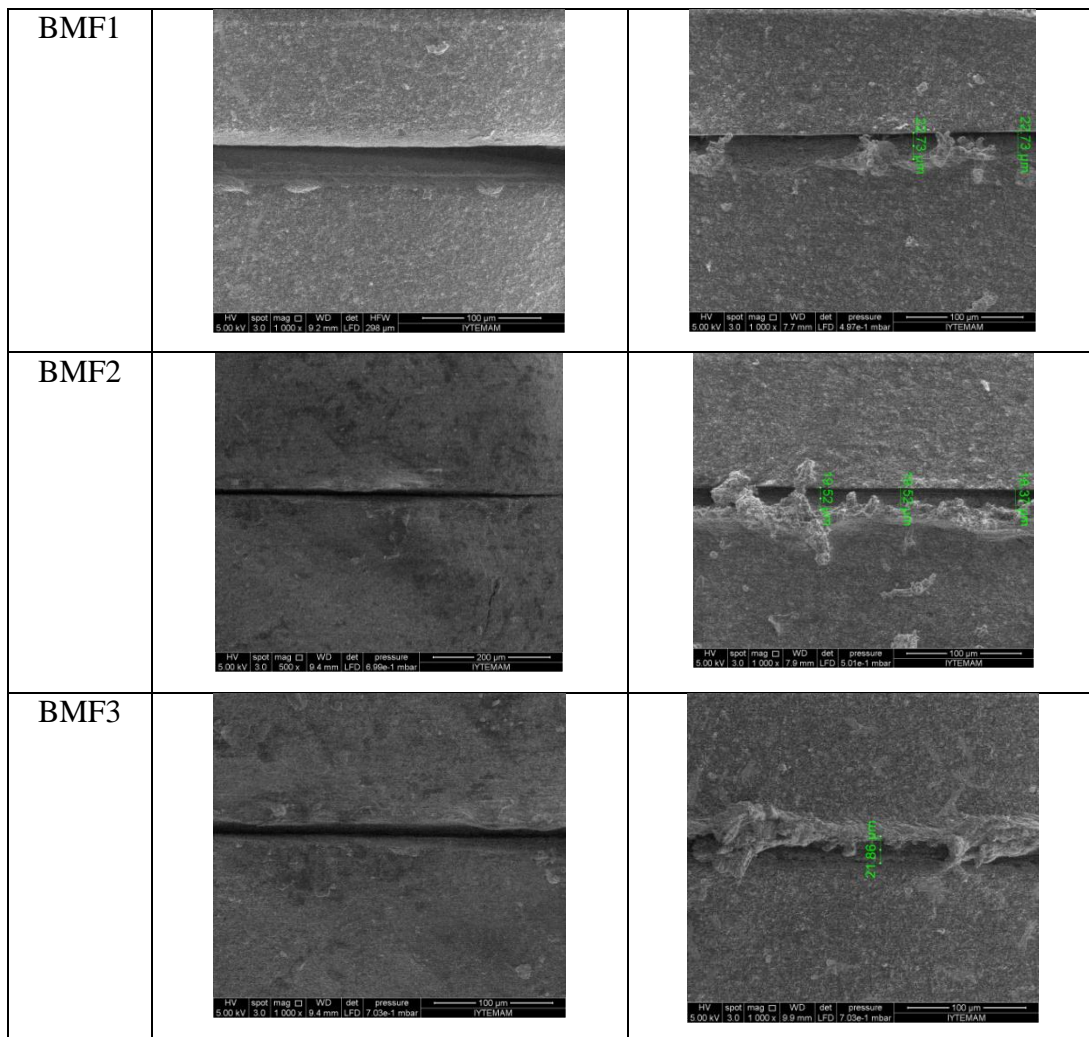


Figure 4.54 Self healing properties of multifunctional composite coatings.

Generally speaking from all figures, self-healing property can be determined as like branches of the tree, fill and seal the open cracks. As, there is no any healing behaviour in AMF0, chitosan rate is 0.00%, it can be said that chitosan's self healing effect appeared clearly with spanning the gap of a thin scratch. Epoxy polymer composites at room temperature far below the glass transition temperature tried to diffuse across those gaps. If this is a cross-linked network of epoxy composites working by the agency of chitosan, sample of AMF0 also should have that kind of healing property. This is important for the possible diffusion processes. On the other hand, the distinctions on the crack tips were measured and written on the micrographs, the self healing may not be determined according to those values,

because, as mentioned above, branches were developed like the arms for a wound the heal. That is to say, self-healing mechanism might be operated with those branches.

The self-healing results agree with Kessler *et al.* When they allowed the specimens to heal, partially cured poly (DCPD-dicyclopentadiene), strands were observed bridging the crack behind the crack tip. Present on the surface are several strands of poly(DCPD) that bridged the two surfaces of the delamination before ultimately rupturing and collapsing in a folded film on the fracture surface (Kessler, Sottos and Whiteb, 2003). On the other hand, as it is explained in detail in Ref. (Wu, Meure and Solomon, 2008), the healing mechanism is similar to molecular interdiffusion method. This method is that when two pieces of the same polymer are brought into contact at a temperature, the interface gradually disappears and the mechanical strength at the polymer–polymer interface increases as the crack heals due to molecular diffusion across the interface. Visual healing of the fracture surfaces was found to occur before a significant recovery in strength was achieved, with the interdiffusion of numerous chain segments being reported as the most likely healing mechanism (Wu, Meure and Solomon, 2008).

Wool and O'Connor (1981) suggested a five stages model to explain the crack healing process in terms of surface rearrangement, surface approach, wetting, diffusion and randomization (Wu, Meure and Solomon, 2008). When it is compared with the SEM photographs, the similarity can be seen. Some researches (Kim, Wool, 1983, Kausch, Jud, 1982) also presented a microscopic theory for the diffusion and randomization stages. They observed that the development of the mechanical strength during the crack healing process of glassy polymers is related to interdiffusion of the molecular chains and subsequent formation of molecular entanglements. The research carried out by Wool *et al.* (1981) confirmed that the phenomena of crack healing in the thermoplastics occur most effectively at or above the T_g of these materials (Wu, Meure and Solomon, 2008, McGarel, Wool, 1987). However, the self healing study in this article was obtained in the room temperature.

As no differences obtained from the morphological analysis of 30 min, 7 days, 20 days and 35 days after scratching, it can be said that the self healing occurs in the first 30 minutes in those coatings. This agrees with the literature of (Kessler, Sottos and White, 2003, Jin, Mangun, Stradley, Moore, Sottos, White, 2012) that the self healing behaviours were obtained in the first 30-60 minutes. However, in Ref. (Zheludkevich, 2011) self-healing was investigated in 1 day and 2 days.

CHAPTER FIVE

CONCLUSIONS AND FUTURE PLANS

Superior combinations of higher performance, lower weight and lower cost are essential properties for the multifunctional materials which are able to respond to environmental stimuli by exhibiting particular changes in some of their properties. The production of those materials is to establish the need to integrate technologies from different disciplines. Depending on the process, any property can be given to material that was not its own characteristic. In this thesis, the production and technical applications of the multifunctional materials were investigated. An epoxy dye was converted to multifunctional materials which are capable of performing multiple functions; antibacterial, flame retardant, radar absorbing and self-healing. Four different types of materials were incorporated into polymer matrix with different grades and with different particle contents; for antibacterial property Ag nanoparticles, for flame retardant characteristic huntite and hydromagnesite minerals, for radar absorbing behaviour barium hexaferrite particles and for self-healing property chitosan. Fundamental structural and functional properties of the materials were investigated to determine the effect of the additives concentration to the structure. The following successful conclusions are obtained from the experimental works:

- Ag nanoparticles were synthesized by a reduction reaction, they had diameter between 1 and 100 nm. Polyurethane paint composites were prepared by adding Ag nanoparticles at different ratio into the polyurethane matrix. Then by coating the glass substrates with this dye composite, different kind of the samples was obtained. For the antibacterial behavior, all test samples and control specimen showed a good antimicrobial activity against the bacteria. Even the lowest test amount of Ag nanoparticles (0.1 %) in the polymer matrix caused an inhibition zone of 12.5 mm and 1.25 mm for *S. aureus* and *E. coli*, respectively. The inhibition zones caused by 30 % were 6.00 mm for *S.aureus* and 2.75 mm for *E.coli*. As unexpected, control specimens, which have 0 % Ag nanoparticles, have higher antimicrobial effect than 30 % silver

containing polyurethane films against test bacteria. This may be explained with several reasons. Firstly, Agar diffusion test is a qualitative test and its reliability depends on diffusion rate of active ingredient(s) to the test media. Secondly, leading to decrease of inhibition zones around coatings by increasing Ag nanoparticle content may be related with that polyurethane matrix prevents Nano silver releasing from the coating. FTIR and XRD results support these data. The results demonstrates that neither XRD pattern nor FTIR graphs show any change in the intensities by increasing or decreasing of the concentrate of Ag nanoparticles. It means that Ag nanoparticles do not change the phase or band structure of the polymer (epoxy dye). They just settle into the empty places between the polymer chains. This limits the movement ability of the chains and leads to rigidity in the polymer structure. Due to this, diffusion ability of polymer composite or Ag nanoparticles is limited. Therefore, increasing the Ag nanoparticle amount increases the limitation. As a matter of the fact, diffusion is not very good property for an antibacterial coating because it can be harmful for living people around coating material. On the other hand diffusion can cause losing the antibacterial material in a short time. Thus, it can be said that limitation in the diffusion mechanism can lengthen the antibacterial life of the coating.

- In the first test of flame retardancy, huntite/hydromagnesite minerals were ground in a ball mill 0, 15, 30, 60 hours, they were blended into an epoxy dye and then glass and plastic substrates were coated with those composite dyes. At the end of the flame retardancy tests, it was found that 30 hours ground material had higher flame retardancy than 15 hours ground. In the second test, fine and coarse huntite and hydromagnesite mineral were blended with boric acid and antimony oxide with the ratio of 1 %, 5 %, 10 %, 15 %, 20 % and 30 % separately. This mineral mixture was then blended into the epoxy dye material with the ratio of 30 %. The glass substrates were coated with this dye-mineral composite. At the end of the flame retardancy tests, it was found that mineral additives increased the flame retardancy properties of the plastic material. Similar with Ag nanoparticle reinforced coatings, the FTIR

analysis of huntite/hydromagnesite reinforced coatings had no any difference comparing with the pure epoxy dye coatings. In DTA-TG testing, the significant differences are obtained that pure dye coated sample and pure plastic substrate was melted at 400 °C, whilst other coated samples kept their structures at the same temperature. This shows the flame retardant effect of the mineral reinforced coatings. When boric acid and antimony oxide compared as a subsidiary flame retardant additive, it was seen that boric acid has more flame retardant effect than antimony oxide for the plastics.

- BaFe₁₂O₁₉ powders were successfully prepared by using sol-gel process as a radar absorbing material. XRD results of the barium hexaferrite powders showed that there were barium ferrite as major phase and iron oxide as minor phase. In SEM micrographs, platelet microstructures of the powders were indicated in hexagonal basal plane. BaFe₁₂O₁₉ powders were added to epoxy dye with different ratio and the coatings were obtained with this composite coatings. With the FTIR analysis of the coatings, characteristics epoxy peaks are observed. It could not be seen any interaction between polymer chains and ferrite or barium hexaferrite particles with this analysis. Similar with Ag nanoparticle or huntite hydromagnesite reinforced coatings, the FTIR analysis of BaFe₁₂O₁₉ reinforced coatings had no any difference comparing with the pure epoxy dye coatings. Higher magnetic saturation values were obtained from barium ferrite powders reinforced coatings. Increasing additive content increased the magnetic saturation. It was not seen any absorbing activity in % 0 additive content dye coating. However, in the BaFe₁₂O₁₉ powders reinforced coating there was a significant absorbing activity. Absorption values increased by increasing additive content.
- Different amounts of chitosan were dissolved completely in acetic acid solution (1 % by v/v) under stirring. Then obtained chitosan colloids were added to epoxy dye with different loading levels to see the concentration dependence of material's self-healing effect. Glass substrates were coated with those polymer composites and after drying for 24 hours at the room

temperature, final coatings were obtained. Self-healing test were performed, in this respect, after scratching the samples with a very thin pin, they were analyzed by SEM periodically. Self-healing property was determined as like putting forth branches like a tree, splits are packed with the composite. Chitosan's self-healing effect appeared clearly. For the comparing the samples by means of self-healing, measuring the distances on the top of the splits did not assist. However, it needs to look at the branches numbers, shapes, orders or thicknesses to evaluate any self-healing occurrence. On the other hand, there is no big difference in the SEM analysis done by the time. Self-healing occurs in the first 30 minutes.

- To produce multifunctional coating, Ag Nano particles were synthesized by a reduction reaction. Huntite/hydromagnesite minerals were ground to Nano size in a ball mill. Barium hexaferrite powders were obtained by sol-gel processing. Chitosan was used as a homogeneous colloid by using an acid solution. Then, obtained additives were added to epoxy dye with different loading levels and the glass, plastic and metal substrates were coated with those polymer composites. At the end of the characterization and functional tests, generally it was obtained almost all composite coating samples depicted very good antibacterial, radar absorbing, flame retardancy and self-healing properties. In detail, regarding the antibacterial property; even AMF0, AMF1 and BMF1 had no Ag nanoparticles, they demonstrated a little bit antibacterial property. AMF0 was 12 % and AMF1 was 16 %, these may come from epoxy dye itself. BMF1 was 49 % and this may come from chitosan. All the other samples having Ag nanoparticles were 100 % antibacterial value. Related with flame retardant property; apart from BMF4, all other samples showed very good flame retardant property. Although BMF4 had higher huntite/hydromagnesite quantity (30 %), flame retardancy results were not good. The reason for this may be having very poor coating surface quality. For the radar absorbing property; AMF4 was the best absorber, which had 20 %, AMF3 was the best after AMF4 which has 10 % barium hexaferrite powders, and the others having barium hexaferrite showed

radar absorbing property lower than AMF4 and AMF3. Regarding the self-healing property; except for AMF0, which has not a chitosan colloid, all samples demonstrated self-healing property. It was indicated that when the cracks were narrow, self-healing activity was obtained better like AMF3 and BMF2. Beside those functional experiments, it is indicated from the surface profilometer test that increasing the mineral additive amount in the coatings decreased the surface smoothness. In this sense, if one of the sample needs to be selected for the best, BMF2 can be chosen due to depicting all four properties. Moreover, having 10 % huntite hydromagnesite and 5 % bariumphaxaferrite, BMF2 has smoother surface, is not heavy and its mechanical property will not be broken down due to having mineral powders.

It can be concluded that multifunctional polymer coatings with four different properties were successfully prepared from different kinds of materials. It was stated that generally all properties were increased with increasing additive loading levels. This was the same for monofunctional samples or multifunctional samples. Therefore, it can be pointed out that even if they were used in the same material, those four type of materials did not influence each other negatively. To examine the optimum loading grades of the additives, it needs to look at the environmental conditions and the needs. According to the requirements, the additive amounts can be determined.

The structural and functional experiment results discussed in this thesis show that after optimizing all parameters, it is going to be possible to prepare prototype applications of these materials. It can be possible to give a material (such as an aircraft) antibacterial, flame retardant, radar absorbing and self-healing activity just by painting that kind of composite dyes. To obtain better surface quality, different kinds of additives can be attempted. In addition, dispersants can be used to stabilize the suspension of the additive particles in the polymer matrix, and emulsifiers can be used to bind the different additive materials to the epoxy. This can allow the materials to mix uniformly and prevent the polymer composite in an emulsion from

separating into layers. In this manner, more homogeneous composite materials and smoother coating surfaces can be achieved.

REFERENCES

- Ajayan, P.M., Schadler, L.S. & Braun P.V. (2003). *Nanocomposite Science and Technology*. WILEY-VCH Verlag GmbH.
- Aksit, A., Onar, N., Ebeoglugil, M.F., Birlik, I., Celik, E. & Ozdemir, I. (2009), Electromagnetic and Electrical Properties of Coated Cotton Fabric with Barium Ferrite Doped Polyaniline Film. *Journal of Applied Polymer Science*. Vol. 113, 1, 358-366.
- Alan, K.T., Lau, J.L., Varadan, V.K., Chang, F.K., Tu, J.P. & Lam, P.M. (2008). Multi-functional Materials and Structures *Advanced Materials Research*, Volumes 47 – 50.
- Amendola, V., Polizzi S. & Meneghetti, M. (2007). Free silver nanoparticles synthesized by laser ablation in organic solvents and their easy functionalization. *Langmuir*. 23, pp. 6766–6770.
- Atiyeh, B.S., Costagliola, M., Hayek, S.N. & Dibo, S.A. (2007). Effect of silver on burn wound infection control and healing: review of the literature. *Burn*, 33, pp. 139–148.
- Balaguera-Gelves, R. (2006). *Detection of nitroexplosives by surface enhanced Raman spectroscopy on colloidal metal nanoparticles*. Master thesis, University of Puerto Rico, Mayaguez Campus.
- Bansal, N.P. (2005). *Handbook of Ceramic Composites*. Kluwer Academic Publisher.
- Basfar, A.A. & Bae, H.J. (2009). Influence of Magnesium Hydroxide and Huntite Hydromagnesite on Mechanical Properties of Ethylene Vinyl Acetate Compounds Crosslinked by DiCumyl Peroxide and Ionizing Radiation. *Journal of Fire Sciences*. Vol: 00, DOI: 10.1177/0734904109340765.

- Beaulieu, C. (2005). *Chitin and Chitosan*. Université du Québec à Rimouski.
- Belgacem, M.N. & Gandini, A. (2008). *Monomers, Polymers And Composites From Renewable Resources*. Ch.25. Elsevier. Oxford, UK.
- Benito, G., Morales, M.P., Requena, J., Raposo, V., Vazquez, M. & Moya, J.S. (2001). Barium hexaferrite monodispersed nanoparticles prepared by the ceramic method. *J. Magn. Magn. Mater.* 234, 65–72.
- Birlik, I. (2011). *Synthesis of superconducting films and improvement of their flux pinning properties with barium zirconate nanoparticles using chemical solution deposition method*. Msc Thesis. Dokuz Eylul University.
- Boonsongrit, Y., Mueller, B.W. & Mitrevej, A. (2008). Characterization of drug–chitosan interaction by H NMR, FTIR and isothermal titration calorimetry. *Eur J Pharm Biopharm*, (69), 388-395.
- Bras, M.L., Wilkie, C.A. & Bourbigot, S. (2005). *Fire Retardancy of Polymers-New Applications of Mineral Fillers*. Published by The Royal Society of Chemistry. Cambridge, UK. pp 4-6.
- Brown, S.D. (1998). *Investigation into the suitability of using water ionized with copper and silver to treat E.Coli infection in slaughtering house*. Cranfield Biotechnology Centre. M. Sc. Thesis.
- Butkus, M.A., Labare, M.P., Starke, J.A., Moon, K. & Talbot, M. (2004). Use of aqueous silver to Enhance inactivation of coliphage MS-2 by UV disinfection. *Appl Environ Microbiol.* 70, (5), pp. 2848–2853.

- Carrillo-Castillo, A. & Osuna-Alarcón, J.G. (2011). Preparation and Characterization of Hybrid Materials of Epoxy Resin Type Bisphenol A With Silicon and Titanium Oxides by Sol Gel Process. *J. Mex. Chem. Soc.* 55 (4), 233-237.
- Castellano, J.J., Shafii, S.M., Ko, F., Donate, G., Wright, T.E. & Mannari, R.J. (2007). Comparative evaluation of silver-containing antimicrobial dressings and drugs. *Int Wound J.* 4, (2), pp. 114–122.
- Chem424 (2012). *Synthetic Polymer Chemistry*. Retrieved 15.12.2012 from <http://chem.chem.rochester.edu/~chem424/epoxy.htm>.
- Chen, M., Feng, Y., Wang, X., Li, T., Zhang J. & Qian, D. (2007). Silver nanoparticles capped by oleylamine: formation, growth, and self-organization. *Langmuir.* 23, pp. 5296–5304.
- Chopra, I. (2007). The increasing use of silver-based products as antimicrobial agents: a useful development or a cause for concern?, *J Antimicrob Chemother.* 59, pp. 587–590.
- Colloid (2012). *Britannica Online Encyclopedia*. Retrieved 25.12.2012 from <http://www.britannica.com/EBchecked/topic/125898/colloid>
- Crocker, J. (2007). Materials Technology. *Advanced Performance Materials*. Volume 22, pp. 238-241.
- Culha, O., Ebeoglugil, M. F., Birlik, I., Celik, E. & Toparli, M. (2009). Synthesis and Characterization of Semiconductor Tin Oxide Thin Films on Glass Substrate by Sol–gel Technique, *Journal of Sol-Gel Science and Technology* 5, 32–41.
- Culha, O., Zor, M., Gungor, M. A., Arman Y. & Toparli, M. (2009). Evaluating the Bond Strength of Opaque Material on Porcelain Fused to Metal Restorations (PFM) Alloys by Scratch Test Method. *Materials and Design*, 30, 3225–3228.

- Diaz, R. (2012). *Fundamentals of Electromagnetic waves*. Arizona State University, ARC Technologies, Inc.
- Donnan, S. (2012), Retrieved 14.08.2012 from <http://www.healingzone.info/silver>
- Dorjnamjin, D., Ariunaa, M. & Shim, Y.K. (2008). Synthesis of silver nanoparticles using hydroxyl functionalized ionic liquids and their antimicrobial activity. *Int J Mol Sci.* 9, pp. 807–820.
- Ebeogluligil, M.F. (2011). *Processing, characterization and development of rare earth doped lead magnesium niobate ferroelectric ceramic capacitors by sol-gel technique*. Dokuz Eylul University PhD Thesis, 133-134.
- Ebert, M. et al (1991). *Polymer Preprints*, 32, (3), 139.
- Efra, (2012). *Flame retardants integral to fire safety*. Retrieved 15.08.2012 from http://www.cefic-efra.com/index.php?option=com_content&view=article&id=3&Itemid=216&lang=en
- Fehling, H. (1849). Die quantitative Bestimmung von Zucker und Stärkmehl mittelst Kupfervitriol. *Annalen der Chemie und Pharmacie.* 72 (1): 106–113. Retrieved 09.08.2012 from http://en.wikipedia.org/wiki/Fehling's_solution
- Feng, Q.L., Wu, J., Chen, G.Q., Cui, F.Z., Kim, T.N. & Kim, J.O. (2000). A mechanistic study of the antibacterial effect of silver ions on *Escherichia coli* and *Staphylococcus aureus*. *J Biomed Mater.* 52, (4), pp. 662–668.
- Ferna'ndez , A.I., Haurie, L., Formosa, J., Chimenos J.M., Antunes, M. & Velasco J.I. (2009). Characterization of poly (ethylene-co-vinyl acetate) (EVA) filled with low grade magnesium hydroxide. *Polymer Degradation and Stability.* 94, 57–60.

- Foner, S. (1959). *Vibrating sample magnetometer*. Retrieved 09.08.2012 from http://en.wikipedia.org/wiki/Vibrating_sample_magnetometer
- Fox, C.L. & Modak, S.M. (1974). Mechanism of silver sulfadiazine action on burn wound infections. *Antimicrob Agents Chemother.* 5, (6), pp. 582–588.
- Fox, V.C., Renevier, N., Teer, D.G., Hampshire J. & Rigato, V. (1999). The structure of tribologically improved MoS₂–metal composite coatings and their industrial applications. *Surface and Coatings Technology.* 116, pp. 492–497.
- Furno, F., Morley, K.S., Wong, B., Sharp, B.L., Arnold P.L. & Howdle, S.M. (2004). Silver nanoparticles and polymeric medical devices: a new approach to prevention of infection? *J Antimicrob Chemother.* 54, pp. 1019–1024.
- Gambit (2011). *US Stealth UAV RQ-170 downed in IRAN*. Retrieved 15.08.2012 from <http://www.defence.pk/forums/iranian-defence/144802-us-stealth-uav-rq-170-downed-iran-38.html>.
- General tests (2012). *Ph determination*. Retrieved 17.08.2012 from [http://www.ffcr.or.jp/zaidan/FFCRHOME.nsf/7bd44c20b0dc562649256502001b65e9/146fd852cd5e269049256f32001a133e/\\$FILE/B30.pdf](http://www.ffcr.or.jp/zaidan/FFCRHOME.nsf/7bd44c20b0dc562649256502001b65e9/146fd852cd5e269049256f32001a133e/$FILE/B30.pdf)
- Gerhard, H. (2012). *The Radar War, 1930-1945*. Radar World. Retrieved 15.08.2012 from <http://www.radarworld.org/radarwar.pdf>
- Ghasemi, A., Saatchi, A., Salehi, M., Hossienpour, A., Morisako, A. & Liu, X. (2006). Magnetic characteristics of Mn–Co–Ti substituted barium ferrite synthesized by sol–gel processing. *Phys. Stat. Sol. (a)*. 203, No. 10, pp. 2513–2521.
- Ghosh, B. & Urban M.W. (2009). Self-Repairing Oxetane-Substituted Chitosan Polyurethane Networks. *Science.* 323, pp. 1458-1460.

- Gong, P., Li, H., He, X., Wang, K., Hu, J., Tan, W., Zhang, S. & Yang X. (2007). Preparation and antibacterial activity of Fe₃O₄@Ag nanoparticles. *Nanotechnology*. 18, pp. 604–611.
- Gupta A. & Silver, S. (1998). Silver as a biocide: will resistance become a problem? *Nat Biotechnol*. 16, pp. 888.
- Hager, M.D., Greil P., Leyens C., Zwaag S. & Schubert U.S. (2010). Self-Healing Materials. *Adv. Mater*. 22, pp. 5424–5430.
- Haijun, Z., Zhichao, L., Chengliang, M., Xi, Y., Liangying, Z. & Mingzhong W. (2002). *Mat. Sci. Eng. B*. 96, pp. 289-295.
- Haurie L., Ferna´ndez, A.I., Velasco J.I., Chimenos, J.M., Cuesta, J.L. & Espiell, F. (2006) Synthetic hydromagnesite as flame retardant. Evaluation of the flame behaviour in a polyethylene matrix. *Polymer Degradation and Stability*. 91, pp. 989-994.
- How radar Works, (2012). *Utig*. Retrieved 15.08.2012 from http://www.ig.utexas.edu/research/projects/mars/education/radar_works.htm
- Jain P. & Pradeep, T. (2005). Potential of silver nanoparticle-coated polyurethane foam as an antibacterial water filter. *Biotechnol Bioeng*. 90, (1), pp. 59–63.
- Jin, H., Mangun, C.L., Stradley, D.S., Moore, J.S., Sottos, N.R. & White, S.R. (2012). Self-healing thermoset using encapsulated epoxy-amine healing chemistry. *Polymer*, (53), pp. 581-587.
- Jotania, R.B., Khomane, R.B., Chauhan, C.C., Menon, S.K. & Kulkarni, B.D. (2008). Synthesis and magnetic properties of barium–calcium hexaferrite particles prepared by sol–gel and microemulsion techniques. *Journal of Magnetism and Magnetic Materials*. 320, pp. 1095–1101.

- Jun, J., Yuan-Yuan, D., Shao-hai, W., Shao-feng Z. & Zhong-yi, W. (2007). Preparation and characterization of antibacterial silver-containing nanofibers for wound dressing applications. *J US-China Med Sci.* 4, (2), pp. 52–54.
- Kausch, H.H. & Jud, K. (1982). Molecular aspects of crack formation and healing in glassy polymers. *Rubber Process Appl.* 2, pp. 265–268.
- Kessler, M.R., Sottos, N.R. & White, S.R. (2003). Self-healing structural composite materials. *Composites: Part A.* (34), pp. 743–753.
- Kildeby, N.L., Roge, R.E., Larsen, T., Petersen, R., Riis J.F. & Bozhevolnyi, S.I. (2005). *Silver nanoparticles, Project Group N344.* Faculty of Physics and Nanotechnology, Aalborg University.
- Kim, Y.H. & Wool, R.P. (1983). A theory of healing at a polymer– polymer interface. *Macromolecules.* 16, pp. 1115–20.
- Kirschbaum, G. (2001) *Minerals on fire, Flame retardants look to mineral solutions,* 3rd Minerals in Compoundings Conference, IMIL-AMI joint conference, 8-10 April 2001.
- Klasen, H.J. (2000) A historical review of the use of silver in the treatment of burns. Part I early uses, *Burns.* 30, pp. 1–9.
- Kojima, H. (1982). *Ferromagnetic Materials: A Handbook on the Properties of Magnetically Ordered Substances.* in: E.P. Wohlfarth (Ed.), vol. 3, ch 5. North Holland, Amsterdam.
- Kumar, A., Vemula, P.K., Ajayan P.M. & John, G. (2008). Silver-nanoparticle-embedded antimicrobial paints based on vegetable oil. *Nature Materials.* 7, (3), pp. 236–241.

- Landsdown, A.B.G. (2002). Silver I: its antibacterial properties and mechanism of action. *J Wound Care*. 11, pp. 125–138.
- Laoutid, F., Bonnaud, L. Alexandre, M. Lopez-Cuesta, J.-M. & Dubois P. (2009). New prospects in flame retardant polymer materials From fundamentals to nanocomposites. *Materials Science and Engineering R*. 63, pp. 100–125.
- Lau, A.K.T., Lu, J., Varadan, V.K., Chang, F.K., Tu J.P. & Lam P.M. (2008). Multi-functional Materials and Structures. *Advanced Materials Research*. 47, pp. 920-923.
- Leaper, D.L. (2006). Silver dressings: their role in wound management. *Int Wound J*. 3, (4), pp. 282–294.
- Lee, K.J., Lee, Y., Shim, I., Jun, B.H., Cho H.J. & Joung, J. (2007). Large-scale synthesis of polymer-stabilized silver nanoparticles. *Sol St Phen*. 124, pp. 1189–1192.
- Leroux, F. & Nanosci J. (2006), *Nanotechnol*. 6, p. 303.
- Li, B., Liu, X., Cao, C., Meng, F., Dong, Y., Cui, T., & Ding, C. (2008). Preparation and antibacterial effect of plasma sprayed wollastonite coatings loading silver. *Applied Surface Science*. 255, (2), pp. 452-454.
- Li, G. (2009). *Antibacterial nanotechnology multi-action materials that work day and night*. Nanowerk, Tsinghua University.
- Li, Y. *et al* (2007) Synthesis and Electro-magnetic Properties of Polyaniline-barium Ferrite Nanocomposite. *Chin. J. Chem. Phys*. 20, pp 739.

- Li, Y., Leung, P., Song, Q.W. & Newton, E. (2006). Antimicrobial effects of surgical masks coated with nanoparticles. *J Hosp Infect.* 62, pp. 58–63.
- Li, Y., Zhang, H., Liu, Y., Wen, Q. & Li, J. (2008). Rod-shaped polyaniline–barium ferrite nanocomposite: preparation, characterization and properties. *Nanotechnology.* 19, pp. 105-605.
- Liau, S.Y., Read, D.C., Pugh, W.J., Furr, J.R. & Russell, A.D. (1997). Interaction of silver nitrate with readily identifiable groups: relationship to the antibacterial action of silver ions. *Lett Appl Microbiol.* 25, pp. 279–283.
- Lin, Y.C., Chen, X., Zhang, H.J. & Wang Z.P. (2006) Effects of hygrothermal aging on epoxy-based anisotropic conductive film. *Materials Letters.* 60, pp. 2958–2963.
- Liu, W.K., Karpov, E.G. & Park, H.S., (2006). *Nano Mechanics and Materials.* Wiley.
- Lkhagvajav, N., Yasa, I., Celik, E., Koizhaiganova, M. & Sari, O. (2011). Antimicrobial activity of colloidal silver nanoparticles prepared by sol-gel method. *Digest Journal of Nanomaterials and Biostructures.* 6, pp. 149-154.
- Lynch, I. & Dawson, K. A. (2008). Protein-nanoparticle interactions. *Nano Today.* Volume 3, Issue 1-2, Pages 40-47.
- Magnetic ceramics, (2012). *Ferrites: composition, structure and properties.* Encyclopaedia Britannica. Retrieved 15.08.2012 from <http://www.britannica.com/EBchecked/topic/357014/magnetic-ceramics>
- Mali, A. & Ataie, A. (2004). Influence of the metal nitrates to citric acid molar ratio on the combustion process and phase constitution of barium hexaferrite particles

- prepared by sol–gel combustion method. *Ceramics International*. 30, pp. 1979–1983.
- Matsumura, Y., Yoshikata, K., Kunisaki S.I. & Tsuchido, T. (2003). Mode of bactericidal action of silver zeolite and its comparison with that of silver nitrate. *Appl Environ Microbiol*. 69, (7), pp. 4278–4281.
- Mcdonnell, G. & Russell, D. (1999). Antiseptics and disinfectants: activity, action, and resistance. *Clin Microbiol Rev*. 12, (1), pp. 147–179.
- McGarel, O.J. & Wool, R.P. (1987). Craze growth and healing in polystyrene. *J Polym Sci Part B—Polym Phys*. 25, pp. 2541–60.
- Mendoza-Suarez, G., Rivas-Vazquez, L.P., Fuentes, A.F., Escalante-Garcia, J.I., Ayala-Valenzuela, O.E. & Valdez, E. (2002). *Mat. Let.* 57, pp. 868-872.
- Monteiro, D.R., Gorup, L.F., Takamiya, A.S., Ruvollo-Filho, A.C., Camargo, E.R. & Barbosa, D.B. (2009). The growing importance of materials that prevent microbial adhesion: antimicrobialeffect of medical devices containing silver. *International Journal of Antimicrobial Agents*. 34, (2), pp 103-110.
- Morgan, A.B., Cogen, J.M., Opperman, R.S. & Harris, J.D. (2007). The effectiveness of magnesium carbonate-based flame retardants for poly(ethylene-co-vinyl acetate) and poly (ethylene-co-ethyl acrylate). *Fire and materials*. 31, pp 387–410.
- Morones, J.R., Elechiguerra, J.L., Camacho, A. & Ramirez, J.T. (2005). The bactericidal effect of silver nanoparticles. *Nanotechnology*. 16, pp. 2346–2353.
- Mozaffari, M., Taheri, M. & Amighian J. (2009). Preparation of barium hexaferrite nanopowders by the sol–gel method, using goethite. *Journal of Magnetism and Magnetic Materials*. 321, pp. 1285–1289.

- Multifunctional materials (2012). *Center for composite materials*. University of Delaware. Retrieved 13.08.2012 from <http://www.ccm.udel.edu/Research/MFM.html>.
- Mureinik, R.J. (1997). *Flame Retardants, Minerals' growth in plastics*. Euromin'97, Barcelona, IMIL Conference, 8-10 June.
- NCCLS (National Committee for clinical Laboratory Standards) 1977. *Performance Standards for Antimicrobial Susceptibility Test*, sixth ed. Approved standard. M2-A6, Wayne, PA.
- Nejezchleba, M., Simaan. A. & Zhvzta. K. (1997). *Magnetic Structure of Hexagonal Ferrites Studied by Mossbauer Spectroscopy*. 7th International Conference on Ferrites J. Phys. IV France 07 C1-345-C1-346.
- Nemat-Nasser Si., Nemat-Nasser, Sy., Plaisted, T., Starr, A. & Amirkhizi, A.V. (2005). *Multifunctional Materials. BIOMIMETICS: Biologically Inspired Technologies*. Edited by Yoseph Bar-Cohen. CRC Press.
- Nikawa, H., Hamada, T.Y., Rahardjo, M.B. & Nakaando, S.M. (1997). Antifungal effect of zeolite-incorporated tissue conditioner against *Candida albicans* growth and/or acid production. *J Oral Rehabil.* 25, pp. 330–357.
- Olenin, A.Y., Krutyakov, Y.A., Kudrinskii, A.A. & Lisichkin, G.V. (2008). Formation of surface layers on silver nanoparticles in aqueous and water-organic media. *Colloid J.* 70 pp. 71–76.
- Onar, N. (2009). *Achieveing of steathing property with modification of electrical, magnetic and microwzve properties of textile materials by using Sol-gel technique*. PhD Thesis. Dokuz Eylul University.

- Osman, Z. & Arof, A.K. (2003). FTIR studies of chitosan acetate based polymer electrolytes. *Electrochimica Acta*. (48), pp. 993-999.
- Pal, S., Tak, Y.K. & Song, J.M., (2007). Does the antibacterial activity of silver nanoparticles depend on the shape of the nanoparticle? A study of the gram-negative bacterium *Escherichia coli*. *Appl Environ Microbiol*. 27 (6) pp. 1712–1720.
- Peniche, C., Argüelles-Monal, W. & Goycoolea, F.M. (2008). *Monomers, Polymers and Composites from Renewable Resources, Chitin and Chitosan: Major Sources, Properties and Applications*. Elsevier. pp. 517-542.
- Phil, M. (2009). *Experimental techniques*. Retrieved 09.08.2012 from http://shodhganga.inflibnet.ac.in/bitstream/10603/1305/9/09_chapter%202.pdf
- Pullar, R.C. (2012). Hexagonal ferrites: A review of the synthesis, properties and applications of hexaferrite ceramics. *Progress in Materials Science*. 57, 7, pp. 1191–1334.
- Purest colloids, (2012). *A Brief History of The Health Support Uses of Silver*. Retrieved 15.08.2012 from <http://www.purestcolloids.com/history-silver.php>.
- Puretex, (2012). *Natural silver anti-bacterial technology*. Retrieved 15.08.2012 from <http://www.hhltechnology.org/puretex>.
- Raafat, D. (2008). *Chitosan as an antimicrobial compound: Modes of action and resistance mechanisms*. ULB, Bonn.
- Rabea, E.I., Badawy, M.E.T., Stevens, C.V., Smaghe, G. & Steurbaut, W. (2003). Chitosan as antimicrobial agent: applications and mode of action. *Biomacromolecules*. 4, pp. 1457–1465.

- Rai, M., Yadav A. & Gade, A. (2009). Silver nanoparticles as a new generation of antimicrobials. *Biotechnology Advances*. 27, pp. 76-83.
- Raimondi, F., Scherer, G.G., Kotz R. & Wokaun, A. (2005). Nanoparticles in energy technology: examples from electrochemistry and catalysis. *Angew. Chem., Int. Ed.* 44, pp. 2190–2209.
- Range of spectrum, (2012). *Spectrum*. Retrieved 15.08.2012 from <http://www.h7h.org/wavelength-range-of-electromagnetic-spectrum/>
- RF Products (2004). *Introduction to microwave absorber*. Retrieved 15.08.2012 from <http://www.emishielding.com.cn/products/show.asp?id=358&gclid=CL2t6caDmLYCFURf3godKn4ARw>
- Riley, D.K., Classen, D.C., Stevens L.E. & Burke, J.P. (1995). A large randomized clinical trial of a silver-impregnated urinary catheter: lack of efficacy and staphylococcal superinfection. *Am J Med.* 98, pp. 349–356.
- Rothon, R. (1994), Mineral Requirements for Flame Retardants, *Industrial Minerals*.
- Rothon, R. (2003). *Particulate-Filled Polymer Composites*. Rapra Technology Limited.
- Sardar, R., Park J.W. & Shumaker-Parry J.S. (2007). Polymer-induced synthesis of stable gold and silver nanoparticles and subsequent ligand exchange in water. *Langmuir*. 23, pp. 11883–11889.
- Saville, P. (2005). *Review of Radar Absorbing Materials*. Defence R&D Canada – Atlantic.

- Scattering (2012). *For a short overview of how the Tyndall Effect creates the blue and green colors in animals*, Retrieved 25.12.2012 from <http://www.itp.uni-hannover.de/~zawischa/ITP/scattering.html>
- Schmidt, R. (1999). *In the line of fire, flame retardants overview*. Industrial Minerals, pp. 37-41, February 1999.
- Selvasekarapandian, S. (n.d.). *Multifunctional Materials Research Centre*. Retrieved 13.08.2012 from <http://kalasalingam.ac.in/nano.pdf>
- Shih, F.Y. & Fung, K.Z. (2006). Effect of chitosan on stabilization of acetates-containing solution: A novel precursor for LiMn₂O₄ film deposition. *Journal of Power Sources*. 159, pp. 1370–1376.
- Shrivastava, S., Bera, T., Roy, A., Singh, G., Ramachandrarao, P. & Dash, D. (2007). Characterization of enhanced antibacterial effects of novel silver nanoparticles. *Nanotechnology*. 18, pp. 103–112.
- Singh, P., Babbar, V.K., Razdan, A., Srivastava, S.L. & Puri, R.K. (1999) Complex permeability and permittivity, and microwaveabsorption studies of Ca(CoTi)_xFe_{12-2x}O₁₉ hexaferrite composites in X-band microwave frequencies. *Materials Science and Engineering, B*. 67, (3), pp. 132–138.
- Sondi, I. & Salopek, B. (2007). Silver nanoparticles as antimicrobial agent: a case study on E. coli as a model for gram-negative bacteria. *J Colloid Interface*. 275, pp. 177–182.
- Song, H.Y., Ko, K.K., Oh L.H. & Lee, B.T. (2006). Fabrication of silver nanoparticles and their antimicrobial mechanisms. *Eur Cells Mater*. 11, p. 58.

- Stec, A. (2010). *Small flame ignition and flame spread tests*. University of Central Lancashire. Retrieved 04.08.2012 from http://www.uclan.ac.uk/schools/forensic_investigative/fire_hazards_science/equipment_tests/small_flame.php
- Sun, XG., Gao, M., Li, C. & Wu, Y. (2011). *Microwave Absorption Characteristics of Carbon Nanotubes, Carbon Nanotubes - Synthesis, Characterization, Applications*, Dr. Siva Yellampalli (Ed.), ISBN: 978-953-307-497-9.
- Tan, S., Erol, M., Attygalle, A., Du H. & Sukhishvili, S. (2007). Synthesis of positively charged silver nanoparticles via photoreduction of AgNO_3 in branched polyethyleneimine/HEPES solutions. *Langmuir*. 23, pp. 9836–9843.
- Tarr, M. (2011). *Properties of laminates*. Retrieved 04.08.2012 from http://www.mtarr.co.uk/courses/topics/0140_pl/index.html
- Texcare, Retrieved 14.08.2012 from http://www.texcare.com.tw/e_product_silver_content.htm
- The History of Radar (2003). *BBC*. Retrieved 15.08.21012 from <http://www.bbc.co.uk/dna/ww2/A591545>.
- Thurman, R. & Gerba, C., (1989). A small sample of research and articles supporting the efficacy of silver as an antimicrobial agent follow: The Molecular Mechanisms of Copper and Silver Ion Disinfection of Bacteria and Viruses. *CRC Crit Rev Envir Control*. 18, pp. 295-315.
- Tian, J., Wong, K.K.Y., Ho, C.M., Lok, C.N., Yu, W.Y., Che, C.M., Chiu J.F. & Tam, P.K.H. (2006). Topical Delivery of Silver Nanoparticles Promotes Wound Healing. *Chem Med Chem*. 00, pp. 171–180.
- Ting, T.H., Wu, K.H., Hsu, J.S., Chuang, M.H. & Yang, C.C. (2008). Microwave Absorption and Infrared Stealth Characteristics of Bamboo Charcoal/Silver

- Composites Prepared by Chemical Reduction Method. *Journal of the Chinese Chemical Society*. 55, pp. 724-731.
- Tolaymat, T.M., Genaidy, A., Schekel, K.G., Luxton, T.P. & Suidan, M. (2009). An evidence-based environmental perspective of manufactured silver nanoparticle in syntheses and applications: A systematic review and critical appraisal of peer-reviewed scientific papers. *Science of the Total Environment*. 408, (5), pp. 999-1006.
- Torquato, S., Hyun, S. & Donev, A. (2003). Optimal design of manufacturable three-dimensional composites with multifunctional characteristics. *J. Appl. Phys.*, Vol. 94, No. 9.
- Trask, R.S., Williams, G.J. & Bond I.P. (2007) Bioinspired self-healing of advanced composite structures using hollow glass fibres. *J R Soc Interface*. 4, (13), pp. 363–371.
- Trask, R.S., Williams, H.R. & Bond I.P. (2007). Self-healing polymer composites: mimicking nature to enhance performance". *Bioinspiration and Biomimetics*. 2, pp. 1-9.
- Trujillo, A.P. & Thurman, H.V. (2004) *The Black Arts: Materials and Process Selection and Stealth Technology*.
- Tushar (2010). *Study of Transmitter of radar Report*. Vivekanandinstitute of Tech. And Science, Ghaziabad. UPT/982/B.Tech.
- Varshney, L. (2002). *Radar Principles Syracuse Research Corporation*. Revision No. 3. NY.
- Wang, N.S. (2012). *Glucose assa by dinitrosalictic colorimetric method*. Department of Chemical & Biomolecular Engineering University of Maryland

College Park. Retrieved 09.08.2012 from <http://www.eng.umd.edu/~nsw/ench485/lab4a.htm>

Weber, M. (1999). *Mineral flame retardants, Overview & future trends*. Euromin'99, European Minerals & Markets, Nice, IMIL Conference, 8-10 June.

Welz, B. & Sperling, M. (1999). *Atomic absorption spectroscopy*. Retrieved 10.08.2012 from http://en.wikipedia.org/wiki/Atomic_absorption_spectroscopy - cite_note-isbn3-527-28571-7-0#cite_note-isbn3-527-28571-7-0

White, S. R. (2007). Solvent-Promoted Self-Healing in Epoxy Materials. *Macromolecules*. 40, pp. 8830–8832.

White, S.R., Sottos, N.R., Geubelle, P.H., Moore, J.S., Kessler, M.R., Sriram, S.R, Brown, E.N. & Viswanathan S. (2001) Autonomic healing of polymer composites. *Nature*. 409, pp. 794-797.

Wilde, F.D., & Gibs, J. (1998) *Turbidity*. U.S. Geological Survey TWRI Book. 9, pp. 4-98.

Wool, P.R. & O'Connor, K.M. (1981). Craze healing in polymer glasses. *Polym Eng Sci* 1981, 21, pp. 970–7.

Wool, R.P., O'Connor, K.M. (1981). A theory of crack healing in polymers. *J Appl Phys*. 52, pp. 5953–5963.

Wu, D.Y., Meure, S. & Solomon, D. (2008). Self-healing polymeric materials: A review of recent developments. *Prog. Polym. Sci.* (33), pp. 479–522.

Xanthos, M. (2004). *Functional Fillers for Plastic*. NY: Wiley-VCH.

- Xiu, Z., Zhang, Z., Puppala, H.L., Colvin, V.L. & Alvarez, P.L.L. (2012). Negligible Particle-Specific Antibacterial Activity of Silver Nanoparticles. *Nano Lett.* 12, (8), pp. 4271-5.
- Yamanaka, M., Hara K. and Kudo, J. (2005). Bactericidal Actions of a Silver Ion Solution on Escherichia coli, Studied by Energy-Filtering Transmission Electron Microscopy and Proteomic Analysis. *Appld Env Microbiol.* 71, (11), pp. 7589–7593.
- Yan, J. & Cheng, J. (2005). *Antimicrobial Yarn Having Nanosilver Particles and Methods for Manufacturing the Same*. United States Patent. Patent no: US 6,979,491 B2. Date of Patent: Dec. 27, 2005.
- Yang, J., Lee J.Y. & Too, H. (2005). Core-shell Ag–Au nanoparticles from replacement reaction in organic medium. *J Phys Chem B.* 109, pp. 19208–19212.
- Yeo, S.Y. & Jeong, S.H. (2003). Preparation and Characterization of polypropylene/Silver nanocomposite fibres. *Polymer International.* 52, pp. 1053.
- Yılmaz Atay, H. & Çelik, E. (2010). Use of Huntite/Hydromagnesite Mineral in Plastic Materials as a Flame Retardant. *Polymer Composites.* 31, pp.1692–1700.
- Yılmaz Atay, H. (2008). *Use of Huntite/Hydromagnesite Mineral in Plastic Materials as a Flame Retardant*. Master Thesis, Dokuz Eylul University.
- Yoon, J.A., Kamada, J., Koynov, K., Mohin, J., Nicola,R., Zhang, Y., Balazs, A.C., Kowalewsk, T. & Matyjaszewski, K. (2012). Self-Healing Polymer Films Based on Thiol_Disulfide Exchange Reactions and Self-Healing Kinetics Measured Using Atomic Force Microscopy. *Macromolecules.* 45, pp. 142–149.
- Zang, M.Q. (2008). Self-healing in polymers and polymer composites. Concepts, realization and outlook: A review. *Polymer Letters.* 2, pp. 238–250.

- Zheludkevich, M.L., Freire, T.C.S.R., Fernandes, S.C.M., Kallip, S., Lisenkov, A., Gandini, A. & Ferreira, M.G.S. (2011). Self-healing protective coatings with “green” chitosan based pre-layer reservoir of corrosion inhibitor. *J. Mater. Chem.* 21, pp. 4805.
- Zhou, J., Ma, H., Zhong, M., Xu G., Yue, Z. & He Z. (2006). *Jour. Mag. and Mag. Mat.* 305, pp. 467-469.
- Zhuravlev, V., & Suslyayev, V. (2006). Analysis of the microwave magnetic permeability spectra of ferrites with hexagonal structure. *Russian Physics Journal.* 49, (9), pp. 119-124.
- Zwaag, S. (2007). *Self-healing Materials: an Alternative Approach to 20 Centuries of Materials Science*. Dordrecht, The Netherlands: Springer.